CRANFIELD UNIVERSITY

HUSAM FOUDEH

ADVANCED QUADROTOR CONTROL STRATEGIES
FOR HEALTH MONITORING OF OVERHEAD POWER
LINES

SCHOOL OF AEROSPACE, TRANSPORT AND
MANUFACTURING
Automotive Engineering

PhD
Academic Year: 2019–2021

Supervisors: Prof. Patrick Chi-Kwong Luk , Dr. James
Whidborne
July 2021

CRANFIELD UNIVERSITY

SCHOOL OF AEROSPACE, TRANSPORT AND
MANUFACTURING
Automotive Engineering

PhD

Academic Year: 2019–2021

HUSAM FOUDEH

Advanced Quadrotor Control Strategies for Health
Monitoring of Overhead Power Lines

Supervisors: Prof. Patrick Chi-Kwong Luk , Dr. James
Whidborne
July 2021

Abstract

Research into autonomous control and behavior of mobile vehicles has become increasingly widespread. In particular, unmanned aerial vehicles (UAVs) have seen an upsurge of interest and of the many UAVs available, the multirotor has shown significant potential in monitoring and surveillance tasks. The objective of this research's programme is to develop novel control that enable quadrotors to track and inspect on high voltage electricity networks. This is a research application that has elicited little attention. This thesis provides a succinct and comprehensive literature research in both state-of-art overhead power lines (OPL) inspection technologies, and quadrotor design and control. It proceeds to motivate, develop and evaluate a learning algorithms controller which exploit the repeated nature of the fault-finding task. Very few iterative learning control (ILC) algorithms have been implemented in this area, and no analysis or practical results exist to specifically investigate UAV performance to modelling uncertainty and exogenous disturbances. In particular, novel contributions are made in ILC algorithms are derived and validated by experimental results on an AscTec Hummingbird quadrotor. It has taken a robust comparisons among several ILC approaches (gradient-based, norm optimal and Newton method ICLs), and the comparisons are largely based on analytical calculated results.

In the case of optimal ILC approaches, a new algorithm for nonlinear MIMO systems is developed to cope with exogenous disturbances and noise severely affect UAV as well as a novel tuning method for β_{new} variation is formulated and applied to the problem of reference tracking for a 6-degree-of-freedom UAV with a two-loop structure. The first loop addresses the system lag and another tackles the possibility of a disturbance commonly encountered when inspection of OPL. The new algorithm contributes to good trajectory tracking and very good convergence speed while minimizing disturbance effects. A linearisation design approach has been extended to enable new updates using quadcopters dynamics. Then constraints have embedded to meet the application demands. After overcoming this deficiency, the ILC controller is further extended based on point-to-point through a straight conductor to fulfil the full task and perform a 2-3 sequence of operations. Finally, the ILC development results are given follow-up using 3D analysis approach where these results are the first ever in this key area.

Contents

List of Figures

List of Tables

List of Abbreviations

ACSR   Aluminium Conductor Steel Reinforced

CT   Aluminium Conductor Steel Reinforced

DNO   Distribution Network Operator

DOF   Degrees Of Freedom

LLG   Double Line Ground

EHV   Extra High Voltage

GPS   Global Positioning System

HV   High Voltage

HVDC   High Voltage Direct Current

ILC   Iterative Learning Control

IMU   Inertial Measurement Unit

LG   Line Ground

MIMO   Multi Input Multi Output

OFGEM   Office of Gas and Electricity Markets

PD   Proportional Derivative

SISO   Transmission Network Operator

SATM   School of Aerospace, Technology and Manufacturing

TNO   Single Input Single Output

UAV   Unmanned Aerial Vehicle

UGV   Unmanned Ground Vehicle

VT   Voltage Transformer

List of Nomenclature

Chapter 2

$\delta(x)$ Additional sag

θ_p Angle by motor passively rotate around the pivot

θ_m Angle by rotating single motor toward the cable

L Horizontal spacing

P_1 Suspension point first the tower

P_2 Suspension point second the tower

$\dot{H}$ Vector of the magnetic field generated by the 3-phase OPL

Chapter 3

U_1 Thrust virtual control input

U_2 Roll virtual control input

U_3 Pitch virtual control input

U_4 Yaw virtual control input

p Angular velocity in the body frame around x axis

q Angular velocity in the body frame around y axis

r Angular velocity in the body frame around z axis

ξ Angular frequency

η Euler angles

ω Angular frequency of the ith rotor

ι_{xx} Inertia on x axis

ι_{yy} Inertia on y axis

ι_{zz} Inertia on z axis

m System overall mass

T Thrust force

θ Pitch angle

ϕ Roll angle

ψ Yaw angle

τ Vector of torque

v Linear velocities

$\mathbf{q}_{\Theta}$ Joint angle vector

I Identity matrix

C_T Thrust coefficient for rotor

C_D Drag coefficient for rotor

ρ Density of air

A_r Cross sectional area of the propeller rotation

r   Radius of the rotor

R   rotation matrix

Chapter 4

$\mathbb{R}$ Field of real numbers

$\mathbb{C}$ Field of complex numbers

$\bar{\sigma}$ Maximum singular value

$\times$ Cross product

$\mathbb{N}$ Set of non-negative integers

$\mathbb{R}^n$ Set of *n* dimensional real vectors

$\mathbb{R}^{n \times m}$ Set of $n \times m$ real matrices

$\mathbf{x_k}(t) \in \mathbb{R}^n$ State vector

$u_k(t) \in \mathbb{R}^m$ Input vector

$\mathbf{y_k}(t) \in \mathbb{R}^p$ Output vector

$\mathbf{A} \in \mathbb{R}^{n \times n}$ System matrix

$\mathbf{B} \in \mathbb{R}^{n \times m}$ Input matrix

$\mathbf{C} \in \mathbb{R}^{p \times n}$ Output matrix

L   Learning operator

y_d Desired reference signal

e_k Tracking error

n_r System relative degree

k Trial number

u_k Control input effort

$\bar{A}(t), \bar{B}(t), \bar{C}(t)$ Linearized time-varying system dynamics matrices

γ Constant learning gain of P-type

L Cartesian product of two spaces $\mathbb{X}$ and $\mathbb{Y}$

$\mathbb{X} \times \mathbb{Y}$ Learning operator

β Learning gain

G^T Transpose operator

G^* Adjoint operator

t Time

$L_2^\ell[0,T]$ Space of functions defined on $[0,T]$ whose function value
          belongs to $\mathbb{R}^\ell$ and 2 power is Lebesgue integrable

$L_2^\ell[0,N]$ Space of $\mathbb{R}^\ell$ valued Lebesgue square-summable sequences
          defined on an interval $[0,N]$

R Cost of using the input

Q Cost of deviation from the reference signal

J Cost function

K_p Proportional gain

K_i Integral gain

K_d Derivative gain

T_s Sampling time

Acknowledgements

I would like to thank my supervisor Professor Patrick Luk for his supervision and experienced guidance. His continuous support and encouragements gave me confidence in my work and abilities and helped me complete my project successfully. I would also like to thank my second supervisor Dr. James Whidborne for his valuable discussions, cooperation and support.

This journey would not have been pleasant without my family in Jordan and Algeria. I owe every part of this work, my education and every step forward in my life to both my parents and wife. I would like to thank them for their love, support and encouragement.

Chapter 1

Introduction

1.1 Overview

Unmanned Aerial Vehicles (UAVs) are being increasingly applied to commercial as opposed to solely military applications. UAVs are capable of flying and performing various tasks without necessitating pilot involvement. They may also be designed to operate on the ground or even under water. Primary fields of commercial and research interest include surveillance, monitoring, and object tracking systems. Autonomous UAVs have been used to move goods in industry and to deliver products/services directly to customers' homes. These vehicles have also exhibited significant potential in applications, including disaster monitoring (the natural disasters of Indonesia and the earthquake in Nepal), 3D mapping, and aerial photography. Recently, an American presidential candidate proposed using UAVs for monitoring USA borders as a countermeasure against illegal immigration.

The global UAV payload market was valued at \$43.7 billion at the end of 2012, and is estimated to increase to \$68.6 billion by 2022 [1]. The number of UAVs has increased dramatically in civilian use; for example, in the U.S., the registered number of UAVs in use exceeded 200,000 during the first 20 days of January 2016, just days after the USA Federal Aviation Administration (FAA) started requiring owners to officially register [2].

1

The growing popularity of UAVs is partly attributed to the fact that they have a non-contact and can attain the required heights/positions needed comparing with Unmanned Ground Vehicles (UGVs) in recent years. These autonomous ground vehicles are relatively uncomplicated to control by the operator via the remote use of sensors and video cameras. However, over the last decade, a range of technological advancements in both hardware and software has led to the low cost realisation of UAVs. The superiority of UAVs in terms of workspace and manoeuvrability comes at the expense of their visceral difficulty to stabilise and control. This, in turn, has led to the emergence of automated control techniques applied to UAVs. Moreover, UAVs also have the same challenges as UGVs in terms of path planning, obstacle avoidance, navigation, and collaborative formation behaviour.

The myriad features that make UAVs more advantageous to land based vehicles have been examined in their numerous application areas, of which many would be impractical for ground-based vehicles. This thesis addresses an application area with similar potential that has remained unexploited.

Electrical power lines are a vital component of the power sector and it is essential to carry out preventive maintenance of high voltage transmission lines in a safer and more efficient manner with a view to meeting the rising consumer demand (major industrial/local). However, numerous faults face overhead electricity lines, including snow accumulation on exposed electrical conductors, system architecture is fraught with threats of collapse owing to harsh conditions, wind pressure, corrosion (small holes in the metal), temperature variation and natural ageing due to fractures or damage (ageing or degradation of the equipment). Accordingly, the most vulnerable parts (specifically for a fixed configuration of cable, fittings and pylon features) of the transmission system are needed more inspection compared to other objects. These starting with judgement at a single fault point (single power line, or insulators) and then judging the combination of fault points (obstacles and dealing with different cable structures). Typically, this causes loss of one or more phases. Transmission lines alone represent between 5 and 10 percent of the total cost

of electricity [3]. Significant damage may be inflicted to the Extra High Voltage (EHV) or High Voltage (HV) network. For instance, following the storm in France, approximately 8 percent of the EHV/HV transmission network was out of action in December 1999. It took six months to completely repair the lines at an estimated total cost of 150 million euros [4]. This issue could have been resolved more rapidly by swifter identification of faults.

Frequent inspection is also a key factor in achieving an OPL network that is resilient to adverse weather conditions. This is particularly important for today's OPL network in face of global climate change and aging assets after a long service life, and increased inspection frequently is therefore desirable, but economically infeasible for traditional manual inspection technology. UAVs has been introduced by industry for OPL inspection as one of the automated inspection technology in the last decade. The challenges are that the UAVs carry out a number of tasks, such as precise position control in the face of disturbance such as wind and severe noises, automatic power lines tracking, obstacle avoidance, precise image acquisition, automatic fault detection, measuring OPL safety distance, etc. To achieve them all is not trivial.

This thesis will develop UAV technology to address the aforementioned limitations of monitoring and surveillance of high voltage power lines. It will utilise the potential manoeuvrability of UAVs in this area, where hitherto little attention has been paid for inspection the full tasks of objects through OPL repeatedly. Furthermore, the thesis will seek to produce high performance solutions for automating tasks in inspection, monitoring, and identifying faults on HV electricity grids. Since this is an onerous task due to the structure and components of the system, which comprises power lines, insulators, and pylons of various structures. So, it will require more advanced controllers than currently exist (for example, the feedback control can't achieve accurate tracking performance).

In particular, since the inspection is intrinsically repetitive task and the repetitive nature of the power line geometries lends itself to this approach, where the Learning-type control strategies are forming the basis for a power line inspection system. Accordingly,

learning-type control with a similar strategy can be classified into iterative learning control (ILC) and repetitive control (RC). Whilst ILC strategies modify the input signal (i.e., the control input) in discontinuous operation which significant in repetitive task in OPL to the setting of the initial conditions for each trial, RC methods are intended for continuous operation. Additionally, ILC usually guarantees fast convergence within just a few iterations, but the alternative RC strategies may not. This leads to underscore the importance of developing ILC algorithms for high performance tracking.

ILC has been applied to quadrotors, but only using basic approaches. It has some advantages for PID based as it has no model and they have produced only low levels of performance. These include Proportional-type ILC and Derivative-type ILC, and assume that the reference profile, r, is specified over the entire finite time horizon, $[0, T]$. The thesis has achieved many novelties to address this issue by applying a range of ILC algorithms to quadrotors dynamics, for 1 DOF, 2 DOF, 3 DOF, and 6 DOF scenarios. These include the Gradient, Norm Optimal, and Newton Methods. A new test bed design has been constructed and used to evaluate performance. Then, several new algorithms designs for nonlinear systems are formulated premised on extensions to Newton method-based ILC, but they embed greater freedom in update the permissible structure.

Further extensions have been accomplished to increase robust performance by embedding a constraints associated with the HV line tracking problem (where the output signal is not critical at every time instant, t, along the time horizon). Specifically, they employ point to point framework, while embedding straight line tracking constraints that require the quadrotor to move along the cable. By relaxing the task description in this manner, greater speed and robustness are anticipated. This is important to cope with weather, exogenous disturbances, etc.

1.2   Motivation

The technology of UAVs has certainly matured to meet the level where numerous applications require a healthy, high-precision surveillance system. In fact, many features make the UAVs technology gain superior reliability in the area of monitoring and surveillance system due to their manoeuvrability, accuracy, faster than traditional methods, runtime, non-contact, and versatile platform, thereby promising great utility for future applications. Despite the level of maturity of UAV technology, its application against the backdrop of the challenges faced by state-of-art inspection OPL technologies have many limitations, especially in, not economically viable, time consuming, visual inspection (specifically in the hidden object detection), cover the small scale area, trial-and-error switching, manual process and safety factors. This is mainly because the technology is still undergoing continuous research and development and there are no existing unified framework of applications.

Another urgent gap where no existing approaches have capable of performing high traceability, but need good stability to cope with the weather, exogenous disturbance during inspection processes. This gap appears in UAVs inspection where lacks advanced control (i.e., ILC designs) that have the potential to provide accurate demand in the trajectory tracking, only applied in the configuration SISO rather than MIMO, this is one area that needs significant research. The time has now come to take drone technology to the next level by introducing applications and concepts that would not be possible without it. Concepts such as advanced control strategies and obstacle avoidance, OPL health monitoring across automated vehicles, task automation in inspection, monitoring, and fault identification on high-voltage electrical networks are all examples of what drones are capable of achieving.

1.3 Aims and Objectives

The research project aims to develop advanced control strategies for quadrotors in inspection of OPL that can lead to enhance the stability and agility of movement of a scaled quadrotor amid the presence of wind disturbances and noise which produce high performance solutions. Accordingly, the objectives of this research project can be summarised as follows:

- To design, implement, and evaluate optimal ILC algorithms, namely Gradient-based and Norm Optimal for a UAV model. This includes the formulation of new generalized ILC approaches that leads to good trajectory tracking, convergence speed, and the ability to cope with exogenous disturbances such as wind gusts.

- To develop, simulate and evaluate, further extensions have been achieved to ensure robust performance and inspect more critical points in OPL through the novel point to point ILC.

- To validate and assess the performance of the extended novel ILC algorithms against baseline PID control, Gradient, Norm Optimal and Newton Method, and point to point ILC.

- To evaluate system performance in simulation results of the extended point to point ILC conducted on overhead power line scenarios through (i) their own merits and (ii) hybrid structure combined with feedback controllers.

1.4 Methodology

So far, the research into UAV technology for fault detection in OPL has focused on ILC approaches sequentially in order to improve tracking performance, accuracy, and efficiency. New purpose-built platform and expansion of the state-of-the-art ILC design methods have been developed to improve the performance of the quadrotor model, convergence speed, and minimal tracking error. Although the ILC designs in scheme of linear SISO systems has been shown to operate well, research for nonlinear MIMO systems re-

mains very limited. Therefore, only a few applications have been reported in literature, and minimal benchmarking has been undertaken using the rudimentary ILC framework. Therefore, this thesis mainly focuses on the schemes of nonlinear MIMO systems rather than SISO schemes.

Referring to the Figure 1.1 that shows a block diagram describing the methodology. There are two main parts:
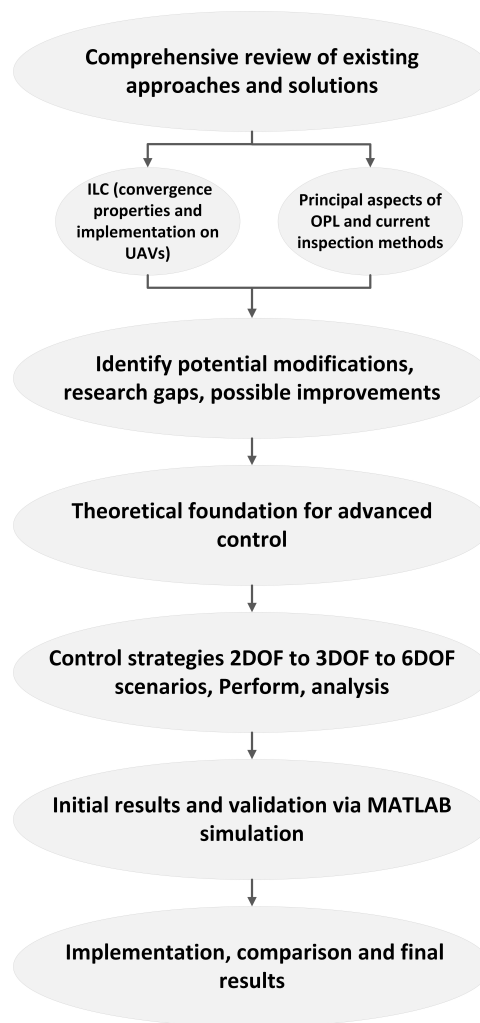
FIGURE 1.1: Methodology overview

1) Theoretical foundation for advanced control

These involve the following methodologies:

- A dynamic model of the quadrotor is derived and the procedure for is elucidated identifying the associated parameters.

- Development of advanced control strategies, centred on ILC, has been undertaken using MATLAB software tools in simulated models.

2) Implementation and validation

This includes experimental implementation of control strategies developed in the simulated models, based on a prototype quadrotor to be tested on a dedicated bench, so as to allow the measurement and benchmarking of key performances. A new set of performance metrics are established for the quadrotor in OPL monitoring applications. These involve the following:

- A dedicated test bed is designed and constructed for performance evaluation.

- A range of model based ILC algorithms have been initially implemented to quadrotors dynamics, for 6 DOF scenarios. These include Gradient, Norm Optimal, Plant inversion, Newton Method, and Hybrid ILC; (includes combined LQR and PID scheme) with ILC frameworks for MIMO systems.

- Several new algorithms designs for nonlinear systems have been simulated. These are premised on extensions to Newton method based ILC, but are embedded with greater freedoms in updating the permissible structure.

1.5   Thesis Structure

In Chapter 2, the motivation of this research is established by reviewing the principal aspects of the transmission line, including the existing methods of inspection of cable fault and cable discontinuities. This reflects the need for autonomous control in this sector of industry. Specifically, the chapter commences by providing a brief overview about the components of a power system and classification of faults covering the principles of inspection techniques, the most popular methods of inspecting methods identified by the Distribution Network Operators (DNOs) and Transmission Network Operators (TNOs). Methods of UAVs and climbing robot-based approaches are then presented to produce an automated system. The chapter ends with several suggested concepts and applications

which can be potentially implemented with UAVs technology.

Chapter 3 describes the principle of operation of UAVs and reviews the models of quadrotors encompassing the kinematics and dynamics of its frame, the properties of its actuators, its surroundings, and associated aerodynamic effects. The chapter then reviews and evaluates the current quadrotor control approaches and introduced a more accurate motion control approach to provide a better understanding of the UAV-based inspection of HV systems with faster flight times.

In Chapter 4, general background information and current research are ILC is discussed. This is followed by an overview of ILC with emphasis on important criteria such as convergence properties and practical implementation for engineering system UAVs. Subsequently, several leading ILC structures are introduced with special focus on optimization based ILC approaches. The chapter ends with a summary and comparison of the presented algorithm approaches and topologies.

Chapter 5 formulates new generalized ILC approaches which extend Newton method based ILC. Subsequently, a dynamic model of the quadrotor is derived, following which the procedure for identifying the associated parameters is explicated. Experimental control approaches are then benchmarked experimentally using this model and the quadrotor hardware. Thereafter, experimental results are presented for each tuning ILC approaches.

Chapter 6 focuses on novel controller design to address the limitations of the standard ILC framework and both gradient ILC and NOILC in inspection HV. The class of algorithms is named point-to-point and the methodology can be extended to the majority of ILC techniques. This chapter also analyzes the method in comparison with standard controllers. This chapter demonstrates how performance to associate closely with the embedding straight-line tracks constraints that require the quadrotor to move along the cable at a greater speed, a finding that is supported by extensive implementation results.

Finally, Chapter 7 reviews the outcomes of the work presented in this research project and concludes the thesis. This chapter also presents recommendations for future work.

1.6 Contributions

The work in this research has resulted in the following contributions:

- A more accurate technology of UAV trajectory tracking during the OPL inspection has been introduced. Nonlinear ILC design is identified as an enabling technology for a 6-DOF quadrotor in OPL inspection. The developed nonlinear MIMO framework can determine how the UAV carries out a number of tasks, such as precise position control in the face of disturbance and automatic OPL tracking.

- ILC controller combined with a hybrid PD/PID control for a UAV model has been developed featuring simplicity, the basis for a power line inspection system due to the repetitive nature of the power line geometries lends itself to this approach and improves the robustness/tracking performance of the UAV model when compared with other complex control methods.

- A novel method of optimal ILC approaches based on nonlinear MIMO systems with a two-loop structure has been formulated and applied to the problem of reference tracking for UAV. The improved method is contributing to good trajectory tracking and very good convergence speed while minimizing exogenous disturbances.

- Novel tuning methods have been presented which is based on iterative real-time auto-tuning of modified parameters β_{old} rather than heuristically selecting from the previous range. The tuning method calculates the new optimal β_{new} parameters during the flight from the establishing of varying gain equations and minimising the cost function.

- Several new algorithm (PID-type, gradient-based, norm optimal) designs for nonlinear systems have been formulated. These are premised on extensions to a novel Newton method based ILC, but embed greater freedom in updating the permissible structure.

- Further extensions of point-to-point ILC have been accomplished through a straight conductor for the overhead line monitoring task. This allows for enhanced performance by embedding the constraints associated with the HV line tracking problem.

- A 3D analysis approach has been applied to the convergent property of the proposed ILC point to point law, thus supplying a new tool for follow-up ILC development for 2D systems.

1.7 Publications

The publications of this thesis are the following:

- H. A. Foudeh, P. Luk, and J. F. Whidborne. Application of norm optimal iterative learning control to quadrotor unmanned aerial vehicle for monitoring overhead power system. *Energies*, 13 (12):3223, 2020.

- H. A. Foudeh, P. Luk, and J. F. Whidborne. Quadrotor system design for a 3dof platform based on iterative learning control. *In 2019 Workshop on Research, Education and Development of Unmanned Aerial Systems (RED UAS)*, pages 53–59, Nov 2019.

- H. A. Foudeh, P. Luk, and J. F. Whidborne. An Advanced Unmanned Aerial Vehicle (UAV) Approach via Learning-based Control for Overhead Power Line Monitoring: A Comprehensive Review. *IEEE ACCESS* ,03 September 2021.

- H. A. Foudeh, P. Luk, and J. F. Whidborne. Extended of Iterative Learning Control (ILC) with Highly Convergent for Multirotor in Overhead Power Line inspection. *IET Control Theory & Applications*.

Chapter 2

High Voltage Fault Inspection Approaches

2.1 Introduction

Modern electrical power systems are intrinsically complex and sophisticated. In many countries, they extend for very long distances and are interconnected between countries. An example is the existing bi-directional link between Britain and France based on 2,000MW High Voltage Direct Current (HVDC) infrastructure [5]. Electrical power systems comprise power lines distributed through overhead lines, as evidenced in Figure 2.1, underground cables and submarine cables in some cases.

Damage can occur to these components in numerous ways, thus triggering a total breakdown of the network. In addition, significant impact such as problems in maintenance, time, and effort may be expended on identifying the location of failure. Regulatory action of non-ministerial UK government departments such as OFGEM (Office of Gas and Electricity Markets) imposes various demands to guarantee the quality of supply besides ensuring the reliability of the electrical network [6]. Heavy fines are imposed on the failure to comply with these regulations.

Distribution Network Operators (DNOs) and Transmission Network Operators (TNOs)
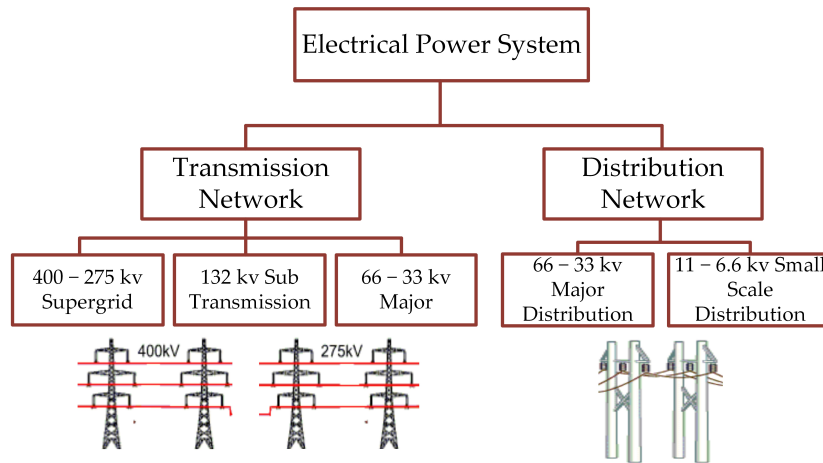
FIGURE 2.1: Electrical power network structure with pre-determined voltage levels.

are responsible for maintaining the network. They spend huge amounts of money on inspecting the status of their overhead lines spread over many thousands of kilometres. Table 2.1 illustrates the expenditure required to maintain different types of conductor in the UK system and the responsibilities of the DNO and TNO. This guarantees the sustainability of network stability and minimizes the number of faults that develop due to critical weather conditions [7]. However, faults are always present and DNOs and TNOs are constantly under pressure to rectify the situation as soon as possible whenever it occurs.

TABLE 2.1: The approximate length and cost of conductor line owned by typical DNOs and TNOs

Company	Length of Line	Type of Conductor			
		Overhead		*Underground*	
		Capital Build Cost Per km	Maintenance Per km	Capital Build Cost Per km	Maintenance Per km
National Grid (TNO)	7,000 km	£1.6m	£4.0m	£16.7m	£18.9m
Western Power Distribution (DNO)	92,000 km	Depending on size cable	£800	Depending on size cable	£1,000

The Network Losses in the UK for both TNOs and DNOs such as - SP Energy Networks, Electricity Northwest, Northern Power Grid, UK Power Networks, SSE, Western

Power distribution and NIE are illustrated in Table D.1. The DNOs and TNOs often use conventional OPL methods to provide protection to the power grid, including foot patrol, visual inspection, and mechanical devices. Devices employed to protect the power network include switchgear, instrument transformers such as a Current Transformer (CT), Voltage Transformer (VT), or potential transformer and associated protection relays.

The usage of conventional methods is the preferred choice as it entails a simple inspection, with devices being stationary and motionless. However, network reliability and stability is under permanent and continuous threats such as environmental threats, operational threats, human, and animal threats. Accordingly, due to difficult weather conditions and long-distance for OPL, companies must impose preventive methods of pre and post observation protection. Relying on conventional methods to minimize the risk and execution of complex tasks within power systems may no longer be a practical solution. Therefore, new live operation applications (i.e., unmanned systems) that are mobile/non-contact and guarantee safety of tasks are being developed.

Inspection via unmanned systems (i.e., climbing robots, UAVs), instead of using conventional methods may seem a plausible alternative to survey the condition of overhead line supports and insulators due to the potential to save energy, time, and money. In addition, the assessment of the OPL elements condition can be done at any time of the day, as well as in bad weather conditions. However, many design challenges and technological obstacles need to be addressed. The following literature review aims to:

- Present the current knowledge about the components of a power system as well as classification of faults.

- Discuss the most popular methods of inspection faults identified by DNOs and TNOs.

- Introduce the inspections propagation models for UAVs and robot-based approaches.

- Review the current research state in UAVs based inspection approach.

- Identify the gaps in UAVs based inspection approach that require further investigation and research.

2.2   Current Methods of Inspection Faults by DNOs and TNOs

The power system components that are most susceptible to natural hazards include the transmission and distribution lines which have the most extreme working conditions, and are subject to numerous types of faults. For example, the installed system may cause repeated failure over a distance of 3 km in 500 kV transmission lines in rough terrains such as mountainous areas in the Liangshan region of China. This is caused by a small error generating a sequence of failures extending long distances until a point of failure is found. The maintenance crew may have to walk 6 km in mountainous areas to determine the exact location of the fault point [8]. In 2003, outages of the power grid in the Northeastern United States and Canada demonstrated that transmission faults can have a devastating impact on the national grid and on interdependent systems such as telecommunications networks [9]. A recent study showed that the failure of transmission lines during winter caused by snow accumulation on aluminium conductor steel-reinforced (ACSR) cable in Jordan caused severe difficulties for the maintenance crew [10].

The complexity of most power grids often makes it difficult to identify faults, especially as there are many types of power failure in an Overhead Transmission (OH) line. Examples include storms, lightning, freezing rain and fog, partial discharges (corona), insulation breakdown, and short circuits caused by birds or other external objects coming into contact with the line, or tree branches hitting the lines [11]. These causes are summarised in Figure 2.2. Faults on transmission lines can generate a huge current flow through the cables, unbalance the phases, or create under voltage. When a fault occurs, the characteristic impedance values can change dramatically,causing an interruption in operation of the power system, electrical fires, and various failures of associated equipment [12].

In a three phase transmission line, faults can be classified as: single Line to Ground (LG), Double Line (LL), Double Line to Ground (LLG), and three phase to ground

[13, 14]. Statistics such as those compiled by authors in [15] have shown that LG faults are the most common type in power systems. According to the statistics provided by authors in [16], more than 90% of overhead transmission line fault consisted of LG faults. The proportion of LG faults occurring on 220 kV transmission lines is 87.07%, and the percentage increases drastically for 330 kV transmission lines to 98.11%, and is 92.68% for 500 kV lines.
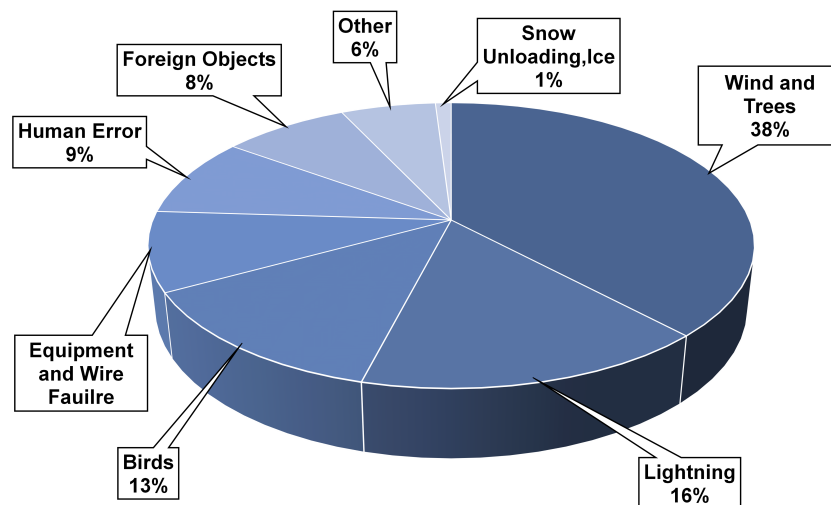
FIGURE 2.2: Causes of faults on distribution networks.

Some faults may be avoided through design. The authors in [17] pointed out that the faults involving conditions such as wind pressure, snow, and temperature variation on the transmission line can be mitigated by designing the system to meet the corresponding mechanical loading demand. Mechanical consideration in the design could be leveraged to avoid a serious deterioration caused by these effects, at the cost of added expense. However, the DNOs and TNOs must still monitor cables personally to detect anomalies or malfunctions which may accompany the critical conditions for dynamic line rating.

One of the main objectives of the inspection by TNOs and DNOs is to check fittings (i.e., dampers and spacers) on a HV power line to identify the; (1) abnormal points and (2) assess the surrounding environment of lines as shown in Figure 2.3. This enables TNOs and DNOs to obtain sufficient information access on the failure points. The abnormal

points recognized through inspection steps mainly include; (i) preliminary inspection and (ii) autonomous inspection [18]. For the latter, there is ongoing investigation. In general, this preliminary step is performed via the inspection objects on HV power line, which, in turn, is classified into five categories depending on geometric characteristics, position, type, structure, the merits, as well as the demerits of these techniques as presented in Table 2.2.
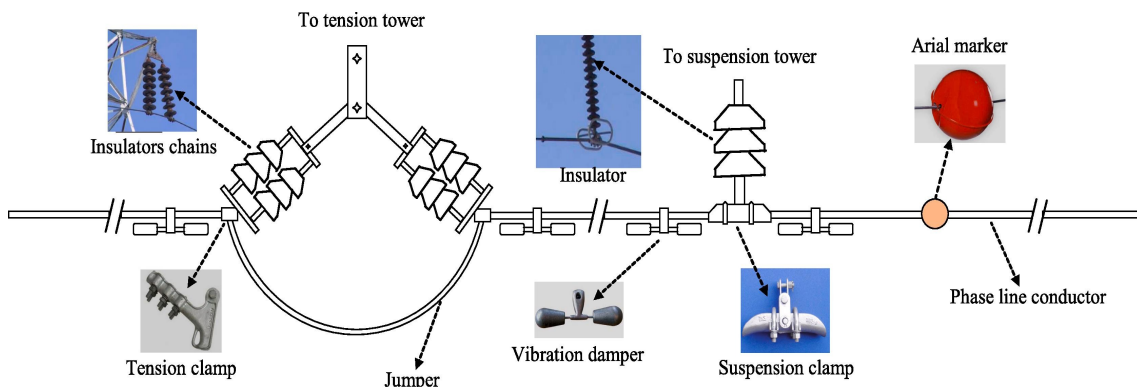
FIGURE 2.3: The major components in the OPL geometric consist of devices and obstacles [19].

The most common method to detect line faults is based on visual inspection, which may be conducted via a helicopter or four-wheel drive vehicle, in addition to primitive methods based on the technique of load separation and identifying faults [20, 21]. The studies in [22, 23] and [24] showed that the process of visual inspection may involve getting a complete, continuous picture of conductor behavior along with thermal images (observing hot spots on cables as evidence of presence faults). Visual inspection may have multiple aims, including thermographic fault detection with infra-red cameras, visual line inspection with video cameras, and insulator fault detection with ultra-violet cameras.

Traditional methods of detecting location faults are often economically unfeasible and may not ensure the quality/reliability of the network over time. For example, a comprehensive review in [25] showed that the Ofgem and Western Power Distribution estimated the level of unplanned outages to be £300.28 million in Great Britain. This reflects the increased number of disconnection faults based on conventional methods along with the

TABLE 2.2: Characteristic rules for current methods of inspection targets in power system

Object Name	Target	Features location/shape	Task	Techniques	Merits	Demerits	Ref.
Tower (T)	Tower (torsion, suspension, anchor, beeline...etc) (T$_1$)	Attached to the power line, T shape, Cylindrical structure	The main aims are to inspect the electrical equipment on T$_1$ (Lightning arresters,..) and structures of Transmission/Distribution	Patrol Crew, Helicopter, Video cameras	Fastest, Quickly and easily reach the tower, Not restricted by region, Ability for long-distance inspection, Unlimited loading of equipment, Contactless sensing methodology	Less safety and security inspection service, High maintenance cost, Manual process, Inaccurate, Highly influenced by the operating environment (higher buildings in urban areas, weather-dependent)	[26, 27]
	Overhead ground wires (T$_2$)	Attached to upper portions of the power line, Line shape	The main aims are to inspect the strands broken by lightning, burnout of T$_2$ due to the electric discharge	Patrol Crew, Helicopter	Fastest, Not restricted by region, Ability for long-distance inspection, Contactless sensing methodology	Less safety and security inspection service, High maintenance cost, Manual process, Highly influenced by the operating environment (higher buildings in urban areas, weather-dependent)	[28, 29]
Line (L)	Phase Conductor (L$_1$)	Attached to the power line, Curve shape	The main aims are to inspect the cracking/rupture, Broken strand, Detect temperature increase /Overheating, Increase of resistance, Check the condition of zinc layer and corrosion L$_1$	Mechanical devices, (i.e., hot stick), Impedance-based (IB) techniques, Travelling-wave (TW) techniques, Video cameras	Simple implementation, Not complex, live-line working, Contact/Contactless sensing methodology	Trial-and-error switching, Long distance to inspect, Inaccurate, High maintenance cost, Damage of object, Time consuming, No sufficient acquisition of information, Requiring measurements with a very high sampling rate, Dependent on line parameters estimation, Very limited field tests in distribution networks	[30], [31], [32, 33]
Insulators (I)	Insulators string (I$_1$)	Attached to the power line, Circle shape	The main aims are to repair and replace electrical devices on Insulators and to detect partial discharge, I$_1$ replacement	Patrol Crew, Mechanical devices (i.e., ROBTET), Helicopter, Elevators (i.e., Elevator I,II,...), Ground Vehicles (i.e., Four wheel car, Boom Truck)	Short distance, Not Safe, less time, Contact/Contactless sensing methodology	Overlapping due to shooting distance, Effect angle of aerial images by Helicopter, Trial-and-error switching, Damage of object, Manual process, No sufficient acquisition of information, Highly inaccurate,	[34, 35]
	Insulators unit (I$_2$)	Attached to the power line, Circle shape	The main aims are to inspect and replace electrical devices on I$_2$ and to detect partial discharge, Loss of insulation, Electrical flashover, Pinpoint corona and arcing	Patrol Crew, Helicopter, Mechanical devices, Elevators (i.e., Elevator I,II,), Ground Vehicles (i.e., Four wheel car, Boom Truck)	Short distance, Not Safe, Less time, Contact/Contactless sensing methodology	Environmental conditions (i.e., light intensity, weather, and distracting background), Camera stability, Trial-and-error switching, Manual process, Time consuming, No sufficient acquisition of information, Not simple implementation,	[36, 37]
Fitting (F)	Vibration damper (F$_1$)	Artificial facility Attached to the power line, T shape	Inspection of Electrical Devices (i.e., Break Circuit), Drooping or missing Damper Slipping	Visual inspections, Inspection from the ground, Carts, Arm with Blades,	Live-line working, Contact/Contactless sensing methodology, Simple	Unreliable due to potential risks on crews (i.e., live work), High maintenance cost, Manual process, Time consuming	[38]
	Clamps (F$_2$)	Artificial facility Attached to the power line, X shape	Detect broken strands at clamps end, Missing nuts from clamps	Climbing and Visual inspection, Mechanical devices Arm with wrench	Safe, Simple, Contact/Contactless sensing methodology	First breaks occur under clamps and are not detectable, Damage of object, Manual process, Time consuming	[39]
	Spacer (F$_3$)	Artificial facility Attached to the power line, X shape	Inspection of failures, Defective spacers, Loosened spacers	Climbing and Visual inspection, Mechanical devices, Video cameras	Safe, Simple, Contact/Contactless sensing methodology	First breaks occur under spacers and are not detectable, Damage of object, Manual process, Time consuming	[40]
Environment (E)	Tree crown (E$_1$)	Under the power line (Large size), Sphere shape, Planar shape, Irregular shape	The main aims are to install patches on the road and to eliminate E$_1$ around transmission lines, Management of vegetation encroachment and Creeping	Patrol Crew, Ground Vehicles, Mechanical devices, Arm with Blades (i.e., tree trimming),	Safe, Very simple, Contributes to protection From future faults, Economic feasibility, Contact sensing methodology	High maintenance cost, Manual process, Time consuming	[41, 42]

probability of faults times, and the failure rate tending to be worse on 132 kV lines.

Consequently, there is a close relationship between the time needed to determine the faults and maintenance strategy, which is critical to the cost. Therefore, the authors in [43] and [44] concluded that life cycle cost (LCC) analysis is useful for customizing the inspection and maintenance strategies which, in turn, impacts the quality and overall effectiveness of both power networks and delivery. Recently, these ideas are gaining growing traction due to increasing efforts to pursue profit and the fact that modern policies for liberalization of power and global energy markets may lead to declining reliability levels in electrical transmission systems and stress in operation.

Through the above review, the DNOs and TNOs have been performing traditional techniques for fault inspection based on visual inspection, for a small scale area (i.e., foot patrol) and larger scale area (i.e., helicopter or automobile). The intrinsic limitations of the conventional techniques based on visual inspection pose more problems than solutions. Trial-and-error switching, high maintenance cost, long term damages to HV lines equipment,and time consuming, manual processes are considered some of the major setbacks of inspection techniques.

Due to these predicaments, a substantial quantity of literature has been published on the development of new approaches to identify fault locations for accelerating the operation of locating faults [45–47]. In [32], the authors stated that faults may be divided into temporary or permanent: the former category includes line shorts to earth through tree branches, whereas the latter includes conductor or pinholes in the insulator. Typically, the relays and locator devices can track the location of both temporary and permanent faults as well as the response time after occurring in the power system. However, there is no clear assessment of mechanical damage after permanent faults. Conversely, temporary faults can be cleared automatically if the location of the fault is located. Thus, temporary faults can expedite the restoration of the line or be estimated with reasonable accuracy [33].

Researchers are attempting to locate a dependable and efficient method to fault location identification. The conventional methods currently in used for fault locating meth-

ods can be divided under three headings; (i) impedance-based (IB) techniques [48], (ii) travelling-wave (TW) techniques [49] and (iii) artificial intelligent techniques [50–52]. For these techniques, it is necessary to sense the magnetic field caused by current flows through a cable or conductor. A device such as a fault indicator can be installed either in a substation or on a tower over an overhead electrical transmission line. These have several merits and demerits when it comes to composed fault location identification techniques [33].

In the above section, we have provided an overview of significant traditional methods inspection of power systems. In the next two sections, we will address the limitations of traditional methods and focus on the new promising techniques. In particular, UAVs and climbing robot-based approaches have been used to produce an automated system. This, however, is a challenging task due to the structure and components of the system, which comprises power lines, insulators, and pylons of various structures.

2.3 Electromechanical Method for Inspection HV

Robotic devices or climbing robots were initially developed for the inspection of transmission lines over two decades ago. Their introduction was motivated by safety factors, the need to access remote areas, and increased operational efficiency. Due to their direct contact with the system, climbing robots had only been designed specifically for a fixed configuration of cable [53], fittings [54] and pylon features [55]. The following sections describe the evolution of climbing robots, starting with inspection along a single power line, then adding obstacle avoidance, and dealing with different cable structures. This is followed by a discussion on the robots that can transfer from the cable to a specific type of pylon.

A climbing robot that uses wheels to travel along and inspect a single power line is elucidated in [56]. Weighing 17.8 kg, this robot uses eddy current sensors to detect corrosion in live ACSR cables and was developed by Light SESA, a power distributor

in Brazil. This device cannot cross over towers or overcome most obstacles, and has a maximum line voltage of 350 kV.

The robotic device in [57] tackled power line inspection and cleaning and added the capability of avoiding obstacles. Weighing just 13.7 kg, the prototype uses V-grooved wheels to grip the cable and successfully move down a line, passing obstacles such as splices. It has only been tested in laboratory conditions, however, and embeds only basic functions: for example, a single camera is used for inspection and an ultrasonic sensor is used for open loop motion control. Additionally, it takes around 60 mins for the battery to charge fully.

Another device, designed by Shanghai University and described in [58, 59], adds obstacle avoidance and uses a more sophisticated structure to enhance its speed. This robot weighs 38 kg and takes eight seconds to move over spacers and counterweights. The structure has two arms with three degrees of freedom, enabling the robot to avoid obstacles by adjusting the arm length. However, this sophisticated structure only works with 110 kV transmission lines, and moves very slowly with a battery life of 6.0 hours. In addition, this study only considered a single power line.

In [60], the climbing robot's ability is expanded to transfer from the cable to a suspension tower through combined design with a three-frame structure wherein the device then moves manually from one side of a tower to the other, as illustrated in Figure 2.4.

The device is controlled by a semi-mobile ground station and was developed by Hydro-Québec TransÉnergie in Canada. Named "LineScout Technology" (LT), this mechanical device attaches to HV cables and weighs 100 kg. The prototype has been tested in field conditions, where it has been shown to effectively overcome a variety of impediments. However, LT is only semi-autonomous, and was originally designed to inspect a single type of transmission line (735 kV). It is also complex/expensive and equipped with a generic electrical resistance sensor to assess conductor status, as illustrated in Figure 2.5.
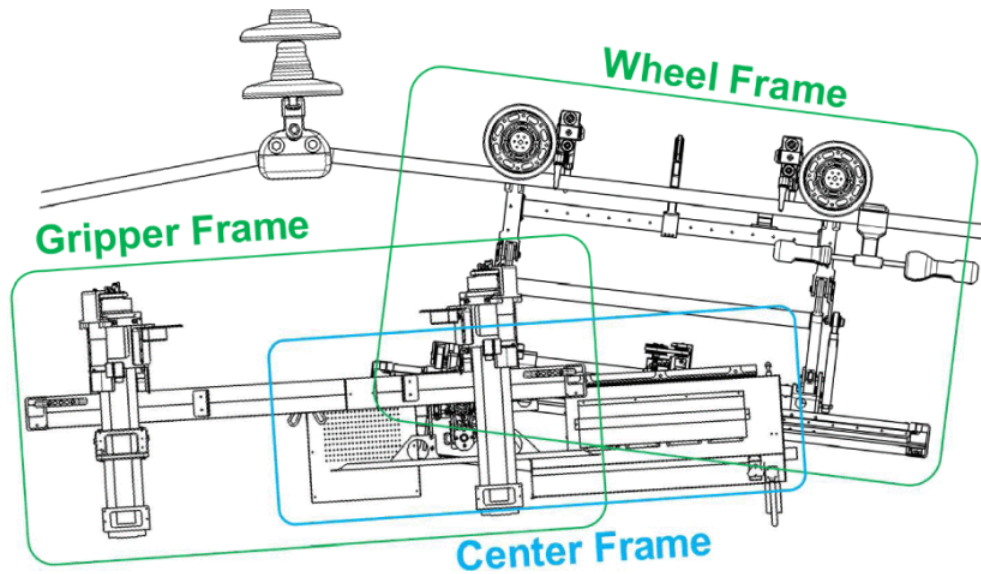
FIGURE 2.4: The three frames are structured as the following: first frame is supporting the wheels, the second frame is supporting a pair of grippers, and thrid frame is supporting the (a) the battery, (b) electronics cabinet, (c) and communications system [60].
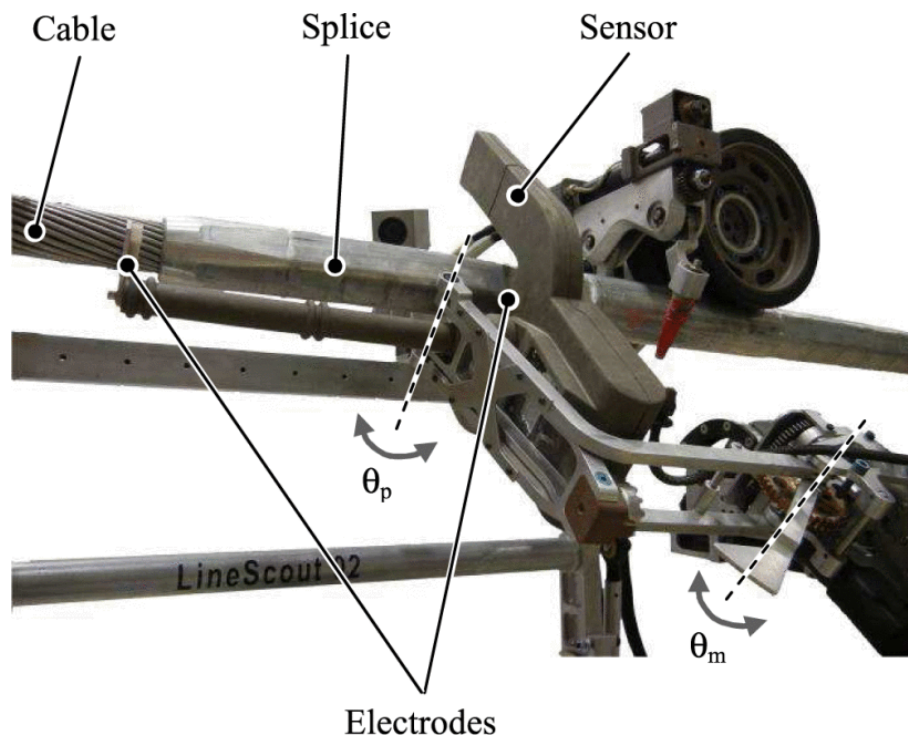
FIGURE 2.5: The LT robot is equipped with a sensor with two electrodes. The first touches the cable when one motor is moving θ_m, while the second one is spins around the axis θ_p to measure the resistance of the electric cable [60].

A similar approach was employed in the design of the "Expliner" system, developed

by the HiBot Corporation in Japan [61, 62]. In this case, however, the robotic device is capable of performing more detailed inspection of bundled conductors. The prototype has a carbon-fibre structure with a T-shaped base and two degrees of freedom, enabling it to travel down live transmission lines while overcoming obstacles in its path. At least seven people are needed to load the Expliner and attach it to a cable, a process that takes about two and a half hours. This operation must be repeated at each tower. Nevertheless, it is possible to pre-equip the tower with the clamps, bases, and pulleys necessary to lift the equipment, thereby lowering the preparation time as well as the cost, time and complexity. However, this robot is designed only for the specific type of bundled transmission lines used in Japan.

Mechanical inspection robots have, therefore, been successfully implemented on transmission lines and comprise a reasonably reliable method to assess cables' physical condition. However, they suffer from significant disadvantages– the most sophisticated devices are specialized for only one type of HV and are very large, complex, and expensive. In addition, they use a balancing mechanism to ensure dynamical stability, which increases their overall weight and renders them very slow. These issues are readily expounded in Figure 2.6 [62].

Other important constraints also exist: each robot must be manually attached and can only be used on one section of a transmission line (i.e., between each set of towers). The towers on which the robot is to be installed may only be accessible over very bumpy roads. In addition, live-line installation methods may require boom trucks, helicopters, and remote manipulation with insulated sticks. Finally, mechanical shocks during transportation or field installation may damage the electronic boards and key mechanical components. The inability to transition between lines and pylons is another fundamental limitation. Furthermore, not much work has been undertaken to develop additional technologies to develop bundled conductors, thus bypassing strain pylons and pylon/line docking.

(a) Additional sag of the walking ground wire.

(b) CIR climbing robot is walking through ground wire.
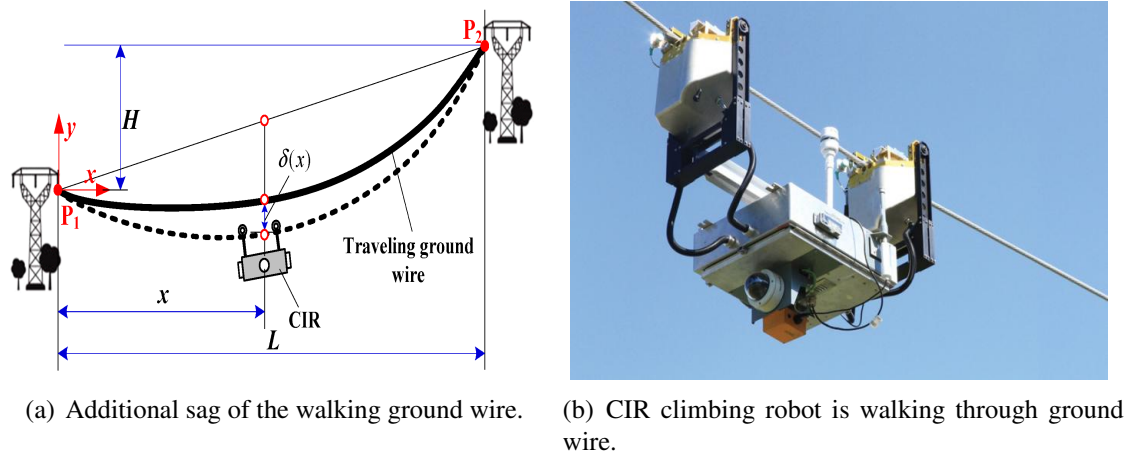
FIGURE 2.6: The cables are subject to additional sag with function, $\delta(x)$ due to the additional weight of climbing robot. To express the sag, various factors are taken into consideration: The suspension points (i.e., P_1 and P_2) on the tower, the cross-sectional area of cables, L signifies the horizontal spacing, horizontal stress of power line, and impact effect. This impact effect represents the vibrations from robot and wind (left) and robot on the double 315-kV circuits (right) [62].

2.4   UAVs Method for Inspection HV

The emergence of UAV technology has the potential to address the aforementioned limitations, due to their inherent advantages of cost, manoeuvrability, speed, and ease of set-up. They also do not require contact and can attain the required heights/positions needed to perform major inspection tasks. UAVs can also operate in weather conditions and in places that are either dangerous or unreachable for humans [63–66]. This subsection reviews the approaches employed in this area, which are classified into those focusing solely on power lines, those focusing solely on pylons/insulators, and those combining these two areas. The first group is initially reviewed.

The study in [67] used a UAV with thermal imaging to inspect joints in power lines by analysing their temperature, thereby avoiding expensive service interruptions. The study showed that it is possible to detect relevant temperature anomalies in the electric lines and devices. Even from short distances, however, it was impossible to achieve accurate temperature measurements of the electrical faults. Similarly, the helicopter system in [68] used thermal imaging to inspect joints in power lines, but focused on long-distance qualitative inspection. The results showed that the joints have a higher temperature than

other parts of the towers and can be detected as hot spots in thermal images. However, the accuracy achieved in both the studies was poor due to the large measurement spot size compared to the small target size, as well as the long measurement range, object reflection, and weather conditions. Furthermore, neither study provided an in-depth analysis of their results. Although this inspection method allowed access to hard-to-reach locations and increased inspection speed, it suffered from many shortcomings. As the helicopter was manually controlled, it was costly and necessary close control of speed and other physical parameters to enable the collection of higher quality data.

A smaller quadrotor was developed in [69] to again detect power lines, now using remote sensing spectral-spatial methods. The UAV was manually launched from the ground and automatically flew over a three-phase 220 V distribution line. The UAV weighed 1.5 kg and was fitted with a GoPro HD Hero2 camera used for inspection. Its lithium polymer (LiPo) battery imparted a maximum flight time of around 20 min. The simple PID (Proportional Integral Derivative) control system performed poorly amid the presence of radio noise emitted by the power lines. Coupled with crude image processing, it implied that the quality of the inspection was poor despite the fact that the experiment only considered a simple power line structure.

The UAV in [70], meanwhile, focused on the inspection of medium-voltage power lines. This type of line has increased height and distance compared to a distribution (low voltage) power line and requires a strain tower as opposed to a suspension tower. This provides a greater challenge, due to the additional supports of the strain tower. Accordingly, a bigger UAV platform was selected in the form of a V-TOL Aerospace BAT-3. Camera-based image processing was used to capture data. First, a filter based on the Pulse Coupled Neural Network (PCNN) was applied to remove the background. Then, straight lines were detected using the Hough transform. Finally, spurious linear objects were eliminated using the K-means clustering approach. These approaches focus on the tracking process for power lines only. However, they suffer from many drawbacks, such as low speeds and inaccuracy. Although the images were satisfactory, the overall system

was found to lack accuracy and speed due to the trade-off involved in selecting a more sophisticated vision system at the expense of a simple control structure.

The UAV in [71] again focused on tracking high-voltage overhead transmission lines, but used a large size fixed-wing UAV system to demonstrate feasibility in different application scenarios. The system was equipped with a 6RQ/I-6000 camera and Gopro Hero 3 camera to capture both visible light images and video. In addition, the UAV had a maximum load capacity of 30 kg. Due to its large platform, the distance from the landing point to the destination power line occupies 15% of the entire flight. It also suffers from many limitations, such as low speeds and inaccuracy. This kind of inspection requires the helicopter to go slow and stop at every tower without detecting it, thus resulting in a considerable increase in the inspection time (and cost). This was due to use of a large UAV without an accurate control system.

Similar to the above, UAV in [72] is used again for tracking the 500 kV high-voltage overhead transmission line system; however, it used a small commercial platform. The authors proposed a novel parameter reconstruction method for overhead transmission lines to keep the UAV's track and safety. Besides, theoretical simulation indicated that this approach has the ability to perform real-time transmission line monitoring and UAV trajectory control. In this study, the problem of the magnetic field fluctuation accompanying the transmission lines is omitted, especially when power outages occur as illustrated in Figure 2.6.

In this case, the method will face a new dilemma. Moreover, the study suffers from the following limitations; (i) no accurate control methods are used for UAV in the presence of magnetic field interference (when a shunt fault occurs) to prevent trajectory deviation, and (ii) the experiment is conducted in a laboratory environment.

The next group of papers considers the inspection of insulators. An unmanned helicopter was used in [73] to detect faults on many insulators appearing on the travel path in a medium power transmission line system at 11 kV. In addition, using theoretical tech-
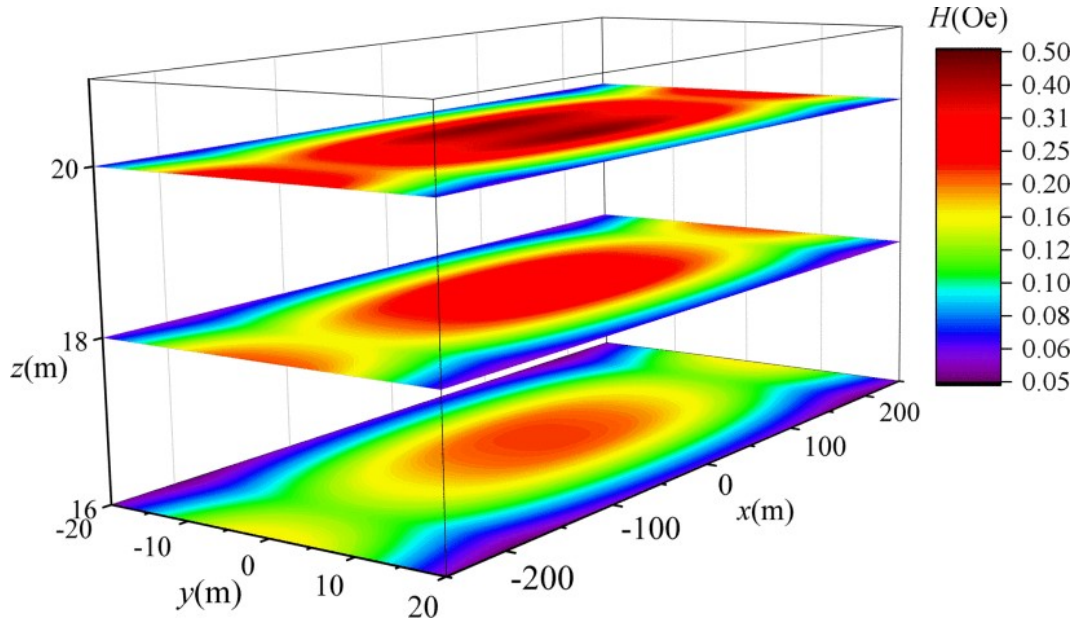
FIGURE 2.7: The influence of irregular magnetic field distribution on the horizontal xy-plane, where $\dot{H}$ denotes the vector of the magnetic field generated by the three-phase transmission lines starting from the heights 20, 18, and 16 m. [72].

niques, many attempts were made to determine the camera and lens combination that would provide the best quality images of faults. Ultimately, a Canon 5D Mark II SLR camera with a 105 mm focal length was selected for optimal performance. The results, however, showed that a large camera is always needed to obtain high accuracy. For example, a 200 mm focal length is needed to distinguish the metal pins on the insulator, resulting in a camera weight of 1210 g which is both massive and expensive.

The UAV in [74], meanwhile, focused on inspecting insulators in high tension power lines while applying Faster R-CNN (Region-based Convolutional Neural Networks) as a means of reducing the costs involved in inspecting and maintaining dead-end body components (DEBC) (a full tension device that is used to attach the conductor structure to the insulator string). In the UAV's test flight, images of the live high-voltage power lines were collected by flying the UAV approximately 15–20 m from the imaged DEBCs. Furthermore, a sensor comparable to the Sony NEX 7 was used for data collection. These data were processed through simple image techniques, which served to augment 146 input images to create 2437 training samples. The system was tested on 111 aerial inspec-

tion photos, achieving 83.7% accuracy and 91% precision. The detection accuracy and precision were increased to 97.8% and 99.1% by adding 270 additional training images and including a new insulator class. Both [73] and [74] were only interested in the inspection of insulators instead of the other system components, such as cables and power pylons. They focused on improving the accuracy of camera solutions to allow objects at a distance. This need arose because the UAVs reviewed so far only used basic, generic controllers, thus implying the necessity of a sophisticated camera .

The following papers expand the UAV scope to attempt the transition between HV power lines to the lines, with the UAV launched manually from the ground tower. In [75], the UAV operated between 6 and 10 m of a live line, before transitioning over the HV power lines with a rating of 315 to 735 kV to skip the tower and detect the cable only as shown in Figure 2.8. Due to the challenges of this planned travel path, the base frame of the UAV was modified to weigh just 14 kg.
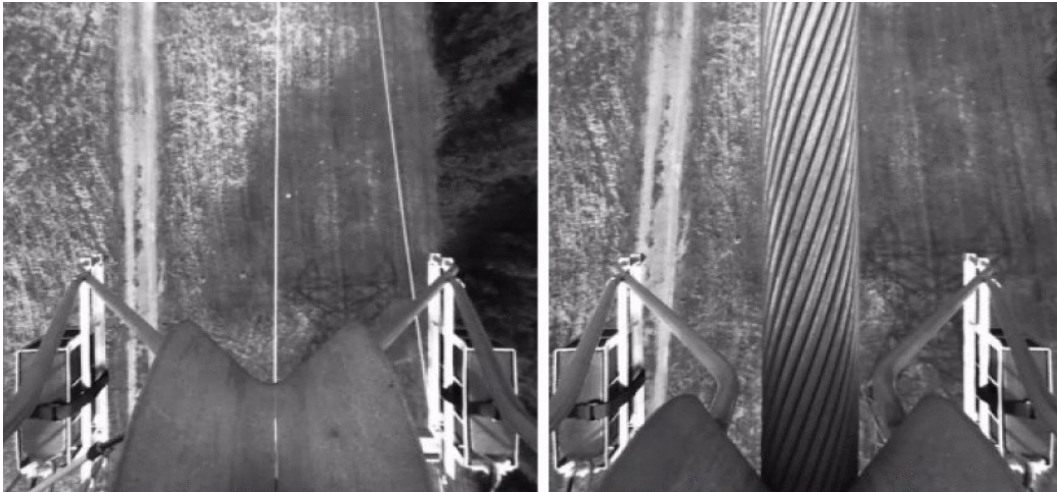
FIGURE 2.8: Images of a power line taken at the closest point distance during the landing mission. As the UAV descends, the power lines' thickness reaches first 1 pixels in width (left) and 50 pixels in width at the end (right) [75].

The UAV was loaded with LiDAR and had a camera with a resolution of 1280 × 1024 pixels. Both measured the correct distance to the power line. At a distance of 10 m from the power line, however, the line appeared as a 1 pixel wide ridge in the image.

Additionally, the accuracy of these results were poor in terms of the appearance of the 35 mm power line thickness versus the viewing distance function as illustrated in Figure 2.9. ACSR cables appeared as a small line with insufficient detail to distinguish faults due to the reliance on conventional control approaches. Finally, the system was complex and very slow during this transition, thus requiring a significant amount of hardware.
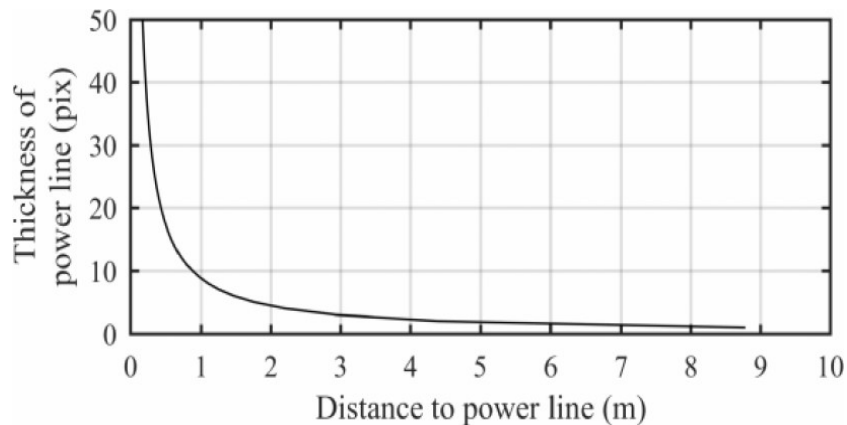
FIGURE 2.9: Camera resolution effect with 1280 x 1024 pixels on distance estimation. At a distance of about 8.8 m, the theoretical thickness of the 35 mm power line is 1 pixel. [75].

The UAV described in [76] focused on transition from tower to tower, and then from tower to HV power lines. It attempted to resolve the problem of continuous and robust navigation along one side of overhead transmission lines. This paper employed a refitted DJI Matrice 100 quadrotor platform equipped with a pan and tilt camera along with two advanced embedded processors, namely NVIDIA TK1 and NVIDIA TX2. The paper suggests integrating tracking and deep learning-based detection for real-time and reliable transmission tower localization. The UAV attempts to transition using two cameras: one to follow tower to tower and the second to follow from tower to lines. In most conditions, however, the tracking suffered from a serious drift which impacted the detection. Since this was caused by a lack of prior knowledge of the object, the paper attempted to resolve this by combining the tracking with deep learning-based detection which could be trained in advance over many samples. This learnt knowledge could be used to re-initialize tracking when drift occurred. For this study, the problem was limited to one type of learning algorithm, thus compromising the detection's accuracy. Another fundamental limitation

lies in the fact that the UAV was unable to charge and land automatically during this transition.

Finally, in [77], a large unmanned helicopter was used to perform a full and autonomous inspection of overhead transmission lines, pylons, and insulators. This large helicopter was equipped with a multiple sensor platform (LiDAR, thermal camera, ultraviolet camera, short-focus camera, and long-focus camera) to acquire information about power line components and surrounding objects. The experiments were carried out on a 4.2 km long transmission line, with 13 towers and 78 insulators, at Qingyuan in Guangdong Province, China. This paper adopted a double-closed loop control method to achieve automatic target tracking. The outer loop employed a distance control method, which enabled the camera to start aiming and tracking when the helicopter was close enough to the task point. The inner loop employed an attitude control method, which used the camera's projection centre's real-time coordinates to adjust the camera's posture by gradually adjusting the stabilized platform. This method had to be completed within a time limit, however; in case it gets exceeded, the task would be abandoned and the UAV would move to the next task. Moreover, using multiple sensors proved to be a good solution for full inspection for both insulators and cables, but the additional components increased not only the weight and cost but also the complexity of the UAV system. It is notable that the study neglected the role of control systems, thus implying that data collection was regularly abandoned due to the time limit built into the algorithm.

2.5   Quadrotors in Industry and Research

UAVs can be traced back 100 years to military devices developed in the First World War. Following this, interest was initially focused on military application across all theatres of inter and post Second World War conflict [78]. The purpose of UAVs can be basically classified as follows: reconnaissance, combat, logistics and target and deploy. In addition to military use, UAVs have been employed in a range of civilian activities, including

aerial photography, terrain mapping, and sampling inspection for agricultural purposes. Civilian UAVs have fewer critical demands placed upon them, and hence can be manufactured from light, cheap, and less rigorously-tested materials with electric systems. Consequently, they can be smaller, lighter, and cheaper. Recent advances in energy supplies, sensor, actuators, computing power, and wireless communication have produced a wide array of devices for the civilian market.
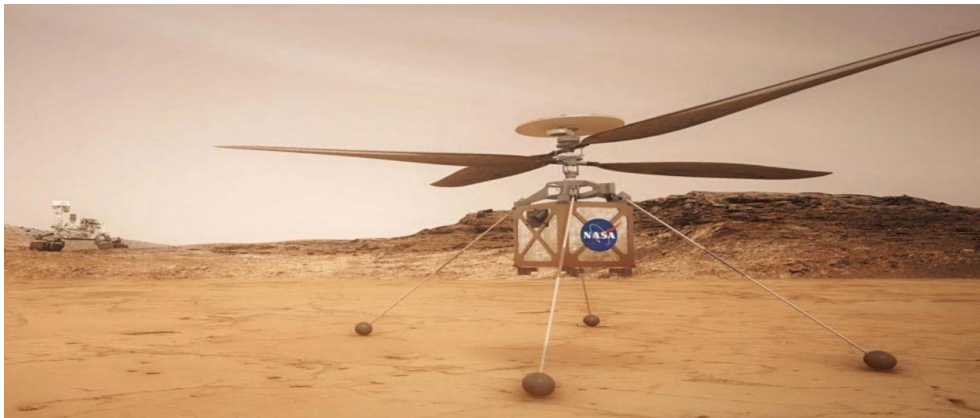
FIGURE 2.10: NASA's Mars Ingenuity UAV have reached the red planet [79].
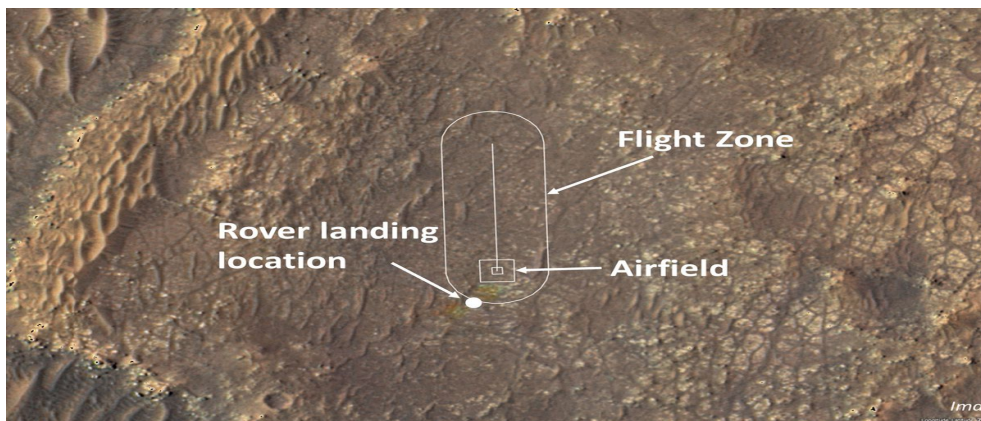
FIGURE 2.11: The flight zone map with a predefined trajectory was captured by a high-resolution orbital camera for NASA's Ingenuity Mars, where the map shows: a) the rover landing site locations, b) the trajectory tracking , c) the flight area [79].

More recently, NASA has tapped into this potential, allowing UAV to unleash their creativity. In this endeavor, NASA used a small unmanned aircraft weighing 1.8 kg as the first controlled flight to obtain a successful tracking with a predefined trajectory on

another planet as shown in Figure 2.10 and 2.11.

Recent miniature UAV designs means that less powerful propulsion can be employed; electrical motors and batteries become feasible in particular. The most popular design of this type is the quadrotor, which employs four motorised propeller units.

The quadrotor is viewed as a practical alternative to the high cost and complexity of standard rotorcraft. Employing four rotors to generate differential thrust, the quadrotor hovers and moves without the complex system of linkages and blade elements existing on the standard single rotor vehicles. The quadrotor may be classified as an under actuated system, because only four actuators (rotors) are used to control all six Degrees of Freedom (DOF). These four rotors directly affect z-axis translation (altitude) and rotation about each of the three principal axes [80]. The other two DOFs comprise translation along the x-axis and y-axis. These two remaining DOF are coupled, which means that they depend directly on the overall orientation of the vehicle (the other four DOF). Furthermore, other advantages related to the quadrotor design include swift manoeuvrability and increased payload. On the other hand, drawbacks may include an overall larger quadrotor size and a higher energy consumption, thus giving rise to lower flight times [81].

The quadrotor is an inherently difficult platform to control. It is only recently that advances in technology and inertial measurement units (IMUs) have made this task possible, which is why the quadrotor has seen little industrial application to until recently. When compared with other UAVs (and especially its nearest relative, the helicopter) quadrotors have many distinct advantages, such as better manoeuvrability, good hovering ability, a simpler mechanical structure, and a larger payload to volume ratio [82], [83]. Thus it is considered by many to be an ideal platform for autonomous aerial activity.

The popularity of small, affordable UAV designs, such as the quadrotor, has been reflected by research undertaken at institutions such as Massachusetts Institute of Technology, Stanford University, University of Pennsylvania and University of Oldenburg, Swiss Federal Institute of Technology in Zurich (ETHZ) [84]. This research covers all aspects of their design and function. Table 2.3 compares their merits and illustrates the

correlation between performance and cost. There are numerous commercially produced quadrotors available and Table 2.3 provides a succinct description of the most popular varieties that are currently available.

Of particular research interest is swarm-based task management, in which several quadrotor vehicles co-operate together to achieve a task, such as lifting heavy payloads or manipulating objects. Another area is formation control, in which quadrotor must achieve a coordinated spatial trending objective. To achieve this, various communication and control strategies have been put forth, using both central controllers, and purely local 'agent-based' controllers with no central control. Swarm properties have also been studied using large numbers of miniature quadrotors whose autonomy are typically governed only locally [85]. Recently, the Automatic Coordination Teams (ACT) in University of Southern California Lab attempted to validate the system architecture for a large swarm using a very small quadrotor with a 49 formation flight which operates indoors and communicated over three radios. These vehicles use a motion-capture system for localization [86]. Other research derived the Reynold's basic rules (basically designed for control of 2D holonomic particles) from behaviours observed in schools of fish which can be used by swarm properties to avoid obstacles without mutual collisions [87].

Table 2.4, compares the most popular quadrotors in terms of leading characteristics: power, control, payload, manoeuvrability, stationary flight, speed, vulnerability, endurance, miniaturization, and indoor usage. It assesses them on a scale of 1 to 3, denoting poor, moderate, and good performance, respectively.

2.6 Applications of Quadrotors

Operating autonomously in complex environments without external inputs from humans requires the UAV to integrate perception, learning, real-time control, reasoning, decision-making, and planning capabilities [88], at least to some extent. In the past decade, sig-

TABLE 2.3: Table showing the most popular current quadrotor models

Product	Specification	Wingspan	Cost	Picture
Assassin 180 FPV Eachine **CHINA**	Flight time: 7 minutes Max Payload: 288g Using for racing	180 mm	£140	
IRIS+ 3D Robotics **USA**	Max Payload: 400g Only basic flight controller	500 mm	£400	
Ascending Technologies Hummingbird **GERMANY**	Max Payload: 200g Have LV and HL to programmable the control using c code	500 mm	£3,515	
Phantom 3 Standard DJI **CHINA**	Operates via a smart phone/tablet Weight 1216 g - 300g Payload	590 mm	£509	
Ascending Technologies Firefly **GERMANY**	Max Payload: 600 g	665 mm	£5,695	
Guardian Draganfly **CANADA**	Max Payload: 1,320g	725 mm	£6603	
Indago Lockheed Martin **USA**	Long run time (4 - 8 hours) A ready to fly weight of 2,268 g. with payload included (2,268 g)	812 mm	£20562	

TABLE 2.4: Comparison of the quadrotor properties (1 = Poor, 3 = Good)

Categories	Assassin 180 FPV	IRIS+	Phantom 3	Hummingbird	Firefly	Guardian	Indago	DJI
Power	1	1	2	3	3	3	3	3
Control	1	1	1	2	2	3	3	2
Payload/volume	1	1	3	2	2	2	3	1
Manoeuvrability	1	1	1	2	2	3	3	2
Stationary flight	1	1	1	2	2	2	3	1
Speed	1	1	2	3	3	3	3	3
Vulnerability	1	2	2	2	2	1	1	2
Endurance	1	1	2	2	3	3	3	2
Miniaturization	1	1	2	3	3	2	1	3
Indoor usage	3	3	2	2	1	1	1	3
Total	12	13	18	23	23	23	24	23

nificant improvements have been made to this aspect of the autonomy of UAVs. As discussed, a primary area of quadrotor use is the acquisition of information over a defined area [89] to reduce outage. Examples in this area will now be examined, due to their relevance to the potential use of quadrotors for HV overhead power line inspection. Here, examples include environmental monitoring by scanning wooded areas for fire prevention [90], inspection of industrial plants [91], agriculture, surveillance, and weather observation [92–95].

We present this area of data acquisition as a crucial task for a full pose to enable the quadrotor control for OPL inspection using different types of sensor technologies by grouping them into two heading; (i) Non-Vision Based, (ii) Vision-Based. We also dedicate a review of available studies to inspect power infrastructure based on vision sensing, as it is a less explored field. Furthermore, we highlight the level of autonomy in the UAVs used by the works as shown in Table 2.5.

2.6.1 Non-Vision Based Sensing Approaches

Typically, the main path planning task for an autonomous flying UAVs is to reach a desired location in an uncensored manner, for example, without human interference. Currently, there are several effective systems for indoor and outdoor navigation of UAVs. The study

in [96] involved a quadrotor platform and focused on outdoor operation by adopting a non-vision approach. The application of this system was performed outdoors and had the benefit of utilizing a global positioning system (GPS) and IMU measurements. The UAV platform in [97], achieved the same performance using different IMU.

Similar to [97], the authors in [98] examined the same approach to enable UAVs to perform remote sensing of agriculture application. The considered problem was solved by GPS to give the UAVs information pertaining to their location and height. However, the major drawback in using GPS is that signals may be lost in indoor environments and most urban areas. Moreover, it is not always possible to acquire adequate signal strength [99]. A UAV with GPS cannot sense its environment immediately , but only receives the height and position relative to known general parameters. Consequently, in practice, these strategies are not effective for the inspection of power infrastructure. A UAV with GPS cannot immediately sense its environment, but only receives the height and position relative to known general parameters. This implies that problems frequently arise when the environment changes rapidly and unpredictably.

In a similar context, the study in [100] also focused on an autonomous flight of quadrotor by employing another non vision sensor (a laser range finder). In [101], the authors attempted to provide solutions to aid a quadrotor UAV in landing on an unknown surface based on laser range finder sensor. The laser system was found to plausibly measure the inclination of a surface that varies with time to suitably design a landing trajectory. Thus, the system can track the surface angle during the transition to zero incline. Both of these works aim to provide range measurements for obstacle detection during take-off and landing.

Again, in [102] and [103], the authors expanded the controller manoeuvres such as taking off and landing by integrated non-vision sensors. However, this time, they added a filter for estimating in real-time the roll, pitch, and yaw angles based on data from a gyroscope. Due to inadequate performance, the authors in [104] proposed the use of PD^2 feedback controller based on quaternions for greater stability during take off and landing.

Furthermore, the authors in [105] suggested that the use of an intuitive strategy based controller could improve stability in take off and landing. Accordingly, the extra both of signal processing and gyroscopes can mitigate some of the limitations of IMUs.

Other studies also confirm that height sensors are paramount to altitude stabilization. In [106], four SRF10 ultrasound range finders were used to achieve altitude control and obstacle avoidance. It was found that the sensor pointing straight down achieved satisfactory control. In [107], the authors aims to achieve altitude stabilization for a quadrotor, by using; (i) 3D telemetry (to communicate with the ground station), (ii) an ultrasonic sensor (to measure the height). Thus, this leads to the modification of the on-board quadrotor platform to constitute more of weight and cost, namely an Arduino board, microcontroller, and ultrasonic sensor.

2.6.2   Vision Based Approaches

Vision-based automatic methods are attractive because they do not require special equipment, only needing a camera and a vision processing unit. Currently, a lot of research goes into vision-based systems for UAVs. Based on vision sensor configuration, the vision techniques may be classified into; (i) monocular (using one camera), (ii) stereo (using two cameras). The advantage of stereo vision is that it can be used to measure a distance whereas monocular vision cannot. Thus, when image is captured in three dimensional (3D) space, any information of distance in the image projection is lost because 3D space is projected onto an image plane, which is in two dimensional (2D) space. However, the utilization of two cameras makes it possible to create solutions using a depth map which retains this information. In the following, we review the monocular vision and stereo vision strategies.

Although the monocular vision is not as diverse as stereo vision, research efforts in landing applications often focus on monocular vision. Thus, the authors in [108] and [109], adopted the monocular vision to estimate and stabilize the quadrotor's orientation. Similar to [108] and [109], the authors in [110] also focus on monocular vision, taking

off and landing applications for a quadrotor platform. The difference is that the landing involved uses a SRF10 ultrasound range finder. In addition, computation time is the main concern with monocular vision, even though this form of vision requires only half the amount of processing in comparison to stereo vision.

The authors in [109] and [111] attempted to provide solutions in order to handle computation time with monocular vision. Under the first approach [109], the authors suggested the establishment of a wireless link to communicate with a base station where image processing is performed. Then, based on the obtained results, the amount of data transmitted is minimized by running certain processing applications on-board the quadrotor to limit the size of the image transmitted. However, wireless interference causes a significant impact between the quadrotor vehicle and surrounding areas. Under the second approach [111], the authors used a separate on-board microcontroller to send parameters to the main control board of the microcontroller via a wired serial link. The proposed approaches are shown to guarantee a feasible solution. Moreover, the second approach offers a greater advantage of preventing the quadrotor from remaining within the range of the base station.

In Table 2.5, we have systematically grouped some of the most recent applications of vision based on UAV technologies for power system inspection.

Unlike the above studies, references [121] and [122] considered stabilizing a quadrotor by using stereo vision. In [121], the study aims to obtain stability of roll, pitch, and yaw for accelerometers, gyros, and a compass. In fact, the system used the stereo vision system to provide the quadrotor with additional information about its horizontal and vertical movement in relation to the target seen. However, the main drawback was the computationally intensive algorithms which need to be done on a computer with the control parameters before being sent to the microcontroller on the UAV.

Reference [123] proposed a technique combining optical flow measurements with stereo vision information (stereoflow) to obtain a 3D map of the obstacles within the scene. However, the combination of stereo and optical flow is more significant to navi-

TABLE 2.5: Application of UAV in vision-based for power infrastructure

Vehicle type	Infrastructure	Sensors/tech.	Weight	Output	Limitations and level of autonomy	Ref.
Helicopter	Power line	Stereo rig	–	Image	LQG controller for Roll and Pitch, while a PID for Yaw, Task level autonomy (For one or more task in Infrastructure)	[112]
Ducted-fan	Power line	Camera	25 kg	Image	Consists of two cranked link to power line, Only work with same physical Configuration of power line, Conditional autonomy (Assistance and Supervised)	[113]
Simulation, no platform	Power tower	–	–	Image	No experiment have been done here, Conditional autonomy (Assistance and Supervised)	[114]
–	Power tower	–	–	Image + tower	Manual control, No autonomy (Human function)	[115]
SmartCopter UAH	Power line	Stereo vision, laser scanner	12.3 kg	Image + track	GPS based, The structure limits its flexibility and makes it challenging to stabilize, Conditional autonomy (Assistance and Supervised)	[116]
CAS Quadrotor	One side of power lines	Monocular-based	2.7 kg	Image	Data garnered is sketchy, Small flight time, Conditional autonomy (Assistance and Supervised)	[117]
ZN-2 UAH	Power line	visible-light camera, infrared camera,	7 kg	Image + thermal	Gas engine based UAH, Quick inspection, Conditional autonomy (Assistance and Supervised)	[118]
–	Insulators	Monocular-based	–	Image	Manual control, No autonomy (Human function)	[119]
–	Power line	Camera	–	Image + track	Aims to identify the necessary parameters and system components for only monitoring power lines, Task level autonomy (one or more task in Infrastructure)	[120]

gate in urban canyons when compared with the technique based on a single vision sensor. Another related work in [122] presented a technique for path planning with stereo-based vision may allow UAVs to navigate safely in external environments while performing tasks such as HV line inspection. However, the system failure rate was too high because the stereo-based techniques specifically designed for this application are unlikely to detect thin impediments such as transmission lines.

In general, vision-based approaches are potentially useful for inspecting and data ac-

quisition in all related works. As previously reviewed, the performance of UAVs for inspection can be demoted due to: 1) vision-based approaches, 2) not respecting payload constraints, and 3) using inaccurate generic control system, which impacts the level of autonomy.

2.7 Conclusions

This review has summarised the many attempts to use UAVs to automate inspection for conductors, pylons, and power components. None of these methods, however, have been able to demonstrate accurate inspection of the complete system in an autonomous manner. This is ascribed to the following factors:-

Firstly, most of the attempts comprised task-specific approaches for the inspection of power lines, insulators and transition, respectively. For power line inspection, the results showed that the UAV either needs to fly relatively close to the lines in order to take detailed images of the conductor's physical condition or farther away. However, additional sensors and larger cameras are also needed, which involve larger, heavier, more complex, and thus, more expensive UAVs.

Secondly, many attempts have been made to identify broken insulators but autonomous inspection has not been made possible. While they are capable of inspecting basic power components and results have shown that high quality is indeed possible using non-contact sensing, the process requires expensive equipment and efficient control of the camera.

Finally, the transition task has elicited less attention. In addition, it has proved challenging to move from power line to pylon and from line to line. Implementations have been very slow and complex, needing a lot of hardware. This is mainly attributed to an absence of sophisticated and intelligent control. In addition, the UAVs' ability to land and charge during this traveling path has been largely neglected.

This review has demonstrated the potential to use UAV-acquired data for pose to enable the quadrotor control for OPL inspection. Current limitations, however, can only be

addressed by (i) more accurate motion control, (ii) faster flight times, (iii) the ability to perform automatic transition tasks, (iv) the acquisition of data from more than one type of sensor, and (v) the ability to charge and land automatically.

Chapter 3

Modelling and Control of Quadrotors

3.1 Introduction

The previous chapter has motivated the need to develop quadrotor technology to facilitate HV inspection. It has also demonstrated potential hardware and sensing approaches that may be exploited to realise this. The limitations of the new application related to the constraints of power lines are more challenging and unique conditions and different from a conventional applications such as manufacturing where the ILC has been used. This area is non-trivial since quadrotors are under-actuated and unstable with significant non-linearity and strong dynamic coupling. Moreover, the UAV aims to fly autonomously near fault points by the optimum trajectory which constitute all possible tracking motions during the OPL inspection. To obtain that, control approaches to solve the trajectory tracking problem is considered in controlled trajectories of the orientation angles and position, velocity error, and obstacles. Because of these difficulties, this chapter provides an established design of a modelling quadrotor and review of current control approaches in order to highlight limitations and areas of potential exploitation which will utilized later for a final solution to perform transition and horizontal trajectory.

3.2   Modelling Approaches

A model of a quadrotor encompasses the kinematics and dynamics of its frame, the properties of its actuators, its surroundings and associated aerodynamic effects. These components are now discussed.

3.2.1   Airframe Body Kinematics and Dynamics

Kinematics it is a branch of mechanics focusing on representing the position and motion of a system of bodies. Quadrotors are almost uniformly assumed to require 6 DOF in order to characterise the position of the quadrotor reference frame with respect to a fixed reference frame. Dynamics is the study of the effect of forces and torques on the motion of a system of bodies. The model complexity depends highly on underlying assumptions of the geometry and mass distribution. In terms of quadrotors, most studies in the field of UAVs employ models based on first order approximations which have been successfully utilized in various quadrotor control designs. The most common assumptions are as follows [124–128]:

- The structure is rigid.
- The structure is symmetrical.
- The CoG (center of gravity) and the body fixed frame origin to coincide.

These significantly simplify the subsequent dynamic equation. The first two assumptions are satisfied in the vast majority of the quadrotor designs. The third assumption can always be satisfied by translating the body fixed frame. The inherent symmetry of quadrotors also simplifies structural properties, for example the inertia matrix I which appears in the dynamic model can often be taken to be diagonal [128]. The quadrotor Body and Earth frames are shown in Figure 3.1 which appear in all kinematic representations.

The Earth frame is a Newtonian system. The origin of the Body frame is defined at the centre of mass of the quadrotor, with axes fixed with respect to the quadrotor arms. Euler angles are the most popular approach to define the kinematic transforms between frames,

due to the similarity between linear coordinates and angular coordinates. However any sequence of three rotations can equally be employed.
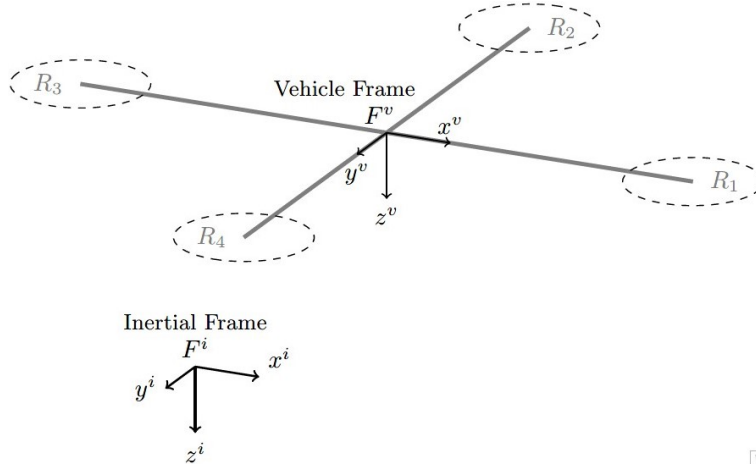
FIGURE 3.1: The configuration of quadrotor UAV with respect to its frames.

A problem appears in the process of uniquely representing orientation using Euler angles. This is due to the lack of uniqueness in the transformation between joint angles and the resulting orientation, and is termed gimbal lock. In this problem the pitch angle θ loses its meaning. So to overcome this, the pitch angle θ can be constrained between $(-90^\circ, +90^\circ)$ [129].

Every quadrotor consists of four actuators as shown in Figure 3.1, where Ω_i, T_i, f_i are the speed, torque and force produced by rotors. The actuators are positioned at the same distance to the center of mass to create a symmetric structure [130]. The general form of dynamics relating the joint angle vector $\mathbf{q}_\Theta$ to the applied torque generated about each axis is given as:

$$M(q_\Theta)\,\ddot{q}_\Theta + B(q_\Theta, \dot{q}_\Theta)\,\dot{q}_\Theta + G(q_\Theta) = \tau + \Gamma(q_\Theta), \quad q_\Theta = \begin{bmatrix} \phi \\ \theta \\ \psi \\ x \\ y \\ z \end{bmatrix} \tag{3.1}$$

$$\tau = \begin{bmatrix} \tau_\theta \\ \tau_\phi \\ \tau_\psi \\ f_x \\ f_y \\ f_z \end{bmatrix} = \begin{bmatrix} l(f_2 - f_4) \\ l(f_1 - f_3) \\ T_1 + T_2 + T_3 + T_4 \\ 0 \\ 0 \\ f_1 + f_2 + f_3 + f_4 \end{bmatrix} \tag{3.2}$$

where $M(\cdot)$ is the inertial matrix, $B(\cdot)$ is the Coreolis matrix and $G(\cdot)$ is the gravitational vector, τ is the vector of torque for each coordinate and $\Gamma(q)$ embeds the gyroscopic effect. See equation (F.1),(F.25),(F.27),(F.28) and (F.30) in Appendix C for full derivation of these terms.

Euler angle is the most commonly used approach to describe the orientation of a rigid body. Therefore, they will be adopted in representation of angles. Also, the reference system frames of the quadrotor is shown in Figure 3.1. The position of the quadrotor is expressed in the inertial frame F^i as $(x, y, z)^T$ axes with ξ. The attitude, is defined with three Euler angles η, First frame F^i is rotated around its z by ψ, to produce frame F^{v2}. Then F^{v2} is rotated about its y axis by θ to produce F^{v1}. Lastly F^{v1} is rotated about its x axis by ϕ to produce F^v. The frame F^v has the same orientation as body frame F^b as shown in Figure 3.1. The translation and rotation position vectors are defined as

$$\xi = \begin{bmatrix} x \\ y \\ z \end{bmatrix}, \eta = \begin{bmatrix} \phi \\ \theta \\ \psi \end{bmatrix} \tag{3.3}$$

The velocity $(\varsigma, v, w)^T$ and the angular velocity $(p, q, r)^T$ of the quadrotor are defined with respect to the body frame F^b.

$$\begin{bmatrix} \varsigma \\ v \\ w \end{bmatrix}, \begin{bmatrix} p \\ q \\ r \end{bmatrix} \tag{3.4}$$

The transformation from a point p^v in F^v to a point p^{v1} in F^{v1} is given by $p^{v1} =$

$R_v^{v1}(\psi)p^v$, where

$$R_v^{v1}(\psi) = \begin{bmatrix} C_\psi & -S_\psi & 0 \\ S_\psi & C_\psi & 0 \\ 0 & 0 & 1 \end{bmatrix} \tag{3.5}$$

$$R_{v1}^{v2}(\theta) = \begin{bmatrix} C_\theta & 0 & S_\theta \\ 0 & 1 & 0 \\ -S_\theta & 0 & C_\theta \end{bmatrix}$$

$$R_{v2}^{b}(\phi) = \begin{bmatrix} 1 & 0 & 0 \\ 0 & C_\phi & -S_\phi \\ 0 & S_\phi & C_\phi \end{bmatrix} \tag{3.6}$$

The transformation from the vehicle frame to the body frame is given by

$$R_v^b(\phi; \theta; \psi) = R_{v2}^b(\phi)R_{v1}^{v2}(\theta)R_v^{v1}(\psi) =$$

$$\begin{bmatrix} C_\psi C_\theta & S_\psi C_\theta & -S_\theta \\ C_\psi S_\theta S_\phi - S_\psi C_\phi & S_\psi S_\theta S_\phi + C_\psi C_\phi & C_\theta S_\phi \\ C_\psi S_\theta C_\phi + S_\psi S_\phi & S_\psi S_\theta C_\phi - C_\psi S_\phi & C_\theta C_\phi \end{bmatrix} \tag{3.7}$$

The positions $(x,y,z)^T$ are inertial frame quantities, where velocities $(\varsigma, v, w)^T$ are body frame quantities. Therefore the relationship between position and velocities is given by

$$\frac{d}{dt}\begin{bmatrix} x \\ y \\ z \end{bmatrix} = (R_b^v)^{-1}\begin{bmatrix} \varsigma \\ v \\ w \end{bmatrix} = (R_v^b)^T\begin{bmatrix} \varsigma \\ v \\ w \end{bmatrix} \tag{3.8}$$

in which $S_x = \sin(x)$ and $C_x = \cos(x)$. Therefore,

$$R_b^v = \begin{bmatrix} C_\psi C_\theta & C_\psi S_\theta S_\phi - S_\psi C_\phi & C_\psi S_\theta C_\phi + S_\psi S_\phi \\ S_\psi C_\theta & S_\psi S_\theta S_\phi + C_\psi C_\phi & S_\psi S_\theta C_\phi - C_\psi S_\phi \\ -S_\theta & C_\theta S_\phi & C_\theta C_\phi \end{bmatrix} \tag{3.9}$$

The transformation between body angular velocities $(p,q,r)^T$ and rate of change of

Euler angles $(\dot{\phi}, \dot{\theta}, \dot{\psi})^T$ is given by

$$
\begin{bmatrix} \dot{\phi} \\ \dot{\theta} \\ \dot{\psi} \end{bmatrix} = \begin{bmatrix} 1 & S_\phi T_\theta & C_\phi T_\theta \\ 0 & C_\phi & -S_\phi \\ 0 & S_\phi/C_\theta & C_\phi/C_\theta \end{bmatrix} \begin{bmatrix} p \\ q \\ r \end{bmatrix},
\tag{3.10}
$$

3.2.2 Propellers and Motor Characteristics

To relate rotor command input to the torque and force terms appearing in dynamics (3.1), a representation of the actuator characteristics is needed. Quadrotors movements such as, hovering, take off, landing and trajectory tracking are conducted by controlling the actuator demand signal since the actual rotors are fixed and cannot be tilted [131]. There are two types of propellers that are used mostly in UAVs. The first type is called the "fixed-pitch" propellers and the second type is the variable-pitch propellers. For fixed-pitch propellers, in Figure 3.2 only change in the angular velocity will produce an adjustment of the thrust force, and in this case the angle of attack of propellers is constant. On the contrary, the angle of attack of propellers is changed in the case of "variable-pitch" propeller [132]. Fixed-pitch propellers are characterized by mechanical and aerodynamic simplicity as well as low production and maintenance costs compared to the variable-pitch ones. However, the advantage of the variable type is the ability to handle aggressive manoeuvres based on the complex underlying mechanics it utilises [133].

The thrust f_i and torque T_i produced by the ith motor propeller system can be defined as a function of rotor speed in general terms as follows:

$$
f_i = C_T \rho A_r r^2 \Omega_i^2
$$
$$
T_i = C_D \rho A_r r^2 \Omega_i^2
\tag{3.11}
$$

Here the C_T is thrust coefficient for rotor, and C_D is drag coefficient ρ, is the density of air, A_r is the cross sectional area of the propeller rotation, r is the radius of the rotor, Ω_i is the angular velocity of the ith rotor. Propeller dynamics are usually neglected or lumped in

with the motor dynamics. A full characterization involves considering the aerodynamics of the surrounding environment is conducted in [134].

According to [134], each rotor may be thought of as a rigid disc rotating around the axis z in the body frame, with angular velocity ω_i. The rotor's axis of rotation is itself moving with the angular velocity of the frame. This leads to the following gyroscopic torques applied to the airframe:

$$\Gamma(q) = J_p \begin{bmatrix} p \\ q \\ r \end{bmatrix} \times \begin{bmatrix} 0 \\ 0 \\ 1 \end{bmatrix} \Omega_r \qquad (3.12)$$

Here $\Gamma(q)$ is the gyroscopic propeller matrix appearing in (3.1), and J_p is the total rotational moment of inertia around the propeller axis, Ω_r is the rotor rotation rate sum. The direction of Ω_r coincides with the z -axis of the body coordinate frame whereas all its other components are zero. It is easy to see that the gyroscopic effects produced by the propeller rotation are just related to the rotational and not the transnational equations.
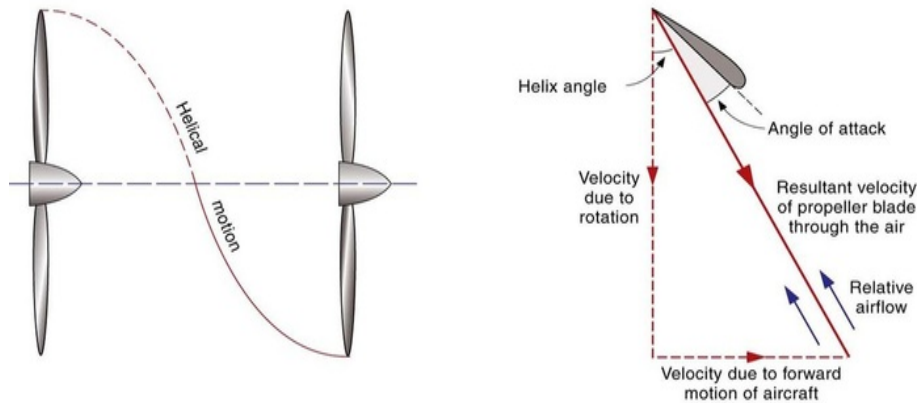
FIGURE 3.2: The angle formed between the relative airflow and the blade chord line is the blade angle of attack [132].

3.2.3 Aerodynamic Phenomena

The dynamics of quadrotor s during aerodynamic effects have been studied to build a robust system which takes aerodynamic dynamics is to consideration. However, many studies have neglected aerodynamics due to the fact that their focus is only on stability during hovering. However, in the case of flight trajectories and flight manoeuvres, these aerodynamic phenomena can significantly impact the overall quadrotor's dynamics [135].

Many researchers have stressed the importance of dealing with the full nonlinear dynamics of the quadrotor. Bouabdallah and Sigwart highlighted the importance of the actuator dynamics and analysis of the forces and moments caused by aerodynamic effects [106]. However, they neglected the effect in the control system derivation in order to enable simplification. Huang et al. investigated two important aerodynamic effects. The first is blade flapping and second is thrust variation as shown in Figure 3.3. They presented control techniques in order to compensate for these effects [136]. However, just an altitude controller was designed based on a nonlinear design method. There is another phenomenon that appears clearly which is called the "ground effect", this happens when a rotor operates near the ground and this effect can be observed when the quadrotor is driven away from the ground by a thrust augmentation. This force pushes from the ground and is related to a reduction of the induced airflow velocity [137].
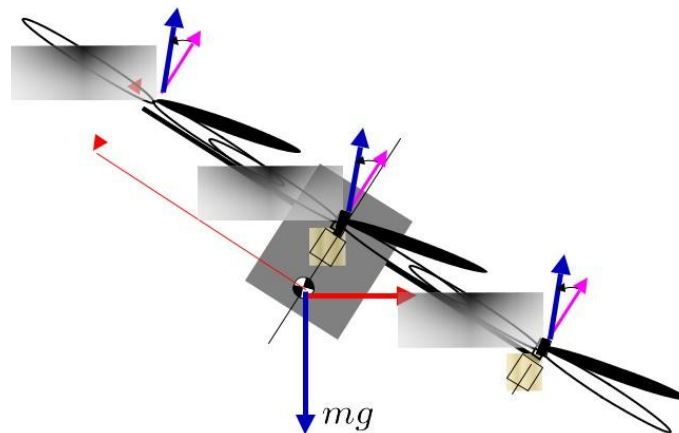
FIGURE 3.3: Effect of blade flapping [106].

3.2.4 Modelling for Control

To derive the term (3.1), there are two approaches to modelling the dynamics of quadrotors: Newton-Euler and Euler-Lagrange formulations [138]. Newton-Euler depends on the spatial Cartesian coordinates to describe the system equations of motion and is obtained by projecting the external forces that affect the quadrotor onto these coordinates. The Euler-Lagrange approach is less dependent on the coordinate system and instead makes use of conservation of energy to derive the equations of motion.

The efficiency of the Lagrangian formulation is well known but there is no fundamental difference in computational efficiency between Lagrangian and Newton-Euler formulations. However, the perceived efficiency of Newton-Euler formulation is due to two factors: the recursive structure of the computation and the representation chosen [138], [139]. The Newton-Euler dynamics includes the solution to the problem of the effect of the external force and moment acting on the terminal link [138], [139]. However, Euler-Lagrange formalism has the advantage that the mechanics can take the same form in any system of generalized coordinates. On the other hand, it has been noted that the Newton- Euler method is easy to be understood if compared with the Euler-Lagrange mechanics. Nevertheless, both methods have a very consistent dynamic description and are used to produce almost all dynamic models for quadrotors.

It is possible to describe the quadrotor dynamics by considering the formulation of Newton-Euler is most common due to its efficiency which can be rearranged as follows

$$m\frac{\mathrm{d}\nu}{\mathrm{d}t_i} = F \tag{3.13}$$

where F is the total applied to the CoG, and $\frac{\mathrm{d}}{\mathrm{d}t_i}$ is the time derivative in the inertial frame. The translational equation of motion can be derived from Newton's law as follows

$$m\left(\frac{\mathrm{d}\nu}{\mathrm{d}t_i} + \omega_{b/i} \times \nu\right) = F \tag{3.14}$$

where $\omega_{b/i}$ is the angular velocity of the airframe with respect to the inertial frame. Since

the control force is computed and applied in the body coordinate system, and since ω is measured in body coordinates, we will express the equation (3.14) in body coordinates, where $v^b = (\varsigma, v, w)^T$, and $\omega^b_{b/i} = (p, q, r)^T$. Therefore, in the body frame, equation (3.14) can be defined as

$$\begin{bmatrix} \dot{\varsigma} \\ \dot{v} \\ \dot{w} \end{bmatrix} = \begin{bmatrix} rv - qw \\ pw - r\varsigma \\ q\varsigma - pv \end{bmatrix} + \frac{1}{m} \begin{bmatrix} f_x \\ f_y \\ f_z \end{bmatrix} \tag{3.15}$$

The rotational equation of motion can also be derived from Newton's law as follow

$$I \frac{d\omega}{dt} + \omega \times I\omega = \mathbf{T} \tag{3.16}$$

where $\mathbf{T}$ is the total moments applied to the quadrotor. The control inputs related to each rotor speed Ω_i are defined as follows:

$$U = \begin{bmatrix} U_1 \\ U_2 \\ U_3 \\ U_4 \end{bmatrix} = \begin{bmatrix} b & b & b & b \\ 0 & lb & 0 & -lb \\ lb & 0 & -lb & 0 \\ d & d & d & d \end{bmatrix} \begin{bmatrix} \Omega_1^2 \\ \Omega_2^2 \\ \Omega_3^2 \\ \Omega_4^2 \end{bmatrix} \tag{3.17}$$

where b is the thrust coefficient, d is the drag coefficient and l is the arm length. The coloration of control input with independent control subsystems are illustrated in Figure 3.4.

The full dynamic model for 6 DOF as following:

$$\dot{p} = \frac{1}{\iota_{xx}} [U_2 + qr(\iota_{yy} - \iota_{zz}) + qJ_P\Omega_r] \tag{3.18}$$

$$\dot{q} = \frac{1}{\iota_{yy}} [U_3 + pr(\iota_{zz} - \iota_{xx}) + pJ_P\Omega_r] \tag{3.19}$$

$$\dot{r} = \frac{1}{\iota_{zz}} [U_4 + qp(\iota_{xx} - \iota_{yy})] \tag{3.20}$$

$$\ddot{x} = \frac{1}{m} (\cos\phi \sin\theta \cos\psi + \sin\phi \sin\psi)U_1 \tag{3.21}$$

$$\ddot{y} = \frac{1}{m} (\cos\phi \sin\theta \sin\psi - \sin\phi \cos\psi)U_1 \tag{3.22}$$

$$\ddot{z} = \frac{1}{m} (mg - \cos\phi \cos\theta)U_1 \tag{3.23}$$
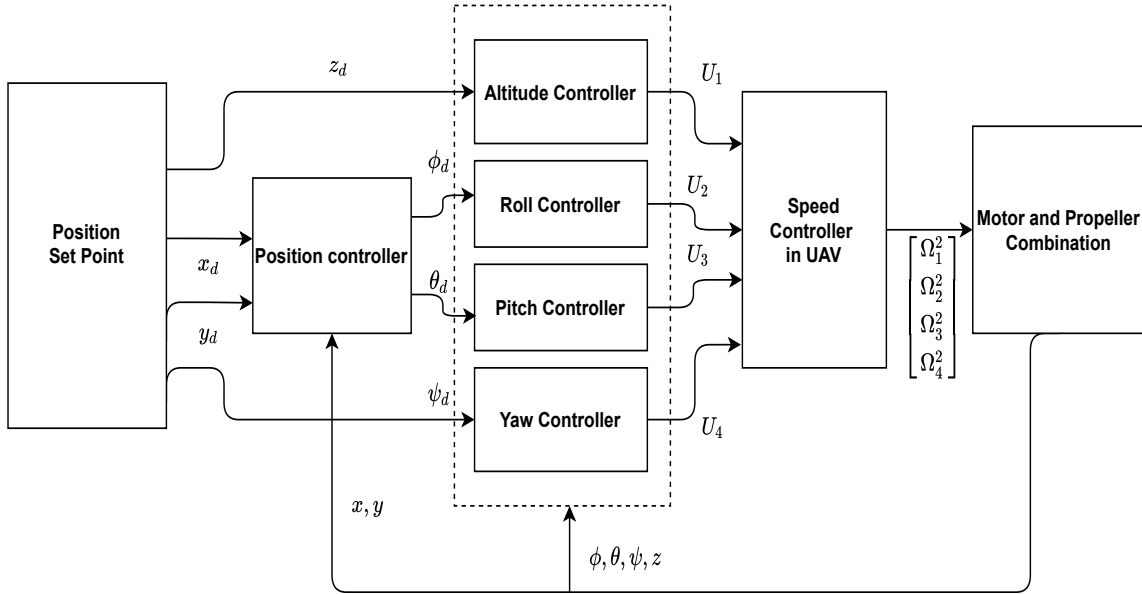
FIGURE 3.4: The proposed of nonlinear coupled model that decomposed into the four independent control subsystems with the coloration of control input U_1, U_2, U_3 and U_4.

3.3 Control Approaches

3.3.1 PID Control

One of the most common methods of controlling a quadrotor is the classical method called Proportional Integral Derivative control. To achieve slightly greater stability, the classical PID control is presented by authors in [140] for the attitude control of a quadrotor. However, in this case the PID controller performed better in the pitch angle tracking but in the roll angle there were observed to be large steady state errors. Another work provided the quadrotor with more stability, and applied PID control of position and orientation in order to stabilize a quadrotor in a low speed wind environment [141]. Another approach was based on PID control by Hoffmann et al. which had another term added to overcome the high acceleration effect by stabilize the rate of the Euler angle [142]. However, in real platforms the PID was tuned due to environmental disturbance which could drive the system towards instability.

To overcome this problem, the authors in [143] proposed an approach based on PID two loops, the first loop for attitude angle control (PI as outer loop) and second loop

(PID as inner loop) to decline the steady state error in order to enhance system stability. However, the results showed that tracking performance of the controllers is still poor. Figure 3.5 shows experimental result conducted by Bouabdallah to control the 1 DOF, however unstable performance occurred at 10s [144].
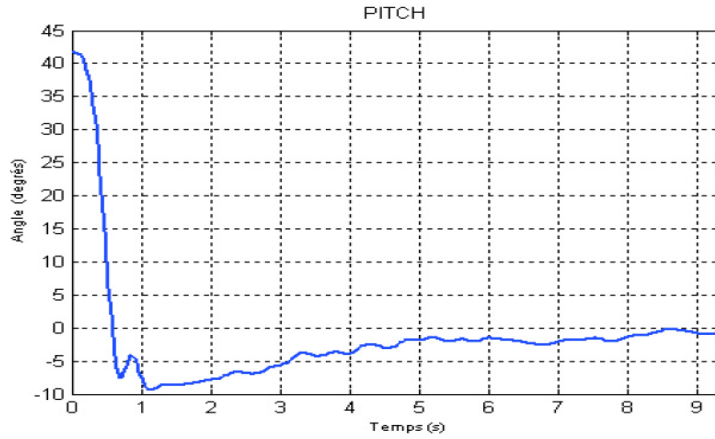
FIGURE 3.5: PID control of pitch on an experimental system [144].

3.3.2 Optimal Control

Linear Quadratic Regulation (LQR) or Linear Quadratic Optimal tracking control have the good of finding a control input which minimizes a performance index (cost function). When employed to control quadrotors, equation of motion (3.1) is as

$$x(t) = \begin{bmatrix} q(t) \\ \dot{q}(t) \end{bmatrix}, \dot{x}(t) = \begin{bmatrix} \dot{q}(t) \\ \ddot{q}(t) \end{bmatrix} = \begin{bmatrix} \dot{q}(t) \\ f(q(t), \dot{q}(t), u(t)) \end{bmatrix} \tag{3.24}$$

where

$$f(q(t), \dot{q}(t), u(t)) = M(q)^{-1}[-B(q, \dot{q})\dot{q} - G(q) + \Gamma(q) + \tau(u)] \tag{3.25}$$

Linearizing around the operating point, typically $(q = 0, \dot{q} = 0)$, gives the general state space form

$$\dot{x}(t) = A(t)x(t) + B(t)u(t) \tag{3.26}$$

The performance index is then given by

$$J = \frac{1}{2} \int_{t_f}^{t_0} \left[x^T(t)Qx(t) + u^T(t)Ru(t) \right] dt \tag{3.27}$$

with the minimising solution

$$u(t) = -Kx(t)$$

where R and Q are real positive weighting matrices.

In 2004 Bouabdallah et al. applied the LQR approach to a quadrotor and compared its performance with PID control. However, the result did not show significant change in performance after applying the LQR algorithm. The only difference is the PID control simplified the quadrotor dynamics and the LQR chould be applied on the complete model [144]. Another study in [145] used LQR control and tried to achieve improvement in the performance of a simple path task, but this control found problems due to obstacles such as wind and other disturbances. However, the development control system based on differential flatness are capable tracking and avoiding obstacles fairly well due to that all constraints are carefully taken into account and therefore the simple LQR controller does not need to fight inaccuracies in the model. Moreover, the quadrotor experiences trajectory deviation after passing half of the obstacle-avoidance mission with a flight time of 3.7 seconds. In order to estimate the unknown state variable and to reduce the effect of noise, Wang in [146] proposed the combination of a Linear Quadratic Estimator (LQE) and Kalman Filter to provide of estimate $x(t)$. So that the LQR algorithm transforms into LQG. This combination improved the stability and slightly improved performance, there were unsatisfactory results in the trajectory tracking.

It is clear that using the LQG can reduce effects of noise but robustness and modelling uncertainty insensitivity are two negative effects which erode performance. To overcome this drawback, Fan in [147] proposed a solution based on using feedforward control in order to compensate the nonlinearity of the model. This design approach using feedforward and LQR had satisfactory performance, but in both stabilization and trajectory tracking.

3.3.3 Nonlinear Control

A commonly applied nonlinear control approach is backstepping control [148], [149]. This provides a recursive solution to stabilize the origin of a system providing it is in strict-feedback form. A general strict-feedback nonlinear system can be expressed as

$$\dot{x} = f_0(x) + g_0(x)z_1$$
$$\dot{z}_1 = f_1(x, z_1) + g_1(x, z_1)z_2$$
$$\dot{z}_2 = f_2(x, z_1, z_2) + g_2(x, z_1, z_2)z_3$$
$$\vdots$$
$$\dot{z}_{k-1} = f_{k-1}(x, z_1, \ldots, z_{k-1}) + g_{k-1}(x, z_1, \ldots, z_{k-1})z_k$$
$$\dot{z}_k = f_k(x, z_1, \ldots, z_k) + g_k(x, z_1, \ldots, z_k)u \tag{3.28}$$

where $x \in R^n$, z_1 to z_k are scalars, function f_i vanishes at the origin, function g_i is nonzero over the domain of interest, and $u \in R^n$ is the control input.

Backstepping control is based on a recursive algorithm in which the designer breaks down the control action into components which stabilize individual subsystems, until the whole system is progressively stabilized. This has the advantage that the control system is capable of handling disturbances using fast and less computational resources. However, its main limitation is poor robustness and an underactuated structure. To overcome this problem, the authors in [150] have applied backstepping control to stabilize a underactuated quadrotor and used Lyapunov stability theory to stabilize the roll and pitch angles. In [151] used another approach for overcoming the problem of underactuation in which the controller consists of an inner loop and outer loop for stabilising the quadrotor (attitude and position, respectively) with the outputs from the outer loop used as inputs to the inner loop. Figure 3.6 shows results using backstepping control to stabilise the attitude [152]. However, robustness is still a major problem, motivating Fang and Gao to increase robustness of the general backstepping algorithm by adding an integrator to produce 'Integra-

tor backstepping control' [153]. This approach has the advantage of eliminating steady-state errors, reducing response time and restraining overshoot of the control parameters.
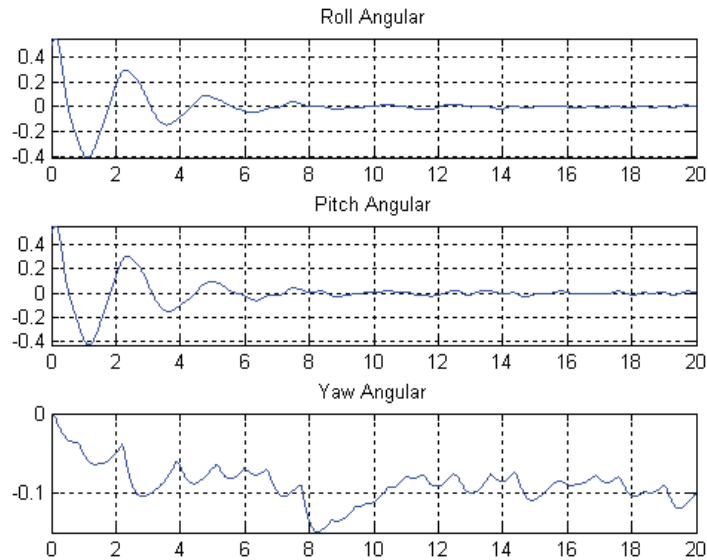
FIGURE 3.6: Backstepping Attitude Control Result [153].

Another common nonlinear control algorithm is Sliding Mode Control (SMC) which has been applied to quadrotors via a discontinuous control signal in order to force it to slide along a prescribed path (sliding surface). The non simplification of dynamics as well as good tracking is one of the main advantages of SMC. Xu and Ozguner applied this control, and results showed good stability and robustness of the system. However, the chattering effect of SMC was observed [154]. To overcome this problem, the authors in [155] suggested an approach which was based on minimizing the pre-determined (sign) function and tracking equations with the saturation function in order to smooth out the control action transitions. Another approach conducted by Lopez et al. implemented an adaptive mechanism to influence the chattering magnitude by controlling the SMC gain [156]. Both SMC controller approaches showed good robustness.

3.3.4   Learning-based Control

ILC relies on performing similar missions multiple times, so that the control can be modified to improve performance over previous operations (i.e., trials, iterations, and passes) through learning. However non-learning systems do not improve their performance due to the same tracking error on each iteration in which despite large model uncertainty and repeating disturbances [157]. Learning-type control strategies can accordingly be classified into ILC, Repetitive Control (RC), neural networks, and adaptive control. Whilst ILC strategies modify the input signal (i.e. the control input), adaptive and neural network learning control methods modify the system (i.e. the controller), and controller parameters, respectively [158]. Additionally, ILC usually guarantees fast convergence within just a few iterations, but the alternative strategies may not [159].

ILC has been applied to quadrotors in a few cases. ILC can be used for systems for which a finite-duration task is repeated. Every iteration should have the same initial conditions and, as the number of trials increase, ILC updates the input signal to ensure that the system output converges to a reference signal. ILC has been applied to many fields, including robotics [160].

The simple D-type ILC form used in [161] for UAV trajectory tracking was based on the Additive State Decomposition (ASD) method. The block diagram shown in Figure 3.7 demonstrates the D-type algorithm, which employs the change of error rate to modify the input for the next iteration in lieu of the error itself. It is evident that the derivative part in the ILC algorithm amplifies small noise signals which may destabilize the system. Ref. [162] has developed another special case of D-type in UAV applications in order to obtain a better tracking performance and lower errors than the typical D-type update rule in [161]. However, although both [161] and [162] use the D-type ILC, they still do not guarantee the rate of convergence in the presence of disturbances.

In [163, 164], the P and D-term ILCs are combined as a PD-type ILC to increase the convergence rate. In [163], three different methods are additionally applied: offline ILC, online ILC, and a combination of both ILCs. These have the respective forms for P-type
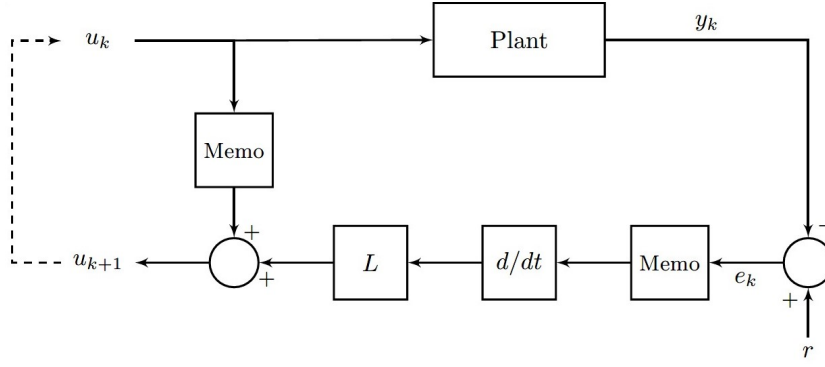
FIGURE 3.7: Block diagram for D-type ILC:- here the $u_k(n)$ it is the input signal was used on k^{th} iterations, L_{opt} is the D-type gain, d/dt the derivative of error, and $r(n)$ and $y_k(n)$ are the reference and the plant output, respectively [162].

ILC.

$$u_{k+1}(n) = \underbrace{u_k(n) + K_P e_k(n)}_{\text{offline P-type}}, \qquad (3.29)$$

$$u_{k+1}(n) = \underbrace{u_k(n) + K_P e_{k+1}(n)}_{\text{online P-type}}, \qquad (3.30)$$

where subscript k denotes the iteration number and subscript n the the sample number.

An inner online PD type ILC update was designed by [163] for quadrotor trajectory tracking control to stabilise the UAV system without taking disturbances into account. The algorithm is

$$u_{k+1}(n) = u_k(n) + K_P e_k(n+1) + K_D \left[e_k(n+1) - e_k(n) \right] \qquad (3.31)$$

The results show a high tracking error. However, the ILC was able to reduce it over subsequent iterations but with low convergence. In [164], ILC was implemented by an adaptive term for enhancing the performance and robustness. This controller term was implemented on a quadrotor platform, where the test results showed improvement in tracking performance, despite the presence of disturbances.

In [165], another ILC form is proposed that includes a combination of the previous two simple structures to include an integral term and is termed PID-type ILC. A controllable flight was optimized using the PID-type ILC after a chnge in mass of the quadrotor. The

method is based only on manual auto-tuning for parameters. In summary, all the previous structures (D-type, PD type, PID-type ILC) are susceptible to process disturbance and measurement error, while rarely being utilized in practical applications.

ILC was applied to achieve quadrotor trajectory tracking while balancing an inverted pendulum [166]. The learning algorithm used was of the form

$$
\begin{cases}
\min_{u_{k+1}} \|S(Fu_{k+1} + \widehat{d_k})\| + \alpha \|Du_{k+1}\| \\
\text{subject to} \quad L_{opt}u_{k+1} \leq q_{max},
\end{cases}
\tag{3.32}
$$

where F is the lifted system matrix, α weights the additional penalty term, and $\widehat{d_k}$ is an updated estimate of disturbance. Via the matrix D, the input derivatives can be penalized. The matrix S allows for the error signal to be scaled or filtered.

The aforementioned approaches are very limited in accuracy. Apart from initial identification procedures and tuning, it is also noted that these approaches demand a large level of computation and do not require an explicit model. Although usability is an advantage of this simplicity, it necessarily degrades performance. There is a great opportunity to assess a wide variety of ILC approaches on UAVs. There is no single algorithm that delivers all of the required features for high performance control while facing uncertain dynamics and environmental factors. Overall, ILC approaches demonstrated the best tracking performance only with medium complexity. Relatively few ILC schemes have been applied to quadrotors, and their evaluation is quite limited.

3.4 Conclusions

This chapter has reviewed several common control algorithms that have been used on quadrotors in the literature. As evident from the review, no single algorithm delivers all the required features for high performance control in the face of uncertain dynamics and environmental factors. It has also been discussed that PID does not require a model but

produces poor tracking; LQG is insensitive to external disturbance but it is not robust to model uncertainty; Integral Backstepping has very good tracking but relies heavily on the dynamics of the system, and also excessive approximation renders the control laws inapplicable; SMC is robust with good tracking but chattering phenomena limits its application; Fuzzy Logic is easy to implement and a standard toolbox exists in Matlab but it is unable to achieve complete stability because compensation for the actual dynamics of the system is not achieved.

ILC exhibited the best tracking performance but has moderate complexity. Few ILC schemes have been applied to quadrotors, and their evaluation is extremely limited. It also been clear that getting the best performance usually requires hybrid control schemes that have the best combination of robustness, adaptability, optimality, simplicity, tracking ability, fast response and disturbance rejection among other factors. The Model Predictive control (MPC) can solve different optimization problems for MIMO systems subjected to multiple constraints due to physical or energy limitations. However, the MPC present limitation as: in order to satisfy the constraints usually it implies a high computational cost [167].

Table 3.1 summarizes the comparison of the various algorithms as applied to quadrotors with all things being equal. The performance of a particular algorithm depends on many factors that may not even be modeled.

TABLE 3.1: Comparison of quadrotor performer with different control algorithms.

Characteristic	Control Algorithm					
	1- PID	2- LQR	3- Backstepping	4- SMC	5- Fuzzy logic	6- ILC
Robustness	1	0	0	1	1	1
Adaptation	0	2	2	2	1	2
Optimality	0	1	0	1	1	1
Tracking ability	1	1	2	2	1	2
Fast convergence	1	1	0	2	1	1
Precision	1	0	1	2	1	2
Simplicity	2	1	0	1	1	1
Disturbance rejection	0	1	2	2	1	1
Manual tuning	2	1	0	0	1	0
(Signal) noise	2	1	0	0	0	0
Chattering	0	0	0	2	0	0

Legend: 0 – low to none; 1 – average; 2 – high. Also, 1 through 2 (Linear); 3 through 4 (Nonlinear); 5 through 6 (Learning-based).

Chapter 4

ILC Controllers

4.1 Introduction

As described in Chapter 3, ILC has shown significant potential when applied to UAVs. However only basic ILC forms have been used on quadrotor s. Therefore, this chapter will review more general ILC forms available with a focus on those that have been applied in practice to engineering systems.

4.2 ILC Framework

The concept of ILC was first proposed in Uchiyama (1978) [168], however, as this paper was written in Japanese, it did not receive significant attention outside Japan. The research of ILC is commonly considered to start in 1984 with the publication Arimoto et al. (1984b) [169]. This defines ILC as a novel control technique applicable to systems operating in a repetitive manner over a finite time interval, [0, T]. Since then, a mature framework has been built up for the development and analysis of linear ILC, and will now be summarised.

A linear ILC system can be described by the discrete state space system

$$\mathbf{x_k}(t+1) = \mathbf{A}\mathbf{x_k}(t) + \mathbf{B}\mathbf{u_k}(t), \qquad 0 \leqslant t \leqslant N$$

$$\mathbf{y_k}(t) = \mathbf{C}\mathbf{x_k}(t)$$

(4.1)

where $\mathbf{x_k}(t) \in \mathbb{R}^n$, $\mathbf{u_k}(t) \in \mathbb{R}^m$, $\mathbf{y_k}(t) \in \mathbb{R}^p$ and $\mathbf{A} \in \mathbb{R}^{n \times n}$, $\mathbf{B} \in \mathbb{R}^{n \times m}$, $\mathbf{C} \in \mathbb{R}^{p \times n}$ are the system matrices. Moreover, $\mathbf{x_k}$, $\mathbf{u_k}$ and $\mathbf{y_k}$ are the states, inputs and outputs vectors respectively as trial k.

The same dynamics can be written in the so called 'lifted' form as

$$\mathbf{y_k} = G\mathbf{u_k} + dx_0$$

(4.2)

where

$$G = \begin{bmatrix} g_0 & 0 & \cdots & 0 \\ g_1 & g_0 & \cdots & \vdots \\ \vdots & \vdots & \ddots & 0 \\ g_{N-1} & g_{N-2} & \cdots & g_0 \end{bmatrix}$$

(4.3)

$$g_k = CA^{k+n_r-1}B \qquad k = 0,1,2....,N-1$$

and

$$d = \begin{bmatrix} CA^{n_r} \\ CA^{n_r+1} \\ \vdots \\ CA^{n_r+N} \end{bmatrix}.$$

(4.4)

Also

$$u = [u(0)^T, u(1)^T, ..., u(N-1)^T]^T \in \mathbb{R}^{mN}$$

$$y = [y(n_r)^T, y(n_r+1)^T, ..., y(N-1+n_r)^T]^T \in \mathbb{R}^{pN}$$

$$(4.5)$$

where n_r is the system relative degree.

The initial state terms x_0 can be absorbed into the reference trajectory to give $x_0 = 0$, and are omitted without loss of generality. ILC updates the input for the next trial using the input and error in the past trials, i.e

$$u_{k+1} = f(u_k, e_k) . \tag{4.6}$$

The most common form of ILC employs the input update law defined as

$$u_{k+1} = u_k + Le_k \tag{4.7}$$

where L is a learning operator, y_d is the desired reference signal, and the error $e_k = y_d - y_k$. The objective of ILC is to force the tracking error, e_k, to converge to zero after sufficient updating trials, and the input, u_k, to converge to a unique signal u^*, i.e.

$$\lim_{k \to \infty} e_k = 0, \qquad \lim_{k \to \infty} u_k = u^* \tag{4.8}$$

The choice of the learning function L is crucial to determine the algorithm robustness and convergence characteristics. A necessary and sufficient condition for convergence is the spectral radius condition

$$\rho(I - GL) < 1 . \tag{4.9}$$

ILC can be combined with an existing feedback controller, as shown in Figure 4.1. In this case G is simply replaced by the closed loop system $(I + GK)^{-1}G$ within the design

process.
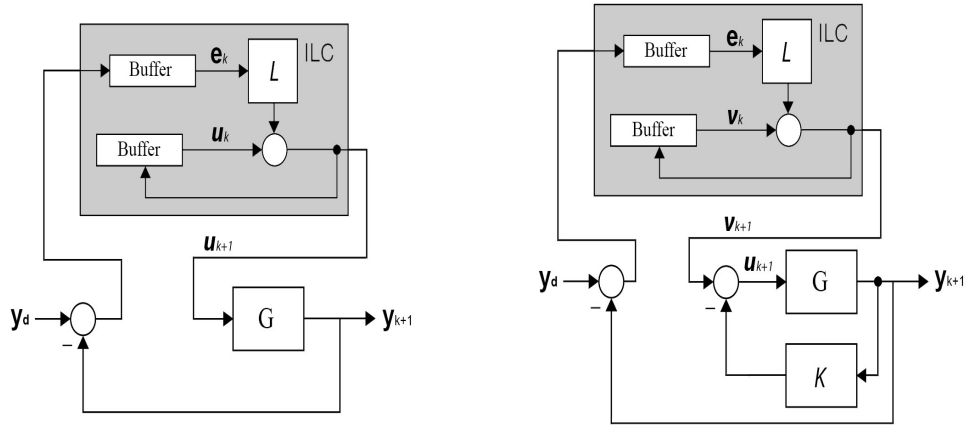
FIGURE 4.1: Basic ILC framework with feedback controller around the plant.

Now ILC forms are reviewed and will focus on those supported by substantial experimental benchmarking.

4.3 Basic ILC

4.3.1 Proportional-type ILC

Proportional-Type ILC or P-type ILC is one of the earliest ILC methods, and was defined by Arimoto for SISO systems [170]. Here the control action correction term for the next trial is proportional to the error from the previous trials, i.e.

$$u_{k+1} = u_k + \gamma e_k \tag{4.10}$$

where the learning gain γ is a constant scalar that influences the rate of convergence. The authors considered linear time invariant, continuous time state space systems, $S(A,B,C)$. Comparison with (4.7) yields

$$L = \gamma I, \tag{4.11}$$

In order to ensure the ILC tracking objective (4.9) is satisfied, the convergence condi-

tion (4.9) is

$$
= \rho \left(I - \gamma \begin{bmatrix} CB & 0 & \cdots & 0 & 0 \\ CAB & CB & \ddots & 0 & 0 \\ CA^2B & CAB & \ddots & \ddots & \vdots \\ \vdots & \ddots & \ddots & CB & 0 \\ CA^{N-1}B & \cdots & \cdots & CAB & CB \end{bmatrix} \right) = |I - \gamma CB| < 1 \quad (4.12)
$$

which agrees with Arimoto et al. (1985) [171]. It should be noted that the convergence condition does not contain A and is hence independent of the system dynamics. It also requires $CB \neq 0$. Note that (4.12) may produce unacceptable transients in the error norm.

4.3.2 Derivative-type ILC

Another approach is D-Type ILC, by Arimoto et al. (1985) [171], which uses the derivative of error to update the controller input. The update law is given by

$$
u_{k+1} = u_k + \alpha \dot{e}_k \quad (4.13)
$$

where $\dot{e}_k$ denotes the derivative of the error e_k. It is similar to the P-type ILC algorithm, but uses the rate of change of the error to update the input of the next trial instead of the error itself. Comparison with (4.7) yields

$$
L = \alpha \begin{bmatrix} 1 & 0 & \cdots & 0 & 0 \\ -1 & 1 & \ddots & 0 & 0 \\ 0 & -1 & \ddots & \ddots & \vdots \\ \vdots & \ddots & \ddots & 1 & 0 \\ 0 & \cdots & \cdots & -1 & 1 \end{bmatrix}, \quad (4.14)
$$

In order to ensure the ILC tracking objective (4.9), the convergence condition is given in [171], [172] as

$$|I - \alpha CB| < 1 . \tag{4.15}$$

Therefore, it should be noted that the convergence condition is independent of matrix A even if the system is unstable because of the finite time interval of each trial [173]. For the same reason as before, it follows that $CB \neq 0$ is required. However, the D-type ILC algorithm is sensitive to measurement error and process disturbance, and it is seldom used in practical cases.

In order to increase the convergence rate and applicable system classs, P-type and D-Type ILC can be combined together. The resulting 'PD-type' ILC update law is given by

$$u_{k+1} = u_k + \gamma e_k + \alpha \dot{e}_k \tag{4.16}$$

The convergence condition is $|I - (\gamma + \alpha)CB| < 1$ [174]. Due to the noise-sensitive D-type component, it also has limited practical use. Inspired by the analogy with traditional proportional plus integral plus derivative control 'PID', the above algorithm has been generalized to include an integral term (Moore, 1993) [175], i.e

$$u_{k+1} = u_k + \gamma e_k + \alpha \dot{e}_k + \beta \int_0^t e_k(s)ds . \tag{4.17}$$

These methods are attractive because the learning process does not rely on the model accuracy and it can easily be generalized for MIMO systems. On the other hand, the derivative action increases the design sensitivity to noise and disturbance. In addition, experimental studies show that, for some MIMO systems, monotonic convergence is not always guaranteed unless the trial is short. PI and PID-type ILC have similar limitations in practical application, due to the same noise sensitivity problem.

4.4   Optimal Approaches

The properties of linear optimal algorithms have been extensively studied, i.e Bristow (2008); Ratcliffe et al. (2005); Donkers et al. (2008); Wang et al. (2010); Barton et al. (2008); Mishra and Tomizuka (2005); Davies et al. (2008); Butcher et al. (2008) [176–183]. Now leading ILC example are introduced with their own specific features.

4.4.1   Gradient ILC

Gradient-based ILC algorithms have received significant attention in the literature due to their attractive theoretical properties. Comparing to a simple ILC controllers, gradient-based ILC relies on the system model to achieve faster error convergence and uses the properties of gradient decent to construct the ILC control action update. Gradient ILC has appeared in [184–186] for SISO systems and was derived for MIMO systems.

An alternative method of guaranteeing (4.9) is to transpose operator G^T. This is the lifted form of the more general adjoint operator G^*. This leads to

$$L = \beta G^* \tag{4.18}$$

which yields the update law

$$u_{k+1} = u_k + \beta G^T e_k \tag{4.19}$$

where the scalar β is the learning gain. The update (4.19) has interpretation of being the gradient descent solution to the minimisation problem $\min_u J(u_k) = \|y_d - Gu_k\|^2$. Substituting $L = \beta G^T$ into the general convergence conditions (4.11) yields

$$\rho \left(I - \beta GG^T \right) = \|I - \beta GG^T\| < 1 \tag{4.20}$$

As stated by Owens et al. (2008) [186], since GG^T is positive definite, the convergence

condition becomes

$$0 < \beta < \frac{2}{\|GG^T\|} = \frac{2}{\|G\|^2} \ . \tag{4.21}$$

Therefore, if (4.21) holds the error converges monotonically to zero as the trials k goes to infinity. Algorithms of the form (4.19) have been tested experimentally [187], and yielded performance that had 10 times higher accuracy than a standard feedback controller.

4.4.2   Norm Optimal Iterative Learning Control

Norm Optimal ILC (NOILC), is a model based algorithm which was introduced in [188]. The ILC input for the next iteration is obtained by optimizing a certain performance index which allows error convergence and input energy to be balanced. NOILC has been applied to many applications and established a platform for further ILC research such as predictive norm-optimal ILC [189] and projections [190]. NOILC uses the quadratic cost function form

$$J(u_{k+1}) = \frac{1}{2}\{[y_d - y_{k+1}]^T Q[y_d - y_{k+1}] + [u_{k+1} - u_k]^T R[u_{k+1} - u_k]\} \tag{4.22}$$

where

$$Q = \{Q(0), Q(1), \cdots, Q(N-1)\} \tag{4.23}$$

$$R = \{R(0), R(1), \cdots, R(N-1)\} \tag{4.24}$$

in which $Q(t)$ and $R(t)$ are symmetric, positive semi-definite weighting matrices.

The performance index in (4.22) is chosen in order to produce ILC control action u_{k+1} in the next trial that minimizes tracking error and the input change from one trial to another which are tuned by the means of the weighting matrices Q and R, respectively. The ILC

optimal input is defined as

$$u_{k+1} = \min_{u_{k+1}} J(u_{k+1}) \tag{4.25}$$

by applying partial differentiation to J_{k+1} with respect to u. This involves the stationary point, $\partial J_{k+1}/\partial u$ being set to zero, leading to the update law

$$u_{k+1} = u_k + G^{\mathsf{T}} e_{k+1} \tag{4.26}$$

where G^{T} is the adjoint operator of the system G, where $G^{\mathsf{T}} = R^{-1} G^T Q$. It can be shown that the convergence condition (4.9), is always satisfied and moreover

$$\|\mathbf{e}_{k+1}\| \leq \frac{1}{1 + \sigma^2(GG^{\mathsf{T}})} \|\mathbf{e}_k\| \leq \|\mathbf{e}_k\| \tag{4.27}$$

where $\sigma^2(GG^{\mathsf{T}})$ is the smallest spectral radius value of symmetric, positive definite operator GG^{T}. Because (4.26) is non-causal, it can be manipulated to produce either a causal feedforward form or feedback and feedforward form by Amann et al. (1996) [191], where

$$L = G^{\mathsf{T}} (I - GG^{\mathsf{T}})^{-1} \tag{4.28}$$

Therefore, the update law is given by

$$u_{k+1} = u_k + G^{\mathsf{T}} (I - GG^{\mathsf{T}})^{-1} e_k \tag{4.29}$$

4.5 Newton Method Based ILC

The Newton method is based upon performing a local linearization of the dynamics, followed by a linear ILC update over the tracking error [192]. A discrete non-linear state

space model is given in the form of the SISO system

$$x_k(t+1) = f(x_k(t), u_k(t))$$
$$y_k(t) = h(x_k(t))$$

(4.30)

with initial state $x(0) = x0$. From (4.30) the algebraic relationship between input and output over the kth trial over the finite horizon $t \in [0, T]$ can be expressed as

$$y_k(0) = h(x_k(0), u_k(0)) = g0(x_k(0), u_k(0))$$
$$y_k(1) = h(x_k(1), u_k(1)) = h(f(x_k(0), u_k(0)), u_k(1))$$
$$: g_1(x_k(0), u_k(0), u_k(1))$$
$$\vdots$$
$$y_k(T) = h(x_k(T), u_k(T))$$
$$= h(f(x_k(T1), u_k(T1)), u_k(T))$$
$$: g_N(x_k(0), u_k(0), u_k(1), ..., u_k(T)) .$$

(4.31)

Thus, the non-linear system (4.30) can be expressed by the algebraic function $g(\cdot)$: $l[0, T] \mapsto l_2[0, T]$ given by

$$y_k = g(u_k), \quad g(\cdot) = [g_0(\cdot), g_1(\cdot), ..., g_T(\cdot)] .$$

(4.32)

The Newton based ILC update law is given by

$$u_{k+1} = u_k + g'(u_k)^{-1} e_k .$$

(4.33)

where the term $g'(u_k)$ is simply a linearization of the system about input u_k. Here the form (4.33) can be replaced by the general form $u_k + 1 = u_k + Ke_k$ with K any learning-gain

operator which ensures convergence of the linearized plant model $g'(u_k)$.

The state space model of the linearized time-varying LTI system can be expressed as

$$\tilde{x}(t+1) = \bar{A}(t)\tilde{x}(t) + \bar{B}(t)\tilde{u}(t)$$
$$\tilde{y}(t) = \bar{C}(t)\tilde{x}(t)$$

(4.34)

where $\bar{A}(t)$, $\bar{B}(t)$ and $\bar{C}(t)$ denote the linearized time-varying system dynamics matrices calculated every iteration by linearizing the nonlinear system in equation (4.30) around (x_k, u_k) as follows

$$\bar{A}(t) = \frac{\partial f}{\partial x}\Big|_{\{x_k(t), u_k(t)\}} \qquad \bar{B}(t) = \frac{\partial f}{\partial u_k}\Big|_{\{x_k(t), u_k(t)\}}$$
$$\bar{C}(t) = \frac{\partial h}{\partial x}\Big|_{\{x_k(t), u_k(t)\}}.$$

(4.35)

This means that the Newton ILC algorithm needs to solve the linear system $\bar{y} = g'(u_k)\bar{u}$ every trial where $g'(u_k)$ is obtained iteratively by replacing the LTI dynamics in (4.3) with the LTV dynamics from equation (4.35). The implementation of the Newton ILC method relies on the existence of the $g'(u_k)$ inverse. To overcome this problem, the input update can be written as

$$u_{k+1} = u_k + \varepsilon_{k+1}$$

(4.36)

where $\varepsilon_{k+1} = g'(u_k)^{-1} e_k$ is easier to obtain by solving the following equation

$$g'(u_k)\varepsilon_{k+1} = e_k$$

(4.37)

Extension to Newton method based iterative learning control were made for a discrete nonlinear systems with constraints by adding inequality constraints, unconstrained convergence conditions [193].

4.6 Other Generalized ILC

The above basic ILC strategies were all based on the assumption that the ILC require a tuning gain matrix and in one case a delay-time constant, and do not require an explicit model. This simplicity aids usability but necessarily degrades performance. Thus, the authors in [194, 195] and [196] used the optimization based ILC approaches to address these limitations. In [194] and [195], the author examines the performance of ILC in gradient-based that enhances a quadrotor's controllability and stability during attitude control. Again in [196], the optimization based ILC approach has applied by researchers at ETH Zurich to achieve quadrotor trajectory tracking while balancing an inverted pendulum. Figure. 4.2 presents the image sequence of application of ILC to a quadrotor by tracking a small trajectory indoors and the convergence of ILC when applied to a quadrotor.
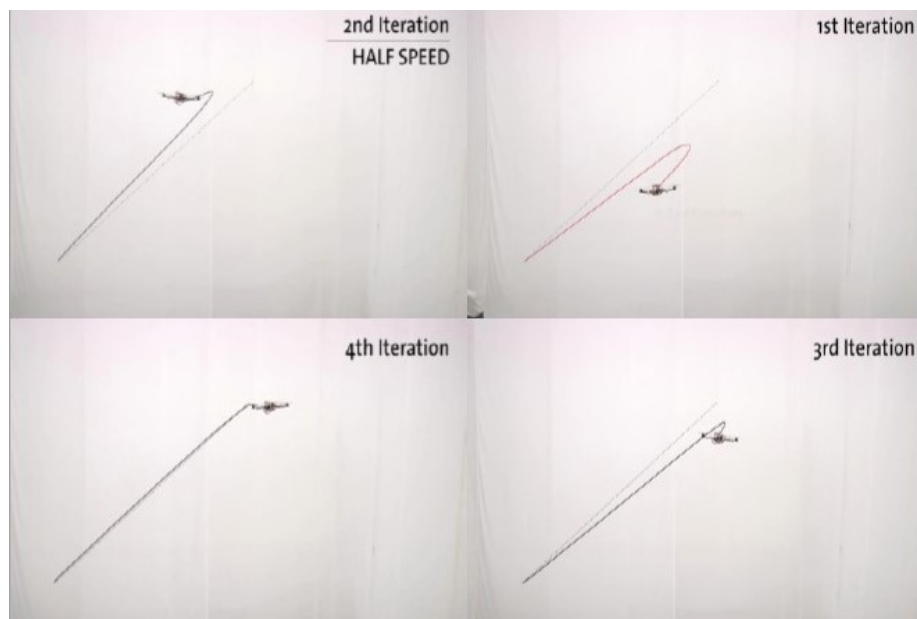
FIGURE 4.2: 1st iteration to 4th Iteration of ILC based trajectory tracking [195].

The experiment in [194, 195] and [196] showed the fast rate of convergence of the norm error which is low after a small number of trials, although in some cases the method is slow as illustrated in Figure. 4.3.
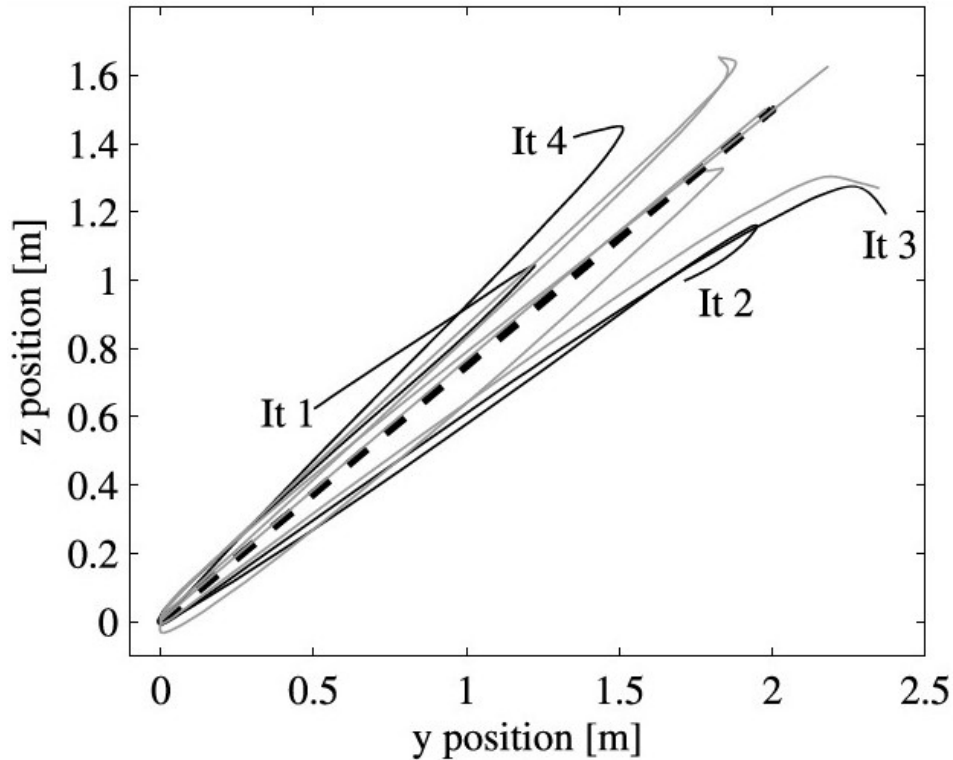
FIGURE 4.3: The diagonal trajectory experiment for quadrotor position in the yz-plane starting from 1st until reach 10th iterations. [196].

It was shown that both study to outperform the strategy proposed in [161], [162], [164] in terms of convergence speed, trajectory tracking performance and robustness. One shortcoming of this strategy is that it neglects the impact of non-repetitive noise on the system output.

Other attempts to address the disturbance using the ILC in combination with different control approaches have been conducted in [197], [198]. In [199], the authors designed back-stepping integral sliding mode control (BISMC) with ILC algorithm for a quadrotor. The back-stepping is responsible for tracking the desired trajectory, then the integral sliding mode controller is designed and analyzed for coping with the uncertainties and external disturbances. Finally, iterative learning control is designed to improve the accuracy of the tracking. In another approach, the authors in [198] introduced a design based on the capabilities of $\mathscr{L}$ adaptive control combined it with ILC form to achieve high-precision trajectory tracking in the presence of unknown and changing disturbances.

TABLE 4.1: Summary of iterative learning control scheduling strategies

Approaches	Applications	System Control	Objective	Constraint	Solution	Performance Evaluation	Ref.
Generalized ILC	Surveillance-based applications in UAVs	Region-to-Region ILC	To minimize the overall distance travelled, guaranteeing passage through region at the specific times	Average time, Location, Constant power source, One-dimensional scenario, Trade-off (Single lost outside defined region)	Apareto optimization	Numerical simulation	[199]
Traditional + Generalized ILC	Aerospace (UAVs)	Adjoint-type ILC	To obtain a planar model of a helicopter, to prove effective in nonlinear non-minimum phase system	Complex computation, Low convergence speed	Linearized input-state system using flat output	Numerical simulation	[200]
Traditional + Generalized ILC	Autonomous Aerial Refueling (AAR) probe-drogue	Derivative-type ILC, Adjoint-type ILC, ILC based on additive state decomposition	To overcome disadvantage of only feedback control, Designing a docking controller in probe-drogue refueling	Sensitivity to (noise and disturbance), Complex computation, Low convergence speed	Additive State Decomposition	Theoretical analysis, Simulation	[201]
Generalized ILC	Autonomous Aerial Refueling (AAR)	Terminal iterative learning control (TILC)	To compensate docking errors caused aerodynamic disturbances model probe aerial refueling	Only terminal positions	ILC initial value estimation method	Simulation	[202]
Generalized ILC	Autonomous Aerial Refueling (AAR)	Terminal iterative learning control (TILC)	To choice the docking control in autonomous aerial refueling, to extending the range and long-time flight	Single point to point movement	Time allocation, 4 docking attempts start at time 50 (fail), 100 (fail), 150 (succeed), and 200 (succeed) s.	Theoretical analysis, Simulation	[203]

The two approaches [197], [198] are similar in term of using same basic ILC, and accuracy (i.e., in case of BISMC+ILC, $\mathscr{L}$+ILC) can be much better than only using (i.e., BISMC, $\mathscr{L}$). However, the constraint described in [198], that the backstepping relies heavily on the dynamics of the system, and the system not given in strict feedback form for both the attitude angles, and the integral sliding mode controller has chattering phenomena that limits its application. Moreover, the main challenge facing the approach in [198] is the training of the UAV to operate in changing environments, which is both complex and time-consuming in terms of both design life cycle and computational intensity.

Finally, in Table. 4.1, we summarize some of the recently developed ILC algorithms in equations applied to UAVs and the strategies of ILC for more generalized and specific tasks, respectively. It is shown from Table IV, that in a large class of practical systems, such as autonomous aerial refueling based on terminal ILC [202] and [203], it is required that the output achieves perfect tracking at more than one defined time instants $t = t_i$ respectively. Therefore, it needs an extension of terminal ILC to solve problems which only require tracking of a number of critical positions at a subset of time instants.

4.7 Conclusions

A range of ILC approaches have been reviewed including simple structure controllers for ILC which have been presented in discrete-time. These controllers require a tuning gain matrix and in one case a delay-time constant, and do not require an explicit model. This simplicity aids usability but necessarily degrades performance. Also PI and PID-type ILC have limitations in practical application, such as unguaranteed monotonic convergence and increases sensitivity to noise due to derivative action. Then a variety of optimal approaches have been evaluated and compared. These yield high performance. Also nonlinear systems can be addressed via linearisation followed by linear ILC design. In addition, relaxing the tracking demand, can produce faster, more robust algorithms. These

conclusions will be used to motivate new ILC algorithms for application to quadrotor s in the next chapter.

Chapter 5

ILC Design and Application to Quadrotors

5.1 Introduction

This chapter describes the implementation of the leading approaches identified in Chapter 4, Chapter 3 and Chapter 2 to UAVs in order to critically compare performance and inform design. Moreover, it will develop new ILC algorithms to address the challenging quadcoptor control problem. Specifically, these problems comprise the difficulty in identification, nonlinearity, and coupled, MIMO dynamics. To address these, the techniques of Newton method based linearisation and optimal ILC approaches will first be expanded and generalised. In Section 5.5, suitable experimental system is selected to provide a test platform. Then in Section 5.7 and Section 5.8 a model is identified and is applied within the leading control approaches.

5.2 Design Guidelines for ILC based

From Chapter 4 and Chapter 3, the ILC architecture during design should carry the same basic general design guidelines that Arimoto maintained, then expanded and generalized

to fulfil the specific tasks (OPL monitoring) in our case. These guidelines:

 – It should be a repetitive nature task to meet control design

 – It should be a fixed amount of time to complete repeated task

 – It should be a predefined output before the passes

 – It should be initial conditions is same for each trial

5.3   Task Definition and Design Case

5.3.1   Initial Design

From the problem described in Chapter 2, and previous attempts made in Section 2.4, the control task can be defined as completing the following ordered movements:

(i) Pylon inspection: The quadrotor is first launched from a base ground point S at position p_0 as shown in Figure 5.1, and must pass through the specific points p_i, where $i = 1, 2, \ldots, n$. At each points maintain the position for τ_i seconds and passing to the next. During this period it must maintain an orientation $\boldsymbol{o}_i$ heading towards the insulator. For each sequence, the quadrotor start from recharge point $\boldsymbol{p}_0$ at time $\boldsymbol{t}_0$.
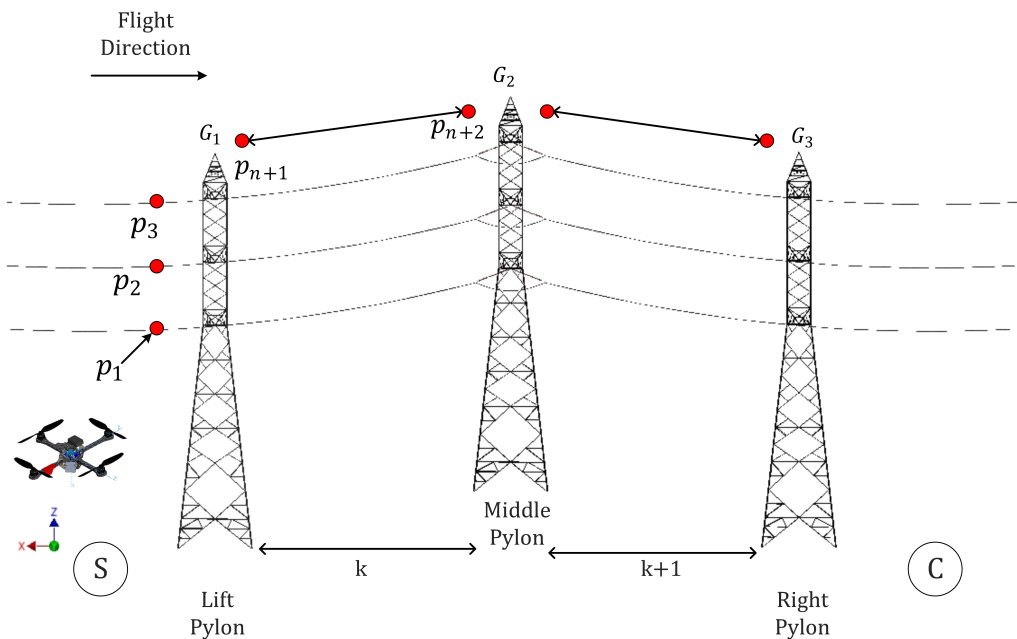
FIGURE 5.1: Full proposed of tracking positional requirement for extraction k.

(ii) Transition: Then the quadrotor must pass through a point p_{n+1} vertically above the insection of the pylon and the power lines, at time t_{n+1} maintaining an orientation $\boldsymbol{o}_{n+1}$ pointing towards the cable. From steps (i),(ii) and since we also specify a length of time for the quadrotor to take a picture of the insulator feature, The position objective is

$$\begin{bmatrix} x \\ y \\ z \end{bmatrix}(t) = \boldsymbol{p}_i, \qquad t \in [t_i, t_i + \tau_i), \qquad i = 1, \cdots n+1 \qquad (5.1)$$

and the quadrotor must maintain an orientation, which is defined as

$$\begin{bmatrix} \phi \\ \theta \\ \psi \end{bmatrix}(t) = \boldsymbol{o}_i, \qquad t \in [t_i, t_i + \tau_i), \qquad i = 1, \cdots n+1 \qquad (5.2)$$

(iii) Power lines: Then the quadrotor moves towards a point p_{n+2} at which the cable meets the next pylon. This movements is restricted either to a straight line or more generally to the x-z plane. The timing t_{n+2} of this movements is arbitrary but the quadrotor must maintain orientation towards the powerlines. Now consider the power-line tracking as seen in Figure 5.2, that takes place between time instants t_{n+1} and t_{n+2}. Here we have a planar position constraint (in x-y plane) of form

$$\underbrace{\begin{bmatrix} -p_{n+2} & 1 & 0 \end{bmatrix}}_{\mathbf{P_t}} \begin{bmatrix} x \\ y \\ z \end{bmatrix}(t) = p_{n+1}, \qquad t \in [t_{n+1}, t_{n+2}] \qquad (5.3)$$

From steps (iii) to specify tracking along a straight line (cable). In this regard, consider a quadrotor moving between two pylons from points p_{n+1} to p_{n+2} to track a cable

$$\underbrace{\begin{bmatrix} -a & 0 & 1 \\ 0 & 1 & 0 \end{bmatrix}}_{\mathbf{P_t}} \begin{bmatrix} x \\ y \\ z \end{bmatrix}(t) = \begin{bmatrix} 0 & 0 & 1 \\ 0 & 1 & 0 \end{bmatrix} p_{n+1} - \begin{bmatrix} 1 & 0 & 0 \end{bmatrix} p_{n+1}(a), \qquad (5.4)$$
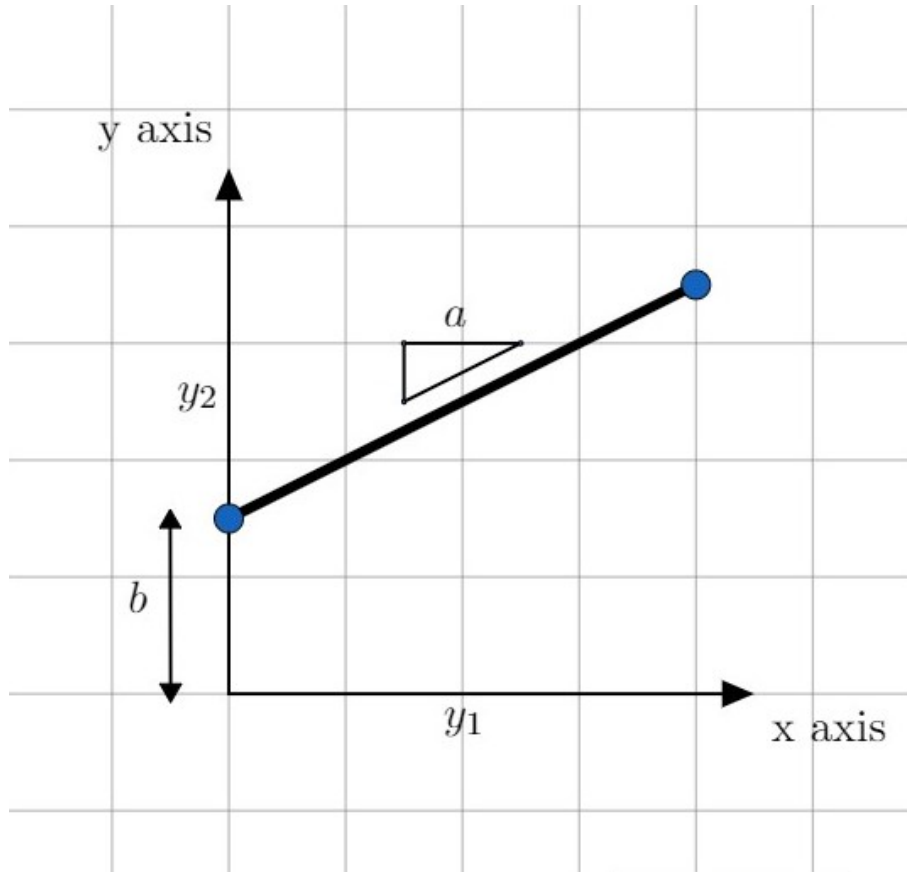
FIGURE 5.2: Planar constraint in $x - y$ plane.

where

$$a = \frac{\begin{bmatrix} 0 & 0 & 1 \end{bmatrix} (p_{n+2} - p_{n+1})}{\begin{bmatrix} 0 & 1 & 0 \end{bmatrix} (p_{n+2} - p_{n+1})}$$

Similarly the simultaneous orientation constraint is

$$\begin{bmatrix} \phi \\ \theta \\ \psi \end{bmatrix} (t) = o_{n+1}, \qquad t \in [t_{n+1}, t_{n+2}], \qquad i = 1, \cdots n \qquad (5.5)$$

(iv) Only 2-3 sequence of operation from (i) to (iii) can be performed due to the hardware and battery life time. Therefore, the quadrotor must reach to the next ground base point C. Here it must sustain zero velocity and maintain an orientation constant. To achieve docking, we require the quadrotor to return to rest at a point p_{n+3} at time t_{n+3} as illustrated in next charge docking.

5.3.2   Charge Docking

To achieve docking, we require the quadrotor to return to rest at a point $\boldsymbol{p}_{n+3}$ at time t_{n+3}.

$$\begin{bmatrix} x \\ y \\ z \end{bmatrix}(t_{n+3}) = \boldsymbol{p}_{n+3}, \qquad \begin{bmatrix} \dot{x} \\ \dot{y} \\ \dot{z} \end{bmatrix}(t_{n+3}) = \boldsymbol{0}, \qquad \begin{bmatrix} \phi \\ \theta \\ \psi \end{bmatrix}(t_{n+3}) = \boldsymbol{o}_{n+3} \qquad (5.6)$$

Steps (i) to (iv) motivate the use of ILC to perform 2-3 sequences of operation, with recharging after each trial as seen in Figure 5.3. The quadrotor now can increase the accuracy of identifying faults by updating the control input for use in the next sequence. Thus, improve the accuracy rather than missing data or skipping data in unexpected weather.
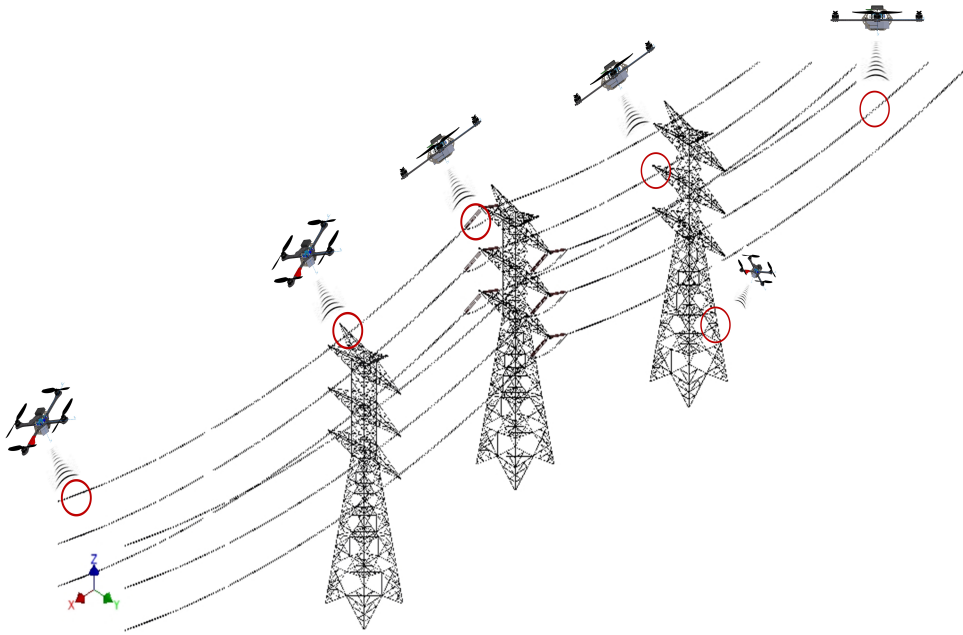
FIGURE 5.3: UAV performs a frequent Inspections through a travel path in the x-y-z plane. The systemic diagram illustrates three levels of the tasks by trajectory tracking, where the tasks will be recurrent in each trial due to the repetitive nature of the OPL geometries.

The next step is to formulate the above motivate into an entitled ILC control system.

5.3.3   Full Task Definition

First consider the general nonlinear discrete-time system and add iteration index k so the MIMO dynamics structure can be given as:

$$\eta_k(t+1) = f(\eta_k(t), u_k(t))$$
$$y_k(t) = h(\eta_k(t), u_k(t)) \qquad \eta(0) = \eta_0 \tag{5.7}$$

where

$$\eta(t) = \begin{bmatrix} q(t) \\ \dot{q}(t) \end{bmatrix}$$

Taking the most general case, our system is then defined by (5.1), (5.2), (5.3), (5.4) and (5.5). Then define

$$h(\begin{bmatrix} \dot{q}_k \\ q_k \end{bmatrix}(t), u_k(t)) = \begin{bmatrix} 0 & 0 & 0 & I \end{bmatrix} \begin{bmatrix} \dot{q}_k \\ q_k \end{bmatrix}(t) \tag{5.8}$$

then the objective is

$$y_k = \begin{bmatrix} x \\ y \\ z \end{bmatrix}(t) \tag{5.9}$$

If instead, we define

$$h(\begin{bmatrix} \dot{q}_k \\ q_k \end{bmatrix}(t), u_k(t)) = \begin{bmatrix} 0 & 0 & I & 0 \end{bmatrix} \begin{bmatrix} \dot{q}_k \\ q_k \end{bmatrix}(t) \tag{5.10}$$

then the objective is

$$y_k = \begin{bmatrix} \phi \\ \theta \\ \psi \end{bmatrix}(t) \tag{5.11}$$

Lastly, instead define

$$h(\begin{bmatrix} \dot{q}_k \\ q_k \end{bmatrix}(t), u_k(t)) = \begin{bmatrix} 0 & I & 0 & 0 \end{bmatrix} \begin{bmatrix} \dot{q}_k \\ q_k \end{bmatrix}(t) \tag{5.12}$$

then the objective is

$$y_k = \begin{bmatrix} \dot{x}_k \\ \dot{y}_k \\ \dot{z}_k \end{bmatrix}(t) \tag{5.13}$$

ILC in our new implementation has more challenging and unique terms related to power line constraints, so the ILC is frequently applied to a fixed time interval and set up in a strict mathematical connection between the ILC framework and the nonlinear equations. ILC is transformed into a nonlinear algebraic function between the input and the output, and so the system dynamics are now expressed as a vector function over the finite horizon $0 \le t \le T$, $g(.)$, defined by

$$
\begin{aligned}
y_k(0) &= h(\eta_k(0), u_k(0)) = g_0(\eta_k(0), u_k(0)) \\
y_k(1) &= h(\eta_k(1), u_k(1)) = h(f(\eta_k(0), u_k(0)), u_k(1)) \\
&\quad : g_1(\eta_k(0), u_k(0), u_k(1)) \\
&\quad \vdots \\
y_k(T) &= h(\eta_k(T), u_k(T)) \\
&= h(f(\eta_k(T1), u_k(T1)), u_k(T)) \\
&\quad : g_N(\eta_k(0), u_k(0), u_k(1), ..., u_k(T)).
\end{aligned}
\tag{5.14}
$$

Thus, the non-linear system (5.7) can be expressed by the algebraic function $g(\cdot) : l_2^m[0, T] \mapsto l_2^p[0, T]$ given by

$$y_k = g(u_k), \quad g(\cdot) = [g_0(\cdot), g_1(\cdot), ..., g_T(\cdot)]^T. \tag{5.15}$$

Next we write the controller (5.1),(5.2),(5.3),(5.4),(5.5) and (5.6) in terms of the system dynamics (5.9)-(5.15), To do this, we employ the lifted formulation

Substitute (5.14) into (5.17) to get lifted velocity system g_v in discrete time this has form

$$\begin{bmatrix} \dot{x}_k \\ \dot{y}_k \\ \dot{z}_k \end{bmatrix} = g_v(u_k) \tag{5.16}$$

So that objective (5.6) equals

$$\Phi g_v(u_k) = \begin{bmatrix} \mathbf{0} \\ \vdots \\ \mathbf{0} \end{bmatrix} \tag{5.17}$$

where $3n \times 3N$ matrix Φ has block-wise components given by

$$\begin{bmatrix} \Phi_{3(i-1)+1,3(j-1)+1} & \cdots & \Phi_{3(i-1)+1,3j} \\ \vdots & \ddots & \vdots \\ \Phi_{3i,3(j-1)+1} & \cdots & \Phi_{3i,3j} \end{bmatrix} := \begin{cases} I, & j = t_i/T_s \\ 0, & \text{otherwise} \end{cases} \tag{5.18}$$

Substitute (5.8) into (5.15) to get g_p in discrete time this has form

$$\begin{bmatrix} x_k \\ y_k \\ z_k \end{bmatrix} = g_p(u_k) \tag{5.19}$$

So that objective (5.1) equals

$$\Phi g_p(u_k) = \begin{bmatrix} \boldsymbol{p}_1 \\ \vdots \\ \boldsymbol{p}_{n+3} \end{bmatrix} \tag{5.20}$$

Substitute (5.12) into (5.15) to get g_o in discrete time this has form

$$\begin{bmatrix} \phi \\ \theta \\ \psi \end{bmatrix} = g_o(u_k) \tag{5.21}$$

So that objective (5.2) equals

$$\Phi g_o(u_k) = \begin{bmatrix} \boldsymbol{o}_1 \\ \vdots \\ \boldsymbol{o}_{n+3} \end{bmatrix} \tag{5.22}$$

The planar objective between times t_{n+1} and t_{n+2} is written as

$$\overbrace{\begin{bmatrix} 0 & 0 & 0 & \mathbf{P_t} & & & & 0 & 0 & 0 \\ \vdots & \vdots & \vdots & & \ddots & & & \vdots & \vdots & \vdots \\ \vdots & \vdots & \vdots & & & \ddots & & \vdots & \vdots & \vdots \\ \vdots & \vdots & \vdots & & & & \ddots & \vdots & \vdots & \vdots \\ \vdots & \vdots & \vdots & & & & & \ddots & \vdots & \vdots & \vdots \\ \vdots & \vdots & \vdots & & & & & & \ddots & \vdots & \vdots & \vdots \\ \underbrace{0 \quad 0 \quad 0}_{t_{n+1}} & & & & & & \mathbf{P_t} & \underbrace{0 \quad 0 \quad 0}_{(T-t_{n+2})} \end{bmatrix}}^{\mathbf{P}_\zeta} g_p u_k = \begin{bmatrix} p_{n+1} \\ \vdots \\ \vdots \\ \vdots \\ \vdots \\ \vdots \\ p_{n+1} \end{bmatrix} \tag{5.23}$$

Consider (5.17), (5.20), (5.22) and (5.23) to get the overall control objective

$$\min_u J(u_k) = \left\| \Phi g_p(u_k) - \begin{bmatrix} \boldsymbol{p}_1 \\ \vdots \\ \boldsymbol{p}_{n+3} \end{bmatrix} \right\|^2 + \left\| \Phi g_v(u_k) - \begin{bmatrix} 0 \\ \vdots \\ 0 \end{bmatrix} \right\|^2 +$$

$$\left\| \Phi g_o(u_k) - \begin{bmatrix} \boldsymbol{o}_1 \\ \vdots \\ \boldsymbol{o}_{n+3} \end{bmatrix} \right\|^2 + \left\| \mathbf{P}_\zeta g_p(u_k) - \begin{bmatrix} p_{n+1} \\ \vdots \\ p_{n+1} \end{bmatrix} \right\|^2 \tag{5.24}$$

$$\left(\Phi g_p'(u_k)\right)^T \left(\Phi g_p(u_k) - \begin{bmatrix} \boldsymbol{p}_1 \\ \vdots \\ \boldsymbol{p}_{n+3} \end{bmatrix} \right) + \left(\Phi g_v'(u_k)\right)^T \left(\Phi g_v(u_k) \right) +$$

$$\left(\Phi g_o'(u_k)\right)^T \left(\Phi g_o(u_k) - \begin{bmatrix} \boldsymbol{o}_1 \\ \vdots \\ \boldsymbol{o}_{n+3} \end{bmatrix} \right) + \left(\mathbf{P}_\zeta g_p'(u_k)\right)^T \left(\mathbf{P}_\zeta g_o(u_k) - \begin{bmatrix} p_{n+1} \\ \vdots \\ p_{n+1} \end{bmatrix} \right) = 0 \tag{5.25}$$

The overall control objective will use later to modify the extended Newton method based and Point to point ILC

5.4 Application to Quadrotors

From Chapter 3, the dynamics of standard quadrotors are well established, and the main equations are given here. Recall the equation (3.17), where the control inputs are related to each rotor speed Ω_i by:

$$\begin{bmatrix} U_1 \\ U_2 \\ U_3 \\ U_4 \end{bmatrix} = \begin{bmatrix} f_1 + f_2 + f_3 + f_4 \\ l(f_2 - f_4) \\ l(f_1 - f_3) \\ -T_1 + T_2 + -T_3 + T_4 \end{bmatrix} = \begin{bmatrix} b & b & b & b \\ 0 & lb & 0 & -lb \\ lb & 0 & -lb & 0 \\ d & d & d & d \end{bmatrix} \begin{bmatrix} \Omega_1^2 \\ \Omega_2^2 \\ \Omega_3^2 \\ \Omega_4^2 \end{bmatrix} \tag{5.26}$$

We define a state variable vector as

$$\mathbf{x} = \begin{bmatrix} \phi & \theta & \psi & x & y & z & \dot{\phi} & \dot{\theta} & \dot{\psi} & \dot{x} & \dot{y} & \dot{z} \end{bmatrix}^T \tag{5.27}$$

where the triplet (x, y, z) is the position of the vehicle in the earth axes, and (ϕ, θ, ψ) are the standard aerospace Euler angles. By approximating the rotation rate triplet (p, q, r) by the Euler angle derivative $(\dot{\phi}, \dot{\theta}, \dot{\psi})$ and from the standard aeronautics navigation equations we get the dynamic model in the form $\dot{\mathbf{x}} = f(\mathbf{x}, u)$ where

$$f(\mathbf{x}, \mathbf{u}) = \begin{bmatrix} \dot{\phi} \\ \dot{\theta}\dot{\psi}a_1 + \dot{\theta}a_2\bar{\Omega} + b_1 U_2 \\ \dot{\theta} \\ \dot{\phi}\dot{\psi}a_3 - \dot{\phi}a_4\bar{\Omega} + b_2 U_3 \\ \dot{\psi} \\ \dot{\theta}\dot{\phi}a_5 + b_3 U_4 \\ \dot{x} \\ \frac{1}{m}(\cos\phi\sin\theta\cos\psi + \sin\phi\sin\psi)U_1 \\ \dot{y} \\ \frac{1}{m}(\cos\phi\sin\theta\sin\psi - \sin\phi\cos\psi)U_1 \\ \dot{z} \\ g - \frac{1}{m}(\cos\phi\cos\theta)U_1 \end{bmatrix},$$

and where m is the mass, g is the gravitational constant, $\bar{\Omega}$ is the rotor rotation rate sum, $a_1 = (I_{yy} - I_{zz})/I_{xx}$, $a_2 = J_p/I_{xx}$, $a_3 = (I_{zz} - I_{xx})/I_{yy}$, $a_4 = J_p/I_{yy}$, $a_5 = (I_{xx} - I_{yy})/I_{zz}$, $b_1 = l/I_{xx}$, $b_2 = l/I_{yy}$, and $b_3 = l/I_{zz}$.

The SISO structure of Equation (4.30) is extended to a MIMO dynamics to give

$$\begin{aligned} x_k(n+1) &= f(x_k(n), u_k(n)), \\ y_k(n) &= h(x_k(n), u_k(n)), \qquad x(0) = x_0. \end{aligned} \tag{5.28}$$

The model $\dot{\mathbf{x}} = f(\mathbf{x}, \mathbf{u})$ can be discretized by an Euler approximation. Full state feedback is assumed, that is $y_k = x_k$.

5.5   Experimental Platform Selection

5.5.1   Physical Parameters

The AscTec Hummingbird is chose as the experimental test platform. This quadrotor is popular, has good performance and is light-weight maneuverable. It has a payload of 200 g and a flight endurance of nearly 20 min. The aircraft component frame is made out of balsa wood and carbon fiber. The vehicle is powered by four brushless DC motors running off an 11.1V Lithium Polymer (LiPo) battery pack. It is equipped with an accelerometer, pressure sensor, magnetic sensor, gyros, and GPS module. These can provide the vehicle state. Some of the technical details are listed in Table 5.1 [204]. The model parameters are given in Table 5.2,

TABLE 5.1: Technical details of the quadrotor [204].

Type of Platform	AscTec HB. UAV
The Producer	AscTec GmbH + Intel
Take-off Weight	480 g
Battery	2100 mAh LiPo
Distance between motors	34 cm
Propeller	Standard propellers (8″), flexible (PP) plastics
Motors	HACKER Motors Germany (X-BL 52 s)
Motor Controllers	X-BLDC controllers
Transmitter	Futaba 2.4 GHz
Wireless Link	Xbee 2.4 GHz

The motor and controller represent a black box system; the data-sheet of the motor is not publicly available and the control algorithms running on the ESCs are proprietary. In order to determine their dynamics system identification is utilised. A series of random step inputs were fed to the motor controller and the response recorded as shown in Figure 5.4 . The response was measured using the motor feedback values read from the LL processor.

In our work, the pitch and roll axes are nonlinear where the ILC algorithms needs to perform over large trajectories and not need to aggressive movements. Therefore, the

transfer function of this system obtains through taking the Laplace transform where the function is stable. Primarily, a PID controller was designed as a baseline for identification, where the transfer function of a closed loop identification model including a PID control as seen in (5.29). Consequently, the system identification toolbox in MATLAB was used in order to fit a transfer function. A first order model was first generated, however it exhibited a poor fit to the estimation data. The second order representation in (5.29) provided a confidence of 75% which can be seen in Figure 5.4, which was deemed acceptable.

$$\frac{1.763s + 4.67}{s^2 + 24s + 4.62} \tag{5.29}$$
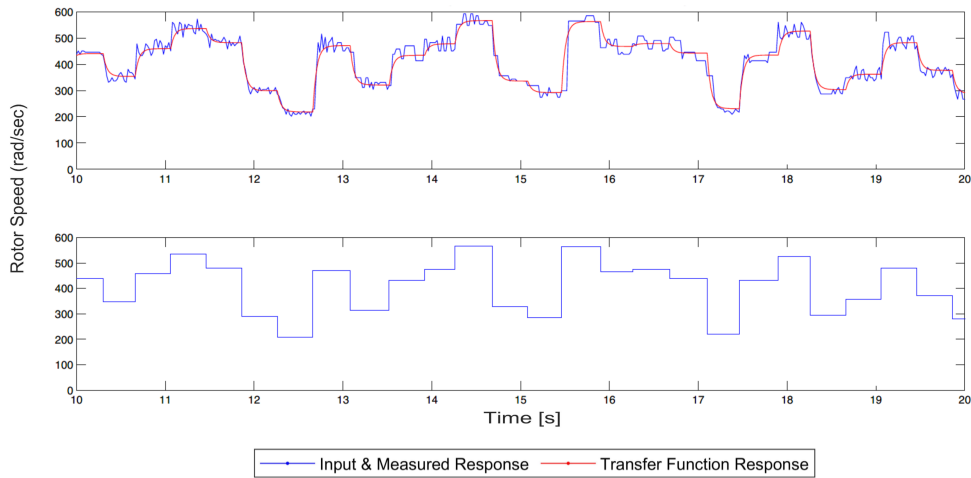
FIGURE 5.4: MATLAB system identification result for motor dynamics.

Six physical parameters $(m, L, I_{xx}, I_{yy}, I_{zz} \text{ and } J_p)$ are required to populate the system model found in the equation (3.18) to (3.23), because the system will remain only confined to the quadrotor in the general form. Therefore, these parameters are allocated to the AscTech Hummingbird. The moments of inertia around the quadrotors inertial frame, the moment of inertia of the rotor, the length of the quadrotor arm and the mass of the quadrotor.

Generally, there are steps to be considered for obtaining parameters:

- A 3D model of the quadrotor was implemented in Autodesk Inventor Professional 2021.

- Measurement sets (Digital callipers and laboratory scales).

The parameters are described in the Table 5.2 and a full description can be found in Appendix B.3. These values have been used in the implementation of the model and control algorithms.

TABLE 5.2: Quadrotor model parameters.

Parameters	Description	Value	Unit
I_{xx}	x axis-Moment Inertia	10.7×10^{-3}	kg·m^2
I_{yy}	y axis-Moment of Inertia	10.7×10^{-3}	kg·m^2
I_{zz}	z axis-Moment of Inertia	18.4×10^{-3}	kg·m^2
J_p	Rotor Inertia	47×10^{-6}	kg·m^2
m	Mass	0.547	kg
l	Arm Length	0.168	m
g	Gravitational constant	9.81	ms^2
Ω_{max}	Maximum rotor speed	200	rad/s

5.5.2   Test Bed

A test bed, designed for analysing the motor's performance and enabling controller tuning, is constructed from steel and finished in black paint and bearings, so that it allows three DOF of rotation. Steel tube was selected because of its easy availability and high density gives the rig stability and rigidity. The UAV is secured in place with a spherical rolling joint. The assembled mechanical design is shown in Figure. 5.5 and 5.6, The UAV installed on the top. A Raspberry Pi 3 is used for the control.

The mechanical system design of the proposed platform provides many benefits in terms of testing the performance of ILC algorithms. The platform test bed is designed 1) to make the ILC controller adapts to the full modes of flight during the OPL inspection, 2) validate ILC in MIMO system possible through unique multiple modes 3) reduce the

cost, 4) and obtain an accurate dynamic model. For example, all model-based ILC were consistent with the design of the platform in term of providing the repetitive test due to Spherical joint. Moreover, the platform is illustrate a significant fit with normal (without disturbances) and specific test (presence of disturbances) in an open space and enclosed laboratory environment.

(a) Spherical joint specification   (b) assemble mechanical part
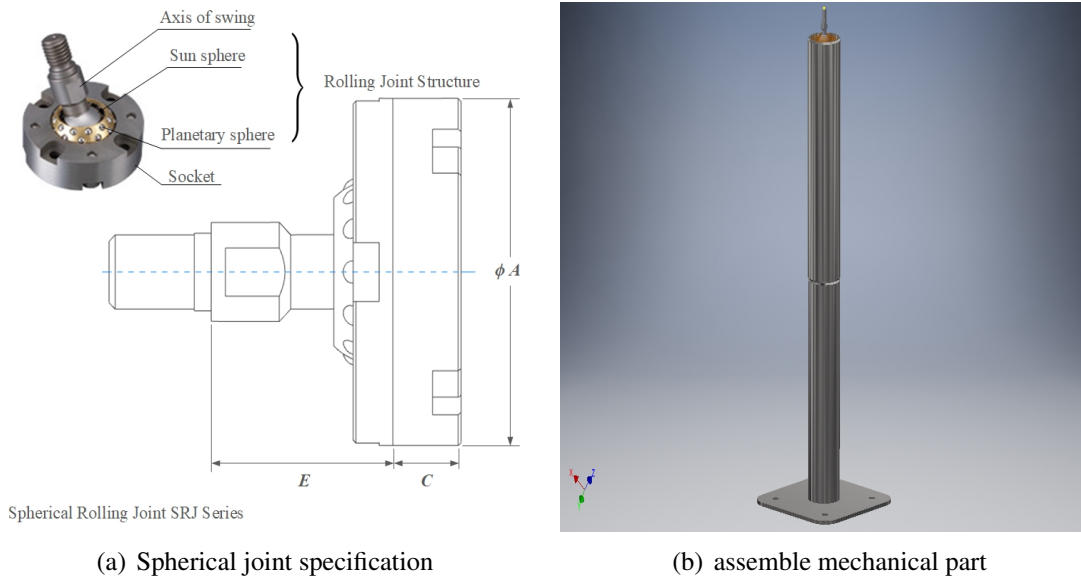
FIGURE 5.5: The complete assembly of proposed mechanical test-bed for quadrotor: (**a**) High precision spherical rolling joints with its features. (**b**) Mechanical-bed reconfiguration with precision rolling joints.

In this specific test, the UAV is installed freely without any friction with the surrounding grille structure in order to provide adequate protection as shown in Figure. 5.6. The UAV configuration is observed to be in the tilted mode (angle) at the first operation stage due instability of the body quadrotor itself and the centripetal force. Accordingly, the UAV configuration transition tilted mode to a full mode (horizontal tracking reference) required initially a control algorithm with step tracking reference. In that case, the quadrotor needs to change the set points before the implementation.

For full detailed about measurement and design for the purchase spherical joint specification, see Appendix B.

FIGURE 5.6: Quadrotor system with complete hardware test frame design for ILC controllers.

5.5.3   Pitch and Roll PID Scheme

As previously explained in the Chapter 3, one of control approaches are needed to evaluate the system performance. Therefore, the use of the PID control system is one of different control approaches, but it can give easy simplification to control one degree of freedom. PID controllers have been designed in order to control the 3 DOF case out of three attitude angles because it is the simplest case. The performance was compared with the proven controllers included on LL processor in order to assess performance. The implementation of these controllers can be found in roll block implementation on quadrotor. For brevity, the yaw is not discussed as it is not utilised in trajectory tracking control however, it will be based on the same PID implementation as the roll and pitch controllers because the performance will be compared with other PID controller.

The truly error value in the process control parameter is expressed as:

$$e(t) = \theta_{ref}(t) - \theta(t) \tag{5.30}$$

Here, $\theta(t)$ refers to the desired Output of the system and $\theta_{ref}(t)$ refers to reference of the system from IMU sensor. The parameters of the PID controller is used to correct the $\theta(t)$

of the System.

The above expression is individually used for each of the Roll and Pitch, so for roll will
be :–

$$U_2 = K_p(\phi_{ref} - \phi) + K_d(\dot{\phi}_{ref} - \dot{\phi}) + K_i \int (\phi_{ref} - \phi)dt \tag{5.31}$$

Initially a PD controller was designed to control the rotation then a PID controller also
was designed, because the experiment was done in indoor environments, the using only
the P and D controllers can give better results only if use it alone. The transfer function
of the closed loop system can be seen in equation (5.32). The root locus suggests setting
a high derivative gain in order move the pole closest to the origin. In practice the noise
from the IMU measurements cause a large degree of vibration, reducing stability and
increasing fuel burn (decrease the battery voltage).

$$C(s) = \frac{K_d s^2 + K_p s + K_i}{0.0732 s^3 + K_d s^2 + K_p s + K_i} \tag{5.32}$$

Having developed the control laws these are now evaluated for state error, transient
response, tracking and speed of response.

5.5.4   PID Control Test Results

The input demand using here is $\theta_{ref} = \sin\theta$ as shown in Figure. 5.7 (Trajectory I). The
following figure shows the variation in pitch over a time of about 30s.

Table 5.3 shows the norm error reduction, where the error value was at the high-
est level when using integral gain $K_i = 0.02$ and the tuning parameters chosen with the
K_p=0.95 with value at 0.1117 but this reduce the error when the integral gain $K_i = 0.9$ is
increased and with the K_p=0.98 at value 0.0455. Unfortunately, any time reduction such
as reduction from t=30s to t=15s or t=10s will impact the results in an undesirable way,
where there is no effect of the increase or decrease by the gain. The step response (Tra-
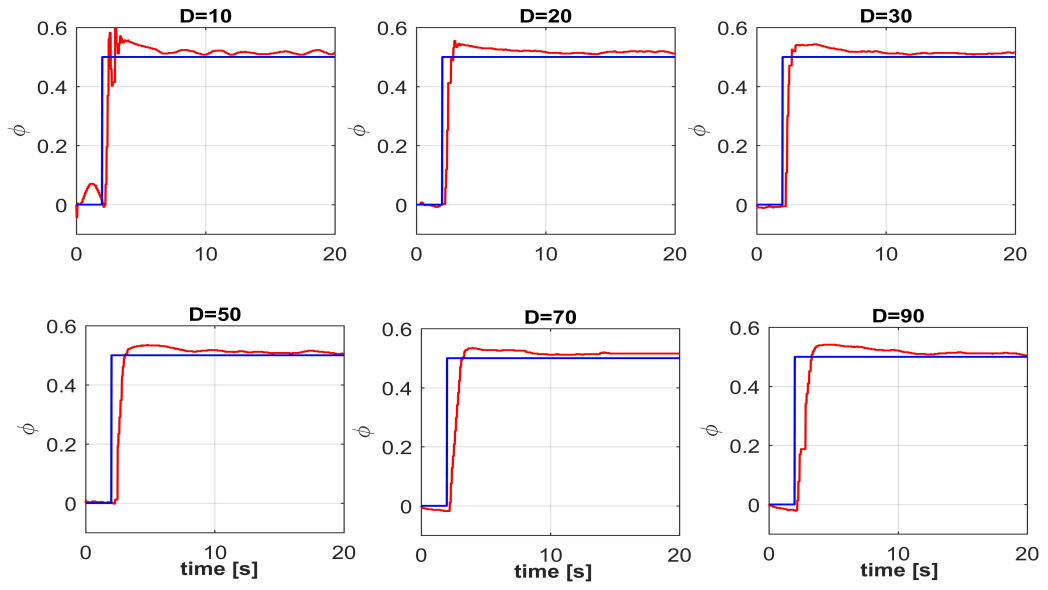
FIGURE 5.7: The PI controller on trajectory I for during variation of ϕ with disturbance.

TABLE 5.3: Experimental via trajectory I and II with K_i and K_d respectively

K_i	$\|\hat{\theta} - \theta\|$	K_d	$\|\hat{\theta} - \theta\|$
0.02	0.1117	0.1	0.0678
0.01	0.0885	0.2	0.0624
0.03	0.0732	0.3	0.0549
0.055	0.0543	0.5	0.0496
0.065	0.0539	0.7	0.0522
0.09	0.0455	0.9	0.0543
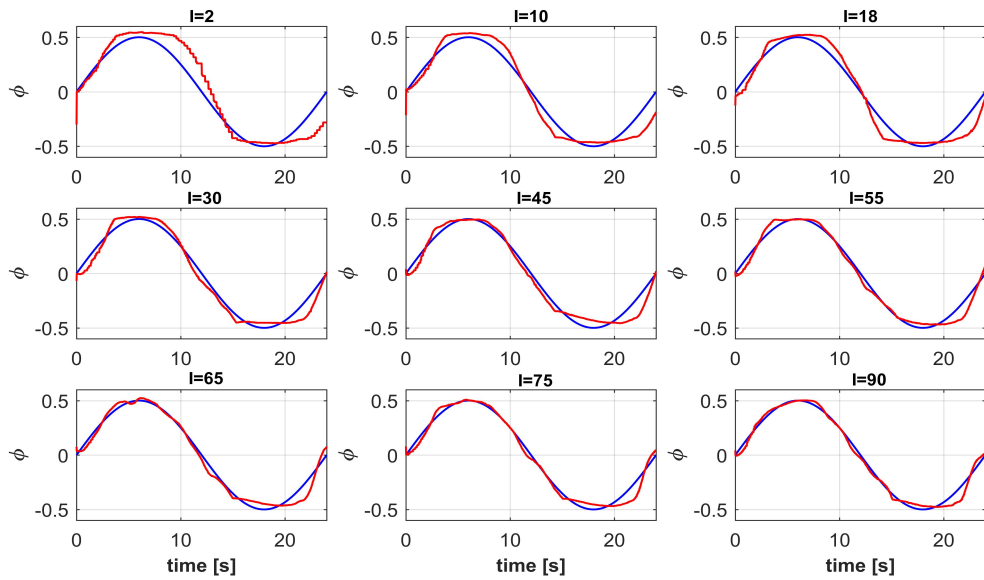
FIGURE 5.8: The PD controller on trajectory II for during variation of θ with disturbance.

jectory II) of the controller Hummingbird quadrotor shown below includes the demand $\theta_{ref} = H(t - t_0)$. Figure. 5.7 demonstrates that there is no delay due to the simulations only without a practical experiment, while the Figure. 5.8 proves that this slightly delay is in the case of practical application within the laboratory environment.

5.6 Backstepping Controller (BSC)

This section contains the derivation for nonlinear systems in strict feedback form for both the attitude angles (roll , pitch and yaw) and altitude. The equations of motion can be written in state space form according to the following states:

$$x_1 = \begin{bmatrix} \phi \\ \theta \\ \psi \end{bmatrix} \quad x_2 = \begin{bmatrix} p \\ q \\ r \end{bmatrix} \quad x_3 = \begin{bmatrix} x \\ y \\ z \end{bmatrix} \quad x_4 = \begin{bmatrix} \dot{x} \\ \dot{y} \\ \dot{z} \end{bmatrix}. \tag{5.33}$$

From the (3.28), the state space equations are then given by

$$\dot{x}_1 = \underbrace{\begin{bmatrix} 1 & s_\phi t_\theta & c_\phi t_\theta \\ 0 & c_\phi & -s_\phi \\ 0 & s_\phi/c_\theta & c_\phi/c_\theta \end{bmatrix}}_{g_0} x_2$$

$$\dot{x}_2 = \underbrace{\begin{bmatrix} a_1 qr - a_2 q\Omega_r \\ a_3 pr + a_4 p\Omega_r \\ a_5 pq \end{bmatrix}}_{f_1} + \underbrace{\begin{bmatrix} \frac{1}{I_{xx}} & 0 & 0 \\ 0 & \frac{1}{I_{yy}} & 0 \\ 0 & 0 & \frac{1}{I_{zz}} \end{bmatrix}}_{g_1} \begin{bmatrix} u_2 \\ u_3 \\ u_4 \end{bmatrix} \tag{5.34}$$

$$\dot{x}_3 = x_4$$

$$\dot{x}_4 = \underbrace{\begin{bmatrix} 0 \\ 0 \\ -g \end{bmatrix}}_{f_2} + \underbrace{\begin{bmatrix} \frac{u_1}{m} s_\psi & \frac{u_1}{m} c_\psi & 0 \\ -\frac{u_1}{m} c_\psi & \frac{u_1}{m} s_\psi & 0 \\ 0 & 0 & \frac{c_\phi c_\theta}{m} \end{bmatrix}}_{g_2} \begin{bmatrix} s_\phi \\ c_\phi s_\theta \\ u_1 \end{bmatrix}$$

where a_1, a_2, a_3, a_4, a_5 are constant coefficients given by

$$a_1 = \frac{(I_{yy} - I_{zz})}{I_{xx}}, \quad a_2 = \frac{J_p}{I_{xx}}, \quad a_3 = \frac{(I_{zz} - I_{xx})}{I_{yy}}, \quad a_4 = \frac{J_p}{I_{yy}},$$
$$a_5 = \frac{(I_{xx} - I_{yy})}{I_{zz}}, \quad b_1 = \frac{l}{I_{xx}}, \quad\quad b_2 = \frac{l}{I_{yy}}, \quad\quad b_3 = \frac{l}{I_{zz}}. \tag{5.35}$$

In the quadrotor dynamics, the roll and pitch angles can be considered as virtual inputs to control the horizontal translational dynamics. In the following equations, a nonlinear controller will be designed based on the integral backstepping approach. The controller's objective will be to ensure the output states $[x(t), y(t), z(t), (t)]$ track the desired trajectory given by $[xd(t), yd(t), zd(t), d(t)]$ in the presence of constant external disturbances.

The control system design of the rotational and the translational can be achieved in four steps as follows

$$\dot{x}_1 = g_0(x_1)v_1, \tag{5.36}$$

which is driven by v_1, the first virtual control input to be designed. Then we define the following two backstepping variables

$$z_1 = x_1^d - x_1$$
$$\xi_1 = \int_0^t z_1(\tau)d\tau' \tag{5.37}$$

where z_1 represents the tracking error, ξ_1 represents its integration and $x_1^d = [\phi_d, \theta_d, \psi_d]^T$. The desired roll ϕ_d and pitch θ_d angles are calculated later. Then proceed by choosing the following quadratic Lyapunov function

$$V_1 = \frac{1}{2}z_1^\top z_1 + \frac{1}{2}\xi_1^\top \Lambda_1 \xi_1, \tag{5.38}$$

where $\Lambda_1 = \Lambda_1^T \varepsilon \mathbb{R}^{3\times3}$, the time derivative of V_1 is given by

$$
\begin{aligned}
\dot{V}_1 &= z_1^\top \dot{z}_1 + \xi_1^\top \Lambda_1 \dot{\xi}_1 \\
&= z_1^\top (\Lambda_1 \xi_1 + \dot{x}_1^d - g_0 v_1).
\end{aligned}
\tag{5.39}
$$

By choosing the virtual control input to be

$$
v_1 = g_0^{-1}(\Lambda_1 \xi_1 + \ddot{x}_1^d + A_1 z_1),
\tag{5.40}
$$

and complete this to obtain

$$
v_2 = g_1^{-1}(-f_1 + g_0^\top z_1 + \dot{v}_1 + A_2 z_2),
\tag{5.41}
$$

$$
v_3 = \Lambda_2 \xi_2 + \ddot{x}_3^d + A_3 z_3,
\tag{5.42}
$$

,

$$
\begin{aligned}
v_4 &= g_2^{-1}(-f_2 + z_3 + \dot{v}_3 + A_4 z_4) \\
&= [v_{4_1}, v_{4_2}, v_{4_3}]^\top,
\end{aligned}
\tag{5.43}
$$

Thus the whole system is asymptotically stable using the control laws (5.40), (5.41),(5.42) and (5.43). Finally, from the equation (5.41) and rearranging for u_2:

$$
u_2 = \frac{1}{l}[I_{xx}(\ddot{\phi}_{ref} + \alpha \dot{e}_1 + \dot{\beta} z_1 + \gamma z_2) - \dot{\theta} \dot{\psi}(I_{yy} - I_{zz}) - \dot{\theta} J_p \Omega_r]
\tag{5.44}
$$

5.6.1 BSC Results

The step response of the controller shown below includes effect of overshoot and oscillation which, as mentioned before. The delay in response (of about 0.2s) is due to the

mechanical form platform.
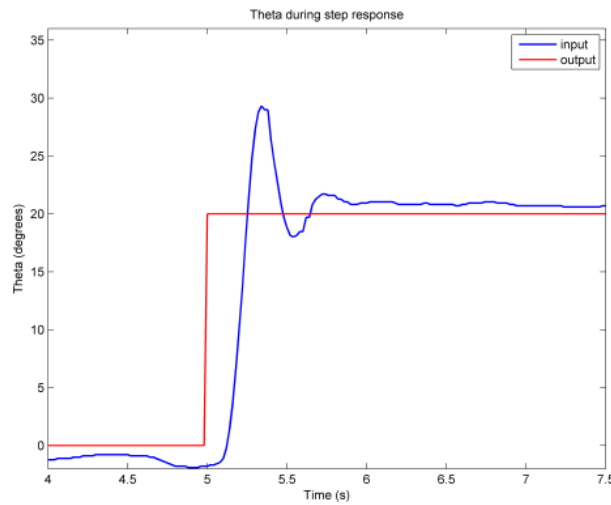
FIGURE 5.9: The BSC controller on trajectory I for during variation of θ with disturbance.

The graph below shows how acceptable the results are. As can be seen the output follows the input almost perfectly, with little overshoot at the top. Overshoot at the bottom is somewhat larger than expected where the control parameters ($\alpha = 105$, $\beta = 130$ and $\gamma = 8$) for the roll controller.
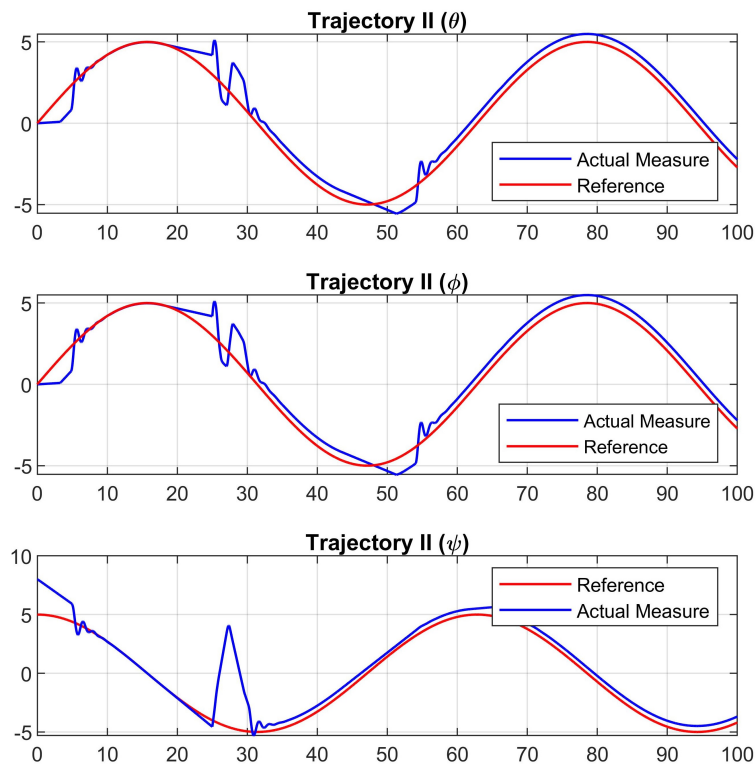
FIGURE 5.10: The BSC controller on trajectory II for during variation of θ, ϕ, ψ with disturbance.

It can be note that the backstepping technique have outliers results during a trajectory tracking where the reason for that is increasing complexity of analytically calculating the derivatives of the virtual control signals in standard backstepping control. In that case, backstepping approach with a command filter is needed to include an integral action and to increase robustness against external disturbances. However, this current research is focused on trajectory tracking and OPL inspection under disturbances conditions with lower control effort.

5.7   ILC Basic Results

In this section, a simple ILC form, gradient-based, norm-optimal ILC are tested to perform a standard UAVs motion for 16 iterations for trajectories as shown in Figure 5.11 for 8s. The G-ILC and NO-ILC algorithms are applied to the test system. Simulations are also performed. The simulations and experiments were conducted on a Laptop (i7) ThinkPad P1 Mobile WorkStation with 16 GB RAM/2.20 GHz via MATLAB R2018b. The reference trajectory is shown in Figure 5.11. The trajectory consists of a single period sin wave and is non-smooth; hence is a challenging task for the ILC algorithm. Sixteen iteration trials were performed for each algorithm.
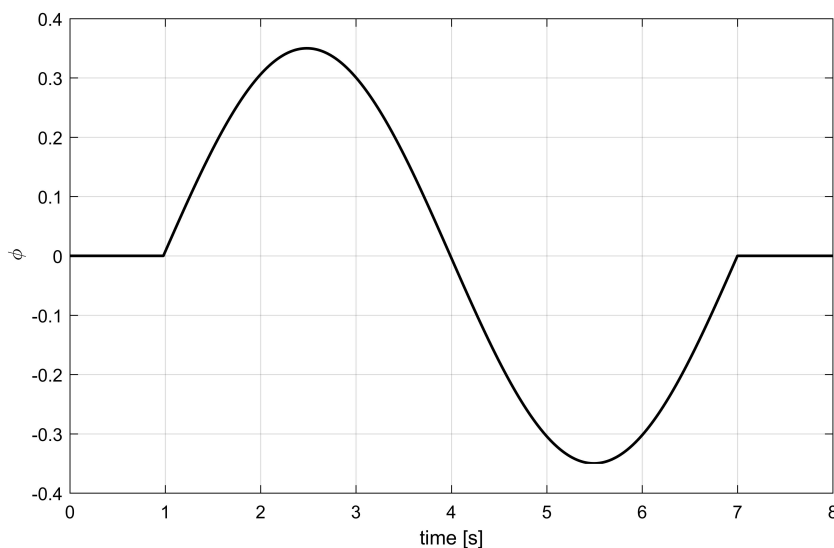
FIGURE 5.11: References for ILC controllers.

5.7.1 Simple Algorithm ILC

This subsection shows the results of the simple learning scheme applied to UAV quadrotor. In order to evaluate quadrotor performance, the P-type ILC and D-type ILC control will be considered to test. And therefore, tracking and step response will quantitatively evaluate the P-type ILC and D-type ILC performance.
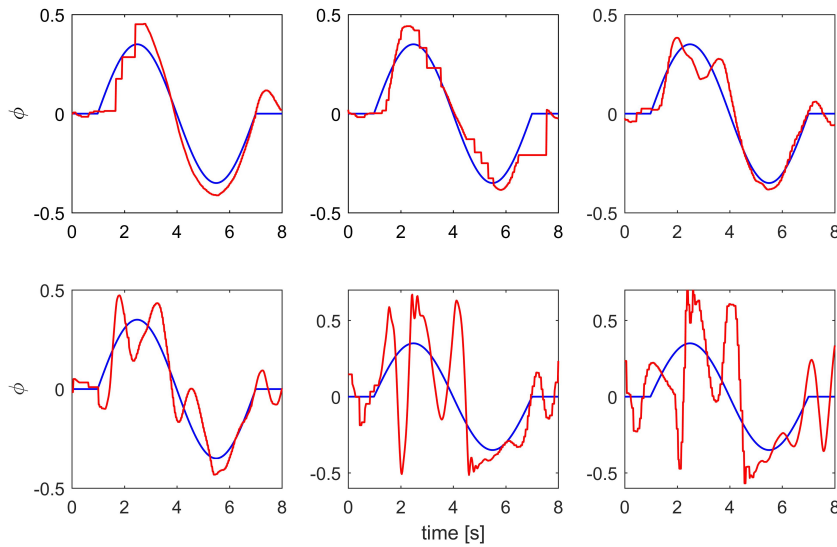
FIGURE 5.12: The variation in ϕ over time for different iteration using P-type ILC.

For all test that using the P-type ILC as shown in Figure 5.12, and when was choose the α gain between 0.01 to 0.2, the error norm keeps increasing and the quadrotor system becomes unstable after the first few trials. The poor performance is not surprising since this method does not employ any model information.

The results for D-type method are displayed in Figure 5.14. The convergence over the first few trials is reasonable for all chosen gain values from 0.01 to 0.2. As shown in Figure 5.13 the error norm diverges after 3 trials while for a 0.2 gain. By comparing with the P-type, the larger the gain the faster the convergence, this is due to it can force the outputs to track references and reduce the error norm after a few trials.
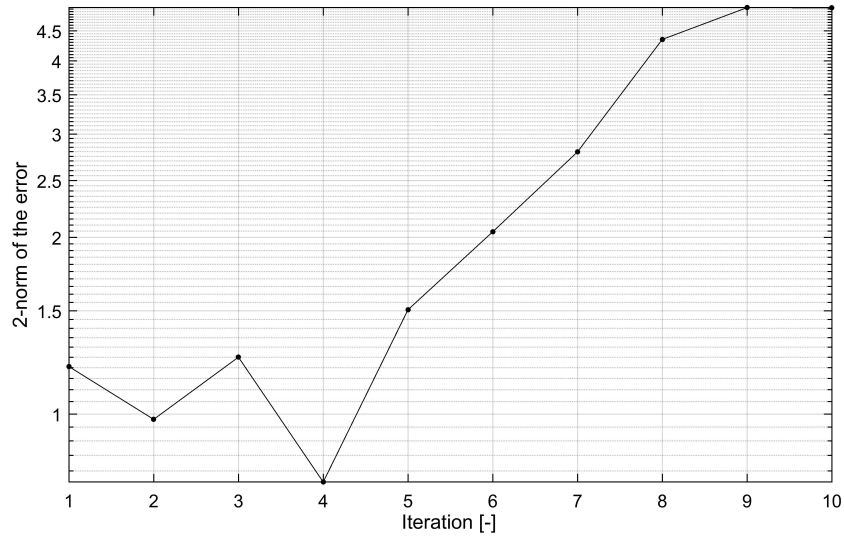
FIGURE 5.13: Attempts to convergence result for P-type ILC.
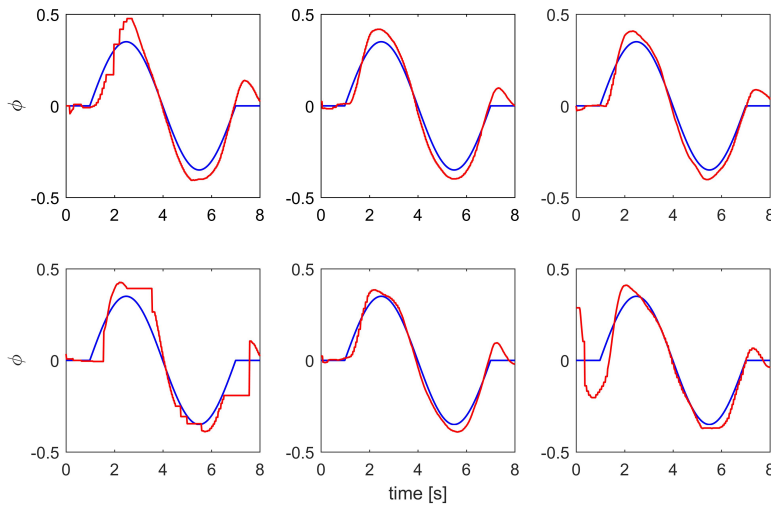
FIGURE 5.14: The variation in ϕ over time for different iteration using D-type ILC.

5.8   Optimal Approach ILCs Results

This section purports to put forward the optimal algorithms (G-ILC, NO-ILC) for the UAV quadrotor. The design of the optimal algorithm is based on the following assumptions and steps :

I. The system is presumed to operate in a repetitive manner (iteratively) for both optimal algorithms, G-ILC and NO-ILC.

II. At the end of every iteration, the state is reset operation toward a particular repetition
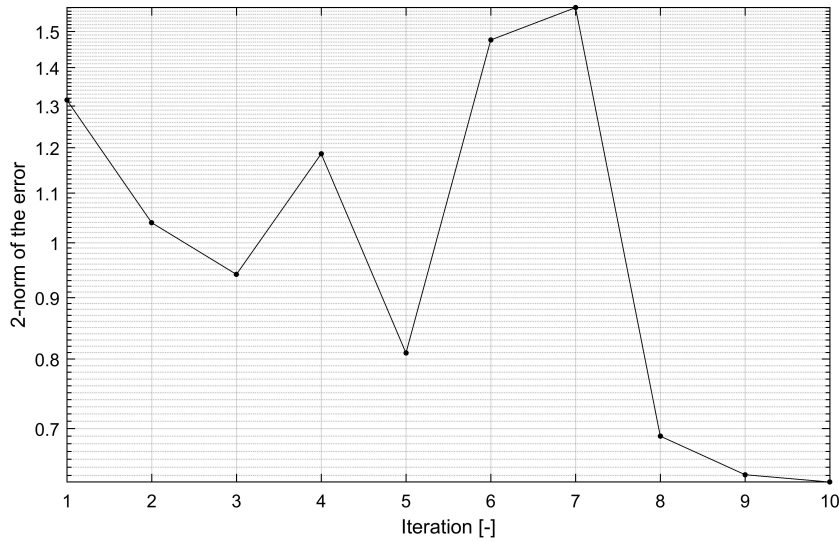
FIGURE 5.15: Attempts to convergence result for D-type ILC.

that have independent initial condition to the next operation.

III. A new control signal might be utilized during this time. A reference signal, $r(t)$, is presumed to be known and the ultimate control objective is to determine an input function $u^*(t)$ such the output function $y(t) = r(t)$ on $[1;N]$.

IV. For G-ILC, the value of the learning gain $\beta_{old}(k)$ is heuristically selected for the first step, and then calculated automatically using the the gain $\beta_{new}(k)$ by establishing the varying gain equations. The established variable will be repeated again for NO-ILC, but with a different learning gain Q_k.

V. To guarantee error convergence, the necessary conditions are $J(\beta_{new}(k)) = \|e_{k+1}\|^2 + \zeta \beta_{new}(k)^2$.

Now, the SISO model is a non-linear, discrete, state space system:

$$x_k(n+1) = f(x_k(n), u_k(n))$$
$$y_k(n) = h(x_k(n)) \tag{5.45}$$

where $x_k(t) \in \mathbb{R}^n$, $u_k(t) \in \mathbb{R}^m$, $y_k(t) \in \mathbb{R}^p$ and $A \in \mathbb{R}^{n \times n}$, $B \in \mathbb{R}^{n \times m}$, $C \in \mathbb{R}^{p \times n}$ are the system matrices. Moreover, x_k, u_k, and y_k are the state vector, input and output respectively, for trial k.

5.8.1   Gradient based ILC

In this subsection the gradient ILC is applied in order to investigate the performance of this algorithm. Both sinusoidal and step references are used with magnitudes of 0.35 from 1s until 7s and then back to 0 magnitudes at the end of reference signal, as displayed in Figure 5.11. Both references have a total length T = 8 seconds. The reference is exactly the same as the version used in the previous Subsection 5.7.1 so that the performance of this method can be compared fairly. The results of the proposed learning scheme applied to quadrotor. In order to evaluate quadrotor performance, the PID control and backstepping will be considered to compare. And therefore, tracking and step response will quantitatively evaluate the Gradient ILC performance as shown in Table 5.4.

TABLE 5.4: Simulation comparison for ϕ and θ with different control approaches.

Control Approaches	Trial No.	Test No.	Parameters Tuning	Norm of Error $\|\hat{\theta} - \theta\|$	Norm of Error $\|\hat{\phi} - \phi\|$
PID	-	1	$K_p = 5.3, K_i = 0.18$	4.21	4.21
		5	$K_d = 0.01$	4.22	4.22
		10	$K_p = 9.2, K_i = 0.18$	2.82	2.82
		15	$K_d = 0.01$	2.82	2.82
BCT	-	1	$\alpha = 75, \beta = 90$	3.82	3.82
		5	$\gamma = 8$	3.81	3.81
		10	$\alpha = 105, \beta = 90$	2.35	2.35
		15	$\gamma = 8$	2.33	2.33
Gradient ILC	1	First Test	Optimal Value $\beta = 0.1$	1.92	1.93
	3			1.38	1.38
	6			0.332	0.331
	16			0.309	0.303

It is also important to prove that the system of Gradient-based ILC is monotonic convergence. The simulation results has shown a significant decrease of the error during different iteration this can be prove by the condition of 2nd norm of the errors as shown in Figure 5.16 with 0.3092 at 16 iteration. Figure 5.16(a) and Figure 5.16(b) the variation in ϕ and θ over time for different iteration.
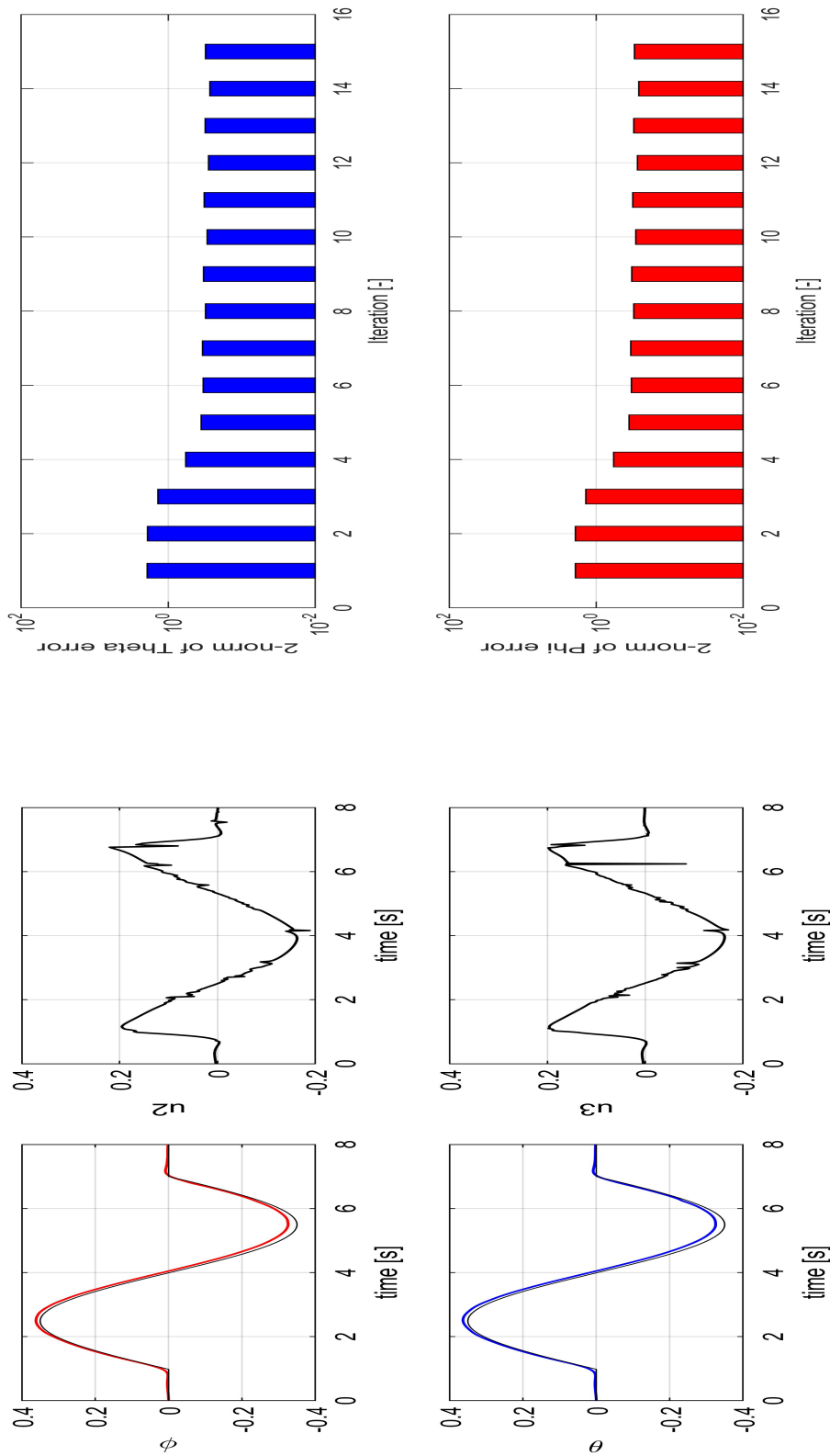
(a) The variation in theta over time for different iterations.

(b) two norm for roll and pitch over time for different iterations.

FIGURE 5.16: G-ILC for different iterations without disturbance.

The G-ILC with updating Equations (4.19) and (4.20) was implemented to track the reference signal. An optimal value of gain, β, is chosen between 0.01 and 1.0. After testing a wide range of values of β, the best performance was found with $\beta = 0.1$. The experimental results show a significant decline in the error over the first five trial iterations as shown in Figure 5.17. A slight increase occurred at the 7th and 10th trials but the trend was from 1.277 at first trial to the value of 0.574 at the 6th trial.
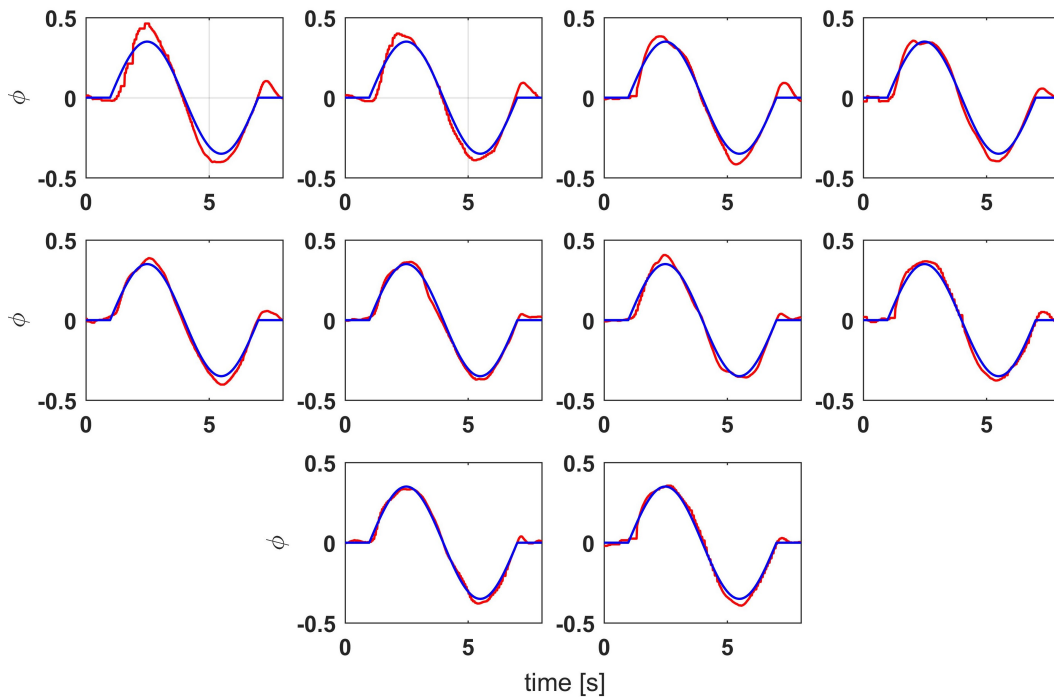
FIGURE 5.17: Experimental results of G-ILC for different iterations with disturbance.

Again It is important to prove that the system of Gradient-based ILC is monotonic convergence as shown in Figure 5.18, this can be prove by the condition of 2nd, the decrease happen from 1.315 at first iteration to the value of 0.548 at 6th iteration.

To improve the performance of the G-ILC algorithm, the value of the learning gain β can be changed. Figure 5.19 shows the effect of β on the convergence rate.

Using gradient descent to solve the optimisation problem given by Equation (4.19)
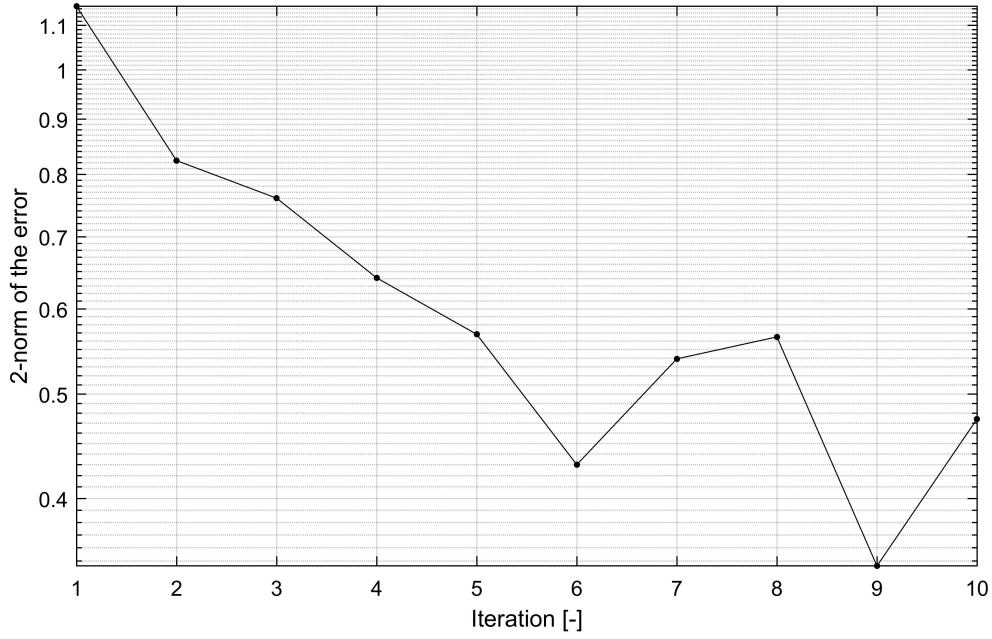
FIGURE 5.18: Monotonic convergence result for gradient based ILC.

gives

$$u_{k+1} = u_k - \beta \bigtriangledown J(u_k) \tag{5.46}$$

$$= u_k - \beta \bigtriangledown \frac{1}{2} \|y_d - Gu_k\|^2 \tag{5.47}$$

$$= Gu_k\beta + u_k - y_d G^T \beta \tag{5.48}$$

$$= u_k + \beta G^T e_k \tag{5.49}$$

where β represents the learning gain.

From Equation (5.49), the error evolution of the G-ILC can be derived as

$$e_{k+1} = y_d - Gu_{k+1} \tag{5.50}$$

$$= G^T G e_k \beta + y_d - u_k G \tag{5.51}$$

$$= (I - \beta GG^T)e_k. \tag{5.52}$$

By choosing the learning gain β from the range $0 < \beta < 2/\bar{\sigma}(G)$, where $\bar{\sigma}(G)$ is the largest singular of the matrix G, it can be easily shown that $\|I - \beta GG^T\| < 1$. Therefore,

the error converges monotonically to zero, as the trials k goes to infinity.

Instead of arbitrarily selecting a value of $\beta_{old}(k)$ from the range, the error convergence rate can be optimized. Repeating Equations (5.48) and (5.52)

$$u_{k+1} = u_k + \beta_{old}(k)G^T e_k \tag{5.53}$$

$$e_{k+1} = (I - \beta_{old}(k)GG^T)e_k \tag{5.54}$$

the optimal iteration-varying $\beta_{new}(k)$ can be obtained by minimising:

$$J(\beta_{new}(k)) = \|e_{k+1}\|^2 + \zeta\beta_k^2. \tag{5.55}$$

where ζ is a small positive weighting constant. Substituting Equation (5.54) into Equation (5.55) we get

$$J(\beta_{new}(k)) = ((I - \beta_k GG^T)e_k)^T((I - \beta_k GG^T)e_k) + \zeta\beta_k^2 \tag{5.56}$$

$$= e_k^T e_k - 2\beta_k e_k^T GG^T e_k + \beta_k^2 e_k^T GG^T GG^T e_k + \zeta\beta_k^2. \tag{5.57}$$

Differentiating Equation (5.57) with respect to $\beta_{new}(k)$ and equating to zero gives the optimal learning gain:

$$\beta_{new}(k) = \frac{e_k^T GG^T e_k}{e_k^T GG^T GG^T e_k + \zeta} \tag{5.58}$$

$$= \frac{(G^T e_k)^T G^T e_k}{(GG^T e_k)^T GG^T e_k + \zeta} \tag{5.59}$$

$$= \frac{\|G^T e_k\|^2}{\|GG^T e_k\|^2 + \zeta}. \tag{5.60}$$

Thus the necessary and sufficient conditions for guaranteeing a convergence of error are

$$\|e_{k+1}\| < \|e_k\| \text{ for all } k \geq 0 \text{ and } \lim_{k\to\infty} e_k = 0. \tag{5.61}$$

From Equation (5.54) we get

$$\|e_{k+1}\|^2 - \|e_k\|^2 = e_k^T e_k (I - \beta_k GG^T)(I - \beta_k GG^T)^T - e_k^T e_k \tag{5.62}$$

$$= e_k^T ((I - \beta_k GG^T)^2 - I)e_k \tag{5.63}$$

$$= e_k^T (-2\beta_k GG^T + \beta_k^2 GG^T GG^T)e_k \tag{5.64}$$

$$= \beta_k^2 (-2\frac{e_k^T GG^T e_k}{\beta_k} + e_k^T GG^T GG^T e_k) \tag{5.65}$$

$$= \beta_k^2 (-2\frac{\|G^T e_k\|^2}{\beta_k} + \|GG^T e_k\|^2). \tag{5.66}$$

Furthermore from Equation (5.59), we get

$$\frac{\|G^T e_k\|^2}{\beta_{new}(k)} = \|GG^T e_k\|^2 + \zeta. \tag{5.67}$$

Substituting Equation (5.66) into Equation (5.67) gives

$$\|e_{k+1}\|^2 - \|e_k\|^2 = \beta_{new}(k)^2(-2(\|GG^T e_k\|^2 + \zeta) + \|GG^T e_k\|^2$$
$$= -\beta_{new}(k)^2(2\zeta + \|GG^T e_k\|^2) \leqslant 0. \tag{5.68}$$

From Equation (5.68) it can be deduced that $\|e_{k+1}\| = \|e_k\|$ if and only if $\beta_k = 0$. Because GG^T is a positive definite matrix, from Equation (5.59) we have that $\beta_{new}(k) = 0$ if and only if $e_k = 0$, Thus the conditions of Equation (5.61) are satisfied and the and the system has monotonic convergence.

Now the Figure 5.19 shows the effect of β on the convergence rate based on this contribution.

Then, an alternative controller is required to improve the tracking performance of the system. In the next subsection another advanced controller is hence analysed.
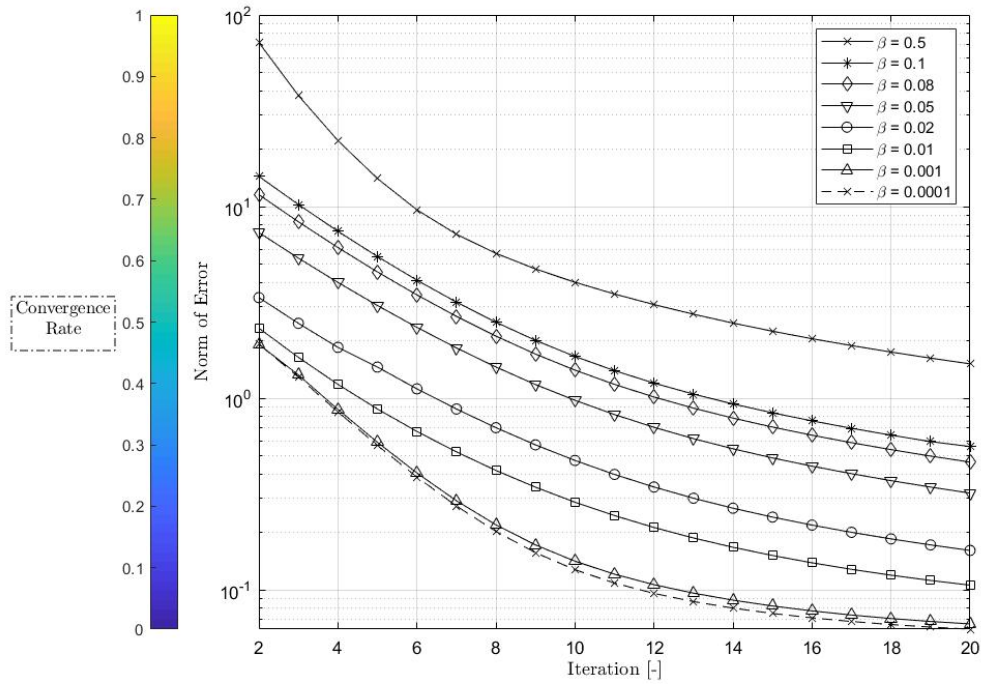
FIGURE 5.19: Optimized error convergence rate with a variation on the learning gain β values, as proposed in Equations (5.60) and (5.67).

5.8.2   Norm Optimal Iterative Learning

In this subsection, the implementations of NOILC algorithms is applied in order to investigate the performance of this algorithm. Figure 5.19 similarly shows the results for the NO-ILC algorithms, The improvement over the G-ILC is noticeable. Again the convergence is shown by the decrease of the error 2-norm. The error 2-norm is 0.1215 at 16th iteration, a considerable improvement over the G-ILC approach

The performance of the NO-ILC algorithm is also investigated with the reference signal shown in Figure 5.11. The results are shown in Figure 5.20(a). The weighting parameter is set to $Q = 0.1$. The value of Q can be increased to improve convergence, but Figure 5.20(b) shows the convergence is similar to that of the G-ILC experiment, with the latter slightly better. Convergence was achieved after 8 iterations.
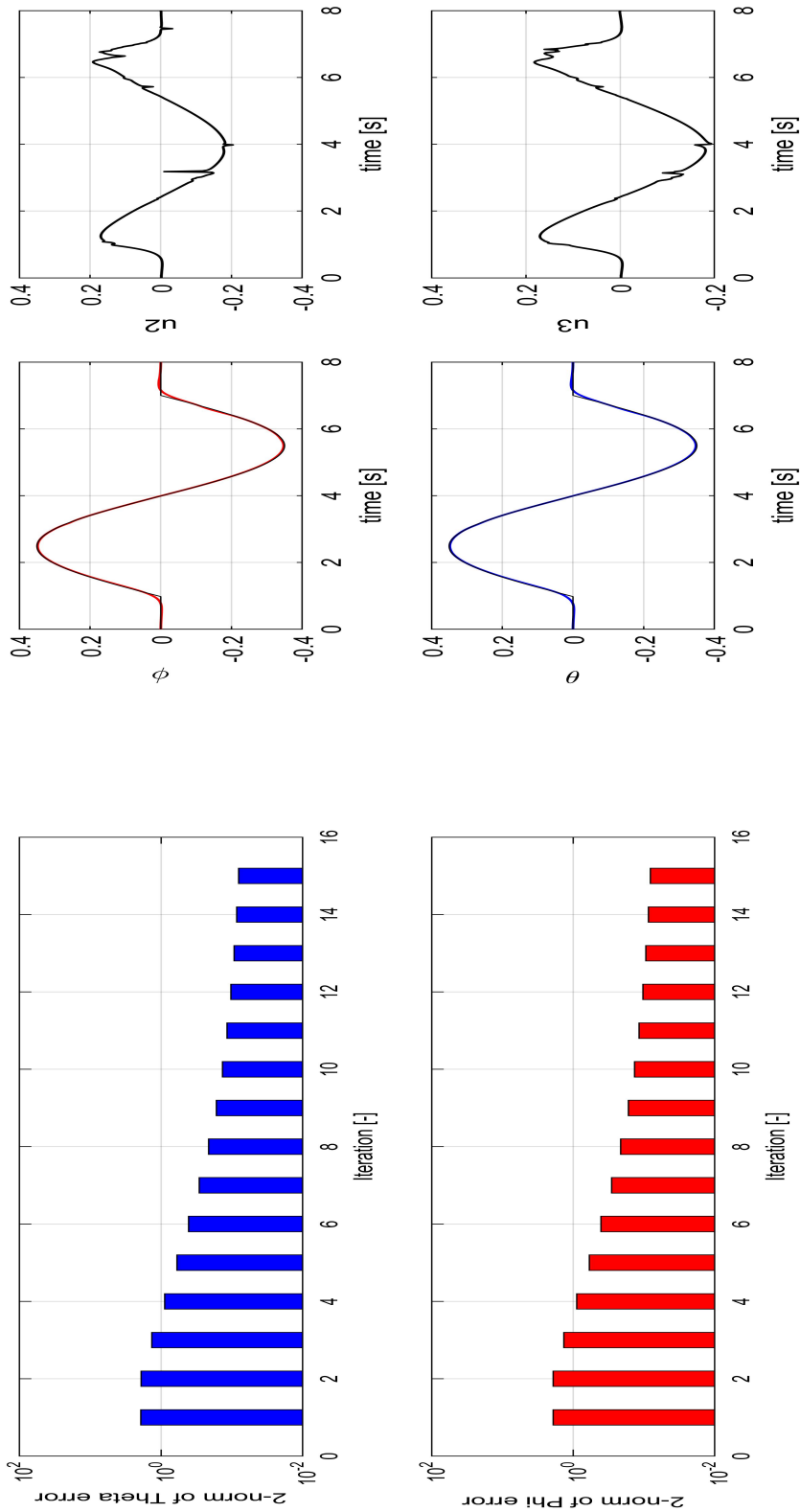
(a) The variation in theta over time for different iteration.

(b) 2norm for Roll and Pitch over time for different iteration.

FIGURE 5.20: NOILC with different iteration.
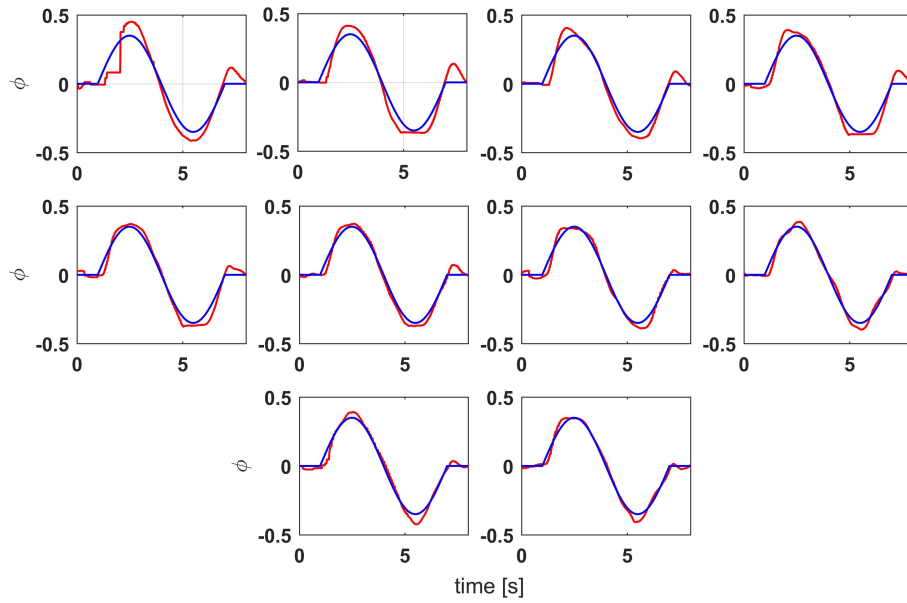
FIGURE 5.21: Experimental of NO-ILC for different iterations with disturbance.
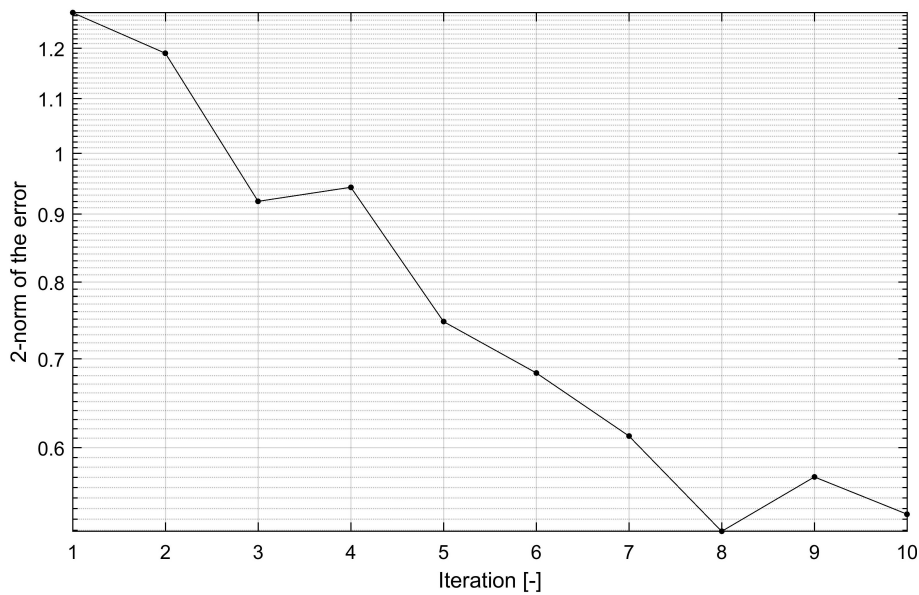
FIGURE 5.22: Monotonic convergence result for Norm Optimal ILC.

It is important to note that the fluctuation at the end of the last two trials (9 and 10) occurred due to 1) the parameters of the weighting matrix Q = 0.1 with a inevitably exists non-periodic random disturbance in the measured error signal and 2) the cause of uncertainty in the model algorithm which cause for diverge.

5.9 Comparing Results

The assessment criteria in comparing the results will rely on the second norm of the error between the reference signal and the actual output and for fair comparison the duration of all simulated algorithms. The trajectory consists of a single period sin wave and is non-smooth; hence is a challenging task for the ILC algorithm. Initially, the baseline (PID) and all proposed ILC methods have been tested to evaluated for standardized 2 DOF control, namely the altitude for angles roll ϕ and pitch θ which have done via matlab simulation and experimental.

In this chapter, Trajectory in Figure 5.11 is a single period sin wave and a non-smooth which instigates an aggressive reaction from the quadrotor because of the instantaneous change in amplitude. For this trajectory, the gradient-based ILC with the optimal gain formulation had a good overall performance and the error norm converged below the baseline value after the 2nd iteration for the attitude angles.

Note that although convergence is established theoretically, in practice the system is subject to disturbances and uncertainty. The effect of disturbances is evaluated in simulation and by experiment for the two approaches. First the performances of the two methods in simulation without disturbance are quantified and compared. The results are shown in Table 5.5. The NO-ILC method had significantly better performance and convergence properties in simulation.

TABLE 5.5: Simulation norm error results for attitude angles without disturbance.

ILC Approaches	Passes No.	$\|\hat{\theta} - \theta\|$	$\|\hat{\phi} - \phi\|$
G-ILC (without disturbance)	1	1.92	1.92
	3	1.38	1.38
	6	0.532	0.532
	16	0.309	0.303
NO-ILC (without disturbance)	1	1.92	1.92
	3	1.24	1.24
	6	0.476	0.476
	16	0.121	0.119

The disturbances took the form of torques that were injected in the ϕ and θ channels. The disturbances defined as exponentially decaying sinusoidal functions $\delta\tau = e^{-0.1t}(\sin t), \cos t, 0)$ for $t \in (2,6)$ s. The results for experiment are shown in Table 5.6. These show the better performance of the NO-ILC but the difference is less marked.

TABLE 5.6: Experimental norm error results for ILC algorithms with disturbance injection.

ILC Approaches	Trial (1)		Trial (3)		Trial (7)		Trial (10)	
	$\|e_\theta\|$	$\|e_\psi\|$	$\|e_\theta\|$	$\|e_\psi\|$	$\|e_\theta\|$	$\|e_\psi\|$	$\|e_\theta\|$	$\|e_\psi\|$
G-ILC + Disturbance Injection	1.277	2.834	0.920	1.281	0.612	0.705	0.574	0.534
NO-ILC + Disturbance Injection	1.283	3.214	0.926	1.212	0.562	0.633	0.434	0.446

Furthermore, as seen in Figure 5.23 and Figure 5.24, gradient-base ILC exhibited fluctuations in the error norms as the iteration increased and although it was minimal for the attitude angles. These fluctuations however did not affect the general trend as the error norm still converged after 10 iterations.
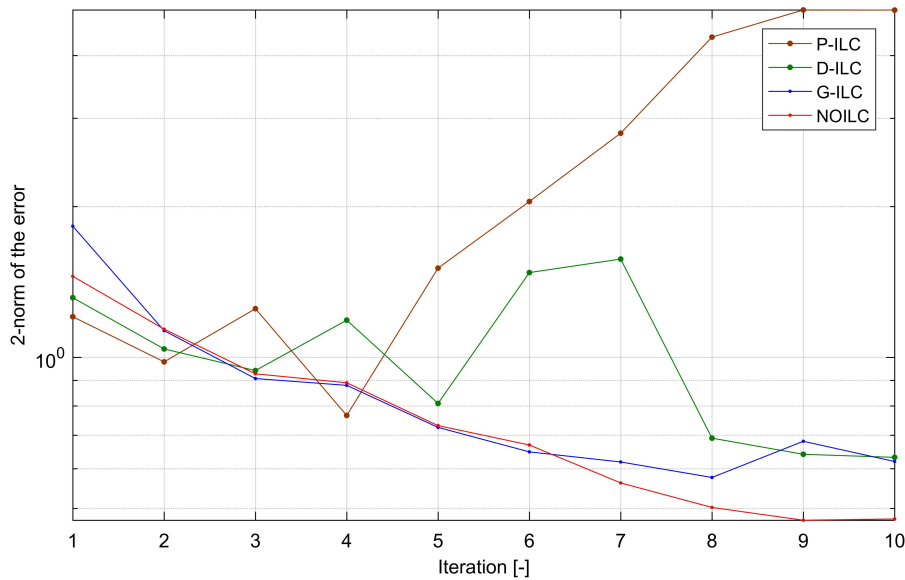
FIGURE 5.23: ILC algorithms error reduction ϕ error norm with disturbance.

On the other hand, the PID and P-type ILC using the gain $\alpha = 0.2$ had the poorest performance amongst all three ILC algorithms for both ϕ attitude despite the fact that the
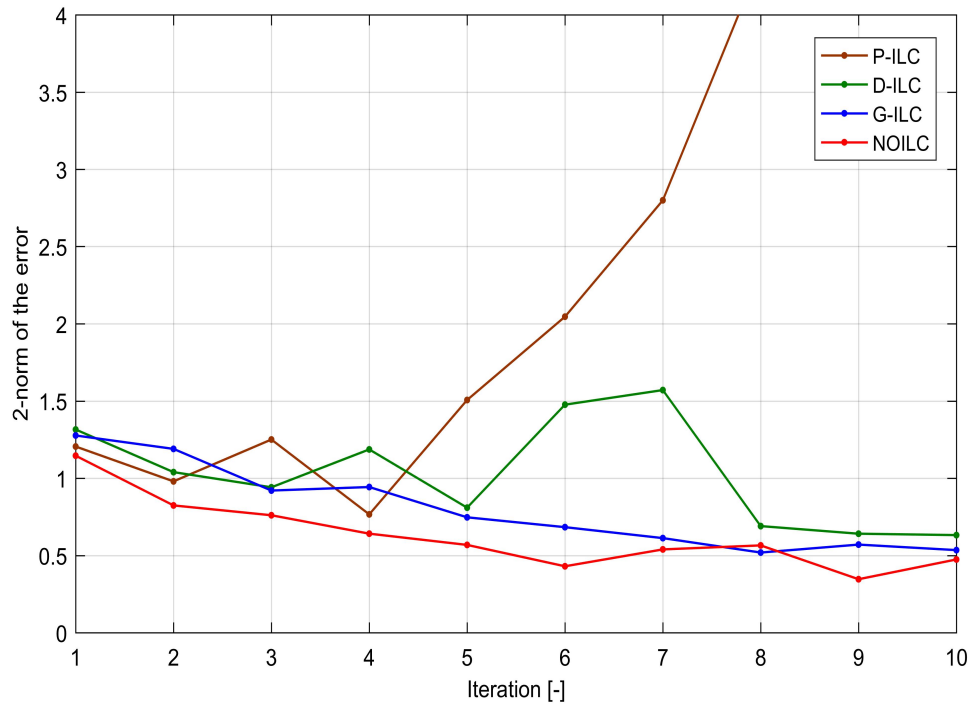
FIGURE 5.24: ILC algorithms error reduction ψ error norm with disturbance.

error norm dropped below the baseline value for both. The P-type algorithms manifest a non convergent result over the 10 trials due to 1) the convergence condition does not contain A and is hence independent of the system dynamics, 2) it follows that CB6= 0 does not hold and the system loses control at the beginning. For D-type algorithm is sensitive to measurement error and process disturbance, and it is seldom used in practical cases. This outcome was expected for several reasons, the fact that unguaranteed monotonic convergence and increases sensitivity to noise due to derivative action. This is clearly presented in Figure 5.12.

Norm optimal ILC with the weighting matrix $Q = 0.1$, exhibited a superior performance over the other two ILC algorithms for trajectory in Figure 5.23 and Figure 5.24 where it has expected demonstrated the fastest rate of monotonic error convergence and managed to significantly reduce the tracking error during the 10 trials. The attitude angles error norm was reduced to nearly 50% of the baseline value. The error norms for all ILC algorithms during different iterations are shown in Table 5.7 for trajectories.

TABLE 5.7: ILC algorithms of attitude angles in error 2-norms

ILC methods	Iteration(1)		Iteration(3)		Iteration(7)		Iteration(10)	
	$\|\mathbf{e}_\theta\|$	$\|\mathbf{e}_\phi\|$	$\|\mathbf{e}_\theta\|$	$\|\mathbf{e}_\phi\|$	$\|\mathbf{e}_\theta\|$	$\|\mathbf{e}_\phi\|$	$\|\mathbf{e}_\theta\|$	$\|\mathbf{e}_\phi\|$
PID	3.392	3.366	3.392	3.366	3.392	3.366	3.392	3.366
BCT	7.178	3.612	7.178	3.612	7.178	3.612	7.178	3.612
P-ILC	1.205	1.208	1.250	1.250	2.796	2.799	4.933	4.927
D-ILC	1.315	1.315	0.941	0.941	1.571	1.570	0.631	0.631
G-ILC	1.277	1.277	0.920	0.920	0.612	0.612	0.534	0.534
NOILC	1.143	1.146	0.761	0.760	0.540	0.539	0.478	0.474

Ultimately, further analysis and simulations were evaluated for the norm ILC which consistently showed the improved performance of all tracks and to obtain the better version of the NO-ILC algorithm, several weighting matrices $Q = \rho I$ were simulated. The results presented in Figure 5.25 shows that, as we increase the weighting parameter ρ, NO-ILC converges more rapidly. This mainly occurs because larger weighting matrix Q values in the NO-ILC cost function (4.22), penalize large error values which causes the error to decay faster. Consequently, the convergence rate of the algorithm will increase. Further increment beyond $\rho = 0.1$ will cause the algorithm to diverge. Therefore, the weighting matrix $Q = 0.1I$ will be chosen to analyze the algorithm robustness.

In addition to what has been achieved, the performance comparison of ILC tracking performance now evaluates the position (X, Y, Z) by adopting the baseline feedback controllers, where the results presented in Figure 5.26 and Figure 5.27 as the following:

I. Tracking performance using ILC algorithms (G-ILC, NO-ILC) in a feedback controller (PID, LQR) without disturbance injection.

II. Tracking performance using ILC algorithms (G-ILC, NO-ILC) in a feedback controller (PID, LQR) with disturbance injection.

The baseline feedback controllers are introduced in term of the standard deviation (SD), standard error of the mean (SEM). The SD δ with disturbance injection estimates
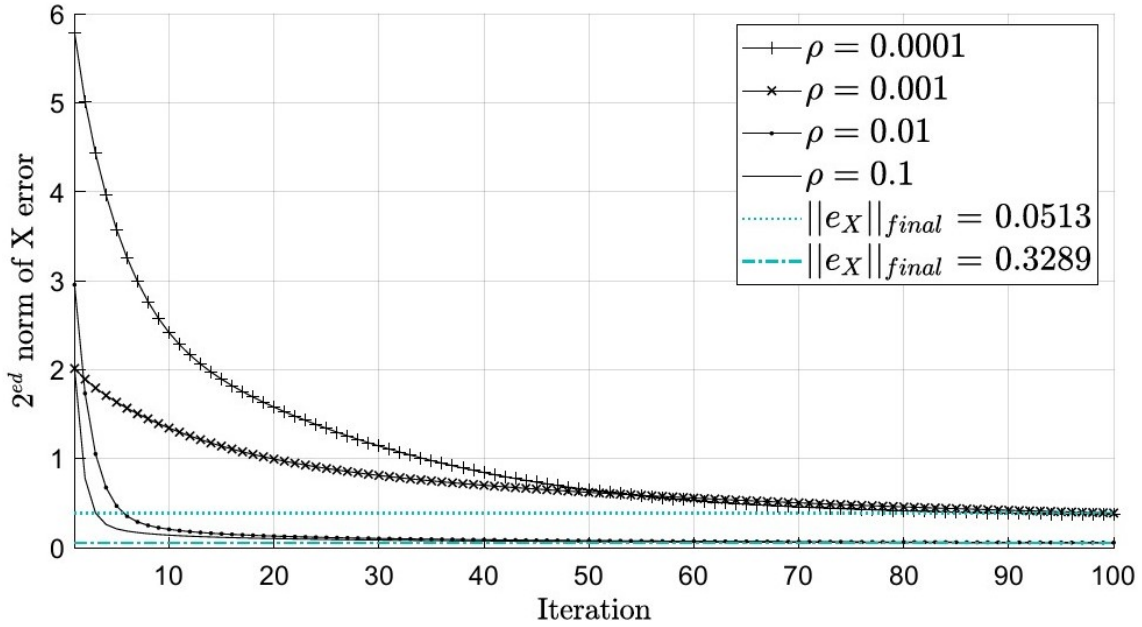
FIGURE 5.25: Various of weighting matrix Q for NO-ILC with disturbance.

dispersion of the individual data values for the mean, while SEM $||e_\varsigma||$ related to average for the true population mean as illustrated in Table 5.8.

TABLE 5.8: Baseline feedback controllers with standard deviation and standard error of the mean

Feedback Controllers		PID (without disturbance)	LQR (without disturbance)	PID (with disturbance)	LQR (with disturbance)
SEM	$||e_{X_\varsigma}||$	0.3598	0.4278	0.3599	0.4279
	$||e_{Y_\varsigma}||$	0.3535	0.4275	0.3535	0.4276
	$||e_{Z_\varsigma}||$	0.2155	0.2486	0.2159	0.2488
SD	δ_X	—	—	0.0147	0.0033
	δ_Y	—	—	0.0145	0.0035
	δ_Z	—	—	0.0032	0.0009

For a large class of practical systems, such as UAV reference tracking (as required for power line surveillance and monitoring) it is required that the output achieves perfect tracking at more than one defined time and enables the system error to converge to zero norm as rapidly as possible. Consequently, it includes future work on an alternative controller (i.e., ILC with hybrid controller) as an extension to enhance the tracking performance at subset (instantaneous in time) for many critical positions.
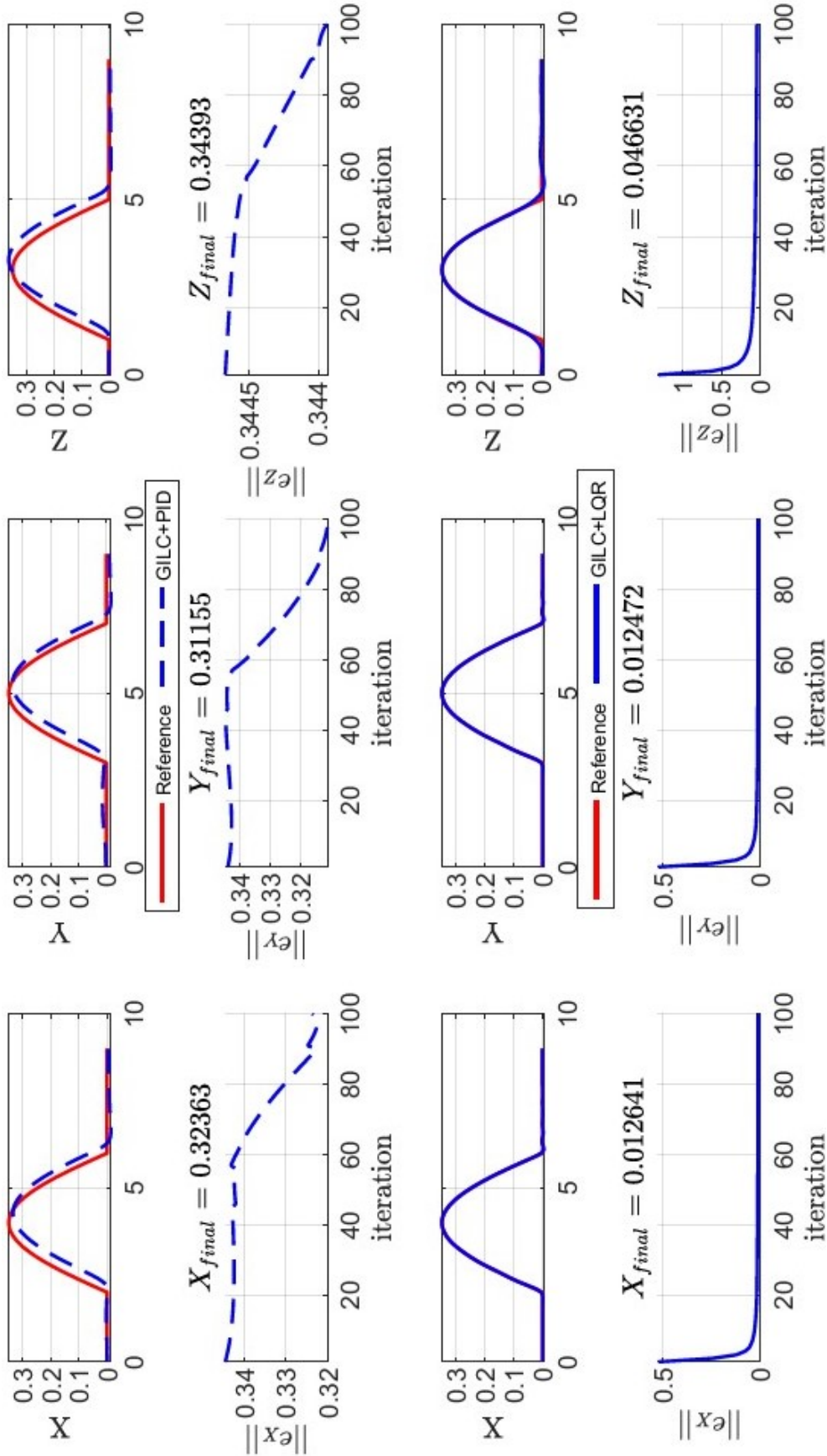
FIGURE 5.26: GILC of PID, LQR Feedback for position control with disturbance.
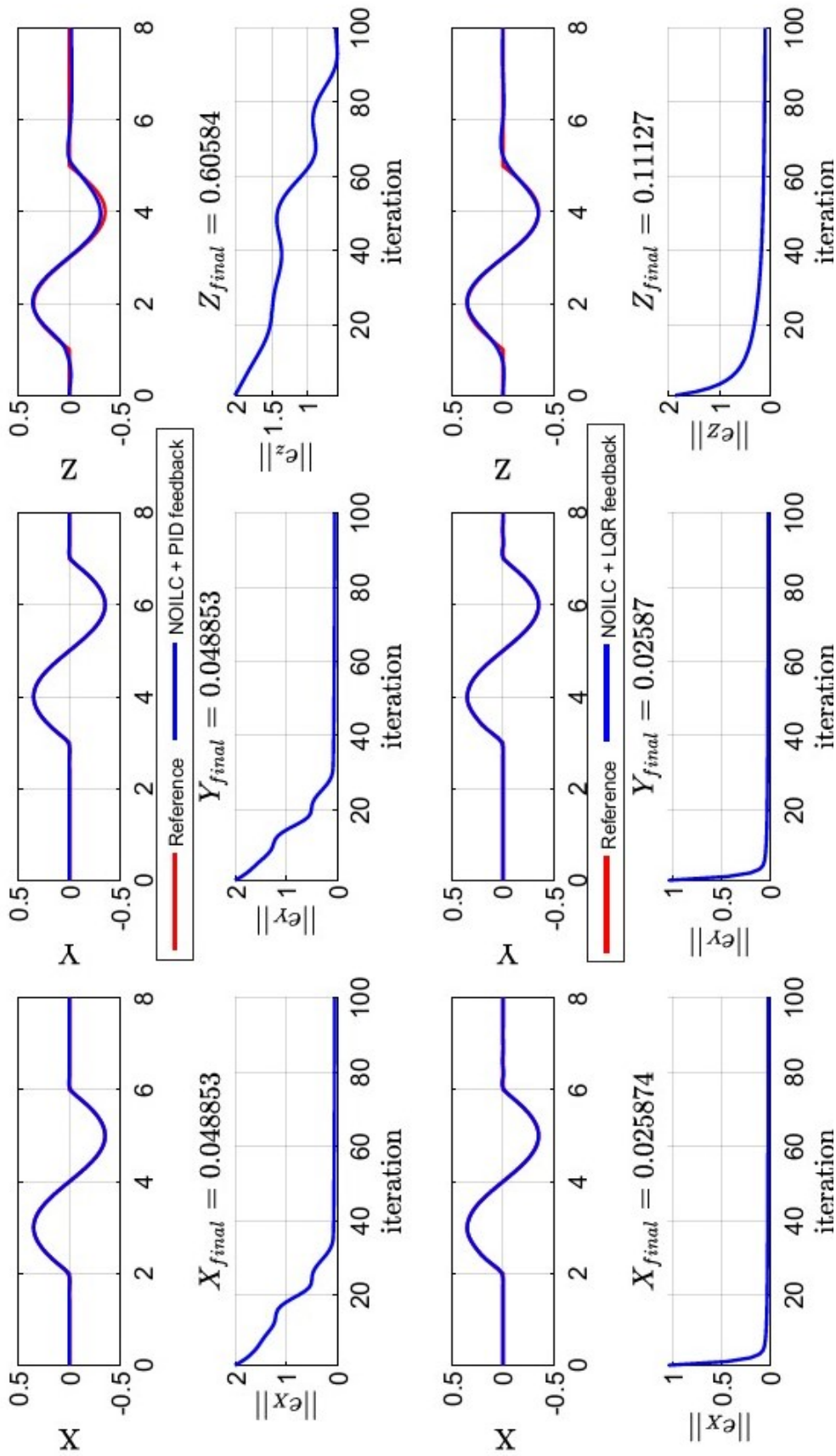
FIGURE 5.27: NOILC of PID, LQR Feedback for position control with disturbance.

5.10 Conclusions

The controllers used in this project have shown good performance. In Chapter 3 the PID controller was reviewed and it was found that existing controllers have experimented comparing with the control in Figure 3.5 which the experimental also done by Bouabdallah to control the 1 DOF. However his result showed unstable performance during 10s while the controller in programme of research has achieve stability to the system. The ILC controllers proposed here have also been shown significant of improvement over the existing controller PID. The results in this chapter serve to demonstrate that the only PID controllers use in this research can not help the controller to track the reference in case if the length time increase more than 30s, so in order to produces better performance than implementing each controller individually, the ILC control have been taken with a combined PID controller. Which can be tuned with to perform very well and from this the reliability of the attitude controller for 3 DOF derived can be inferred. In addition, the integral backstepping control has been implemented. The results showed that the system is much better than if comparing with the PID system in the tracking process, but there is a little efficiency in the case of step response due to the high sensitive nature of the dynamic system also the mechanical frame that have a little bit impact on signal. It shows that based on this control only can not give the desired performance and robustness, so need to testing and development of the advanced controllers than the currently use, to reduce the error and improve the performance with implemented the novel system of ILC, and the simplicity of application to nonlinear dynamics.

The suggested G-ILC and NO-ILC have been formulated and applied to the problem of reference tracking for UAV. When comparing the findings, the NO-ILC has shown superior tracking performance. Furthermore, the suggested NO-ILC has shown substantially improvement over the G-ILC in terms of error decrease and monotonic convergence. The results of the simulations and experiments both with and without an external disturbance show the proposed ILC performance for the two methods. The results the potential potential to achieve good trajectory tracking.

The NO-ILC method could form the basis for a power line inspection system. The repetitive nature of the power line geometries lends itself to this approach. However there are many control challenges to be faced, such as disturbances in the form of steady wind and unsteady wind gusts, and decision-making in the face of uncertainty. This points to the urgent need for additional future work for expanding ILC (i.e., point-to-point with hybrid controller) for tracking identification, for instance, through a straight conductor for a electrical overhead conductors monitoring-task. In addition, relaxing the tracking demand, can produce faster, more robust algorithms. These conclusions will be used to motivate new ILC algorithms for application to quadrotor s in the next chapter.

Chapter 6

Extended Point to Point ILC

The previous ILC approaches that required an existing model or did not have showed limited ability to deal with highly interactive systems and have only focused on reducing the error norm for each point of the reference. Furthermore, a variety of optimal approaches have yielded high performance, but in a real-world environment, there are some specific points high accuracy is required. This freedom has provided by the point to point ILC in section 6.2. Then in section 6.3, the framework of the point to point ILC method with and without disturbance have presented, expanded, and performance evaluation.

6.1   Introduction

In the previous sections, a wide class of ILC algorithms have focused on reducing the error norm for each point of the reference. However, In a real-world environment this might not be necessary. An example for this is a drilling machine which has to drill holes at specific locations. In this case the intermediate points are less of an interest but at some specific points high accuracy is required. This freedom provided by the Point-to-Point ILC method allows for great tracking at the selected points and can improve the performance of highly interacting MIMO systems [205].

Due to practical benefits of Point-to-Point ILC, this method has seen great interest and

has been applied to the main ILC methods. In [205] Point-to-Point ILC has been used to the gradient ILC algorithm and in [206] to both the feedback and the feedforward form of the Norm Optimal ILC. However, the work is limited and inaccurate in terms of 1) includes only 3 degrees of freedom within a framework of work on a robot arm (Don't even reach the level of climbing robots in term of task and motions) in a conventional application such as manufacturing where the ILC has been used 2) point to point is simple algorithms (not take in consideration under-actuated platform and nonlinear MIMO system).

In practice, system constraints have significant relevance to industrial manufacture due to physical limitations or performance requirements. The [206] extended [205] to support constraints such as input, output and input rate constraint. However, this extended based on the simple algorithms (point to point) and used to follow trajectories of the orientation is included while the new application in OPL inspection required an angles and position, velocity error, and obstacles.

6.2 Problem description

Standard ILC structure has recently been extended, to address the problem of practical application. A framework to add both robustness and improved convergence was described in [205], [206] and is now summarised.

Let the plant output be specified at a fixed number, $M \leq N$, of sample instants given by $0 \leq N_1 < N_2 \cdots < N_{M-1} < N_M < N$. The aim is to track only the output at these points. In (6.1) these parts are extracted using the operator $pM \times pN$ matrix Φ given by

$$
\begin{bmatrix}
\Phi_{(i-1)p+1,(j-1)p+1} & \cdots & \Phi_{(i-1)p+1jp} \\
\vdots & \ddots & \vdots \\
\Phi_{ip,(j-1)p+1} & \cdots & \Phi_{ipjp}
\end{bmatrix}
\Rightarrow
\begin{cases}
I_p, & j = N_i + 1, \ i = 1, 2 \cdots M \\
0_p, & otherwise
\end{cases}
\tag{6.1}
$$

in which I_p and 0_p are the identity and zero matrices respectively.

Now, to understand how the matrix Φ are formulated, it is important to highlight these main:

I. Remove the points that do not need to be tracked from the original reference y_d. This resulting decrease a reference vector $y_r \in \mathbb{R}^M$ with a length of

$$M = \sum_{j=1}^{p} M_j$$

II. Define a matrix transformation $\Phi \in \mathbb{R}^{pM \times pN}$ in which the $y_r = \Phi y_d$. Due to that, we first introducing a row vector $\varphi \in \mathbb{R}^{pN}$. Whose i^{th} element is (1) if the ith element of y_d is required to be tracked, and (0) otherwise. The definition of φ as following:

$$\varphi_i = \begin{cases} 1, & if \ \left\lfloor \frac{(i-1)}{p} \right\rfloor \in \mathscr{S}_{i-\lfloor (i-1)/p \rfloor p}, \\ 0, & otherwise \end{cases}$$

where $\mathscr{S} = \{N_j, 1, ..., N_j, M_j\}$ and $\lfloor . \rfloor$ denotes the (floor function).

Now it is easy to produce the matrix Φ through two steps:

- Set $\Phi = \varphi$.

- From first element then increment over the bottom row of Φ, so move all subsequent bottom row (entries) into a bottom row (newly created) in Φ if found a non-zero element. Also, maintaining their position along the row and padding the remaining entries of both rows with zeros. Finally, this formation the matrix Φ

$$\Phi_{i,j} = \begin{cases} 1, & if \ \varphi_j = 1, \ \sum_{q=1}^{j} \varphi_q = i \\ 0, & otherwise. \end{cases}$$

By the block-wise components as seen in (6.2), the matrix Φ has a simpler form as seen in (6.3) than due to the output is required to track a reference point.

$$\underbrace{\begin{bmatrix} \Phi_{(i-1)p+1,(j-1)p+1} & \cdots & \Phi_{(i-1)p+1\,jp} \\ \vdots & \ddots & \vdots \\ \Phi_{ip,(j-1)p+1} & \cdots & \Phi_{ip\,jp} \end{bmatrix}}_{\text{Matrix } \Phi} \quad \underbrace{\Rightarrow}_{\text{Block-wise components}} \quad (6.2)$$

$$\underbrace{\Phi_{i,j} = \begin{cases} I_p, & j = N_i + 1, \ i = 1, 2 \cdots M \\ 0_p, & otherwise \end{cases}}_{\text{Simpler form of matrix } \Phi} \tag{6.3}$$

Many ILC algorithms can be re-formulated for the point-to-point case by deriving an iterative numerical solution to the problem of finding a control input which minimizes the point-to-point error norm. The control objective is to find a sequence of control inputs u_k such that

$$\lim_{k\to\infty} \|y_r - \Phi G u_k\| = 0 \qquad \lim_{k\to\infty} \|u_k - u_d\|^2 = 0, \tag{6.4}$$

where $y_r = \Phi y_d$ are the Mp points to be tracked. The general ILC update state (4.7) now assumes the form

$$u_{k+1} = u_k + L(y_r - \Phi y_k) \tag{6.5}$$

so that the point-to-point error evolution is

$$\Phi e_{k+1} = (I - \Phi GL)\Phi e_k \tag{6.6}$$

and the convergence condition (4.9) becomes

$$\rho(I - \Phi GL) < 1 \tag{6.7}$$

6.2.1 Point-to-Point Gradient Descent

The form (6.5) has been tackled by several authors with different proposed updates. The gradient descent obtain as the following

$$minJ(u), \ J(u) = \lim_{k \to \infty} \|y_r - \Phi G u_k\|^2 \tag{6.8}$$

to yield the update

$$u_{k+1} = u_k + \beta (\Phi G)^T (y_r - \Phi y_k) \tag{6.9}$$

where the convergence condition (6.8) become

$$\rho |I - \beta \Phi G (\Phi G)^T| < 1 \ . \tag{6.10}$$

In Reference160, the equation (6.6) was solved using a norm optimal approaches, both approach yielded results that significantly improved upon standard ILC.

6.2.2 Point-to-Point Norm Optimal

In Reference156 the Point-to-Point ILC method was applied to the feedforward and the feedback version of Norm Optimal ILC. The paper concludes that both Point-to-Point NOILC algorithms can be similarly derived to the original NOILC algorithms. Like the original algorithms, the Point-to-Point versions try to minimize the cost function (6.11).

$$J(u_{k+1}) = \frac{1}{2} \{ [y_r - y_{k+1}]^T Q [y_r - y_{k+1}] + [u_{k+1} - u_k]^T R [u_{k+1} - u_k] \} \tag{6.11}$$

With it the input update law of the feedforward Point-to-Point NOILC to yield the update

$$u_{k+1} = u_k + G^* (I - GG^*)^{-1} (y_r - \Phi y_k) \tag{6.12}$$

where $G^* = R^{-1}(\Phi G)^T Q$

6.2.3 Point to Point ILC for Nonlinear Systems

First the SISO structure of (4.35) [207] is extended to the MIMO dynamics to give

$$
\begin{aligned}
x_k(t+1) &= f(x_k(t), u_k(t)) \\
y_k(t) &= h(x_k(t), u_k(t)) \qquad x(0) = x_0
\end{aligned}
\tag{6.13}
$$

where $g'(u_k) \in \mathbb{R}^p, u_k(t) \in \mathbb{R}^m$. The point to point problem is to construct a sequence of inputs u_k, such that

$$
\lim_{k \to \infty} \|y_r - \Phi g'(u_k)\| = 0,
\tag{6.14}
$$

where

$$
\begin{aligned}
y_k(0) &= h(x_k(0), u_k(0)) = g0(x_k(0), u_k(0)) \\
y_k(1) &= h(x_k(1), u_k(1)) = h(f(x_k(0), u_k(0)), u_k(1)) \\
&\quad : g_1(x_k(0), u_k(0), u_k(1)) \\
&\quad \vdots \\
y_k(T) &= h(x_k(T), u_k(T)) \\
&= h(f(x_k(T1), u_k(T1)), u_k(T)) \\
&\quad : g_N(x_k(0), u_k(0), u_k(1), ..., u_k(T)).
\end{aligned}
\tag{6.15}
$$

where Φ is given by (6.1). Thus, the non-linear system (6.13) can be expressed by the algebraic function $g(\cdot) : l_2^m[0, \ T] \mapsto l_2^p[0, \ T]$ given by

$$
y_k = g(u_k), \ \ g(\cdot) = [g_0(\cdot), g_1(\cdot), ..., g_T(\cdot)].
\tag{6.16}
$$

To solve (6.14) we follow the applications of Newton method based ILC but combine

with the point to point methodology. To solve (6.14), apply the update of (4.33) with $G = g'(u_k)$, to give

$$u_{k+1} = u_k + \beta \Phi g'(u_k)^T e_k \tag{6.17}$$

Then construct a NOILC solution with employ the objective of (4.22) with $G = g'(u_k)$, to give the update

$$u_{k+1} = u_k + \Phi g'(u_k)^T [I - \Phi g'(u_k)g'(u_k)^T]^{-1} e_k \tag{6.18}$$

To implement these updates, note that the linearised form of (6.13) is the LTV system

$$\tilde{x}(t+1) = \bar{A}(t)\tilde{x}(t) + \bar{B}(t)\tilde{u}(t)$$
$$\tilde{y}(t) = \bar{C}(t)\tilde{x}(t) \tag{6.19}$$

Now if $\Phi = I$, (6.17) and (6.18) become

$$u_{k+1} = u_k + \beta g'(u_k)^T e_k \tag{6.20}$$

$$u_{k+1} = u_k + g'(u_k)^T [I - g'(u_k)g'(u_k)^T]^{-1} e_k \tag{6.21}$$

respectively

Here $g'(u_k)$ can be written as

$$g'(u_k) = \begin{bmatrix} \bar{C}(0)\bar{B}(0) & 0 & \cdots & 0 \\ \bar{C}(1)\bar{A}(1)\bar{B}(0) & \bar{C}(1)\bar{B}(1) & \cdots & \vdots \\ \vdots & \vdots & \ddots & 0 \\ \bar{C}(N-1)\prod_{i=1}^{N-1}\bar{A}(i)\bar{B}(0) & \bar{C}(N-1)\prod_{i=2}^{N-1}\bar{A}(i)\bar{B}(1) & \cdots & \bar{C}(N-1)\bar{B}(N-1) \end{bmatrix} \tag{6.22}$$

and $\bar{A}(t)$, $\bar{B}(t)$ and $\bar{C}(t)$ is generated each iteration via (4.35).

6.2.4 Results and Discussion

The reference trajectory is shown in Figure 6.1. The trajectory consists of a single period sin wave and is non-smooth; hence is a challenging task for the ILC algorithm. During that, various numbers of iteration trials were performed for each point to point ILC algorithm. The cause for that it best simulates the requirements of the real world.
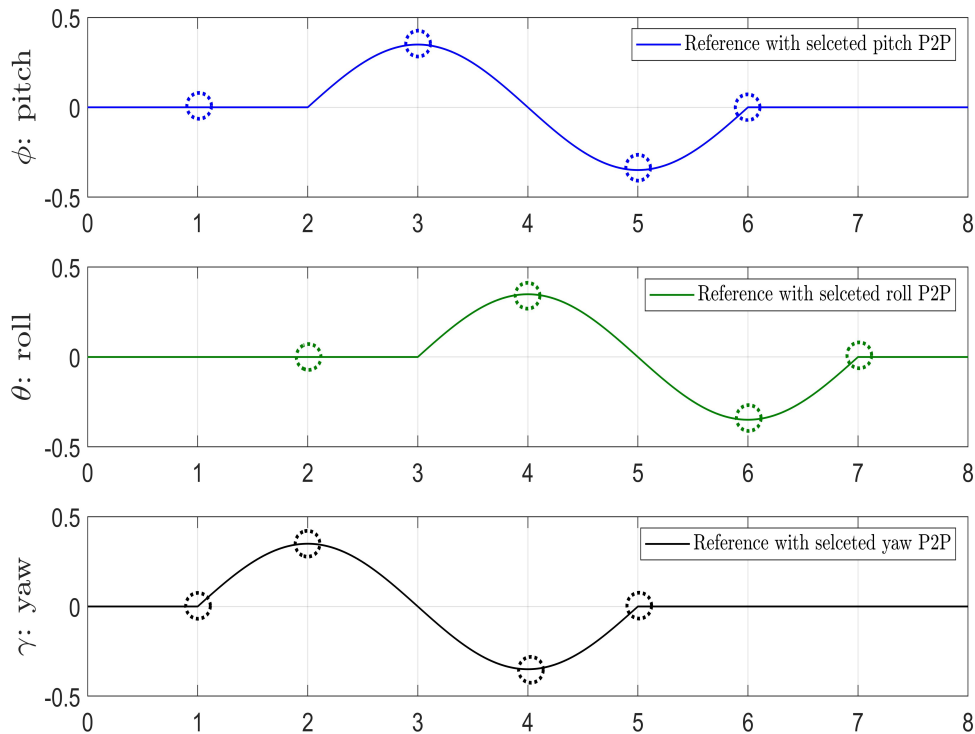
FIGURE 6.1: References for standard and point-to-point ILC controllers.

As illustrated in the Figure 6.1, there are two steps for selected the reference signal more real world as follows: -

I. Increasing the complexity of reference for the point-to-point algorithms in the tracking of the selected points.

II. Adopting completely non-identical reference signals for pitch, roll and yaw, to avoid rotation around an axis spreading from one rotor to the rotor on the opposite side,

and thus would only require the movement of two rotors instead of four. Another important reason is to obtain the lower control effort (i.e., less energy consumption) in a non-linear, multivariable control problem with fast dynamics and noisy measurements.

These points are represented by circles as shown in supplement figure. From the Figure 6.1, point-to-point algorithms (gradient and norm) can track only the specific states of this reference signal. Therefore, the characteristic points, which will be similar to a number of trace points on transmission lines, are as follows,

1. Starting point

2. Maximum amplitude point

3. Final point

4. Critical points outside the non-smooth sinusoidal.

The reference tracking are used both sinusoidal and step references with magnitudes of 0.35 from 1s until 7s and then back to 0 magnitudes at the end of reference signal, as displayed in Figure 6.2.
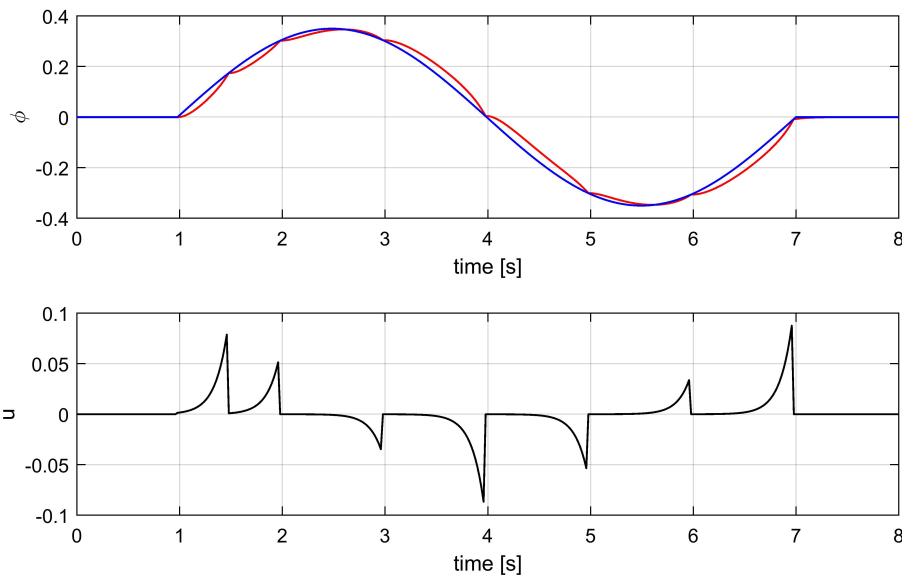
FIGURE 6.2: Point-to-Point result for gradient based ILC.

The references have a total length T = 8 seconds. Six reference points are also defined

for use in point to- point ILC and are given by $y_d = [\,0.18,\ 0.3,\ 0.3,\ 0,\ -0.3,\ -0.3\,]^T$ at the time samples $S_1 = \{\ 1.5,\ 2,\ 3,\ 4,\ 5,\ 6\ \}$.

Point-to-point Gradient ILC and NOILC is implemented to track y_r using update equation in (6.19) and (6.20). A significant change in convergence rate is shown in Figure 6.2 and Figure 6.3. As shown in theory, the point-to-point method only tracks a subset of points and therefore leads to superior results in terms of error norm as confirmed in Figure 6.3. It yields low errors norm and almost reaches zero error after 4 trials in total.
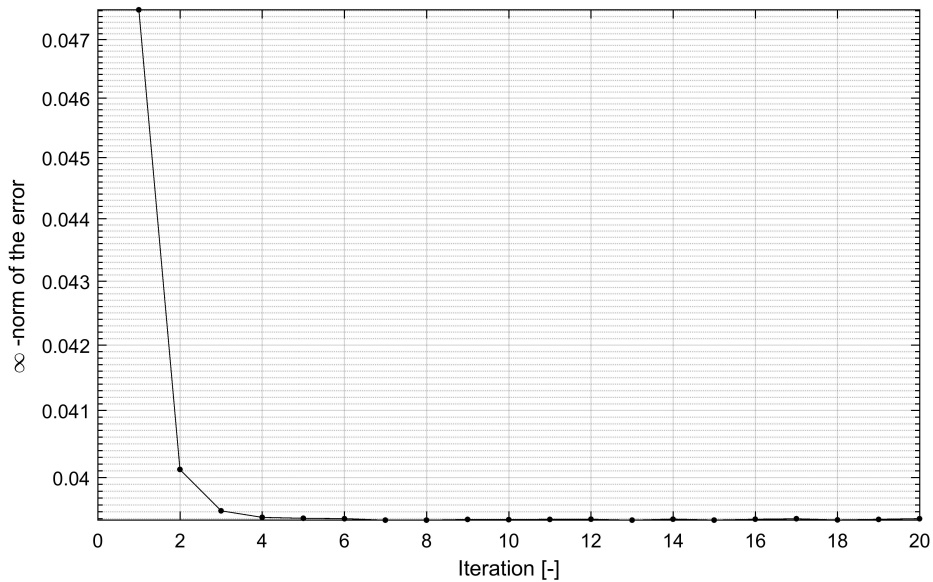
FIGURE 6.3: Monotonic convergence result for Point-to-Point ILC.

6.3 Comparative Analysis of Novel ILC Algorithm

6.3.1 Point-to-Point Gradient ILC

In this subsection, the Gradient point-to-point ILC is holding a similar method to the standard gradient-based ILC. However, the former represents real life scenarios in the requirement of tracking (i.e., not all points in the reference tracking are necessarily important, only specific points are required). Moreover, disturbance is implemented before

the system model for more real-life scenarios. The distribution is normal for disturbance injections at 5% of the respective input value. The error for attitude is elucidated in Figure 6.4 and Figure 6.5 for standard gradient-based and gradient point-to-point, respectively.
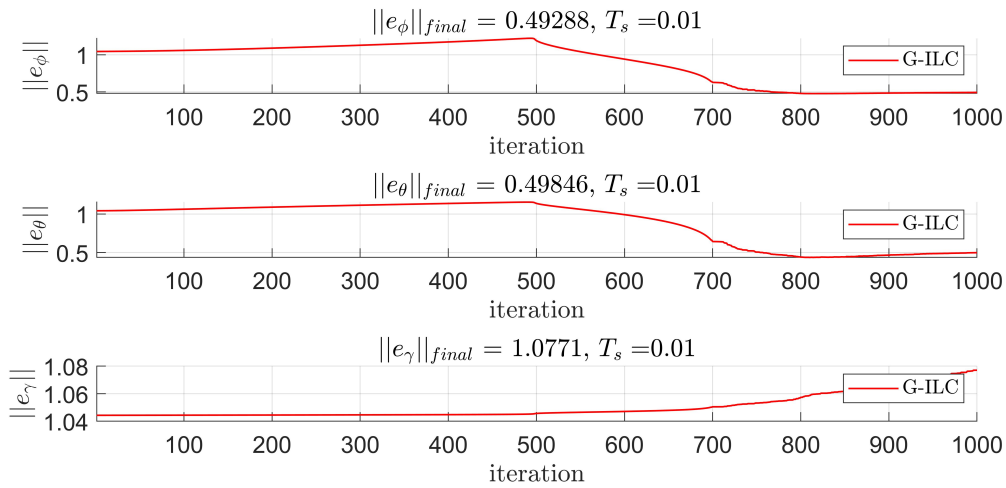
FIGURE 6.4: Convergence result for gradient-based ILC through 1000 iterations.

The Gradient point-to-point method had significantly better performance and able to reduce the error 60 times of improvement than a standard gradient-based ILC as illustrated in Figure 6.5. However, the standard gradient-based ILC is only capable of achieving in half of the error norm after 500 iterations for roll and pitch angles as illustrated in Figure 6.4. Accordingly, the gradient point-to-point method is held a drastic improvement to reach the error norm, for example the roll with 0.15634 as illustrated in Figure 6.5.

To evaluate system performance in the hybrid structure in term of convergence, input norm and robustness properties, the simulation results are conducted between gradient point-to-point against the gradient-based method through (1) their own merits and (2) hybrid structure combined with LQR controllers.

Accordingly, more than one feedback controller has been applied, and the observations have been adopted as follows:-

1. In the case of PID merging, the performance was similar in both algorithms, but with a higher number of iterations on a gradient-based ILC.
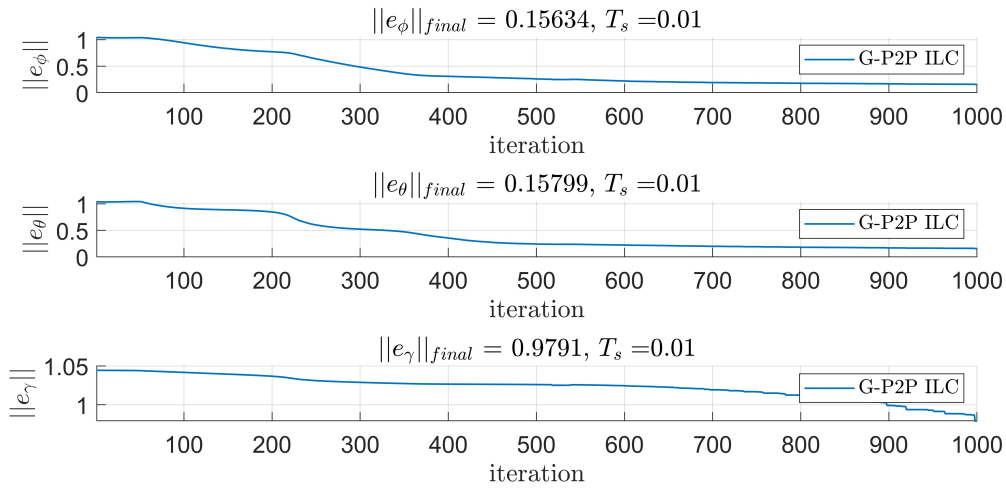
FIGURE 6.5: Convergence result for gradient point-to-point ILC through 1000 iterations.

2. In the case of LQR merging, the performance was significantly superior in a gradient point-to-point algorithm, in particular, it was able to (i) reduce the error norm and (ii) diverges in the first 5 iterations, as illustrated in Figure 6.6 and Figure 6.7.

3. In the case of gradient-based ILC with LQR merging, the maximum single value $\Phi G(\Phi G)^T$ was not reduced monotonously due to trace the entire reference.

4. In the case of gradient point-to-point with LQR merging, the maximum single value $\Phi G(\Phi G)^T$ was reduced monotonously due to fewer points to track.
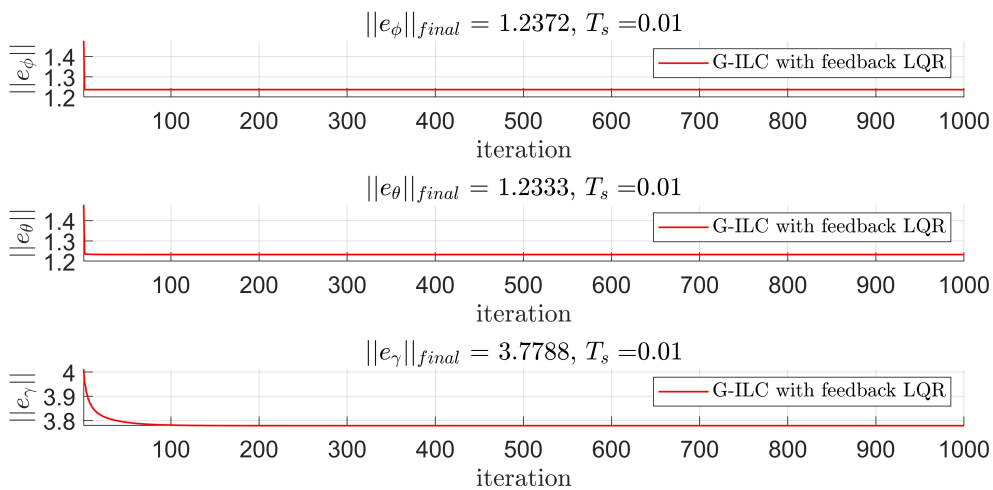
FIGURE 6.6: Monotonic convergence result for gradient-based ILC with LQR.
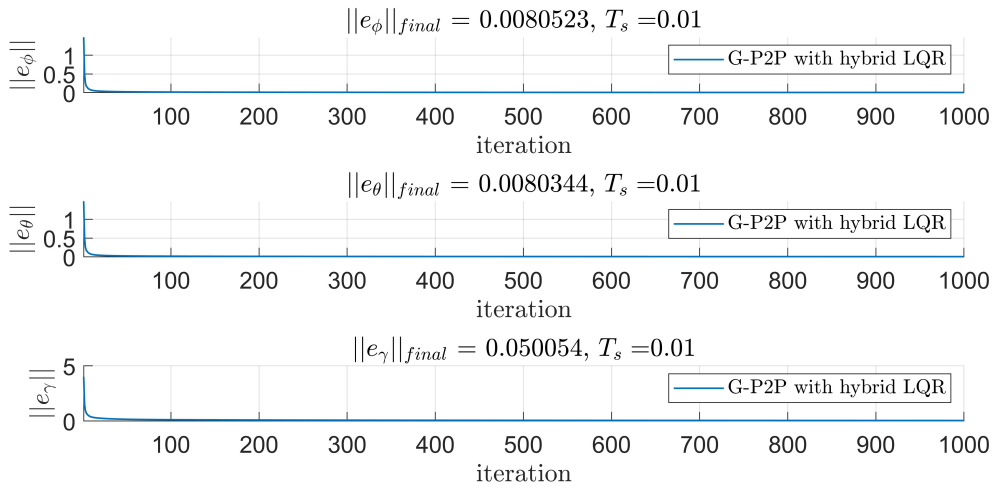
FIGURE 6.7: Monotonic convergence result for gradient point-to-point ILC with LQR.

The convergence rates as illustrated in Figure 6.7 are confirming that the final error norm after 1000 trials is achieved at 0.00805 with fewer points, while the performance as illustrated in Figure 6.6 confirms higher error norm and slower convergence at final error norm equal 1.2372. In general, these characteristics lead to the effect of (i) uncertainty and (ii) increased learning transients, when the plant has to keep track of additional points.

Table 6.1 confirms that the results for standard gradient-based amid the presence of disturbances having somewhat more freedom to track all second reference points after using ILC + LQR but with a very minor divergence. While the pitch, roll and yaw angles are converging quickly in case of gradient point-to-point ILC + LQR. This enhances the ability of point-to-point algorithms to efficiently track critical and selected points in a real system where they have a benefit in (i) allowing more freedom and (ii) significantly reducing the divergence.

6.3.2 Point-to-Point Feed-forward NOILC

In this subsection, the current extension of the point-to-point NOILC with the arrangement of a feedback demonstrates a similar properties to NOILC (non-point-to-point structure). However, current point-to-point extension algorithms for NOILC are significantly

TABLE 6.1: Simulation results for 1000 trails with and without hybrid structure

Controller		No Feedback without disturbance (50 to 500)	No Feedback without disturbance (500 to 1000)	LQR with disturbance (50 to 500)	LQR with disturbance (500 to 1000)
Standard Gradient ILC	$\|e_\phi\|_{final}$	1.048	0.4928	1.2372	1.2372
	$\|e_\theta\|_{final}$	1.051	0.49846	1.2333	1.2333
	$\|e_\gamma\|_{final}$	1.046	1.0771	3.779	3.7788
Gradient Point to Point ILC	$\|e_\phi\|_{final}$	0.2609	0.15634	0.01044	0.00805
	$\|e_\theta\|_{final}$	0.2432	0.15799	0.01038	0.00803
	$\|e_\gamma\|_{final}$	1.026	0.9791	0.06559	0.05005

superior at tracking a specific desired point, and decrease the error for attitude and with-added noise. Therefore, similar reference signal is applied to track only the specific states, y_r, using update equation (6.21) with $R = I$ and $Q = I$ in the point-to-point NOILC with feedback case of subsection 6.2.4 are used and illustrated in Figure 6.1.

The formulation of ILC demonstrates through an either a 1-dimensional (1D) or 2-dimensional (2D) that were conducted in chapter 5 and chapter 6 in section 6.3 over (i) a finite time interval (ii) a series of trials. The analytical approaches are still dealing with tracking, and convergences in one dimension either time or trial number, thus it is important to investigate the convergences in the 3D development. Therefore, the ILC is described in a 2D or 3D as illustrated in Figure 6.8 and Figure 6.9. The first dimension is time (or samples in discrete problems) or in the input delay, the second dimension is the trial number, and the attitude error for 3DOF.

However, the required time cannot be observed in case of transition between each specific point as well as input delay. These are two important factors to achieve high tracking performance in the real application using extended algorithms. Accordingly, the results in Figure 6.8 and Figure 6.9 illustrate the property of convergence in the 3D. Hence, the performance of extended ILC algorithms is characterized a significant decrease and then the final error value is maintained with less time within 1000 iterations, while a small value of the input delay is observed. The value is relatively acceptable in the case
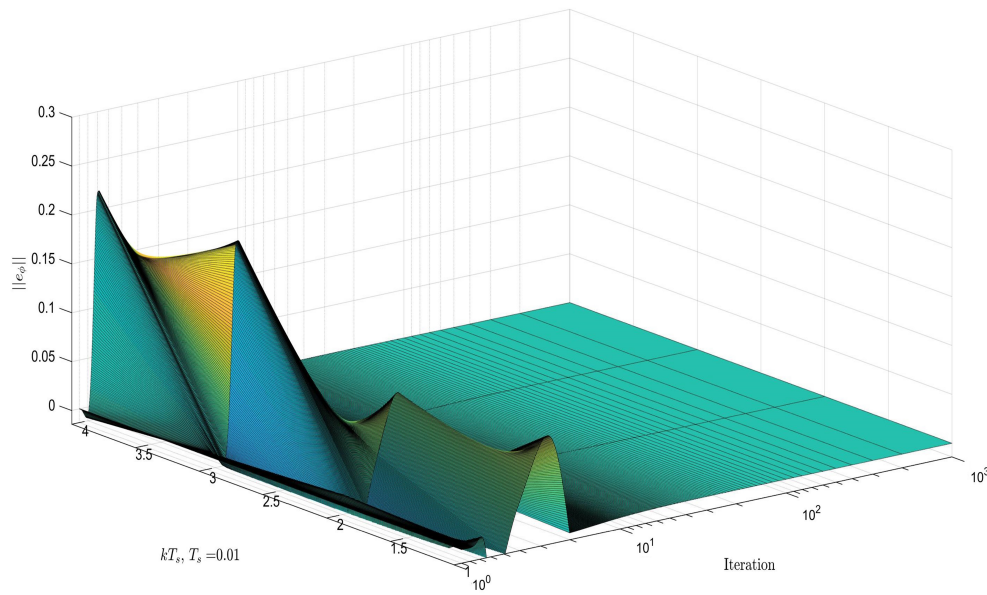
FIGURE 6.8: Tracking error surface with convergence using the gradient point-to-point ILC
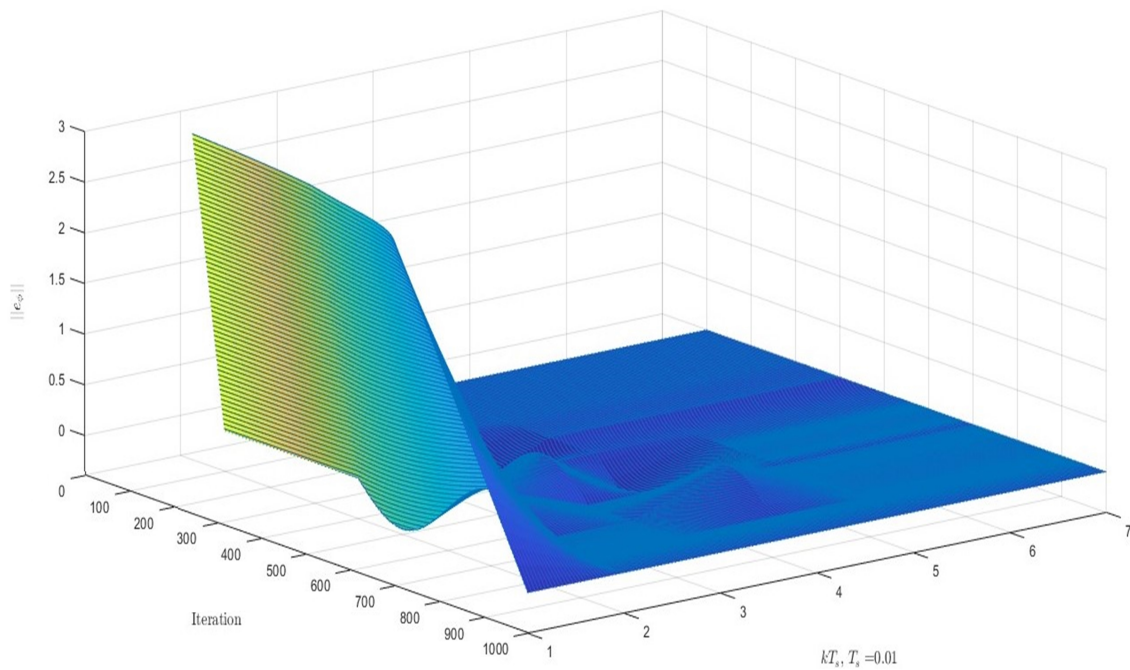
FIGURE 6.9: Tracking error surface with convergence using the point-to-point feed-forward
NOILC

of gradient point-to-point ILC and relatively less in the case of point-to-point NOILC.

Clearly, the point-to-point with the structure of (feed-forward NOILC, graded-based)
are proving an enabling technology in maintaining a very good (i) trajectory tracking,

and (ii) convergence speed while minimizing disturbance effects for multirotor control for OPL inspection.

6.4   Conclusions

The suggested point-to-point with the structure of (feed-forward NOILC, gradient-based) have been formulated and extended properties to encompass this standard ILC framework gradient-based and norm optimal in which the performance improves significantly to the problem of tracking in the OPL inspection. The point-to-point with the extended structure are proving an enabling technology in maintaining a very good (i) trajectory tracking, and (ii) convergence speed while minimizing disturbance effects.

All the point-to-point controllers starting from gradient-based to feed-forward NOILC highlight the impact of LQR in a combination with the new structure. In addition, relaxing the tracking demand, is produce faster, more robust algorithms while using less input effort. For example, the ILC benefits of a point-to-point gradient after extended are: (i) holding a similar property of the standard gradient-based (ii) enhanced the ability to track a specific points are required in OPL. The results of the simulations with and without an external disturbance show the proposed ILC performance for the two methods to enabling it for real life scenarios in OPL inspection. These results confirm the validity of the theoretical predictions elucidated in both chapter 5 and chapter 6.

Finally, the ILC algorithm was introduced by the proposed ILC point convergent property from 2D and 3D perspective. These results demonstrate a new tool for follow-up ILC development by the observed transition between each specific point as well as input delay. This confirms the expected potential to achieve high tracking performance in the real application using extended algorithms.

Chapter 7

Conclusions and Future Work

This chapter summarises the analysis and limitations found in the three main areas of the thesis (overhead power lines, ILC frameworks, trajectory tracking) and then goes on to discuss their implications. It also elucidates future work that will be undertaken to develop a prototype of the overall system in a laboratory environment.

7.1   Conclusion

In recent years, Unmanned Aerial Vehicles have emerged as an efficacious means of tackling and monitoring faults in overhead power lines. This thesis addresses the existing unmet potential within the automate ILC frameworks trajectory tracking formation for conductors, pylons, and power components amid the presence of wind disturbances and severe noises, which have elicited significant research interest in the recent past.

In Chapter 2, various aspects of research into Unmanned Aerial Vehicles (UAV) have been reviewed. The current design limitations of quadrotors have been extracted and a comparison of their merits has been undertaken via characteristics such as power, control, payload, manoeuvrability, stationary flight, speed, vulnerability, endurance, miniaturization, indoor usage, and the ability to accomplish several tasks in civil areas such as monitoring transmission lines. With regard to the tracking of electrical transmission lines, a review was conducted to access the methods of faults inspection in terms of types of error.

According to these findings, most faults on the electrical network system are LG faults occurring on 220 and 330 kV transmission lines with a range of 92 %. This means that it is difficult to identify faults and that current technologies are insufficient. In this regard, the potential of quadrotor technology has largely remained unexploited.

According to the first and second objectives, the attempts comprising task-specific approaches for the inspection of power lines, insulators, transition, modelling quadrotor, and current control approaches, respectively were discussed in Chapter 2 and Chapter 3. For power line inspection, the review demonstrated that the UAV needs to fly relatively close to the lines to take detailed images of the physical condition of the conductor or farther away, before using additional sensors and larger cameras, which, in turn, require larger, heavier, more complex, and more expensive UAVs. Chapter 3 was provided an established design of a modelling quadrotor and current control approaches in order to highlight limitations and areas of potential exploitation which was utilized later in Chapter 5 and Chapter 6 for a final solution to perform transition and horizontal trajectory. This was led to more understand of the new application related to the constraints of power lines are more challenging and unique conditions and different from a conventional application such as manufacturing where the ILC has been used as well as identified a nonlinear ILC design as an enabling technology for a 6-DOF quadrotor in OPL inspection. Therefore, this requires expensive equipment and fine control of the camera. Moreover, more accurate motion control and faster flight times as well as ability to perform transition tasks via trajectory tracking.

To meet the first and second objectives in which the design, implement, and evaluate optimal ILC algorithms, namely Gradient-based and Norm Optimal for a UAV model. A novel method of optimal ILC approaches based on nonlinear MIMO systems with a two-loop structure were formulated in Chapter 4 and Chapter 5. The first loop was addressing the system lag and another was tackling the possibility of a disturbance commonly encountered when inspection of OPL. The improved method is contributing to good trajectory tracking and very good convergence speed while minimizing exogenous

disturbances with an 89% and 86.7% improvement in error reduction compared to PID and nonlinear BCT, respectively. Moreover, the develop design was include a novel tuning method for β_{new} variation for nonlinear MIMO systems as seen in (Algorithm 5.55), (Algorithm 5.57), (Algorithm 5.60). All the tuning methods were formulated and applied to the problem of reference tracking implemented and successfully validated. Therefore, the first and second objectives of this research was successfully met.

Referring to the third objective of this research, a several new algorithms (PID-type, gradient-based, norm optimal) designs for nonlinear systems were extended to a novel Newton method based ILC, but embed greater freedom in updating the permissible structure. The work in Chapter 4 significantly derived the various ILC convergence condition and control effort comprising non model based (P, D and PID-type) (Algorithm 4.12), (Algorithm 4.14) and model based (Gradient descent, and Norm optimal and Newton-Based) ILC framework (Algorithm 4.33) to maintain precise tracking as well as generalisation of Newton method based ILC to generalise linear ILC forms instead of simply employing inverse ILC. In addition to proving the potential of extended ILC, the experimental results show that PID performs poorly when trying to make the trajectory more complicated, which is why PID is used as a baseline with backstepping and compared with different ILC forms such as Proportional-type, Derivative-type, Gradient, Norm Optimal, and Newton Method. This generalized ILC algorithm illustrated how the Newton method-based techniques can be integrated with OPL inspection to expand the problem scope in term of tracking trajectory. Moreover, it was provided superior more accurate motion control with disturbance where baseline feedback controllers were introduced in term of SD and SEM. Furthermore, a faster flight times (to maintain a low error norm in 8s for 100 iterations) with the best automatic tuning weighting matrix Q with a 0.1. Therefore, the first and second objectives of this research was successfully met.

As mentioned in third and final objective, a new further extensions of point-to-point ILC for OPL inspection under more extreme external environmental disturbances such as strong winds was accomplished in Chapter 6. The novel controller's purpose is to ad-

dress the repeated disturbance at each trial as well as a real application scenario where inevitably the exists a non-periodic random disturbance in the measured error signal. In Chapter 5, both P and D-type ILC show limitations in practical application, such as unguaranteed monotonic convergence and increased sensitivity to noise caused by derivative action. With regard to gradient ILC, it shows better tracking but there are fluctuations in some iterations, although the performance remains good. Furthermore, NOILC exhibited accurate experimental results with good convergence during the first eight iterations. However, it was revealed that both gradient ILC and NOILC can be improved using point to point ILC in Chapter 6. The application has been extended to more than 2-D systems analysis to the convergent property of the proposed ILC law by applying a 3-D analysis approach, thus supplying a new tool for follow-up ILC development as illustrated in Chapter 6.

In this thesis, all point-to-point ILC algorithms proposed have solid theoretical derivations, and are able to track significantly only at certain points of the reference in comparison to the standard gradient descent algorithm with LQR control for 1000 iterations. According to the findings, the proposed point-to-point (gradient descent and feed-forward NOILC) with a hybrid LQR algorithms exhibit a greater speed, thus allowing for greater freedom of tracking point and anticipating robustness. However, it is imperative to ascertain the practical performance of the tracking in more complicated scenarios, especially in cases of snow accumulation and random disturbance winds.

The next step entails adding auxiliary elements to the quadrotor system. Therefore, additional sensors have been considered and contribute to an effective/robust system when combined with vision. In terms of control, existing quadrotor approaches are not impervious to limitations. In particular, very few benefits are known to accrue from learning over experience. Achieving inspection using quadrotors implies preparing better control systems, developing image processing, and combining them with the leading hardware. By reviewing controllers, it is apparent that ILC is an under-researched technique which will be employed first.

7.2 Research Impact

This subsection will discuss the potential impact in terms of enabling ILC technology that has been developed through this thesis and potential impact on quadrotor control for OPL inspection, other repetitive inspection tasks (bridges, border and security fence integrity, gas pipeline inspection etc), autonomous recharging strategies and COVID-19 pandemic.

7.2.1 ILC Framework and OPL Inspection

From the findings (experimental of optimal ILC + simulation of extended point-to-point ILC) shows that the ILC approaches including a simple structure controller for ILC which have been presented in discrete-time. These controllers require a tuning gain matrix and in one case a delay-time constant, and do not require an explicit model. This simplicity aids/impact usability but necessarily degrades performance. Also, the findings clearly shown after validation and implementation the NOILC has shown superior performance in terms tracking performance. Furthermore, NOILC controllers proposed here have demonstrated significant improvement over the G-ILC regarding error reduction and monotonic convergence with and without an external disturbance for the two methods.

In particular, the development of control method based on an extended ILC have potential impact also to be applied easily for inspection power system such as towers, cable, or fitting in the presence of external disturbances without affecting the tracking process, which justifies the fact that ILC algorithm have good performance and has smoother transitions in a way of tracking this type of reference. These confirm the theoretical predictions given in this research project. The new findings shows that the expand ILC (i.e., point-to-point with hybrid controller) to specify tracking points, for instance, through a straight conductor for an electrical overhead conductors monitoring-task have more efficient and rapid convergence in the case of critical points. Also, this is significantly clear when applied the 3-D analysis approach to the convergent property of the proposed novel ILC it is show more details follow-up ILC development.

7.2.2 Other Repetitive Inspection Tasks

The ILC technology developed in this thesis will have an impact of improving the transient response performance of the system which runs frequently over a specified period of time until perfect tracking is achieved for different repetitive inspection applications such as bridges, border and security fence integrity, gas pipeline inspection due to the similarity in tasks. This project has impact on introducing a real-time quadrotors to perform health inspection of repetitive applications compared to traditional approaches. In addition, ILC approaches demonstrate a greater ability to transition between one specific point to another with faster and less control effort, this will have significant impact in a similar repetitive task. Furthermore, the ILC approach in this thesis has (i) requires less calculation, (ii) requires less a prior knowledge about the system dynamics, which will be a great impact to implement on real system such as gas pipeline inspection.

7.2.3 Autonomous recharging strategies in OPL

From the development the ILC in this thesis, the UAV-based inspection method will save energy, simplify access to mostly damage items on OPL, reduce inspection costs due to using accurate control approaches and less depend on expensive sensors, and automate the inspection process. However, automation of the inspection process still cannot achieve full automation, and with compromised performance due to the battery capacity of a medium scale drone that limits their travel distance and mission duration. The extended point to point ILC will be the most feasible and reliable technique to provide (i) stability pose of quadrotor and (ii) prolonged UAV's mission duration via learning term from mistakes during the charge UAV from power lines.

7.2.4 COVID-19 Pandemic

Finally, as the world changes in light of the COVID-19 outbreak, it is also time for effective and proportionate change in these new circumstances. Moreover, Integration of

technological solutions such as UAVs in the power system will have a profound impact on mitigating the impact of COVID-19. Since it is a technology that does not depend on social communication and are restricted by the non-contact sensing technologies. ILC is a solution that demonstrates a great potential and opens the doors to a more independent world, which of course increases the industry attractiveness of a comprehensive inspection system.

7.3 Future Work

The gradient ILC approach has not previously been applied in conjunction with vision based sensing, which is why there is substantial novelty in this area. The ILC gradient based method has been selected for investigation due to its attractive robustness properties, and the simplicity of application to nonlinear dynamics. New forms of ILC, which learn repeated manoeuvres that can occur asynchronously at any order, will be derived. Techniques to reduce the tracking error will include NOILC and Newton Method based ILC. In the medium-term, the thesis will focus on selection lightweight and high quality camera. For example (LiDAR,CMOS,PTZ), the purchase time will be given sufficient attention during this work, along with the implementation and benchmarking of controllers for the quadrotor using ultra-sound sensors to track obstacles and to control its altitude. Highest priority will be accorded o calibrate sensor and test low-cost, light-weight sensors. Then, the emphasis will be placed on investigating edge detection detection technique to identify simple classes of faults (such as missing phase lines).

The long-term future work of the project comprises the future development and experimental evaluation of the quadrotor system. Finally, at the end of the this project, a low-cost,weight and energy of portable hardware will be integrated with image processing methods for fault finding on the HV electricity grids to reduce time and cost for autonomous monitoring of overhead faults. In light of this system, the elements will collectively provide an integrated system capable of tracking faults on overhead power line

with good performance.

Future works will include a development and evaluation of both the vision algorithms, such as spatial tracking, and flight controller based on ILC Point to Point used in the final solution. Due to the required processing power, a Raspberry Pi will be used to perform all these calculations and dispatch commands to the four motors using Communication Interface (ACI in C). In this regard, it will be necessary to integrate the additional hardware into the UAV. This can be accomplished by powering the Raspberry Pi off the LiPo battery pack. As the Pi works off 3.3V, methods to step down the voltage will be required. Given as a theoretical solution, it is supported with tests that ensure its feasibility.

Moreover, in practical power systems, inspection usually require UAV to track other components which normally remain hidden with the level of ground such as grounded cables, and optimization of multiple cost functions. In future works, the design framework will be generalized and ILC approaches will be explored to carry out the new targeting task and multiple cost function by adopting the Pareto optimization as a trade-off in the total cost function.

Appendix A

Background on Kinematics and Dynamics

A.1 Rotation Matrices

We begin by considering the two coordinate systems shown in Figure 1.
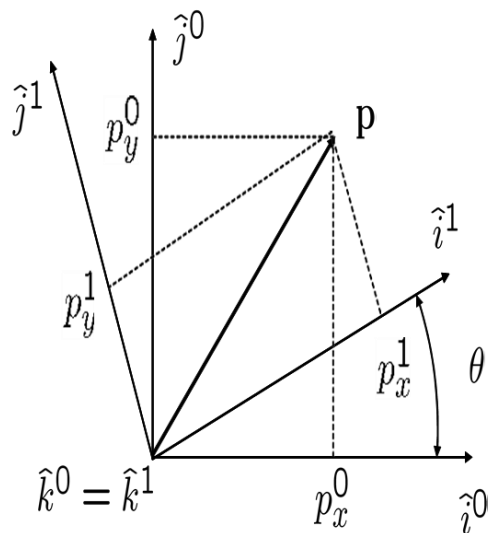
The vector p can be expressed in both the F_0 frame (specified by $(\hat{i}^0; \hat{j}^0; \hat{k}^0)$) and in

the F_1 frame (specified by $(\hat{i}^1; \hat{j}^1; \hat{k}^1)$). In the F_0 frame we have

$$p = p_x^0 \hat{i}^0 + p_y^0 \hat{j}^0 + p_z^0 \hat{k}^0.$$

Alternatively in the F_1 frame we have

$$p = p_x^1 \hat{i}^1 + p_y^1 \hat{j}^1 + p_z^1 \hat{k}^1.$$

Setting these two expressions equal to each other gives

$$p_x^1 \hat{i}^1 + p_y^1 \hat{j}^1 + p_z^1 \hat{k}^1 = p_x^0 \hat{i}^0 + p_y^0 \hat{j}^0 + p_z^0 \hat{k}^0.$$

Taking the dot product of both sides with $\hat{i}^1$, $\hat{j}^1$, and $\hat{k}^1$ respectively, and stacking the result into matrix form gives

$$p^1 = \begin{pmatrix} p_x^1 \\ p_y^1 \\ p_z^1 \end{pmatrix} = \begin{pmatrix} \hat{i}^1 \cdot \hat{i}^0 & \hat{i}^1 \cdot \hat{j}^0 & \hat{i}^1 \cdot \hat{k}^0 \\ \hat{j}^1 \cdot \hat{i}^0 & \hat{j}^1 \cdot \hat{j}^0 & \hat{j}^1 \cdot \hat{k}^0 \\ \hat{k}^1 \cdot \hat{i}^0 & \hat{k}^1 \cdot \hat{j}^0 & \hat{k}^1 \cdot \hat{k}^0 \end{pmatrix} \begin{pmatrix} p_x^0 \\ p_y^0 \\ p_z^0 \end{pmatrix}.$$

From the geometry of Figure 1 we get

$$p^1 = R_0^1 p^0$$

where

$$R_0^1 = \begin{bmatrix} C_\theta & S_\theta & 0 \\ -S_\theta & C_\theta & 0 \\ 0 & 0 & 1 \end{bmatrix}$$

The notation R_0^1 is used to denote a rotation matrix from coordinate frame F_0 to coordinate frame F_1. Proceeding in a similar way, a right-handed rotation of the coordinate system about the y-axis gives

$$R_0^1 = \begin{bmatrix} C_\theta & 0 & -S_\theta \\ 0 & 1 & 0 \\ S_\theta & 0 & C_\theta \end{bmatrix}$$

and a right-handed rotation of the coordinate system about the x-axis resultes in

$$R_0^1 = \begin{bmatrix} 1 & 0 & 0 \\ 0 & C_\theta & S_\theta \\ 0 & -S_\theta & C_\theta \end{bmatrix}$$

The matrix R_0^1 in the above equations are examples of a more general class of rotation matrices that have the following properties:

P.1. $(R_a^b)^{-1} = (R_a^b)^{-T} = R_a^b$.

P.2. $R_b^c R_a^b = R_a^c$.

P.3. $\det R_a^b = 1$.

In the derivation of Equation (1) note that the vector p remains constant and the new coordinate frame F_1 was obtained by rotating F_0 through a righted handed rotation of angle θ.

We will now derive a formula, called the rotation formula that performs a left-handed rotation of a vector p about another vector $\hat{n}$ by an angle of μ. The vector p is rotated, in a left-handed sense, about a unit vector $\hat{n}$ by an angle of μ to produce the vector q. The angle between p and $\hat{n}$ is ϕ. By geometry we have that

$$q = \vec{ON} + \vec{NW} + \vec{W}Q :$$

The vector $\vec{ON}$ can be found by taking the projection of p on the unit vector $\hat{n}$ in the direction of $\hat{n}$:

$$\vec{ON} = (p \cdot \hat{n})\hat{n}.$$

The vector $\vec{NW}$ is in the direction of $p - \vec{ON}$ with a length of $NQ\cos\mu$. Noting that the length NQ equals the length NP which is equal to $\left\| p - \vec{ON} \right\|$ we get that
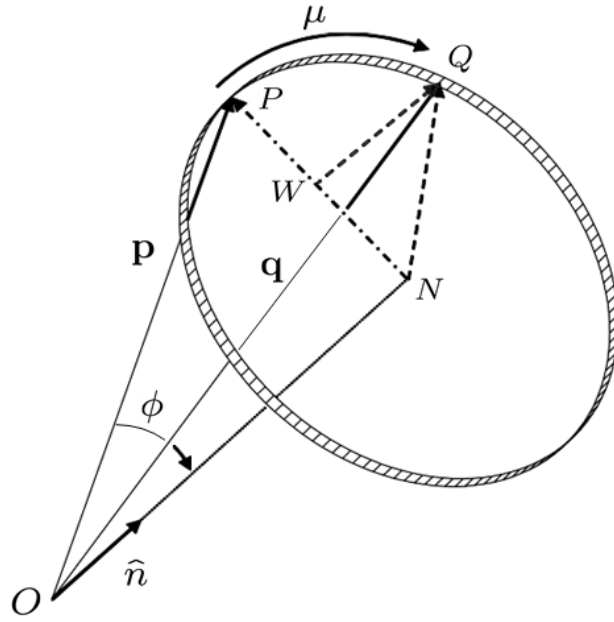
FIGURE A.2: Left-handed rotation of a vector p about the unit vector $\hat{n}$ by an angle of μ to obtain the vector q.

$$\vec{NW} = \frac{p - (p \cdot \hat{n})\hat{n}}{\left\| p - (p \cdot \hat{n})\hat{n} \right\|} NQ \cos \mu = (p - (p \cdot \hat{n})\hat{n}) \cos \mu$$

The vector $\vec{WQ}$ is perpendicular to both p and $\hat{n}$ and has length $NQ \sin \mu$. Noting that $NQ = \left\| p \right\| \sin \phi$ we get

$$\vec{WQ} = \frac{p \times \hat{n}}{\left\| p \right\| \sin \phi} NQ \sin \mu = -\hat{n} \times p \sin \mu$$

Therefore Equation (2) becomes

$$q = (1 - \cos \mu)(p \cdot \hat{n})\hat{n} + \cos \mu\, p - \sin \mu (\hat{n} \times p)$$

which is called the rotation formula.

As an example of the application of Equation (3) consider a left handed rotation of a vector p^0 in frame F_0 about the z-axis as shown in Figure 3. Using the rotation formula we get
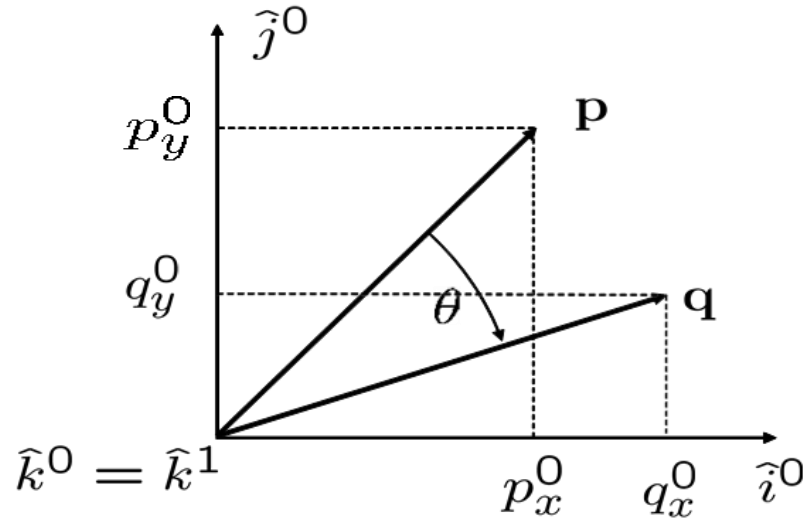
FIGURE A.3: Rotation of p about the z-axis.

$$q^0 = (1 - \cos\theta)(p \cdot \hat{n})\hat{n} + \cos\phi\, p - \sin\phi\, \hat{n} \times p$$

$$= (1 - \cos\phi)p_z^0 \begin{pmatrix} 0 \\ 0 \\ 1 \end{pmatrix} + \cos\phi \begin{pmatrix} p_x^0 \\ p_y^0 \\ p_z^0 \end{pmatrix} - \sin\phi \begin{pmatrix} -p_y^0 \\ p_x^0 \\ 0 \end{pmatrix}$$

$$= \begin{bmatrix} C_\phi & S_\phi & 0 \\ -S_\phi & C_\phi & 0 \\ 0 & 0 & 1 \end{bmatrix} p^0$$

$$= R_0^1 p^0$$

Note that the rotation matrix R_0^1 can be interpreted in two different ways. The first interpretation is that it transforms the fixed vector p from an expression in frame F_0 to an expression in frame F_1 where F_1 has been obtained from F_0 by a right-handed rotation. The second interpretation is that it rotates a vector p though a left-handed rotation to a new vector q in the same reference frame. Right-handed rotations of vectors are obtained

by using $(R_0^1)^T$.

A.2   Quadrotor Coordinate Frames

For quadrotors there are several coordinate systems that are of interest. In this section we will define and describe the following coordinate frames: the inertial frame, the vehicle frame, the vehicle-1 frame, the vehicle-2 frame, and the body frame.

The inertial frame F^i

The inertial coordinate system is an earth fixed coordinate system with origin at the defined home location. As shown in Figure 4, the unit vector $\hat{i}^i$ is directed North, $\hat{j}^i$ is directed East, and $\hat{k}^i$ is directed toward the center of the earth.
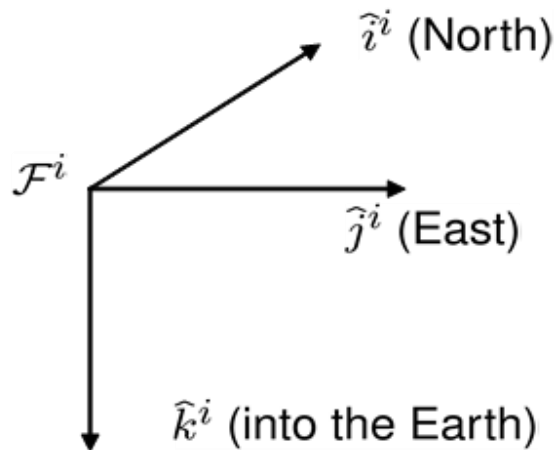
FIGURE A.4: The inertial coordinate frame.

The vehicle frame F^v

The origin of the vehicle frame is at the center of mass of the quadrotor. However, the axes of F^v are aligned with the axis of the inertial frame F^i. In other words, the unit vector $\hat{i}^v$ points North, $\hat{j}^v$ points East, and $\hat{k}^v$ points toward the center of the earth, as shown in Figure 5.

The vehicle-1 frame F^{v1}

The origin of the vehicle-1 frame is identical to the vehicle frame, i.e, the the center

of gravity. However, F^{v1} is positively rotated about $\hat{k}^v$ by the yaw angle ψ so that if the airframe is not rolling or pitching, then $\hat{i}^{v1}$ would point out the nose of the airframe, $\hat{j}^{v1}$ points out the right wing, and $\hat{k}^{v1}$ is aligned with $\hat{k}^v$ and points into the earth. The vehicle-1 frame is shown in Figure 6.

The transformation from F^v to F^{v1} is given by

$$p^{v1} = R_v^{v1}(\psi)p^v,$$

where

$$R_v^{v1}(\psi) = \begin{bmatrix} C_\theta & S_\theta & 0 \\ -S_\theta & C_\theta & 0 \\ 0 & 0 & 1 \end{bmatrix}$$

The vehicle-2 frame F^{v2}

The origin of the vehicle-2 frame is again the center of gravity and is obtained by rotating the vehicle-1 frame in a right-handed rotation about the $\hat{j}^{v1}$ axis by the pitch angle θ. If the roll angle is zero, then $\hat{i}^{v2}$ points out the nose of the airframe, $\hat{j}^{v2}$ points out the right wing, and $\hat{k}^{v1}$ points out the belly, a shown in Figure 7.

The transformation from F^{v1} to F^{v2} is given by

$$p^{v2} = R_{v1}^{v2}(\theta)p^{v1},$$

where

$$R_{v1}^{v2}(\theta) = \begin{bmatrix} C_\theta & 0 & -S_\theta \\ 0 & 1 & 0 \\ S_\theta & 0 & C_\theta \end{bmatrix}$$

The body frame F^b

The body frame is obtained by rotating the vehicle-2 frame in a right handed rotation about $\hat{i}^{v2}$ by the roll angle ϕ . Therefore, the origin is the center-of-gravity, $\hat{i}^b$ points out the nose of the airframe, $\hat{j}^b$ points out the right wing, and $\hat{k}^b$ points out the belly. The

body frame is shown in Figure 8.

The transformation from F^{v2} to F^b is given by

$$p^b = R^b_{v2}(\phi)p^{v2},$$

where

$$R^{v2}_{v1}(\phi) = \begin{bmatrix} 1 & 0 & 0 \\ 0 & C_\phi & S_\phi \\ 0 & -S_\phi & C_\phi \end{bmatrix}$$

Appendix B

Modelling and Parameter Identification

Some of the model parameters are easy to measure, such as the mass of the quadrotor and the arm length this quadrotor shown in Figure B.1 . In order to identify the thrust drag coefficient, the construction of a test bed is necessary. The inertia matrix, rotational and translational drag coefficients can be approximated by calculation, where some sort of measurement must be done. We shall start by identifying the airframe rigid-body parameters and then move on to the rotors.
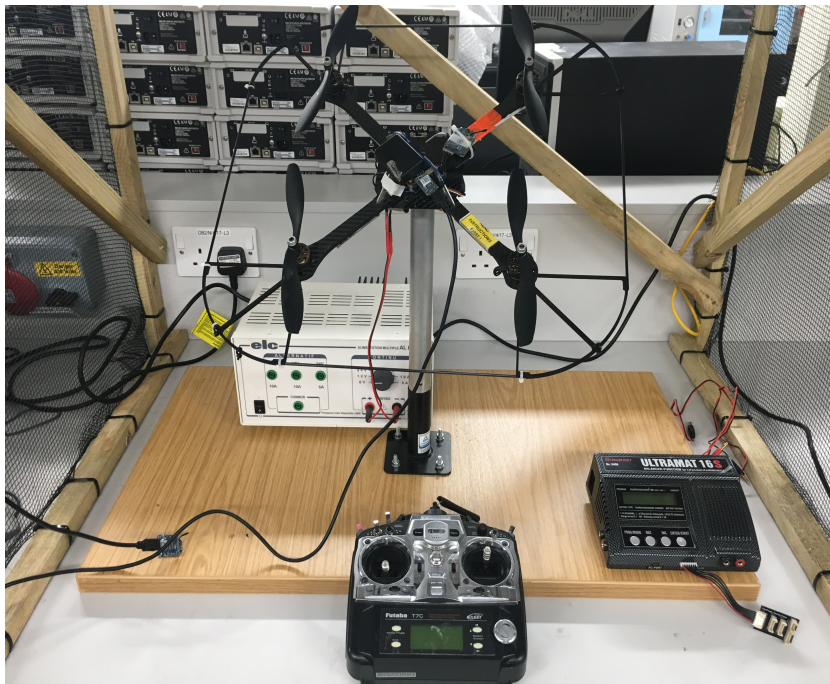
FIGURE B.1: Quadrotor system in the lab for testing purposes

A test bed, designed for analysing the motor's performance and enabling controller tuning, is constructed from steel and finished in black paint and bearings, so that it allows three DOF of rotation. Steel tube was chosen as it was easy to obtain and allows for reconfiguration of the test bed if required, also it is solid and give the structure bed more strength to avoid effect of vibration which happen when in case of testing the controller of quadrotor.

Steel tube was selected because of its easy availability and high density gives the rig stability and rigidity. The UAV is secured in place with a spherical rolling joint. The design of the test bed is shown in and Figure B.2, the quadrotor sits in-top and connected by bearing (Spherical Rolling Joints), this type of bearings is expensive due to have features include, high precision in which the movable part has less frictional resistance due to its rolling joint structure under reload, achieving high precision, provide multiple degrees of freedom this is due to superfine inner spherical machining technology.
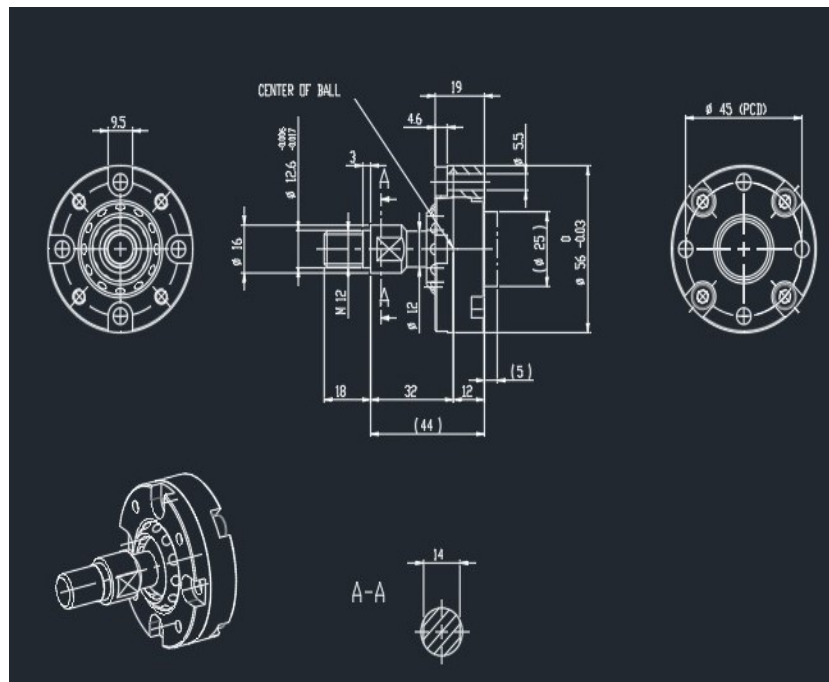
FIGURE B.2: Quadrotor system in the lab for testing purposes

B.1 Aerodynamic Parameters

The dynamics of quadrotor s during aerodynamic effects have been studied to build a robust system which takes aerodynamic dynamics is to consideration. However, many studies have neglected aerodynamics due to the fact that their focus is only on stability during hovering. However, in the case of flight trajectories and flight manoeuvres, these aerodynamic phenomena can significantly impact the overall quadrotor's dynamics [135].

Many researchers have stressed the importance of dealing with the full nonlinear dynamics of the quadrotor. There is another phenomenon that appears clearly which is called the "ground effect", this happens when a rotor operates near the ground and this effect can be observed when the quadrotor is driven away from the ground by a thrust augmentation. This force pushes from the ground and is related to a reduction of the induced airflow velocity [137].

B.1.1 Thrust Factor

To relate rotor command input to the torque and force terms appearing in dynamics (3.1), a representation of the actuator characteristics is needed. Quadrotors movements such as, hovering, take off, landing and trajectory tracking are conducted by controlling the actuator demand signal since the actual rotors are fixed and cannot be tilted [131]. There are two types of propellers that are used mostly in UAVs. The first type is called the "fixed-pitch" propellers and the second type is the variable-pitch propellers. For fixed-pitch propellers, in Figure 3.2 only change in the angular velocity will produce an adjustment of the thrust force, and in this case the angle of attack of propellers is constant. On the contrary, the angle of attack of propellers is changed in the case of "variable-pitch" propeller [132]. Fixed-pitch propellers are characterized by mechanical and aerodynamic simplicity as well as low production and maintenance costs compared to the variable-pitch ones. However, the advantage of the variable type is the ability to handle aggressive manoeuvres based on the complex underlying mechanics it utilises [133].

The thrust f_i and torque T_i produced by the ith motor propeller system can be defined as a function of rotor speed in general terms

$$F_b = b\omega^2 \qquad (B.1)$$

The AscTec Hummingbird is chose as the experimental test platform. This quadrotor is popular, has good performance and is light-weight maneuverable. It has a payload of 200 g and a flight endurance of nearly 20 min. The aircraft component frame is made out of balsa wood and carbon fiber. The vehicle is powered by four brushless DC motors running off an 11.1V Lithium Polymer (LiPo) battery pack. It is equipped with an accelerometer, pressure sensor, magnetic sensor, gyros, and GPS module. These can provide the vehicle state. The test setup can be seen in Figure **??**.

$$F_b = \frac{282.6F}{169.4} = \frac{282.6M_{exp}g}{169.4} = 16.4M_{exp} \qquad (B.2)$$

$$b = 9.19 \times 10^{-6} Ns^2 \qquad (B.3)$$

B.1.2   Drag Factor

The relation of propeller angular velocity to the force generated perpendicular to the thrust is called drag factor. From this relationship, it can distinguish the similar to the trust factor. However, the drag factor is numerous lower relatively compare with the effective fan. Because of the contribution between the equations of motion and thrust factor, there is a near version of the code element theory that can be employed within.

B.2 Dynamics of Motor

The motor and controller are concentration a black box system; the data-sheet of the motor is not publicly available and the control algorithms running on the ESCs are proprietary. In order to determine their dynamics system identification is utilised. A series of random step inputs were fed to the motor controller and the response recorded as shown in Figure 5.4 . The response was measured using the motor feedback values read from the LL processor. The system identification toolbox in MATLAB was used in order to fit a transfer function. A first order model was first generated, however it exhibited a poor fit to the estimation data. The second order representation in (5.29) provided a confidence of 75% which can be seen in Figure 5.4, which was deemed acceptable.

$$\frac{1.763s + 4.67}{s^2 + 24s + 4.62} \tag{B.4}$$

B.3 Equation of Motion Parameters and Derivation

Some of the model parameters are simple to evaluate using a scale, or a ruler, in particular, the mass of the quadrotor and the arm length.

Six physical parameters $(m, L, I_{xx}, I_{yy}, I_{zz} \text{ and } J_p)$ are required to populate the system model found in the equation (3.18) to (3.23), because the system will remain only confined to the quadrotor in the general form. Therefore, these parameters are allocated to the AscTech Hummingbird. The moments of inertia around the quadrotors inertial frame, the moment of inertia of the rotor, the length of the quadrotor arm and the mass of the quadrotor. Table B.3 and Table B.1 show the standard formulae that have been used in the calculations and Table B.2 shows the weight of the separate components:

Beam:

TABLE B.1: Parallel and perpendicular axes theorems

Parallel Axis Theorem If a body has a moment of inertia I_{cm} about its centre of mass then its inertia about a parallel axis a perpendicular distance r away is given by:	$I = I_{cm} + mr^2$
Perpendicular Axis Theorem If x, y and z are perpendicular to each other with the body lying in the xy plane then:	$I_z = I_x + I_y$

TABLE B.2: Weight of the Hummingbird and components

Component	Weight
Hummingbird (without battery)	402.5g
Battery	159.0g
Frame and Additional Components	205.0g
Single Boom	10.60g
Single Motor	27.95
Propeller	6.33g

Next find the inertia of one of the cross beams of the quadrotor:

$$
\begin{aligned}
I_h &= \frac{1}{12}m\left(w^2 + l^2\right) = \frac{1}{12}(10.60)[(20.0)^2 + (170.0)^2] = 258.76\,g\,cm^2 \\
I_w &= \frac{1}{12}m\left(h^2 + l^2\right) = \frac{1}{12}(10.60)[(5.0)^2 + (170.0)^2] = 255.44\,g\,cm^2 \qquad \text{(B.5)} \\
I_l &= \frac{1}{12}m\left(h^2 + w^2\right) = \frac{1}{12}(10.60)[(5.0)^2 + (20.0)^2] = 3.75\,g\,cm^2
\end{aligned}
$$

Using the parallel axis theorem again results in the inertia about the centre of mass of the quadrotor as:
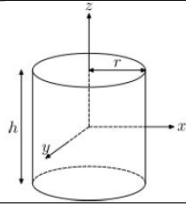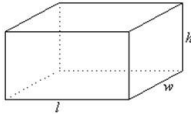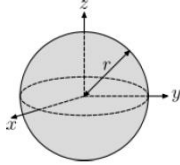
$$
\begin{aligned}
I_{zz\ beam\,quad} &= 258.76 + (10.60)(10.5)^2 = 1427.13g\,cm^2 \\
I_{xx\ beam\,quad} &= 255.44 + (10.60)(10.5)^2 = 1423.81g\,cm^2 \qquad \text{(B.6)} \\
I_{yy\ beam\,quad} &= I_d = 3.75\,g\,cm^2
\end{aligned}
$$

Propellers:

Using a similar model to that for the beam the inertia of the quadrotor may be found to be:

$$
47 \times 10^{-6} kg\,m^2
$$

TABLE B.3: Formula for moments on inertia of common shapes

Description	Figure	Formula
Point Mass	Mass m, Distance r from axis of rotation	$I = mr^2$
Solid Cylinder		$I_{zz} = mr^2$ $I_{xx} = I_{yy} = \frac{1}{12}m\left(3r^2 + h^2\right)$
Cuboid		$I_h = \frac{1}{12}m\left(w^2 + l^2\right)$ $I_w = \frac{1}{12}m\left(h^2 + l^2\right)$ $I_l = \frac{1}{12}m\left(h^2 + w^2\right)$
Sphere (solid)		$I = \frac{2m^2}{5}$

Central Body Sphere:

The inertia of the central sphere is given by:

$$I_{sphere,\,quad} = 25mr^2 = 25(381.48)(4.5)^2 = 3089.99\,g\,cm^2 \tag{B.7}$$

Where r is given as 45mm.

Additional Components:

Finally the inertia of the two point masses representing the additional components carried

about the *x*, *y* and *z* axes are:

$$I_{zz\,payload\,quad} = 2mr^2 = 2[(102.5)(6.0)^2] = 7380.0\,g\,cm^2$$

$$I_{yy\,payload\,quad} = 2mr^2 + md^2 = 2[(102.5)(6.0)^2] + (205)(4.0)^2 = 10660\,g\,cm^2 \quad (B.8)$$

$$I_{xx\,payload\,quad} = 0 + md^2 = (205)(4.0)^2 = 3280.0\,g\,cm^2$$

Total System:

The total moments of inertia of the system about the three axes required are:

$$I_{zz} = \sum I_{zz\,about\,quad}$$

$$= I_{sphere} + 4I_{zz\,motor\,quad} + 4I_{zz\,beam\,quad} + I_{zz\,payload}$$

$$= 18.4 \times 10^{-3} kg\,m^2$$

$$I_{xx} = \sum I_{xx\,about\,quad}$$

$$= I_{sphere} + 2I_{xx\,motor\,quad} 2I_{yy\,motor\,quad} + 2I_{xx\,beam\,quad} 2I_{yy\,beam\,quad} + I_{xx\,payload} \quad (B.9)$$

$$= 10.7 \times 10^{-3} kg\,m^2$$

$$I_{yy} = \sum I_{yy\,about\,quad}$$

$$= I_{sphere} + 2I_{xx\,motor\,quad} 2I_{yy\,motor\,quad} + 2I_{xx\,beam\,quad} 2I_{yy\,beam\,quad} + I_{yy\,payload}$$

$$= 10.7 \times 10^{-3} kg\,m^2$$

TABLE B.4: Summary of system parameters

Parameter	Value
I_{xx}	$10.7 \times 10^{-3} kg\,m^2$
I_{yy}	$10.7 \times 10^{-3} kg\,m^2$
I_{zz}	$18.4 \times 10^{-3} kg\,m^2$
Rotor $I_{zz}(J_p)$	$47 \times 10^{-6} kg\,m^2$
Quadrotor Mass	0.547 kg
Arm Length	0.168 m

Measured mass and length of arm can be seen below in Figure B.3.

FIGURE B.3: Experimental for measured mass and length of arm

The system identification of a dynamic system consists of several steps, as shown in Figure B.4.

The first step is the design of an experiment which will acquire the input/output data over a time interval. Acquiring data is not trivial and can be very laborious and expensive. This involves careful planning of the inputs to be applied such that sufficient information about the system dynamics is obtained. The second step defines the structure of the system, for example, the type and the order of the differential equation relating the input to the output. The third step is identification/estimation, which involves determining the numerical values of the structural parameters, which minimize the error between the system to be identified, and its model. The estimation method that is used in this research is the prediction error method. The final step, validation, consists of relating the system to the identified model responses in the time or frequency domain to instill confidence in the obtained model. If the identified model is not accepted, a more complex model structure must be considered, its parameters estimated, and the new model validated.
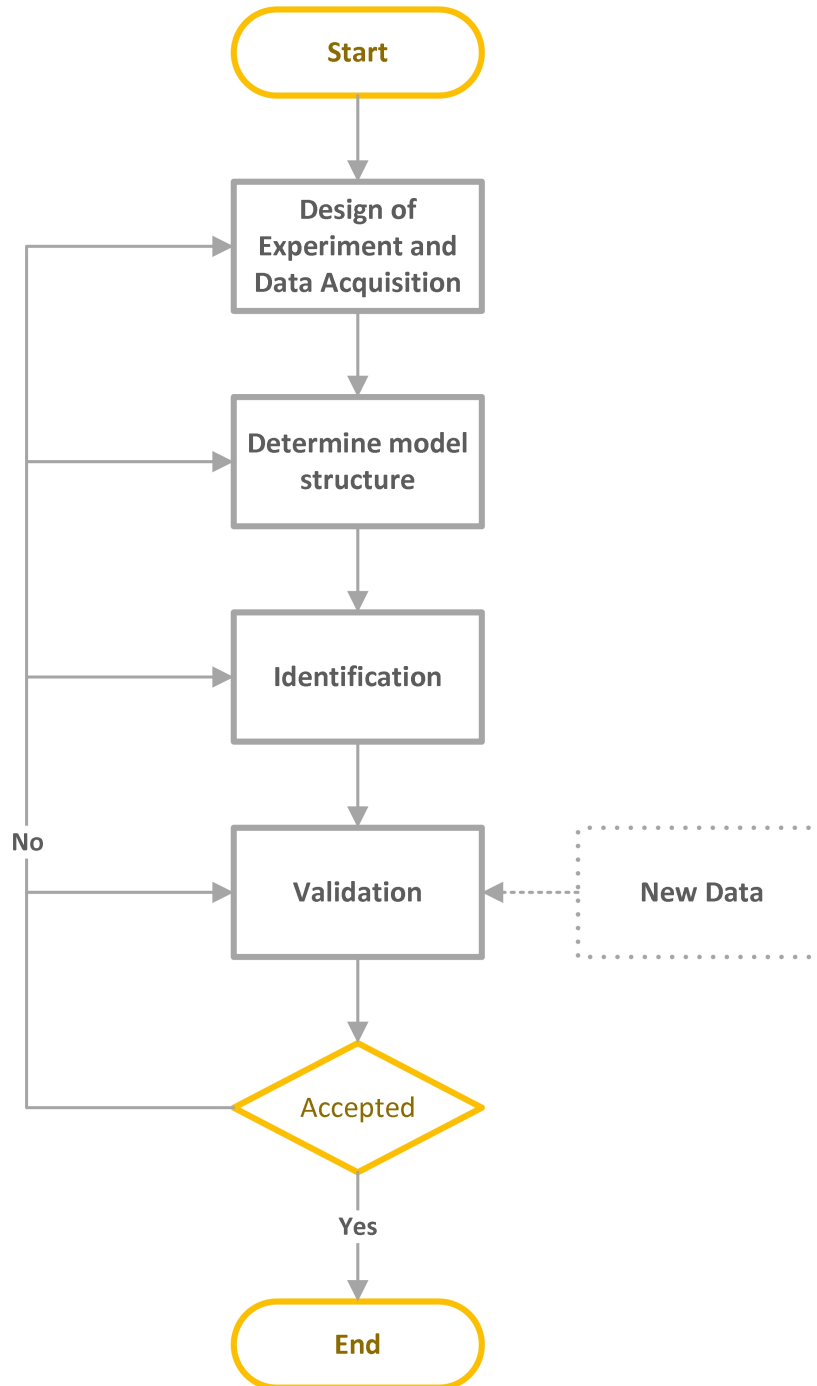
FIGURE B.4: Schematic flowchart of the system identification process
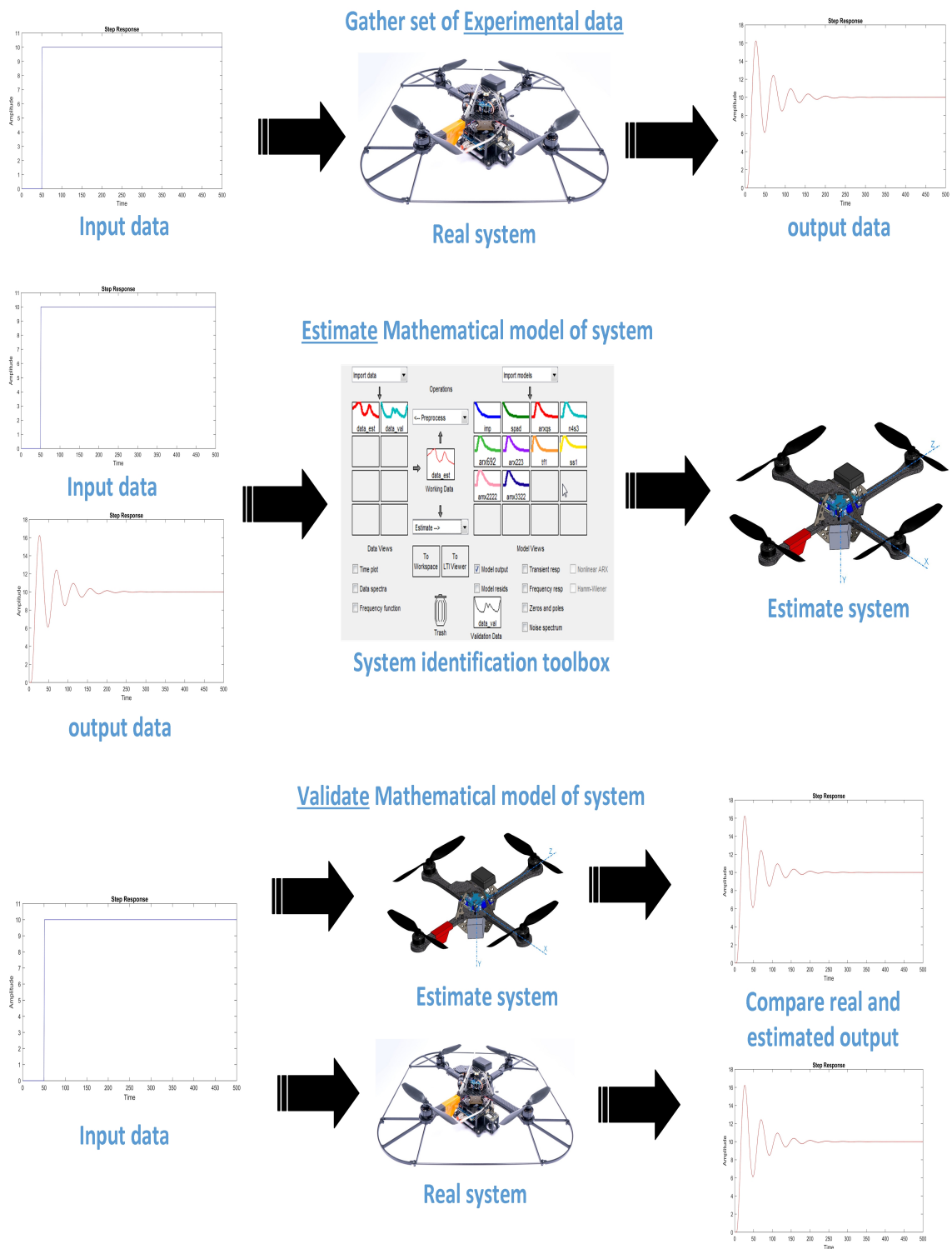
FIGURE B.5: Process of Building Models form Data

Appendix C

Modelling of Quadrotor Dynamics

C.1 Mathematical Modelling of Quadrotor Dynamics

As mentioned in Chapter 3, Euler angles are most commonly used to describe orientation of a rigid body. Therefore they will be adopted in representation of angles. Also the plus configuration seen in Figure 3.1 is adopted hence their dynamics are identical to the cross configuration as discussed previously. The quadrotor structure is presented in Figure 3.1 including the corresponding angular velocities, torques, forces (f_i) and speed (Ω_i) created by the four rotors. This section summaries the derivation of a suitable, widely used, quadrotor model as introduced in Chapter 3.
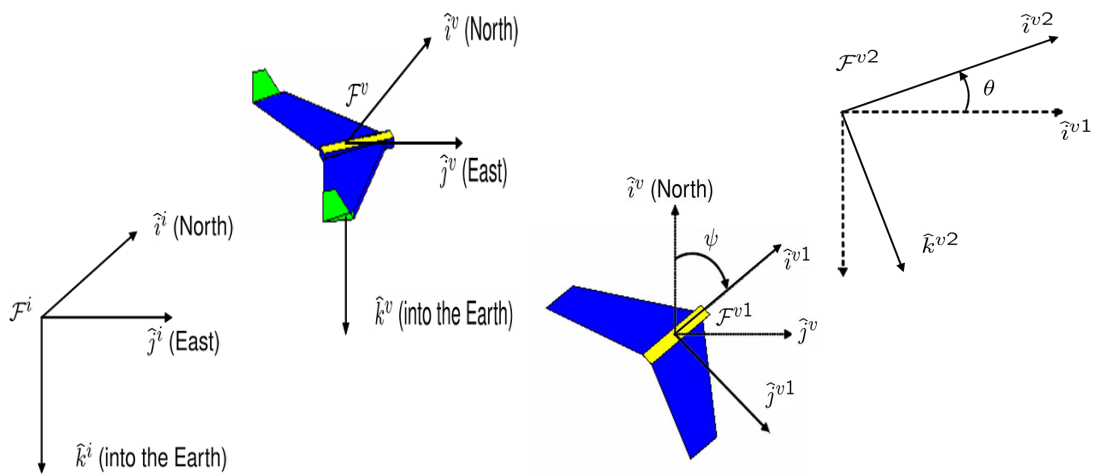
FIGURE C.1: The inertial, vehicle, vehicle-1 and vehicle-2 frames of a quadrotor

The position of the quadrotor is expressed in the inertial frame F^i as $(x, y, z)^T$ axes with ξ. The attitude, is defined with three Euler angles η, First frame F^i is rotated around its z by ψ, to produce frame F^{v2}. Then F^{v2} is rotated about its y axis by θ to produce F^{v1}. Lastly F^{v1} is rotated about its x axis by ϕ to produce F^v. The frame F^v has the same orientation as body frame F^b. As defined in Chapter 3, equation (3.2) defines vector q which contains the linear and angular position vectors

$$\xi = \begin{bmatrix} x \\ y \\ z \end{bmatrix} , \ \eta = \begin{bmatrix} \phi \\ \theta \\ \psi \end{bmatrix} , q_\Theta = \begin{bmatrix} \xi \\ \eta \end{bmatrix} \tag{F.1}$$

The origin of the body frame is at the center of mass of the quadrotor. The velocity $(\varsigma, v, w)^T$ and the angular velocity $(p, q, r)^T$ of the quadrotor are defined with respect to the body frame F^b. Also p is the roll rate measured along $\hat{i}^b$ in F^b, q is the pitch rate measured along $\hat{j}^b$ in F^b, and r is the yaw rate measured along $\hat{k}^b$ in F^b.

The transformation from a point p^v in F^v to a point p^{v1} in F^{v1} is given by $p^{v1} = R_v^{v1}(\psi)p^v$, where

$$R_v^{v1}(\psi) = \begin{bmatrix} C_\psi & -S_\psi & 0 \\ S_\psi & C_\psi & 0 \\ 0 & 0 & 1 \end{bmatrix} \tag{F.2}$$

in which $S_x = \sin(x)$ and $C_x = \cos(x)$. Similarly, the transformation from F^{v1} to F^{v2} is given by

$$R_{v1}^{v2}(\theta) = \begin{bmatrix} C_\theta & 0 & S_\theta \\ 0 & 1 & 0 \\ -S_\theta & 0 & C_\theta \end{bmatrix} \tag{F.3}$$

Finally, the transformation from F^{v2} to F^b is given by

$$R_{v2}^b(\phi) = \begin{bmatrix} 1 & 0 & 0 \\ 0 & C_\phi & -S_\phi \\ 0 & S_\phi & C_\phi \end{bmatrix} \tag{F.4}$$

The transformation from the vehicle frame to the body frame is given by

$$R_v^b(\phi;\theta;\psi) = R_{v2}^b(\phi)R_{v1}^{v2}(\theta)R_v^{v1}(\psi) = \begin{bmatrix} C_\psi C_\theta & S_\psi C_\theta & -S_\theta \\ C_\psi S_\theta S_\phi - S_\psi C_\phi & S_\psi S_\theta S_\phi + C_\psi C_\phi & C_\theta S_\phi \\ C_\psi S_\theta C_\phi + S_\psi S_\phi & S_\psi S_\theta C_\phi - C_\psi S_\phi & C_\theta C_\phi \end{bmatrix}$$

$$\text{(F.5)}$$

The positions $(x,y,z)^T$ are inertial frame quantities, where velocities $(\varsigma,v,w)^T$ are body frame quantities. Therefore the relationship between position and velocities is given by

$$\frac{\mathrm{d}}{\mathrm{d}t}\begin{bmatrix} x \\ y \\ -z \end{bmatrix} = R_b^v \begin{bmatrix} \varsigma \\ v \\ w \end{bmatrix} = (R_v^b)^T \begin{bmatrix} \varsigma \\ v \\ w \end{bmatrix}$$

$$= \begin{bmatrix} C_\psi C_\theta & C_\psi S_\theta S_\phi - S_\psi C_\phi & C_\psi S_\theta C_\phi + S_\psi S_\phi \\ S_\psi C_\theta & S_\psi S_\theta S_\phi + C_\psi C_\phi & S_\psi S_\theta C_\phi - C_\psi S_\phi \\ -S_\theta & C_\theta S_\phi & C_\theta C_\phi \end{bmatrix} \begin{bmatrix} \varsigma \\ v \\ w \end{bmatrix} \quad \text{(F.6)}$$

where note that rotation matrices are orthogonal thus $R_b^v = (R_v^b)^{-1} = (R_v^b)^T$, the rotation matrix from the inertial frame to the body frame. The relationship between absolute angles ϕ, θ and ψ, and the angular rates $(p,q,r)^T$ is defined in F^b the roll angle ϕ is defined in F^{v2}, the pitch angle θ is defined in F^{v1}, and the yaw angle ψ is defined in the vehicle frame F^v. Therefore, we need to find the relation between body angular velocities $(p,q,r)^T$ and rate of change of Euler angles $(\dot{\phi},\dot{\theta},\dot{\psi})^T$. Since $\dot{\phi}$, $\dot{\theta}$, $\dot{\psi}$ are small and noting that

$$R_{v2}^b(\dot{\phi}) = R_{v1}^{v2}(\dot{\theta}) = R_v^{v1}(\dot{\psi}) = I$$

by using transformations defined in equation (F.7), one can obtain angular velocities $[p,q,r]$ as follows

$$
\begin{bmatrix} p \\ q \\ r \end{bmatrix} = R_{v2}^{b}(\dot{\phi}) \begin{bmatrix} \dot{\phi} \\ 0 \\ 0 \end{bmatrix} + R_{v2}^{b}(\phi)R_{v1}^{v2}(\dot{\theta}) \begin{bmatrix} 0 \\ \dot{\theta} \\ 0 \end{bmatrix} + R_{v2}^{b}(\phi)R_{v1}^{v2}(\theta)R_{v}^{v1}(\psi) \begin{bmatrix} 0 \\ 0 \\ \dot{\psi} \end{bmatrix} \tag{F.7}
$$

$$
\begin{bmatrix} p \\ q \\ r \end{bmatrix} = \begin{bmatrix} \dot{\phi} \\ 0 \\ 0 \end{bmatrix} + R_{v2}^{b}(\phi) \begin{bmatrix} 0 \\ \dot{\theta} \\ 0 \end{bmatrix} + R_{v1}^{v2}(\theta)R_{v2}^{b}(\phi) \begin{bmatrix} 0 \\ 0 \\ \dot{\psi} \end{bmatrix} \tag{F.8}
$$

$$
= \begin{bmatrix} \dot{\phi} \\ 0 \\ 0 \end{bmatrix} + \begin{bmatrix} 1 & 0 & 0 \\ 0 & C_\phi & S_\phi \\ 0 & -S_\phi & C_\phi \end{bmatrix} \begin{bmatrix} 0 \\ \dot{\theta} \\ 0 \end{bmatrix} + \begin{bmatrix} C_\theta & 0 & -S_\theta \\ 0 & 1 & 0 \\ S_\theta & 0 & C_\theta \end{bmatrix} \begin{bmatrix} 1 & 0 & 0 \\ 0 & C_\phi & S_\phi \\ 0 & -S_\phi & C_\phi \end{bmatrix} \begin{bmatrix} 0 \\ 0 \\ \dot{\psi} \end{bmatrix} \tag{F.9}
$$

$$
= \begin{bmatrix} 1 & 0 & -S_\theta \\ 0 & C_\phi & S_\phi C_\theta \\ 0 & -S_\phi & C_\phi C_\theta \end{bmatrix} \begin{bmatrix} \dot{\phi} \\ \dot{\theta} \\ \dot{\psi} \end{bmatrix} \tag{F.10}
$$

This can be inverted to give

$$
\begin{bmatrix} \dot{\phi} \\ \dot{\theta} \\ \dot{\psi} \end{bmatrix} = \begin{bmatrix} 1 & S_\phi T_\theta & C_\phi T_\theta \\ 0 & C_\phi & -S_\phi \\ 0 & S_\phi/C_\theta & C_\phi/C_\theta \end{bmatrix} \begin{bmatrix} p \\ q \\ r \end{bmatrix}, \tag{F.11}
$$

in which $T_x = \tan(x)$. As illustrated in Chapter 3, the quadrotor is assumed to have symmetric structure with the four arms aligned with the body x- and y-axes. Therefore, the inertia matrix has the diagonal form

$$
I = \begin{bmatrix} \iota_{xx} & 0 & 0 \\ 0 & \iota_{yy} & 0 \\ 0 & 0 & \iota_{zz} \end{bmatrix} \tag{F.12}
$$

in which $\iota_{xx} = \iota_{yy}$.

C.1.1   Newton-Euler Dynamic Formulation

As stated in Chapter 3, the formulation of Newton-Euler is most common due to its efficiency. Based on the review of Chapter 3, the quadrotor is assumed to comprise a rigid body, with 6 DOF dynamic taking into account mass of the body, m [*kg*] and inertia matrix *I*. Newton's laws only hold in inertial frames, therefore Newton's law applied to the translational motion yields

$$m\frac{\mathrm{d}v}{\mathrm{d}t_i} = F \tag{F.13}$$

where F is the total applied to the quadrotor, and $\frac{\mathrm{d}}{\mathrm{d}t_i}$ is the time derivative in the inertial frame. From the equation of Coriolis we have

$$m\left(\frac{\mathrm{d}v}{\mathrm{d}t_i} + \omega_{b/i} \times v\right) = F \tag{F.14}$$

where $\omega_{b/i}$ is the angular velocity of the airframe with respect to the inertial frame. Since the control force is computed and applied in the body coordinate system, and since ω is measured in body coordinates, we will express the equation (F.14) in body coordinates, where $v^b = (\varsigma, v, w)^T$, and $\omega^b_{b/i} = (p, q, r)^T$. Therefore, in body coordinates, equation (F.14) becomes

$$\begin{pmatrix} \dot{\varsigma} \\ \dot{v} \\ \dot{w} \end{pmatrix} = \begin{pmatrix} rv - qw \\ pw - ru \\ qu - pv \end{pmatrix} + \frac{1}{m}\begin{pmatrix} f_x \\ f_y \\ f_z \end{pmatrix} \tag{F.16}$$

For rotational motion, Newton's second law states that

$$\frac{\mathrm{d}h^b}{\mathrm{d}t_i} = T \tag{F.17}$$

where h is the angular momentum and T is the applied torque. Using the equation of Coriolis we have

$$\frac{\mathrm{d}h}{\mathrm{d}t_i} = \frac{\mathrm{d}h}{\mathrm{d}t_b} + \omega_{b/i} \times h = T \tag{F.18}$$

where $h = I\omega_{b/i}^b$ where I is the constant inertia matrix and

$$I^{-1} = \begin{bmatrix} \frac{1}{\iota_{xx}} & 0 & 0 \\ 0 & \frac{1}{\iota_{yy}} & 0 \\ 0 & 0 & \frac{1}{\iota_{zz}} \end{bmatrix} \tag{F.19}$$

Recall equation (3.11) in Chapter 3, in which T^b can be defining as $T^b = (\tau_\phi, \tau_\theta, \tau_\psi)^T$, and $F^b = (f_x, f_y, f_z)^T$. Therefore, equation (F.18) can be written in body coordinates as

$$\begin{pmatrix} \dot{p} \\ \dot{q} \\ \dot{r} \end{pmatrix} = \begin{pmatrix} \frac{1}{\iota_{xx}} & 0 & 0 \\ 0 & \frac{1}{\iota_{yy}} & 0 \\ 0 & 0 & \frac{1}{\iota_{zz}} \end{pmatrix} \left[\begin{pmatrix} 0 & r & -q \\ -r & 0 & p \\ q & -p & 0 \end{pmatrix} \begin{pmatrix} \iota_{xx} & 0 & 0 \\ 0 & \iota_{yy} & 0 \\ 0 & 0 & \iota_{zz} \end{pmatrix} \begin{pmatrix} p \\ q \\ r \end{pmatrix} + \begin{pmatrix} \tau_\phi \\ \tau_\theta \\ \tau_\psi \end{pmatrix} \right] \tag{F.20}$$

$$= \begin{pmatrix} \frac{\iota_{yy}-\iota_{zz}}{\iota_{xx}}qr \\ \frac{\iota_{zz}-\iota_{xx}}{\iota_{yy}}pr \\ \frac{\iota_{xx}-\iota_{yy}}{\iota_{zz}}pq \end{pmatrix} + \begin{pmatrix} \frac{1}{\iota_{xx}}\tau_\phi \\ \frac{1}{\iota_{yy}}\tau_\theta \\ \frac{1}{\iota_{zz}}\tau_\psi \end{pmatrix}$$

The six degree of freedom model for the quadrotor kinematics and dynamics can be summarized from equation (F.6), equation (F.16), equation (F.20) and equation (F.11) as follows:

$$\begin{bmatrix} \dot{x} \\ \dot{y} \\ \dot{z} \end{bmatrix} = \begin{bmatrix} C_\psi C_\theta & C_\psi S_\theta S_\phi - S_\psi C_\phi & C_\psi S_\theta C_\phi + S_\psi S_\phi \\ S_\psi C_\theta & S_\psi S_\theta S_\phi + C_\psi C_\phi & S_\psi S_\theta C_\phi - C_\psi S_\phi \\ S_\theta & -C_\theta S_\phi & -C_\theta C_\phi \end{bmatrix} \begin{bmatrix} \varsigma \\ v \\ w \end{bmatrix} \tag{F.21}$$

$$\begin{bmatrix} \dot{\varsigma} \\ \dot{v} \\ \dot{w} \end{bmatrix} = \begin{bmatrix} rv - qw \\ pw - r\varsigma \\ q\varsigma - pv \end{bmatrix} + \frac{1}{m}\begin{pmatrix} f_x \\ f_y \\ f_z \end{pmatrix} \tag{F.22}$$

$$
\begin{bmatrix} \dot{\phi} \\ \dot{\theta} \\ \dot{\psi} \end{bmatrix} = \begin{bmatrix} 1 & S_\phi T_\theta & C_\phi T_\theta \\ 0 & C_\phi & -S_\phi \\ 0 & S_\phi/C_\theta & C_\phi/C_\theta \end{bmatrix} \begin{bmatrix} p \\ q \\ r \end{bmatrix}, \tag{F.23}
$$

$$
\begin{bmatrix} \dot{p} \\ \dot{q} \\ \dot{r} \end{bmatrix} = \begin{bmatrix} \frac{\iota_{yy}-\iota_{zz}}{\iota_{xx}}qr \\ \frac{\iota_{zz}-\iota_{xx}}{\iota_{yy}}pr \\ \frac{\iota_{xx}-\iota_{yy}}{\iota_{zz}}pq \end{bmatrix} + \begin{bmatrix} \frac{1}{\iota_{xx}}\tau_\phi \\ \frac{1}{\iota_{yy}}\tau_\theta \\ \frac{1}{\iota_{zz}}\tau_\psi \end{bmatrix} \tag{F.24}
$$

Therefore, recalling equation (3.11) it is possible to rewrite equation (3.11) in the general matrix form

$$
M(\mathbf{q}_\Theta)\,\ddot{\mathbf{q}}_\Theta + B(\mathbf{q}_\Theta,\dot{\mathbf{q}}_\Theta) + G(\mathbf{q}_\Theta) = \Gamma(\mathbf{q}_\Theta) + \tau(U), \tag{F.25}
$$

Where the inertial matrix and the Coriolis-centripetal matrix

$$
M(\mathbf{q}_\Theta) = \begin{bmatrix} m & 0 & 0 & 0 & 0 & 0 \\ 0 & m & 0 & 0 & 0 & 0 \\ 0 & 0 & m & 0 & 0 & 0 \\ 0 & 0 & 0 & \iota_{xx} & 0 & 0 \\ 0 & 0 & 0 & 0 & \iota_{yy} & 0 \\ 0 & 0 & 0 & 0 & 0 & \iota_{zz} \end{bmatrix}, \quad B(\mathbf{q}_\Theta,\dot{\mathbf{q}}_\Theta) = \begin{bmatrix} 0 & 0 & 0 & 0 & m\dot{z} & -m\dot{y} \\ 0 & 0 & 0 & -m\dot{z} & 0 & m\dot{x} \\ 0 & 0 & 0 & m\dot{y} & -m\dot{x} & 0 \\ 0 & 0 & 0 & 0 & \iota_{zz}\dot{\psi} & -\iota_{yy}\dot{\theta} \\ 0 & 0 & 0 & -\iota_{zz}\dot{\psi} & 0 & \iota_{xx}\dot{\phi} \\ 0 & 0 & 0 & \iota_{yy}\dot{\theta} & -\iota_{xx}\dot{\phi} & 0 \end{bmatrix} \tag{F.26}
$$

Next, in the vehicle frame F^v, the gravity force acting on the center of mass is given by

$$
f_g^v = \begin{bmatrix} 0 \\ 0 \\ mg \end{bmatrix}
$$

However, since v in the equation (F.14) is expressed in F^b, we need to transform to the body frame to give

$$
f_g^b = R_v^b f_g^v
$$

$$
G(\mathbf{q}_\Theta) = f_g^b = R_v^b \begin{bmatrix} 0 \\ 0 \\ mg \end{bmatrix} = \begin{bmatrix} -mgS_\theta \\ mgC_\theta S_\phi \\ mgC_\theta S_\phi \end{bmatrix} \tag{F.27}
$$

From equation (3.12), the gyroscopic effect due to the rotation of the propellers is

$$\Gamma(\mathbf{q}_\Theta) = \begin{bmatrix} 0_{3\times4} \\ J_p \begin{bmatrix} -\dot\theta \\ -\dot\phi \\ 0 \end{bmatrix} \Omega \end{bmatrix} = J_p \begin{bmatrix} 0 \\ 0 \\ 0 \\ \Omega_1\dot\theta - \Omega_2\dot\theta + \Omega_3\dot\theta - \Omega_4\dot\theta \\ -\Omega_1\dot\phi + \Omega_2\dot\phi - \Omega_3\dot\phi + \Omega_4\dot\phi \\ 0 \end{bmatrix} \tag{F.28}$$

Where the J_p is the propeller moment of inertia around its rotational axis. Using equation (3.1) in Chapter 3, the torque and force due to the angular velocity of the four propellers can be represented as

$$\underbrace{f_i = C_T\rho A_r r_i^2 \Omega_i^2}_{b}$$

$$\underbrace{T_i = C_D\rho A_r r_i^2 \Omega_i^2}_{d} \tag{F.29}$$

By using equation (3.1) and equation (F.29), and setting b equal to $C_T\rho A_r r_i^2$ and d equal to $C_D\rho A_r r_i^2$. the control inputs can be defined as:

$$
\begin{aligned}
\tau(U) &= \begin{bmatrix} l(f_2 - f_4) \\ l(f_1 - f_3) \\ T_1 + T_2 + T_3 + T_4 \\ 0 \\ 0 \\ f_1 + f_2 + f_3 + f_4 \end{bmatrix} = \begin{bmatrix} 0 & lb & 0 & -lb \\ lb & 0 & -lb & 0 \\ d & d & d & d \\ 0 & 0 & 0 & 0 \\ 0 & 0 & 0 & 0 \\ b & b & b & b \end{bmatrix} \begin{bmatrix} \Omega_1^2 \\ \Omega_2^2 \\ \Omega_3^2 \\ \Omega_4^2 \end{bmatrix} \\
&= \begin{bmatrix} 0 & lb & 0 & -lb \\ lb & 0 & -lb & 0 \\ d & d & d & d \\ 0 & 0 & 0 & 0 \\ 0 & 0 & 0 & 0 \\ b & b & b & b \end{bmatrix} \begin{bmatrix} 0 \\ 0 \\ \begin{bmatrix} 1 & 1 & 1 & 1 \\ 0 & -1 & 0 & 1 \\ 1 & 0 & -1 & 0 \\ 1 & -1 & 1 & -1 \end{bmatrix}^{-1} U \end{bmatrix}
\end{aligned} \tag{F.30}
$$

in which l is the distance between the rotor and the center of mass of the quadrotor . From

equation (F.25) and using equation (F.30), equation (F.21) and equation (F.24)

$$\ddot{\mathbf{q}}_\Theta = M(\mathbf{q}_\Theta)^{-1}(-B(\mathbf{q}_\Theta, \dot{\mathbf{q}}_\Theta)\dot{\mathbf{q}}_\Theta + G(\mathbf{q}_\Theta) + \Gamma(\mathbf{q}_\Theta) + \tau) \tag{F.31}$$

the complete dynamic model are

$$\ddot{x} = \frac{1}{m}(c\phi s\theta c\psi + s\phi s\psi)U_1 \tag{F.32}$$

$$\ddot{y} = \frac{1}{m}(c\phi s\theta s\psi - s\phi c\psi)U_1 \tag{F.33}$$

$$\ddot{z} = \frac{1}{m}(mg - c\phi c\theta)U_1 \tag{F.34}$$

$$\ddot{\phi} = \frac{1}{\iota_{xx}}\left[lU_2 + \dot{\theta}\dot{\psi}(\iota_{yy} - \iota_{zz}) + \dot{\theta}J_P\Omega_r\right] \tag{F.35}$$

$$\ddot{\theta} = \frac{1}{\iota_{yy}}\left[lU_3 + \dot{\phi}\dot{\psi}(\iota_{zz} - \iota_{xx}) + \dot{\phi}J_P\Omega_r\right] \tag{F.36}$$

$$\ddot{\psi} = \frac{1}{\iota_{zz}}\left[U_4 + \dot{\phi}\dot{\theta}(\iota_{xx} - \iota_{yy}) + \dot{\psi}J_P\Omega_r\right] \tag{F.37}$$

Appendix D

The Current Electricity Network in UK

D.1 UK's Electricity Network System

The UK' electricity network system consists of two layers of electricity networks, Transmission and Distribution (T&D):

- Transmission network: consists of high voltage transmission lines ($>$132kV in England and Wales) [208]. The transmission network is the backbone of the electricity network system. Transmission networks are typically at 275kV and 400kV.

- Distribution network: consists of low voltage ($<$132kV) power lines. These are like the ribs of the electricity system.

Electricity from power stations or other forms of electricity generators for example offshore wind farms travels down the transmission networks into the distribution networks. It then passes through a series of substations to the end customer, as shown in the Figure D.1. Smaller generators such as medium sized wind farms connect to the distribution networks. As the electricity passes through each substation the voltage drops until it is 230V (the voltage used in homes).
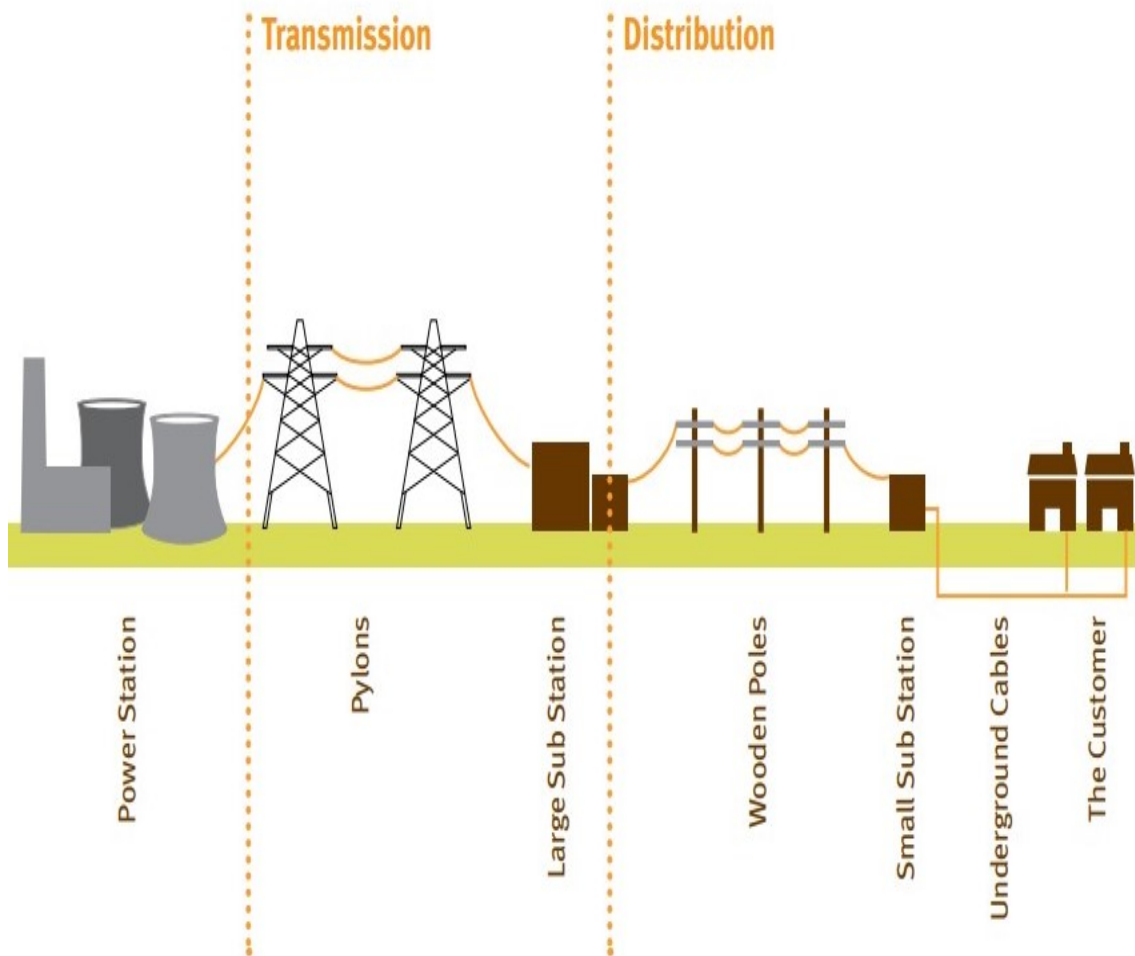
FIGURE D.1: The general delivery of electricity in UK

D.2 Various TNOs and DNOs in UK

- Transmission: Electricity transmission assets are owned and maintained by regional monopoly Transmission Owners (TOs): National Grid Electricity Transmission plc (NGET) in England, Scottish Power Transmission Limited (SPTL) in southern Scotland and Scottish Hydro-Electric Transmission Limited (SHETL) in northern Scotland.

- Distribution: There are 14 Distribution Network Operators (DNOs) owned by seven different groups 5. There are also four independent network operators who own and run smaller networks embedded in the DNO networks.

The different network operators are shown in the Figure D.2 below

FIGURE D.2: The general delivery of electricity in UK

The electricity losses during transmission and distribution increased in 2020. Despite a fall in the electricity demand, the electricity transmission and distribution losses for 2020 were 27.45 TWh, equating to 9.43% of the total annual consumption. The average annual electricity losses during transmission and distribution in the UK is 28.59 TWh [209].

The Network Losses Minimization Strategy for both TNOs and DNOs express requirement is to develop approaches to assess losses in the network and develop effective methods to reduce these losses with the available devices and components in the net-
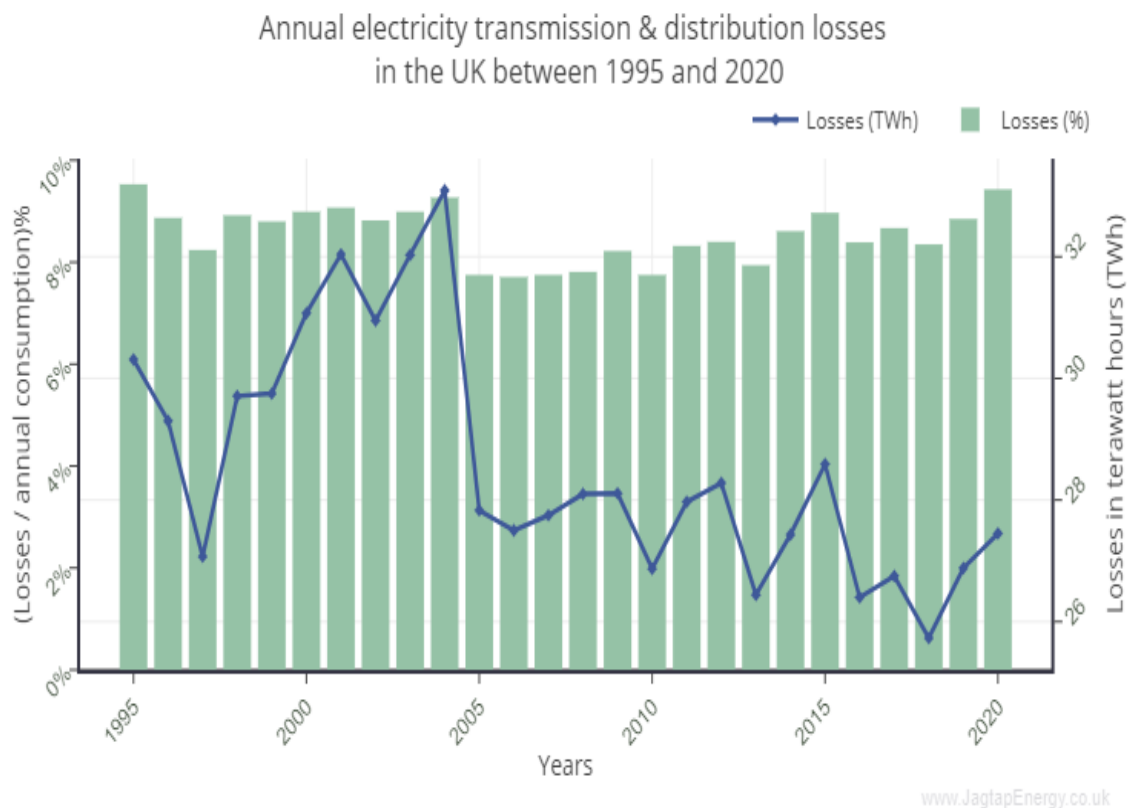
FIGURE D.3: Annual electricity transmission and distribution losses in the UK

work [210]. Losses in the UK for both TNOs and DNOs such as the SP Energy Networks, Electricity Northwest, Northern Powergrid, UK Power Networks, SSE, Western Power distribution and NIE are illustrated in Table D.1.

TABLE D.1: Losses in the UK for TNOs and DNOs

Company/Region	Transmission or Distribution	Losses (%)
UK EDFE EPN	Distribution	3.7%
UK CN East	Distribution	3.9%
UK CN West	Distribution	4.3%
UK Electricity North West	Distribution	4.8%
UK CE NEDL	Distribution	5.0%
UK WPD S Wales	Distribution	5.1%
UK CE YEDL	Distribution	5.5%
UK EDFE SPN	Distribution	5.6%
UK SP Distribution	Distribution	5.9%
UK SEE Southern	Distribution	6.2%
UK WP Manweb	Distribution	6.6%
UK See Hydro	Distribution	8.1%

References

[1] Strategic Defence Intelligence. The global uav payload market 2012-2022. *Strategic Defence Intelligence: White Papers*, 2013.

[2] Guoru Ding, Qihui Wu, Linyuan Zhang, Yun Lin, Theodoros A Tsiftsis, and Yu-Dong Yao. An amateur drone surveillance system based on the cognitive internet of things. *IEEE Communications Magazine*, 56(1):29–35, 2018.

[3] ICF CONSULTING. Overview of the potential for undergrounding the electricity networks in europe. *DG TREN/European Commission [En ligne]*, 2003.

[4] Dusko P Nedic. Simulation of large system disturbances. *Electr. Eng. Electron.*, 2003.

[5] D. Geach, D. Barron, L. Crompton, and N. Tart. Improving network security and stability using an integrated operational tripping system. *IET 9th International Conference on Developments in Power System Protection (DPSP 2008)*, pages 375–379, March 2008.

[6] J. Adams and K. A. Parlikad. Dynamic maintenance based on criticality in electricity network. *Asset Management Conference 2015*, pages 1–7, November 2016.

[7] National grid education/electricity transmission national grid assets. 2013.

[8] Q. Huang, W. Zhen, and P. W. T. Pong. A novel approach for fault location of overhead transmission line with noncontact magnetic-field measurement. *IEEE Power Energy Society General Meeting*, 27(3):1186–1195, July 2012.

[9] A. Bernstein, D. Bienstock, D. Hay M. Uzunoglu, and G. Zussman. Power grid vulnerability to geographically correlated failures-analysis and control implications. *IEEE INFOCOM Conference on Computer Communications*, pages 2634–2642, April 2014.

[10] H. Foudeh and A. S. Mokhtar. Elimination of total harmonic distortion in transmission lines using adaptive fuzzy logic in de-icing process. *Jordanian International Electrical and Electronics Engineering Conference (JIEEEC)*, pages 1–6, October 2015.

[11] J. Liu and Z. Zheng. Fault location and type identification on transmission line using a novel traveling wave method. *International Conference on High Voltage Engineering and Application*, pages 290–293, September 2012.

[12] P. A. Gulbhile, J. R. Rana, and B. T. Deshmukh. Review for overhead line fault detection using GSM technology. *International Journal of Advanced Research in Electrical*, 5(12):1186–1195, December 2016.

[13] J. Han, W. K. Kim, J. W. Lee, and C. H. Kim. Fault type classification in transmission line using STFT. *IET International Conference on Developments in Power Systems Protection (DPSP 2012)*, pages 1–5, April 2012.

[14] M. A. Jarrahi, H. Samet, and A. Sahebi. An EMD based fault type identification scheme in transmission line. *Iranian Conference on Electrical Engineering (ICEE)*, pages 422–427, May 2016.

[15] T. Bouthiba. Fault location in EHV transmission lines using artificial neural networks. *International Journal of Applied Mathematics and Computer Science*, 14(1):69–78, May 2004.

[16] L. Shang and J. LV. A new approach for identification of the fault type on transmission lines. *International Conference on Systems and Informatics (ICSAI 2014)*, pages 132–136, November 2014.

[17] M.V. Deshpande. *Electrical Power System Design*. McGraw-Hill, 1984.

[18] Xinyan Qin, Gongping Wu, Jin Lei, Fei Fan, Xuhui Ye, and Quanjie Mei. A novel method of autonomous inspection for transmission line based on cable inspection robot lidar data. *Sensors*, 18(2):596, 2018.

[19] Xinyan Qin, Gongping Wu, Jin Lei, Fei Fan, Xuhui Ye, and Quanjie Mei. A novel method of autonomous inspection for transmission line based on cable inspection robot lidar data. *Sensors*, 18(2):596, 2018.

[20] Helicopter operator qualifications for line work. *IEEE Transactions on Power Delivery*, 15(1):326–332, Jan 2000.

[21] C. C. Whitworth, A. W. G. Duller, D. I. Jones, and G. K. Earp. Aerial video inspection of overhead power lines. *Power Engineering Journal*, 15(1):25–32, Feb 2001.

[22] Recommended practices for helicopter bonding procedures for live-line work. *IEEE Transactions on Power Delivery*, 15(1):333–349, Jan 2000.

[23] H. Manninen, J. Kilter, and M. Landsberg. Advanced condition monitoring method for high voltage overhead lines based on visual inspection. In *2018 IEEE Power Energy Society General Meeting (PESGM)*, pages 1–5, Aug 2018.

[24] M. de Nigris, I. Gutman, and A. Pigini. Live-line maintenance of ac overhead lines equipped with non ceramic insulators (NCI). In *IEEE PES T D 2010*, pages 1–6, April 2010.

[25] ESMOL Subcommittee. Safety considerations when placing a person with tools in an air gap to change porcelain and glass insulators on transmission systems of 345 kv and above, using ladder and aerial lift methods. *IEEE Transactions on Power Delivery*, 17(3):805–808, July 2002.

[26] L. Martin. Transmission structure risk management. *IEEE Power and Energy Magazine*, 14(5 Supplement):28–33, Sep. 2016.

[27] C. C. Whitworth, A. W. G. Duller, D. I. Jones, and G. K. Earp. Aerial video inspection of overhead power lines. *Power Engineering Journal*, 15(1):25–32, Feb 2001.

[28] M. Yokoya, Y. Katsuragi, Y. Goda, Y. Nagata, and Y. Asano. Development of lightning-resistant overhead ground wire. *IEEE Transactions on Power Delivery*, 9(3):1517–1523, July 1994.

[29] Xinyan Qin, Gongping Wu, Jin Lei, Fei Fan, and Xuhui Ye. Detecting inspection objects of power line from cable inspection robot lidar data. *Sensors*, 18(4):1284, April 2018.

[30] L. Matikainen et al. Remote sensing methods for power line corridor surveys. *ISPRS J. Photogramn. Remote Sens*, 119:10 –31, Sep 2016.

[31] M. Ghassemi, M. Farzaneh, and W. A. Chisholm. Three-dimensional fem electrical field calculation for frp hot stick during ehv live-line work. *IEEE Transactions on Dielectrics and Electrical Insulation*, 21(6):2531–2540, December 2014.

[32] M. Abad, M. García-Gracia, N. El Halabi, and D. López Andía. Network impulse response based-on fault location method for fault location in power distribution systems. *IET Generation, Transmission Distribution*, 10(15):3962–3970, November 2016.

[33] S.S. Gururajapathy, H. Mokhlis, and H.A. Illias. Fault location and detection techniques in power distribution systems with distributed generation: A review. *Renewable and Sustainable Energy Reviews*, 74:949–958, 2017.

[34] Y. Zhai, R. Chen, Q. Yang, X. Li, and Z. Zhao. Insulator fault detection based on spatial morphological features of aerial images. *IEEE Access*, 6:35316–35326, June 2018.

[35] G. H. Vaillancourt, S. Carignan, and C. Jean. Experience with the detection of faulty composite insulators on high-voltage power lines by the electric field measurement method. *IEEE Transactions on Power Delivery*, 13(2):661–666, April 1998.

[36] S. Han, R. Hao, and J. Lee. Inspection of insulators on high-voltage power transmission lines. *IEEE Transactions on Power Delivery*, 24(4):2319–2327, Oct 2009.

[37] O. Menendez, F. A. Auat Cheein, M. Perez, and S. Kouro. Robotics in power systems: Enabling a more reliable and safe grid. *IEEE Industrial Electronics Magazine*, 11(2):22–34, June 2017.

[38] V. T. Morgan. The detection and damping of overhead-line conductor vibration. *Proceedings of the IEE - Part A: Power Engineering*, 109(3):239–250, 1962.

[39] André Leblond and Keith E. Lindsey. Maintenance. In Konstantin O. Papailiou, editor, *Overhead Lines*, pages 1151–1208. Springer International Publishing, Cham, 2017.

[40] Mostafa Nayyerloo, XiaoQi Chen, WH Wang, and J Geoffrey Chase. Cable-climbing robots for power line inspection. 2009.

[41] S. D. Guikema, R. A. Davidson, and Haibin Liu. Statistical models of the effects of tree trimming on power system outages. *IEEE Transactions on Power Delivery*, 21(3):1549–1557, July 2006.

[42] T. Dokic and M. Kezunovic. Predictive risk management for dynamic tree trimming scheduling for distribution networks. *IEEE Transactions on Smart Grid*, 10(5):4776–4785, Sep. 2019.

[43] Zhenyu Zhu, Siyao Lu, Bingtuan Gao, Tao Yi, and Bin Chen. Life cycle cost analysis of three types of power lines in 10 kv distribution network. *Inventions*, 1(4), 2016.

[44] T.S. Kishore and S.K. Singal. Optimal economic planning of power transmission lines: A review. *Renewable and Sustainable Energy Reviews*, 39:949 – 974, 2014.

[45] Y. Q. Chen, O. Fink, and G. Sansavini. Combined fault location and classification for power transmission lines fault diagnosis with integrated feature extraction. *IEEE Transactions on Industrial Electronics*, 65(1):561–569, Jan 2018.

[46] A. de Souza Gomes, M. A. Costa, T. G. A. de Faria, and W. M. Caminhas. Detection and classification of faults in power transmission lines using functional analysis and computational intelligence. *IEEE Transactions on Power Delivery*, 28(3):1402–1413, July 2013.

[47] J. Izykowski, R. Molag, E. Rosolowski, and M. M. Saha. Accurate location of faults on power transmission lines with use of two-end unsynchronized measurements. *IEEE Transactions on Power Delivery*, 21(2):627–633, April 2006.

[48] S. F. Alwash, V. K. Ramachandaramurthy, and N. Mithulananthan. Fault-location scheme for power distribution system with distributed generation. *IEEE Transactions on Power Delivery*, 30(3):1187–1195, June 2015.

[49] Sheng Lin, ZY He, XP Li, and QQ Qian. Travelling wave time–frequency characteristic-based fault location method for transmission lines. *IET generation, transmission & distribution*, 6(8):764–772, 2012.

[50] G. Cardoso, J. G. Rolim, and H. H. Zurn. Application of neural-network modules to electric power system fault section estimation. *IEEE Transactions on Power Delivery*, 19(3):1034–1041, July 2004.

[51] B. Ravikumar, D. Thukaram, and H. P. Khincha. Application of support vector machines for fault diagnosis in power transmission system. *IET Generation, Transmission Distribution*, 2(1):119–130, January 2008.

[52] A. K. Pradhan, A. Routray, and B. Biswal. Higher order statistics-fuzzy integrated scheme for fault classification of a series-compensated transmission line. *IEEE Transactions on Power Delivery*, 19(2):891–893, April 2004.

[53] J. Sawada, K. Kusumoto, Y. Maikawa, T. Munakata, and Y. Ishikawa. A mobile robot for inspection of power transmission lines. *IEEE Transactions on Power Delivery*, 6(1):309–315, Jan 1991.

[54] S. Han, R. Hao, and J. Lee. Inspection of insulators on high-voltage power transmission lines. *IEEE Transactions on Power Delivery*, 24(4):2319–2327, Oct 2009.

[55] J. Park, J. Lee, B. Cho, and K. Oh. An inspection robot for live-line suspension insulator strings in 345-kv power lines. *IEEE Transactions on Power Delivery*, 27(2):632–639, April 2012.

[56] C. F. Barbosa and F. E. Nallin. Corrosion detection robot for energized power lines. In *Proceedings of the 2014 3rd International Conference on Applied Robotics for the Power Industry*, pages 1–6, Oct 2014.

[57] Rebecca Miller, Farshid Abbasi, and Javad Mohammadpour Velni. Power line robotic device for overhead line inspection and maintenance. *Industrial Robot: An International Journal*, 44:75–84, 08 2016.

[58] J. Jin, H. Zhu, and G. Zhang. Counterweight-navigation of a mobile inspection robot working on the ground wires. In *2009 IEEE International Conference on Automation and Logistics*, pages 278–282, Aug 2009.

[59] Zheng Li and Yi Ruan. Autonomous inspection robot for power transmission lines maintenance while operating on the overhead ground wires. *International Journal of Advanced Robotic Systems*, 7(4):25, 2010.

[60] N. Pouliot, P. Richard, and S. Montambault. Linescout technology opens the way to robotic inspection and maintenance of high-voltage power lines. *IEEE Power and Energy Technology Systems Journal*, 2(1):1–11, March 2015.

[61] P. Debenest and M. Guarnieri. Expliner — from prototype towards a practical robot for inspection of high-voltage lines. In *2010 1st International Conference on Applied Robotics for the Power Industry*, pages 1–6, Oct 2010.

[62] O. Menendez, F. A. Auat Cheein, M. Perez, and S. Kouro. Robotics in power systems: Enabling a more reliable and safe grid. *IEEE Industrial Electronics Magazine*, 11(2):22–34, June 2017.

[63] H. Shakhatreh, A. H. Sawalmeh, A. Al-Fuqaha, Z. Dou, E. Almaita, I. Khalil, N. S. Othman, A. Khreishah, and M. Guizani. Unmanned aerial vehicles (uavs): A survey on civil applications and key research challenges. *IEEE Access*, 7:48572–48634, April 2019.

[64] S. Jordan, J. Moore, S. Hovet, J. Box, J. Perry, K. Kirsche, D. Lewis, and Z. T. H. Tse. State-of-the-art technologies for uav inspections. *IET Radar, Sonar Navigation*, 12(2):151–164, February 2018.

[65] C. Yan, L. Fu, J. Zhang, and J. Wang. A comprehensive survey on uav communication channel modeling. *IEEE Access*, 7:107769–107792, August 2019.

[66] M. H. Choi, B. Shirinzadeh, and R. Porter. System identification-based sliding mode control for small-scaled autonomous aerial vehicles with unknown aerodynamics derivatives. *IEEE/ASME Transactions on Mechatronics*, 21(6):2944–2952, Dec 2016.

[67] Li Zheng and Ruan Yi. Fault diagnosis system for the inspection robot in power transmission lines maintenance. In *International Conference on Optical Instruments and Technology: Optoelectronic Imaging and Process Technology*, volume 7513, page 75130E. International Society for Optics and Photonics, 2009.

[68] L. F. Luque-Vega, B. Castillo-Toledo, A. Loukianov, and L. E. Gonzalez-Jimenez. Power line inspection via an unmanned aerial system based on the quadrotor helicopter. In *MELECON 2014 - 2014 17th IEEE Mediterranean Electrotechnical Conference*, pages 393–397, April 2014.

[69] Rishav Bhola, Nandigam Hari Krishna, K.N. Ramesh, J. Senthilnath, and Gautham Anand. Detection of the power lines in uav remote sensed images using spectral-spatial methods. *Journal of Environmental Management*, 206:1233 – 1242, 2018.

[70] Z. Li, Y. Liu, R. Hayward, J. Zhang, and J. Cai. Knowledge-based power line detection for uav surveillance and inspection systems. In *2008 23rd International Conference Image and Vision Computing New Zealand*, pages 1–6, Nov 2008.

[71] W. Yi, C. Liming, K. Lingyu, Z. Jie, and W. Miao. Research on application mode of large fixed-wing uav system on overhead transmission line. In *2017 IEEE International Conference on Unmanned Systems (ICUS)*, pages 88–91, Oct 2017.

[72] Y. Wu, G. Zhao, J. Hu, Y. Ouyang, S. X. Wang, J. He, F. Gao, and S. Wang. Overhead transmission line parameter reconstruction for uav inspection based on tunneling magnetoresistive sensors and inverse models. *IEEE Transactions on Power Delivery*, 34(3):819–827, June 2019.

[73] Lei Dai, Juntong Qi, Jianda Han, Zhiming Wang, Weichun Ge, Chenggang Wang, Gang Liu, Yong Xia, Ke Du, and Ling Wang. Camera selection for unmanned helicopter power line inspection. In *IEEE PES Innovative Smart Grid Technologies*, pages 1–4, May 2012.

[74] Ian E. Nordeng, Ahmad Hasan, Doug Olsen, and Jeremiah Neubert. Debc detection with deep learning. In Puneet Sharma and Filippo Maria Bianchi, editors, *Image Analysis*, pages 248–259, Cham, 2017. Springer International Publishing.

[75] F. Mirallès, P. Hamelin, G. Lambert, S. Lavoie, N. Pouliot, M. Montfrond, and S. Montambault. Linedrone technology: Landing an unmanned aerial vehicle on a power line. In *2018 IEEE International Conference on Robotics and Automation (ICRA)*, pages 6545–6552, May 2018.

[76] X. Hui, J. Bian, X. Zhao, and M. Tan. Deep-learning-based autonomous navigation approach for uav transmission line inspection. In *2018 Tenth International Conference on Advanced Computational Intelligence (ICACI)*, pages 455–460, March 2018.

[77] X. Xie, Z. Liu, C. Xu, and Y. Zhang. A multiple sensors platform method for power line inspection based on a large unmanned helicopter. *Sensors*, 17(6):1222, 2017.

[78] M. Matthee, B. Toebes, and M. Brus. Armed conflict and international law: In search of the human face. *Springer*, 2013.

[79] J Balaram, MiMi Aung, and Matthew P Golombek. The ingenuity helicopter on the perseverance rover. *Space Science Reviews*, 217(4):1–11, 2021.

[80] M. Fanni and A. Khalifa. A new 6-DOF quadrotor manipulation system: Design, kinematics, dynamics, and control. *IEEE/ASME Transactions on Mechatronics*, 22(3):1315–1326, June 2017.

[81] S. Bouabdallah and R. Siegwart. *Design and Control of a Miniature Quadrotor*, pages 171–210. Springer Netherlands, Dordrecht, 2007.

[82] J. Escareno, S. Salazar-Cruz, and R. Lozano. Embedded control of a four-rotor UAV. *American Control Conference*, pages 3936–3941, June 2006.

[83] P. Pounds, R. Mahony, and P. Corke. Modelling and control of a large quadrotor robot. *Control Engineering Practice*, 18(7):691–699, 2010.

[84] V. Kumar, D. Mellinger, and M. Shomin. Control of quadrotors for robust perching and landing. *Proceedings of the International Powered Lift Conference*, pages 205–225, October 2010.

[85] M. Saska. MAV-swarms: Unmanned aerial vehicles stabilized along a given path using onboard relative localization. *International Conference on Unmanned Aircraft Systems (ICUAS)*, pages 894–903, June 2015.

[86] J. A. Preiss, W. Hönig, G. S. Sukhatme, and N. Ayanian. Crazyswarm: A large nano-quadcopter swarm. *IEEE International Conference on Intelligent Robots and Systems (IROS)*, pages 5002–5018, October 2016.

[87] M. Saska, J. Vakula, and L. Přeućil. Swarms of micro aerial vehicles stabilized under a visual relative localization. *IEEE International Conference on Robotics and Automation (ICRA)*, pages 3570–3575, May 2014.

[88] Z. Fang, X. Wang, and J. Sun. Design and nonlinear control of an indoor quadrotor flying robot. pages 429–434, 2010.

[89] G. S. Avellar, G. A. Pereira, L. C. Pimenta, and P. Iscold. Multi-uav routing for area coverage and remote sensing with minimum time. *Sensors*, 15(11):27783–27803, 2015.

[90] D. W. Casbeer, D. B. Kingston, R. W. Beard, and T. W. McLain. Cooperative forest fire surveillance using a team of small unmanned air vehicles. *International Journal of Systems Science*, 37(6):351–360, 2006.

[91] J. Nikolic, M. Burri, J. Rehder, S. Leutenegger, C. Huerzeler, and R. Siegwart. A uav system for inspection of industrial facilities. pages 1–8, 2013.

[92] Matthew Dunbabin and Lino Marques. Robots for environmental monitoring: Significant advancements and applications. *IEEE Robotics & Automation Magazine*, 19(1):24–39, 2012.

[93] Sonia Waharte and Niki Trigoni. Supporting search and rescue operations with uavs. In *2010 International Conference on Emerging Security Technologies*, pages 142–147. IEEE, 2010.

[94] Antonio Barrientos, Julian Colorado, Jaime del Cerro, Alexander Martinez, Claudio Rossi, David Sanz, and Joao Valente. Aerial remote sensing in agriculture: A practical approach to area coverage and path planning for fleets of mini aerial robots. *Journal of Field Robotics*, 28(5):667–689, 2011.

[95] Francesco Nex and Fabio Remondino. Uav for 3d mapping applications: a review. *Applied geomatics*, 6(1):1–15, 2014.

[96] G. Hoffmann, D. G. Rajnarayan, S. L. Waslander, D. Dostal, J. S. Jang, and C. J. Tomlin. The stanford testbed of autonomous rotorcraft for multi agent control (starmac). In *The 23rd Digital Avionics Systems Conference (IEEE Cat. No.04CH37576)*, volume 2, pages 12.E.4–121, Oct 2004.

[97] S. Bouabdallah, M. Becker, and R. Siegwart. Autonomous miniature flying robots: coming soon! - research, development, and results. *IEEE Robotics Automation Magazine*, 14(3):88–98, Sep. 2007.

[98] Antonio Barrientos, Julian Colorado, Jaime del Cerro, Alexander Martinez, Claudio Rossi, David Sanz, and Joao Valente. Aerial remote sensing in agriculture: A practical approach to area coverage and path planning for fleets of mini aerial robots. *Journal of Field Robotics*, 28(5):667–689, 2011.

[99] G. Conte and P. Doherty. An integrated uav navigation system based on aerial image matching. In *2008 IEEE Aerospace Conference*, pages 1–10, March 2008.

[100] Wang Fei, CUI Jin-Qiang, CHEN Ben-Mei, and H LEE Tong. A comprehensive uav indoor navigation system based on vision optical flow and laser fastslam. *Acta Automatica Sinica*, 39(11):1889–1899, 2013.

[101] J. Dougherty, D. Lee, and T. Lee. Laser-based guidance of a quadrotor uav for precise landing on an inclined surface. In *2014 American Control Conference*, pages 1210–1215, June 2014.

[102] P. McKerrow. Modelling the draganflyer four-rotor helicopter. In *IEEE International Conference on Robotics and Automation, 2004. Proceedings. ICRA '04. 2004*, volume 4, pages 3596–3601 Vol.4, April 2004.

[103] M. G. Earl and R. D'Andrea. Real-time attitude estimation techniques applied to a four rotor helicopter. In *2004 43rd IEEE Conference on Decision and Control (CDC) (IEEE Cat. No.04CH37601)*, volume 4, pages 3956–3961 Vol.4, Dec 2004.

[104] A. Tayebi and S. McGilvray. Attitude stabilization of a four-rotor aerial robot. In *2004 43rd IEEE Conference on Decision and Control (CDC) (IEEE Cat. No.04CH37601)*, volume 2, pages 1216–1221 Vol.2, Dec 2004.

[105] N. Guenard, T. Hamel, and V. Moreau. Dynamic modeling and intuitive control strategy for an "x4-flyer". In *2005 International Conference on Control and Automation*, volume 1, pages 141–146 Vol. 1, June 2005.

[106] S. Bouabdallah and R. Siegwart. Full control of a quadrotor. In *2007 IEEE/RSJ International Conference on Intelligent Robots and Systems*, pages 153–158, Oct 2007.

[107] A. H. Ahmed, A. N. Ouda, A. M. Kamel, and Y. Z. Elhalwagy. Attitude stabilization and altitude control of quadrotor. In *2016 12th International Computer Engineering Conference (ICENCO)*, pages 123–130, Dec 2016.

[108] Glenn Tournier, Mario Valenti, Jonathan How, and Eric Feron. Estimation and control of a quadrotor vehicle using monocular vision and moire patterns. In *AIAA Guidance, Navigation, and Control Conference and Exhibit*, page 6711, 2006.

[109] T. K. Venugopalan, T. Taher, and G. Barbastathis. Autonomous landing of an unmanned aerial vehicle on an autonomous marine vehicle. In *2012 Oceans*, pages 1–9, Oct 2012.

[110] V. Grabe, H. H. Bülthoff, and P. R. Giordano. On-board velocity estimation and closed-loop control of a quadrotor uav based on optical flow. In *2012 IEEE International Conference on Robotics and Automation*, pages 491–497, May 2012.

[111] S. Lange, N. Sunderhauf, and P. Protzel. A vision based onboard approach for landing and position control of an autonomous multirotor uav in gps-denied environments. pages 1–6, June 2009.

[112] Pascual Campoy, Pedro J Garcia, Antonio Barrientos, Jaime del Cerro, Iñaqui Aguirre, Andrés Roa, Rafael Garcia, and José M Muñoz. An stereoscopic vision system guiding an autonomous helicopter for overhead power cable inspection. In *International Workshop on Robot Vision*, pages 115–124. Springer, 2001.

[113] D. Jones. Power line inspection - a uav concept. In *2005 The IEE Forum on Autonomous Systems (Ref. No. 2005/11271)*, pages 8 pp.–, Nov 2005.

[114] H. Wu, M. Lv, C. Liu, and C. Liu. Planning efficient and robust behaviors for model-based power tower inspection. In *2012 2nd International Conference on Applied Robotics for the Power Industry (CARPI)*, pages 163–166, Sep. 2012.

[115] Carol Martinez, Carlos Sampedro, Aneesh Chauhan, and Pascual Campoy. Towards autonomous detection and tracking of electric towers for aerial power line inspection. In *2014 International Conference on Unmanned Aircraft Systems (ICUAS)*, pages 284–295. IEEE, 2014.

[116] S. Hrabar, T. Merz, and D. Frousheger. Development of an autonomous helicopter for aerial powerline inspections. In *2010 1st International Conference on Applied Robotics for the Power Industry*, pages 1–6, Oct 2010.

[117] J. Bian, X. Hui, X. Zhao, and M. Tan. A novel monocular-based navigation approach for uav autonomous transmission-line inspection. In *2018 IEEE/RSJ International Conference on Intelligent Robots and Systems (IROS)*, pages 1–7, Oct 2018.

[118] B. Wang, X. Chen, Q. Wang, L. Liu, H. Zhang, and B. Li. Power line inspection with a flying robot. In *2010 1st International Conference on Applied Robotics for the Power Industry*, pages 1–6, Oct 2010.

[119] D. Sadykova, D. Pernebayeva, M. Bagheri, and A. James. In-yolo: Real-time detection of outdoor high voltage insulators using uav imaging. *IEEE Transactions on Power Delivery*, pages 1–1, 2019.

[120] E. Karakose. Performance evaluation of electrical transmission line detection and tracking algorithms based on image processing using uav. In *2017 International Artificial Intelligence and Data Processing Symposium (IDAP)*, pages 1–5, Sep. 2017.

[121] Z. Zamudio, R. Lozano, J. Torres, and V. Rosas. Stereo vision for the stabilization of a quadrotor. In *2012 16th International Conference on System Theory, Control and Computing (ICSTCC)*, pages 1–6, Oct 2012.

[122] S. Hrabar. 3d path planning and stereo-based obstacle avoidance for rotorcraft uavs. In *2008 IEEE/RSJ International Conference on Intelligent Robots and Systems*, pages 807–814, Sep. 2008.

[123] H. Romero, S. Salazar, and R. Lozano. Real-time stabilization of an eight-rotor uav using optical flow. *IEEE Transactions on Robotics*, 25(4):809–817, Aug 2009.

[124] V. Mistler, A. Benallegue, and N. K. M'Sirdi. Exact linearization and noninteracting control of a 4 rotors helicopter via dynamic feedback. *IEEE International Workshop on Robot and Human Interactive Communication*, pages 586–593, 2001.

[125] A. Mokhtari and A. Benallegue. Dynamic feedback controller of euler angles and wind parameters estimation for a quadrotor unmanned aerial vehicle. *IEEE International Conference on Robotics and Automation (ICRA)*, 3:2359–2366, April 2004.

[126] S. Bouabdallah, P. Murrieri, and R. Siegwart. Design and control of an indoor micro quadrotor. *IEEE International Conference on Robotics and Automation (ICRA)*, 5:4393–4398, April 2004.

[127] M. Odelga, P. Stegagno, and H. H. Bülthoff. A fully actuated quadrotor UAV with a propeller tilting mechanism: Modeling and control. *IEEE International Conference on Advanced Intelligent Mechatronics (AIM)*, pages 306–311, 2016.

[128] T.N. Dief and S. Yoshida. Review: Modeling and classical controller of quad-rotor. *International Journal of Computer*, 5(4), August 2015.

[129] A. L. Salih, M. Moghavvemi, H. A. F. Mohamed, and K. S. Gaeid. Modelling and pid controller design for a quadrotor unmanned air vehicle. *IEEE International Conference on Automation, Quality and Testing, Robotics (AQTR)*, 1:1–5, March 2010.

[130] A. Soumelidis, P. Gaspar, G. Regula, and B. Lantos. Control of an experimental mini quad-rotor UAV. *Mediterranean Conference on Control and Automation*, pages 1252–1257, June 2008.

[131] G. Jithu and P. R. Jayasree. Quadrotor modelling and control. *IEEE International Conference on Electrical, Electronics, and Optimization Techniques (ICEEOT)*, pages 1167–1172, 2016.

[132] M. J. Cutler. *Design and Control of an Autonomous Variable-Pitch Quadrotor Helicopter.* Master's thesis, Massachusetts Institute of Technology. Dept. of Aeronautics and Astronautics, Cambridge, MA, USA, 2012.

[133] M. Cutler, N. Kemal Ure, B. Michini, and J. P. How. Comparison of fixed and variable pitch actuators for agile quadrotors. *Proceedings of the AIAA Guidance, Navigation, and Control Conference (GNC)*, August 2011.

[134] M. Y. Amir and V. Abbass. Modeling of quadrotor helicopter dynamics. *International Conference on Smart Manufacturing Application*, pages 100–105, April 2008.

[135] P. J. Bristeau, P. Martin, E. Salaün, and N. Petit. The role of propeller aerodynamics in the model of a quadrotor uav. *in Proceedings of the 2009 European Control Conference (ECC)*, pages 683–688, August 2009.

[136] H. Huang, G. M. Hoffmann, S. L. Waslander, and C. J. Tomlin. Aerodynamics and control of autonomous quadrotor helicopters in aggressive maneuvering. *In Proceedings of the IEEE International Conference on Robotics and Automation*, pages 3277–3282, May 2009.

[137] C. Powers, D. Mellinger, and A. Kushleyev. Influence of aerodynamics and proximity effects in quadrotor flight. *In Proceedings of the International Symposium on Experimental Robotics*, pages 17–21, 2012.

[138] S. Gupte, Paul Infant Teenu Mohandas, and J. M. Conrad. A survey of quadrotor unmanned aerial vehicles. *2012 Proceedings of IEEE Southeastcon*, pages 1–6, March 2012.

[139] T. Luukkonen. Modelling and control of quadcopter. *Independent research project in applied mathematics, Espoo*, 2011.

[140] K. U. Lee, H. S. Kim, J. B. Park, and Y. H. Choi. Hovering control of a quadrotor. *IEEE International Conference on Control, Automation and Systems*, pages 162–167, October 2012.

[141] J. Li and Y. Li. Dynamic analysis and pid control for a quadrotor. *IEEE International Conference on Mechatronics and Automation*, pages 573–578, August 2011.

[142] G. M. Hoffmann, S. L. Waslander, and C. J. Tomlin. Quadrotor helicopter trajectory tracking control. *AIAA guidance, navigation and control conference and exhibit*, page 7410, August 2008.

[143] J. Ren, D. X. Liu, K. Li, J. Liu, Y. Feng, and X. Lin. Cascade pid controller for quadrotor. *IEEE International Conference on Information and Automation (ICIA)*, 44,(5):120–124, 2016.

[144] S. Bouabdallah, A. Noth, and R. Siegwart. PID vs LQ control techniques applied to an indoor micro quadrotor. *Proceedings of IEEE/RSJ International Conference on Intelligent Robots and Systems (IROS)*, 3(28):2451–2456, October 2004.

[145] I. D. Cowling, O. A. Yakimenko, J. F. Whidborne, and A. K. Cooke. A prototype of an autonomous controller for a quadrotor UAV. pages 4001–4008, July 2007.

[146] W. Wang, H. Ma, and C.Y. Sun. Control system design for multi-rotor MAV. *Journal of Theoretical and Applied Mechanics*, 51(4):1027–1038, 2013.

[147] B. Fan, J. Sun, and Y. Yu. A LQR controller for a quadrotor: Design and experiment. *IEEE Youth Academic Annual Conference of Chinese Association of Automation (YAC)*, pages 81–86, November 2016.

[148] H.K. Khalil. Noninear systems. *Prentice-Hall, New Jersey*, 2(5):5–1, 1996.

[149] P.V. Kokotovic, M. Krstic, and I. Kanellakopoulos. Backstepping to passivity: recursive design of adaptive systems. pages 3276–3280, 1992.

[150] T. Madani and A. Benallegue. Backstepping control for a quadrotor helicopter. *IEEE/RSJ International Conference on Intelligent Robots and Systems*, pages 3255–3260, October 2006.

[151] X. Huo, M. Huo, and H.R. Karimi. Attitude stabilization control of a quadrotor UAV by using backstepping approach. *Mathematical Problems in Engineering*, 2014, 2014.

[152] L. Tan, L. Lu, and G. Jin. Attitude stabilization control of a quadrotor helicopter using integral backstepping. *IEEE International Conference on Automatic Control and Artificial Intelligence (ACAI 2012)*, pages 573–577, March 2012.

[153] Z. Fang and W. Gao. Adaptive integral backstepping control of a micro-quadrotor. *IEEE International Conference on Intelligent Control and Information Processing*, 2:910–915, July 2011.

[154] R. Xu and U. Ozguner. Sliding mode control of a quadrotor helicopter. *Proceedings of the 45th IEEE Conference on Decision and Control*, pages 4957–4962, December 2006.

[155] N. Li, S. Yu, and Z. Xi. Nonlinear control design for a quad rotor unmanned aerial vehicle. *IEEE Chinese Control Conference (CCC)*, pages 469–474, 2016.

[156] R. Lopez, S. Salazar, A. Martinez-Vasquez, I. Gonzalez-Hernandez, and R. Lozano. Altitude control of a quad-rotor using adaptive sliding mode. *IEEE International Conference on Unmanned Aircraft Systems (ICUAS)*, pages 1111–1116, June 2016.

[157] Douglas A Bristow, Marina Tharayil, and Andrew G Alleyne. A survey of iterative learning control. *IEEE control systems magazine*, 26(3):96–114, 2006.

[158] Jian-Xin Xu. A survey on iterative learning control for nonlinear systems. *International Journal of Control*, 84(7):1275–1294, 2011.

[159] Fei Gao, Weisheng Chen, Zhiwu Li, Jing Li, and Bin Xu. Neural network-based distributed cooperative learning control for multiagent systems via event-triggered communication. *IEEE transactions on neural networks and learning systems*, 31(2):407–419, 2019.

[160] Wei He, Tingting Meng, Xiuyu He, and Changyin Sun. Iterative learning control for a flapping wing micro aerial vehicle under distributed disturbances. *IEEE transactions on cybernetics*, 49(4):1524–1535, 2018.

[161] Xufeng Wang, Xingwei Kong, Jianhui Zhi, Yong Chen, and Xinmin Dong. Real-time drogue recognition and 3d locating for uav autonomous aerial refueling based on monocular machine vision. *Chinese Journal of Aeronautics*, 28(6):1667–1675, 2015.

[162] Andreas Hock and Angela P Schoellig. Distributed iterative learning control for a team of quadrotors. pages 4640–4646, 2016.

[163] Pong-in Pipatpaibul and PR Ouyang. Application of online iterative learning tracking control for quadrotor uavs. *International Scholarly Research Notices*, 2013, 2013.

[164] Ma Zhaowei, Hu Tianjiang, Shen Lincheng, Kong Weiwei, Zhao Boxin, and Yao Kaidi. An iterative learning controller for quadrotor uav path following at a constant altitude. pages 4406–4411, 2015.

[165] Wojciech Giernacki. Iterative learning method for in-flight auto-tuning of uav controllers based on basic sensory information. *Applied Sciences*, 9(4):648, 2019.

[166] David H Owens and Jari Hätönen. Iterative learning control—an optimization paradigm. *Annual reviews in control*, 29(1):57–70, 2005.

[167] E.F.Camacho and C.B. Alba. Model predictive control. 2013.

[168] M. Uchiyama. Formation of high speed motion pattern of mechanical arm by trial. *Transactions of the Society of Instrument and Control Engineers*, 19(5):706–712, August 1978.

[169] S. Arimoto, S. Kawamura, and F. Miyazaki. Bettering operations of robots by learning. *Journal of Robotic systems*, 1(2):123–140, 1984b.

[170] Richard W Longman. Iterative learning control and repetitive control for engineering practice. *International journal of control*, 73(10):930–954, 2000.

[171] S. Arimoto, S. Kawamura, F. Miyazaki, and S. Tamaki. Learning control theory for dynamical systems. *In Proceedings of 24rd Conference on Decision and Control*, pages 1375–1380, 1985.

[172] S. Arimoto, S. Kawamura, and F. Miyazaki. Bettering operation of dynamic system by learning: A new control theory for servomechanism or mechatronics systems. *In Proceedings of 23rd Conference on Decision and Control*, pages 1064–1069, 1984a.

[173] H. Ahn, Y. Chen, and K. L. Moore. Iterative learning control: Brief survey and categorization. *IEEE Transactions on Systems, Man, and Cybernetics, Part C (Applications and Reviews)*, 37(6):1099–1121, 2007.

[174] Y. Chen and K. L. Moore. An optimal design of PD-type iterative learning control with monotonic convergence. *Proceedings of the IEEE Internatinal Symposium on Intelligent Control*, pages 55–60, 2002.

[175] K. L. Moore. *Iterative Learning Control for Deterministic Systems*. Springer-Verlag, Berlin, Heidelberg, 1993.

[176] D. A. Bristow. Weighting matrix design for robust monotonic convergence in norm optimal iterative learning control. *In American Control Conference*, pages 4554–4560, 2008b.

[177] J. D. Ratcliffe, L. Van Duinkerken, P. L. Lewin, E. Rogers, and J. J. Hatonen. Fast norm-optimal iterative learning control for industrial applications. *In American Control Conference*, 37:1951–1956, 2005.

[178] T. Donkers, J. Van de Wijdeven, and O. Bosgra. Robustness against model uncertainties of norm optimal iterative learning control. *In American Control Conference*, pages 4561–4566, 2008.

[179] Y. Wang, E. Dassau, and F. J. Doyle. losed-loop control of artificial pancreatic β -Cell in type 1 diabetes mellitus using model predictive iterative learning control. *IEEE Transactions on Biomedical Engineering*, 57(2):211–219, 2010.

[180] K. L. Barton, J. Van de Wijdeven, A. Alleyne, O. Bosgra, and M. Steinbuch. Norm optimal cross-coupled iterative learning control. *IEEE Conference on Decision and Control*, pages 3020–3025, 2008.

[181] S. Mishra and M. Tomizuka. An optimization-based approach for design of iterative learning controllers with accelerated rates of convergence. *In 44th IEEE Conference in Decision and Control*, pages 2427–2432, 2005.

[182] I. L. Davies, C. T. Freeman, P. L. Lewin, E. Rogers, and D. H. Owens. Newton method based iterative learning control of the upper limb. *In Proceedings of the American Control Conference*, pages 3887–3892, 2008.

[183] M. Butcher, A. Karimi, and R. Longchamp. A statistical analysis of certain iterative learning control algorithms. *International Journal of Control*, 81(1):156–166, 2008b.

[184] K. Furuta and M. Yamakita. The design of learning control systems for multivariable systems. *In Proceedings of the IEEE International Symposium on Intelligent Control*, pages 371–376, 1987.

[185] J. Hätönen, C. Freeman, D. H. Owens, P. Lewin, and E. Rogers. Robustness analysis of a gradient-based repetitive algorithm for discrete-time systems. *IEEE Conference on Decision and Control (CDC)*, 57(2):1301–1306, 2004.

[186] D. H. Owens, J. Hätönen, and S. Daley. Robust gradient-based iterative learning control. *IEEE International Conference on Networking, Sensing and Control*, pages 163–168, 2007.

[187] C. T. Freeman, P. L. Lewin, and E. Rogers. Further results on the experimental evaluation of iterative learning control algorithms for non-minimum phase plants. *International Journal of Control*, 80(4):569–582, 2007.

[188] A. Notker, D. H. Owens, and E. Rogers. Iterative learning control for discrete-time systems with exponential rate of convergence. *IEE Proceedings-Control Theory and Applications*, 143(2):143–224, 1996.

[189] A. Notker, D. H. Owens, and E. Rogers. Predictive optimal iterative learning control. *International Journal of Control*, 69(2):203–226, 1998.

[190] B. Chu and D. H. Owens. Accelerated norm-optimal iterative learning control algorithms using successive projection. *International Journal of Control*, 82(8):1469–1484, 2009.

[191] N. Amann, E. Rogers, and D. H. Owens. Iterative learning control using optimal feedback and feedforward actions. *International Journal of Control*, 65(2):277–293, 1996.

[192] T. Lin, D. H. Owen, and J. Hatonen. Newton method based iterative learning control for discrete non-linear systems. *International Journal of Control*, 79(10):1263–1276, 2006.

[193] H. F. Tao, W. Paszke, E. Rogers, K. Gałkowski, and H. Z. Yang. Modified newton method based iterative learning control design for discrete nonlinear systems with constraints. *Systems Control Letters*, 118:35–43, 2018.

[194] H. A. Foudeh, P. Luk, and J. F. Whidborne. Quadrotor system design for a 3 dof platform based on iterative learning control. In *2019 Workshop on Research, Education and Development of Unmanned Aerial Systems (RED UAS)*, pages 53–59, Nov 2019.

[195] Husam A Foudeh, Patrick Luk, and James Whidborne. Application of norm optimal iterative learning control to quadrotor unmanned aerial vehicle for monitoring overhead power system. *Energies*, 13(12):3223, 2020.

[196] Angela P Schoellig, Fabian L Mueller, and Raffaello D'Andrea. Optimization-based iterative learning for precise quadrocopter trajectory tracking. *Autonomous Robots*, 33(1-2):103–127, 2012.

[197] Davood Allahverdy, Ahmad Fakharian, and Mohammad Bagher Menhaj. Backstepping integral sliding mode control with iterative learning control algorithm for quadrotor uavs. *Journal of Electrical Engineering & Technology*, 14(6):2539–2547, 2019.

[198] K. Pereida, R. R. P. R. Duivenvoorden, and A. P. Schoellig. High-precision trajectory tracking in changing environments through l1 adaptive feedback and iterative learning. In *2017 IEEE International Conference on Robotics and Automation (ICRA)*, pages 344–350, May 2017.

[199] K. Barton and D. Kingston. Systematic surveillance for uavs: A feedforward iterative learning control approach. In *2013 American Control Conference*, pages 5917–5922, June 2013.

[200] R. Ogoshi, T. Sogo, and N. Adachi. Adjoint-type iterative learning control for nonlinear nonminimum phase system - application to a planar model of a helicopter

$. In *Proceedings of the 41st SICE Annual Conference. SICE 2002.*, volume 3, pages 1547–1550 vol.3, Aug 2002.

[201] REN Jinrui, QUAN Quan, LIU Cunjia, and CAI Kai-Yuan. Docking control for probe-drogue refueling: An additive-state-decomposition-based output feedback iterative learning control method. *Chinese Journal of Aeronautics*, 2019.

[202] Xunhua Dai, Quan Quan, Jinrui Ren, and Kai-Yuan Cai. Iterative learning control and initial value estimation for probe–drogue autonomous aerial refueling of uavs. *Aerospace Science and Technology*, 82:583–593, 2018.

[203] Xunhua Dai, Quan Quan, Jinrui Ren, Zhiyu Xi, and Kai-Yuan Cai. Terminal iterative learning control for autonomous aerial refueling under aerodynamic disturbances. *Journal of Guidance, Control, and Dynamics*, 41(7):1577–1584, 2018.

[204] Katherine Karwoski. Quadrocopter control design and flight operation. *NASA USRP—Internship Final Report; Marshall Space Flight Center: Huntsville, AL, USA*, 2011.

[205] Chris T Freeman and Ying Tan. Iterative learning control with mixed constraints for point-to-point tracking. *IEEE Transactions on Control Systems Technology*, 21(3):604–616, 2012.

[206] Chris T Freeman. Constrained point-to-point iterative learning control. *IFAC Proceedings Volumes*, 44(1):3611–3616, 2011.

[207] Notker Amann, David H Owens, and Eric Rogers. Iterative learning control for discrete-time systems with exponential rate of convergence. *IEE Proceedings-Control Theory and Applications*, 143(2):217–224, 1996.

[208] Gareth P Harrison, Serafeim Karamanlis, Luis F Ochoa, et al. Life cycle assessment of the transmission network in great britain. *Energy policy*, 38(7):3622–3631, 2010.

[209] Sinan Küfeoğlu and Michael G Pollitt. The impact of pvs and evs on domestic electricity network charges: A case study from great britain. *Energy policy*, 127:412–424, 2019.

[210] Goran Strbac, Michael Pollitt, Christos Vasilakos Konstantinidis, Ioannis Konstantelos, Rodrigo Moreno, David Newbery, and Richard Green. Electricity transmission arrangements in great britain: Time for change? *Energy Policy*, 73:298–311, 2014.